UNIVERSITY OF HERTFORDSHIRE

MASTERS BY RESEARCH THESIS

Searching for Young Substellar Companions to *Gaia* Stars

Author:
Matthew J. RICKARD

Supervised by:
Prof. David J. PINFIELD
Dr. Federico MAROCCO

Centre for Astrophysics Research
School of Physics, Astronomy and Mathematics
University of Hertfordshire

Submitted to the University of Hertfordshire in fulfilment of the requirements of the degree of Masters by Research.

June 2018

Abstract

The aim of this thesis is to select young ultra-cool dwarf (UCD, spectral type later than M7) candidates that are likely companions to primary stars within the Tycho-Gaia Astrometric Solution (TGAS) catalogue. The intention is to identify a sample of "benchmark" UCDs for which youth and age constraints can be established through association with well understood primary stars. Candidate UCDs are identified through searches of two large-area optical surveys, the Sloan Digital Sky Survey (SDSS) and the Panoramic Survey Telescope and Rapid Response System (PanSTARRS), and two large-area infrared surveys, the UKIRT Infrared Deep Sky Survey (UKIDSS) and the VISTA Hemisphere Survey (VHS). Potential benchmark pairings are selected using a cone-search around each TGAS star with a search radius of 10,000 AU at the distance of each TGAS star. Photometric (colour and magnitude) requirements are imposed on possible associations through comparison, in colour magnitude diagrams (CMDs), with the location of established parallax samples of young and normal UCDs. A set of complementary approaches has been implemented to identify indications of youth in both the UCD and the primary components, the results of which have been brought together into a prioritisation scheme which has been used to guide and plan follow-up observing runs during the project. These diagnostics included unusual UCD colours in the near-infrared and optical, main-sequence lifetime constraints for the primaries, and primary over-brightness (as a function of [M/H] and $T_{\rm eff}$) indicative of pre-main sequence evolution. A broad range of database information on the stellar components is also gathered providing additional age limitations. UCD proper motion constraints are determined using multi-epoch astrometry from the search-surveys as well as archival motions from the SuperCOSMOS Science Archive. This extensive search and analysis generated a sample of 1,623 candidate young benchmark associations, twenty-four that already evidence strong youth diagnostics in both UCD and primary star components, fifty that are common-proper-motion associations, thirty where the pairs are in close proximity to each other ($<$ 6 arcseconds), and 348 where the primary candidate has high proper motion leading to expectation that the companion candidate can be rapidly motion-tested. Narrow band near-infrared observations are also presented for ten of the candidate UCD components, in an attempt to search for established H-band morphological indicators of extreme youth. With three of these candidates showing Hs-Hl and J-J3 colours consistent with synthesized predictions using previously known young objects. Finally, high priority followup plans and additional development aimed at near-future Gaia DR2 exploitation are considered as future work.

Declaration

I declare that no part of this work is being submitted concurrently for another award of the University or any other awarding body or institution. This thesis contains a substantial body of work that has not previously been submitted successfully for an award of the University or any other awarding body or institution.

The submission is my own work.

Matthew J. RICKARD
February 2018

Acknowledgements

My thanks to my wife, Anna, for the love and support as I began a new career. Thanks to Alex, Max and Thomas for keeping me sane in the office. Thanks to David and Federico for their time and patience.

Section 2.5 method was carried out and developed further under my supervision by Paaryn Vadgama, a student completing his A-Levels in Summer 2018 who worked on this project as part of a four week Nuffield Research Placement[1].

Radostin Kurtev of the Universidad de Valparaíso submitted numerous observing proposals as part of the observation program of this work and conducted the observing program in November 2017.

Research has made use of the SIMBAD database, operated at CDS, Strasbourg, France. This research made use of the cross-match service provided by CDS, Strasbourg.

Funding for SDSS-III has been provided by the Alfred P. Sloan Foundation, the Participating Institutions, the National Science Foundation, and the U.S. Department of Energy Office of Science. The SDSS-III website is listed in the footnote[2]. SDSS-III is managed by the Astrophysical Research Consortium for the Participating Institutions of the SDSS-III Collaboration including the University of Arizona, the Brazilian Participation Group, Brookhaven National Laboratory, University of Cambridge, Carnegie Mellon University, University of Florida, the French Participation Group, the German Participation Group, Harvard University, the Instituto de Astrofisica de Canarias, the Michigan State/Notre Dame/JINA Participation Group, Johns Hopkins University, Lawrence Berkeley National Laboratory, Max Planck Institute for Astrophysics, Max Planck Institute for Extraterrestrial Physics, New Mexico State University, New York University, Ohio State University, Pennsylvania State University, University of Portsmouth, Princeton University, the Spanish Participation Group, University of Tokyo, University of Utah, Vanderbilt University, University of Virginia, University of Washington, and Yale University.

The Pan-STARRS1 Surveys (PS1) have been made possible through contributions of the Institute for Astronomy, the University of Hawaii, the Pan-STARRS Project Office, the Max-Planck Society and its participating institutes, the Max Planck Institute for Astronomy, Heidelberg and the Max Planck Institute for Extraterrestrial Physics, Garching, The Johns Hopkins University, Durham University, the University of Edinburgh, Queen's University Belfast, the Harvard-Smithsonian Center for Astrophysics, the Las Cumbres Observatory Global Telescope Network Incorporated, the National Central University of Taiwan, the Space Telescope Science Institute, the National Aeronautics and Space Administration under Grant No. NNX08AR22G issued

[1] `http://www.nuffieldfoundation.org/nuffield-research-placements/`

[2] http://www.sdss3.org/

through the Planetary Science Division of the NASA Science Mission Directorate, the National Science Foundation under Grant No. AST-1238877, the University of Maryland, and Eotvos Lorand University (ELTE).

Guoshoujing Telescope (the Large Sky Area Multi-Object Fiber Spectroscopic Telescope LAMOST) is a National Major Scientific Project built by the Chinese Academy of Sciences. Funding for the project has been provided by the National Development and Reform Commission. LAMOST is operated and managed by the National Astronomical Observatories, Chinese Academy of Sciences.

Funding for RAVE has been provided by: the Australian Astronomical Observatory; the Leibniz-Institut fuer Astrophysik Potsdam (AIP); the Australian National University; the Australian Research Council; the French National Research Agency; the German Research Foundation (SPP 1177 and SFB 881); the European Research Council (ERC-StG 240271 Galactica); the Istituto Nazionale di Astrofisica at Padova; The Johns Hopkins University; the National Science Foundation of the USA (AST-0908326); the W. M. Keck foundation; the Macquarie University; the Netherlands Research School for Astronomy; the Natural Sciences and Engineering Research Council of Canada; the Slovenian Research Agency; the Swiss National Science Foundation; the Science & Technology Facilities Council of the UK; Opticon; Strasbourg Observatory; and the Universities of Groningen, Heidelberg and Sydney. The RAVE website is given in the footnotes[3].

This work is based in part on data obtained as part of the UKIRT Infrared Deep Sky Survey. Based on observations obtained as part of the VISTA Hemisphere Survey, ESO Program, 179.A-2010 (PI: McMahon).

This work has made use of data from the European Space Agency (ESA) mission *Gaia*[4], processed by the *Gaia* Data Processing and Analysis Consortium (DPAC[5]). Funding for the DPAC has been provided by national institutions, in particular the institutions participating in the *Gaia* Multilateral Agreement.

This research has made use of data obtained from the SuperCOSMOS Science Archive, prepared and hosted by the Wide Field Astronomy Unit, Institute for Astronomy, University of Edinburgh, which is funded by the UK Science and Technology Facilities Council.

This research has benefitted from the SpeX Prism Spectral Libraries, maintained by Adam Burgasser[6] of the Department of Physics of UC San Diego.

[3] `https://www.rave-survey.org`
[4] `https://www.cosmos.esa.int/gaia`
[5] `https://www.cosmos.esa.int/web/gaia/dpac/consortium`
[6] `http://pono.ucsd.edu/~adam/browndwarfs/splat/`

Contents

Abstract i

Acknowledgements iii

Contents v

List of Figures viii

List of Tables x

List of Abbreviations xi

1 Introduction 1
- 1.1 Brown Dwarfs and Exoplanets . . . 2
- 1.2 Ultracool Dwarfs: Definition and Classification . . . 3
  - 1.2.1 Absorption Features of UCD Spectral Types . . . 3
  - 1.2.2 Colours and Magnitudes of UCDs . . . 9
- 1.3 Ultracool Dwarfs: Evolution . . . 11
- 1.4 Photometric and Spectral Indicators of Young Ultracool Dwarfs . . . 11
  - 1.4.1 Spectral Features of Young UCDs . . . 11
  - 1.4.2 Colours and Magnitudes of Young UCDs . . . 14
  - 1.4.3 Metallicity and Metallicity Effects on UCD Photometry . . . 16
  - 1.4.4 L-T Transition UCD Photometry . . . 17
  - 1.4.5 Narrow Band Photometry . . . 17
- 1.5 Ultracool Dwarfs as Companions . . . 20
  - 1.5.1 Candidate UCD Objects from Optical and NIR Surveys . . . 25
  - 1.5.2 Primary Star Candidates from GAIA . . . 26
- 1.6 Benchmark Brown Dwarfs and Ultracool Dwarf Systems . . . 28
  - 1.6.1 Primary Age . . . 31
  - 1.6.2 Primary Metallicity . . . 32
- 1.7 Aims and Document Structure . . . 33

2 Candidate Selection Process 34
- 2.1 TGAS Sample Selection . . . 34
- 2.2 Cone Search Sky Surveys . . . 35
- 2.3 Colour Conversions for Cross-Comparison between Catalogues . . . 37
  - 2.3.1 Verifying Photometric Consistency Between Surveys . . . 37

2.3.2 Ks to K band conversion . . . 38
2.3.3 Combining Y Band Values for Different Catalogues . . . 38
2.4 Two Catalogue Detections . . . 40
2.4.1 Cross Matching Optical and NIR Surveys . . . 40
2.4.2 Colour Cuts - Two Catalogue Results . . . 41
2.4.3 Colour-Magnitude cuts following known UCD sample . . . 43
2.5 Single Catalogue Detections . . . 46
2.5.1 Cross Matching to Find Optical Non-Detections . . . 47
2.5.2 Colour Cuts - Single Catalogue . . . 47
2.5.3 Colour-Magnitude cuts following known UCD sample . . . 48
2.5.4 Optical Non-Detection Limit . . . 49
2.5.5 Elliptical Cut . . . 49
2.6 Colour - Colour Cuts Following known UCD sample . . . 51
2.7 Proper Motion Calculations . . . 53
2.7.1 Right Ascension and Declination Error . . . 55
2.7.2 Proper Motion Calculations from Two Observations . . . 56
2.7.3 Proper Motion Calculations from Three Observations . . . 57
2.7.4 Matching to SuperCOSMOS Archive . . . 57
2.8 Proper Motion Difference . . . 59
2.9 Common Distance Selection . . . 62
2.10 Dust Extinction Removal . . . 63
2.11 Visual Inspection . . . 64
2.12 Identifying Potential Young Pairs . . . 64
2.12.1 UCD Candidates with Unusually Red $J-K$ . . . 64
2.12.2 Selection Due to Identified Primary Type within SIMBAD . . . 66
2.12.3 Primary Candidate Main Sequence Timescale Based on Photometry . . . 68
2.12.4 Primary Overbright in M_V from Main Sequence compared to Primary Metallicity . . . 70
2.13 Selecting Priority Targets . . . 75

3 Results and Discussion **77**
3.1 Spectral Type Diagnosis of Selected Sample . . . 77
3.2 Summary of Candidate Samples . . . 83
3.3 Narrow Band Photometry . . . 90
3.3.1 Instrumental Setup and Exposure Times . . . 92
3.3.2 Observed Targets and Data Obtained . . . 93
3.3.3 Narrow Band Imaging Data Reduction . . . 95
3.3.4 The Narrow Band 2-Colour Diagram . . . 96
3.3.5 Potential Improvements for and Discussion of Narrow Band Followup . . . 98

4 Conclusion and Future Work **101**
4.1 Conclusion . . . 101
4.2 Future Work . . . 102
4.2.1 NIR Spectroscopic Observation of Candidate UCD Benchmarks . . . 102
4.2.2 Photometric Observations of potential Fast Moving CPM Pairs . . . 102
4.3 Further Future Work . . . 104

A High Priority Targets for NIR Spectroscopy **106**

B Summary Of Observation Proposals **113**
B.1 Spectroscopic Targets 113
B.2 Photometry Observation Targets 114

Bibliography **114**

List of Figures

1.1 Artist Impression of Brown Dwarfs . . . 1
1.2 Optical UCD Spectra . . . 4
1.3 NIR UCD Spectra . . . 5
1.4 J band UCD Spectra . . . 6
1.5 NIR Spectra for First Y Dwarf Discoveries . . . 7
1.6 Spectral Type to Effective Surface Temperature for UCDs . . . 8
1.7 Trent Dupuy Sample J-K to Absolute J . . . 10
1.8 Temperature and Age Degeneracy . . . 12
1.9 Example L0 NIR Spectra . . . 14
1.10 Absolute J Magnitude to J - K CMD for UCDs of all Gravity ranges . . . 15
1.11 J-K against Absolute J for Dupuy sample objects including metal poor and sub-dwarfs . . . 18
1.12 FourStar NIR Camera Design . . . 19
1.13 FourStar Filter Profiles . . . 20
1.14 SPLAT Simulated Narrow Band Colours . . . 21
1.15 2 Colour Diagram Showing Very Low Gravity Selection . . . 22
1.16 SpeX NIR Spectrograph . . . 23
1.17 Simulated UCD sample with Detection Methods Required . . . 25
1.18 VISTA Survey Footprints . . . 26
1.19 Artist Impression of *Gaia* satellite . . . 27
1.20 Stellar Parallax Example . . . 28
1.21 Simulated *Gaia* UCD Benchmark Sample . . . 30

2.1 TGAS Parallax Error . . . 36
2.2 Band Values for Survey Crossmatches . . . 39
2.3 Candidates Y PanSTARRS against Y VHS . . . 40
2.4 Known UCD i - z Against Absolute z Magnitude . . . 44
2.5 Known UCD J - K Against Absolute J Magnitude . . . 45
2.6 Known UCD z - J Against Absolute J Magnitude . . . 46
2.7 Known UCD z-J Non-detection in z Cut Limit . . . 50
2.8 Known UCD J-H Against Y-J . . . 51
2.9 Known UCD H-K Against J-H . . . 52
2.10 Known UCD z-Y Against i-z . . . 53
2.11 Known UCD J-H Against Y-J . . . 54
2.12 Error in RA to J magnitude within UKIDSS results . . . 56
2.13 SuperCOSMOS Archive matching . . . 58
2.14 Error in PM of Candidate Against Sigma PM Difference . . . 60
2.15 Error in PM of Candidate Against Sigma PM Difference - Enlarged section . . . 61

2.16 Young UCDs M_J to $J-K$ CMD 66
2.17 Young UCDs M_J to $J-H$ CMD 67
2.18 Primary Tycho Absolute V magnitude (M_V) against $B-V$ from TGAS parallax 71
2.19 Ammons et al. Metallicity to Delta Absolute Magnitude V in the Main Sequence 72
2.20 LAMOST Metallicity to Delta Absolute Magnitude V in the Main Sequence . . 73
2.21 RAVE Metallicity to Delta Absolute Magnitude V in the Main Sequence 74

3.1 Spectral Type against Absolute J Magnitude 78
3.2 Spectral Type against Various Colours 79
3.3 SpT(izJ) - SpT(M_J) against SpT(NIR) - SpT(M_J) 81
3.4 J-K to M_J Colour Magnitude Diagram with SpT Diagram directions 82
3.5 SpT(izJ) - SpT(M_J) against SpT(NIR) - SpT(M_J) for Sample Candidates 84
3.6 Primary Absolute V Magnitude against B-V 85
3.7 Candidate J-K Against Absolute J Magnitude 86
3.8 Candidate i-z Against Absolute z Magnitude 87
3.9 Candidate J-H Against Y-J 88
3.10 Candidate H-K Against J-H 89
3.11 Candidate z-Y Against i-z 90
3.12 Candidate Y-J Against z-Y 91
3.13 Separation to Distance of Sample 92
3.14 2 Colour Diagram from FourSTAR Observations 97
3.15 J Band FourSTAR Observations 100

4.1 Required Observations to Confirm Relationship 104

List of Tables

2.1 M7 spectral type template absolute magnitudes. 34
2.2 Survey sensitivity limits in multiple bands 35
2.3 Parsec maximums based on survey sensitivity 35
2.4 Quality Cuts for each catalogue search 37
2.5 Quantity of Candidates within 10,000 AU sky projected separation of a TGAS sample objects and passing quality checks. 37
2.6 Quantity of cross matched candidates found in two or more surveys. 41
2.7 Bands available for each catalogue used. 41
2.8 M and L Samples with apparent moving group or association membership and identified as 'young' or 'VL-G' from the Trent Dupuy catalogue and where values for M_J and $J-K$ available. 65
2.9 Young Stellar SIMBAD Flags 67
2.10 Young Variable Stellar SIMBAD Flags 68
2.11 Source for $T_{\rm eff}$ and Spectral Type information 69
2.12 $T_{\rm eff}$ to BC Coefficients of Polynomial Fit from Reed (1998) for use with Equation 2.6. 69

3.1 SpT to M_J Coefficients of Polynomial Fit from Dupuy and Liu (2012) for use with Equation 3.1. 77
3.2 M_J Boundaries for SpT estimation. 80
3.3 Adjusted from Table 1 from Skrzypek et al. (2015). Template colours of M5–L9 dwarfs. Some colours not relevant to this work omitted. Additional colours of i-J, z-J & J-K added based on summing the colours available. 80
3.4 Observed Candidates Spectral Type Estimates 93
3.5 Observed Primary Metallicity Information 93
3.6 Observed Primary Information and Priority Selection 94
3.7 Observed Candidates with CPM Relationships 94

A.1 Proper Motion Source Key 107
A.2 Young Candidate Companions with a Promising CPM Relationship - Candidate Companion Information 108
A.3 Young Candidate Companions with a Promising CPM Relationship - Primary and CPM Information 109
A.4 Common Distance Candidates 110
A.5 Low Proper Motion Primary Candidates 111
A.6 Additional Metallicity Outlier Candidates 112

List of Abbreviations

UCD	**U**ltra **C**ool **D**warf
BD	**B**rown **D**warf
SED	**S**pectral **E**nergy **D**istribution
CMD	**C**olour **M**agnitude **D**iagram
NIR	**N**ear **I**nfra-**R**ed
CPM	**C**ommon **P**roper **M**otion
SDSS	**S**loan **D**igital **S**ky **S**urvey
PanSTARRS	**Pan**oramic **S**urvey **T**elescope **A**nd **R**apid **R**esponse **S**ystem
UKIDSS	**UK**IRT **I**nfrared **D**eep **S**ky **S**urvey
VHS	**V**ISTA **H**emisphere **S**urvey
SSA	**S**uperCOSMOS **S**cience **A**rchive
LAMOST	**L**arge Sky **A**rea **M**ulti-**O**bject **F**ibre **S**pectroscopic **T**elescope
RAVE	**Ra**dial **V**elocity **E**xperiment
VL-G	**V**ery **L**ow surface **G**ravity
INT-G	**Int**ermediate surface **G**ravity
SPLAT	The **S**peX **P**rism **L**ibrary **A**nalysis **T**oolkit
RV	**R**adial **V**elocity

Chapter 1

Introduction

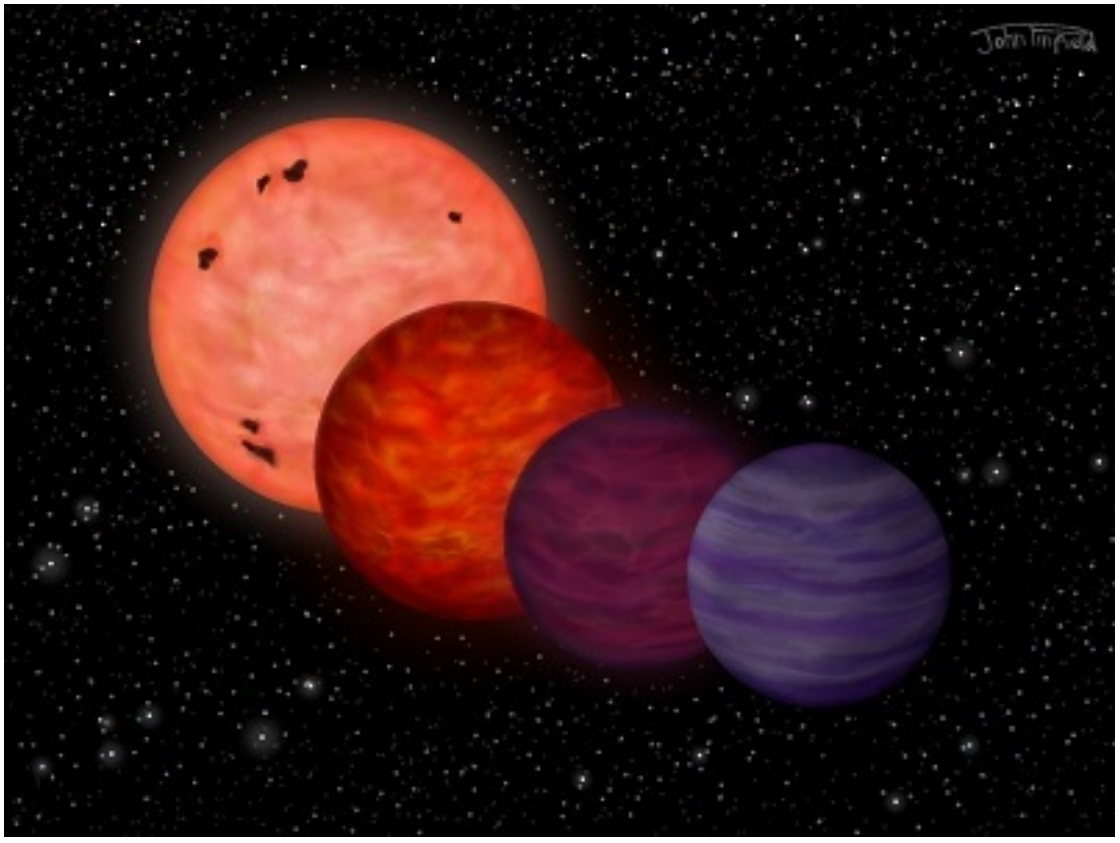

FIGURE 1.1: Artist Impression of Brown Dwarfs, from left to right - Late M Dwarf, L Dwarf, T Dwarf and Y Dwarf. ©John Pinfield.

1.1 Brown Dwarfs and Exoplanets

Substellar objects are low mass stars and planets without the mass to cause the required core pressure to be reached that would enable fusion of Hydrogen through the PP-chain reaction (Hayashi and Nakano, 1963). This mass limit is $\lesssim 0.075\ M_{\odot}$ for solar metallicity objects.

Stars are able to reach the temperature range of $\sim 3 \times 10^6$K in their cores required for the PP-chain reaction due to their gravity driven contraction due to their greater mass increasing core pressure. The radiative pressure from the reaction then supports the star from further contraction and the object settles on the main sequence.

For lower mass objects, the required temperature for the PP-chain is not reached in the core, instead the pressure limit of the Pauli Exclusion Principle is reached prior to the required temperature being attained. This principle of degeneracy where electrons cannot occupy the same quantum spin state, meaning the core cannot be compressed further. This limit creates a pressure preventing further core collapse. These objects are designated "Brown Dwarfs" and were first theorised in the 1960s (Kumar, 1962). "Brown Dwarfs" are a subgroup of observed objects referred to as Ultracool Dwarfs (UCDs). A cool dwarf at the bottom of the main sequence that is identified as sufficiently cool that it may or may not be a "Brown Dwarf" depending upon its mass and metallicity and if the object will reach a state of equilibrium with energy released by PP-chain combination within the core.

Kumar used the term "Black Dwarf" however this term is used to describe the end state of a chemically evolved White Dwarf. The term substellar applies to Brown Dwarfs but also includes Exoplanets. The term "Brown Dwarf" was adopted in 1975 by Jill Tarter to signify a substellar object that formed through the same process as stars but without sufficient mass to fuse hydrogen via the PP-chain (Tarter, 1986).

To differentiate Brown Dwarfs from exoplanets, the deuterium ignition limit of approximately 13 Jupiter masses has been adopted as the lower mass limit for Brown Dwarfs (Boss et al., 2007). This divide between planets and Brown Dwarfs is imperfect as models suggest the actual deuterium burning mass can vary depending upon the helium abundances (Spiegel et al., 2011). A definition that could separate Brown Dwarfs from giant planets that is not based upon mass and instead based upon formation methods would be preferable, but may not provide a definition with a clear method to separate objects from observation.

The first unambiguous discovery of two substellar objects was not made until 1995. GL 229B (Nakajima et al., 1995) was confirmed through common proper motion as a companion to GL 229, resulting in an effective surface temperature that showed the object was likely substellar. Teide 1 was confirmed as a member of the Pleiades open cluster (Rebolo et al., 1995), thus confirming the object's distance and therefore temperature.

1.2 Ultracool Dwarfs: Definition and Classification

A UCD is an object with a spectral type of M7 or later which corresponds to an effective surface temperature ($T_{\rm eff}$) below 2,700K (Steele and Jones, 2001). The effective temperature of a star is estimated by fitting a black body radiation curve to the observed energy distribution of the object. By integrating the flux across all wavelengths, the total luminosity of the object is estimated to calculate the effective surface temperature using the Stefan Boltzmann's equation ($L = 4\pi R^2 \sigma T_{\rm eff}^4$). The radius of UCDs is estimated from models (e.g. Baraffe et al. 1998). As discussed in Section 1.2.1, cooler UCDs begin to have very large scale spectral absorption features effecting their observed spectra. This means that a simple fitted black body curve would overestimate the effective temperature by not considering the reduced flux at absorption frequencies and instead the spectral type of the object is usually identified in order to consider the absorption features and correctly infer the effective temperature (Leggett et al. 1998, 2000a).

An object can be a UCD while not being a Brown Dwarf, meaning that the core is fusing hydrogen through the PP-chain. One of the most famous examples of such an object is Trappist-1 (Gillon et al., 2017), known for the remarkable discovery of a large number of rocky planets in the star's temperate zone. As Trappist-1 has a low effective surface temperature and is actively fusing hydrogen, it is classified as a UCD but not a Brown Dwarf. A very young, high mass Brown Dwarf will have, for the first 10s of Myrs, an effective surface temperature above 2,700K and would have a spectral type earlier than M7, but is a Brown Dwarf as the core is not fusing hydrogen and the object will continue to cool through later spectral types, as discussed in Section 1.3.

1.2.1 Absorption Features of UCD Spectral Types

UCD spectral types begin at $M \gtrsim 7$. The sequence of spectral types continues past M, through L, to T and finally to Y dwarfs. The spectral type sequence defines these spectral types based

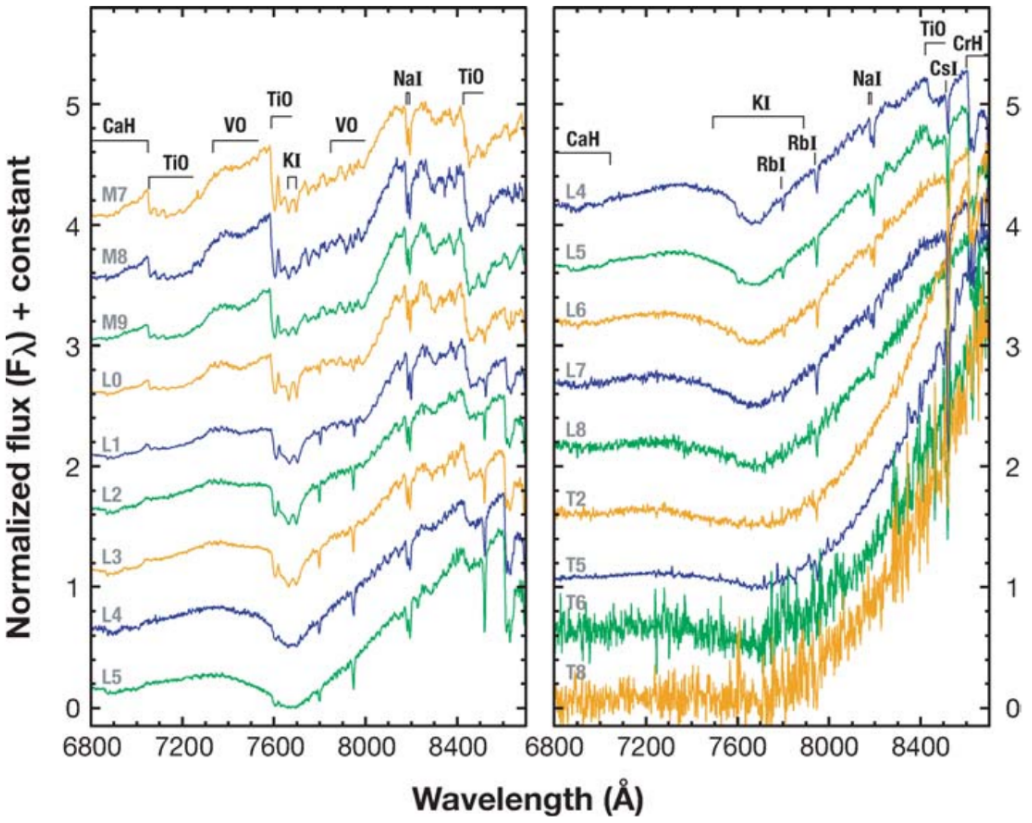

FIGURE 1.2: Optical Spectra for a range of L and T dwarf standards from Kirkpatrick (2005).

on absorption features in the optical and near infrared (NIR) spectra. As the photosphere of a UCD is wavelength dependent due to wavelength dependent opacities (Marley and Robinson, 2015), these absorption features are used to categorise UCDs. These absorption lines come from a variety of atomic and molecular bands.

Late M dwarfs have an effective surface temperature of $\sim 2700-2300$K and have strong absorption bands in H_2O and TiO.

L dwarfs have a $T_{\rm eff}$ range of $\sim 2300-1450$K with weaker TiO absorption. Absorption in hydride bands CrH and FeH and CaOH and atomic lines of Na, Fe, K and Ca increases through the L dwarf range (Kirkpatrick, 2005). H_2O absorption increases through the L sequence. The prototype L dwarf was discovered in 1988 as an ultracool companion to a White Dwarf (Becklin and Zuckerman, 1988). While initially described as an object with spectral type $\geq M10$, this object is the prototype object of the L spectral class (GD 165B) with an effective surface temperature of $\sim 1,800-1,900$K.

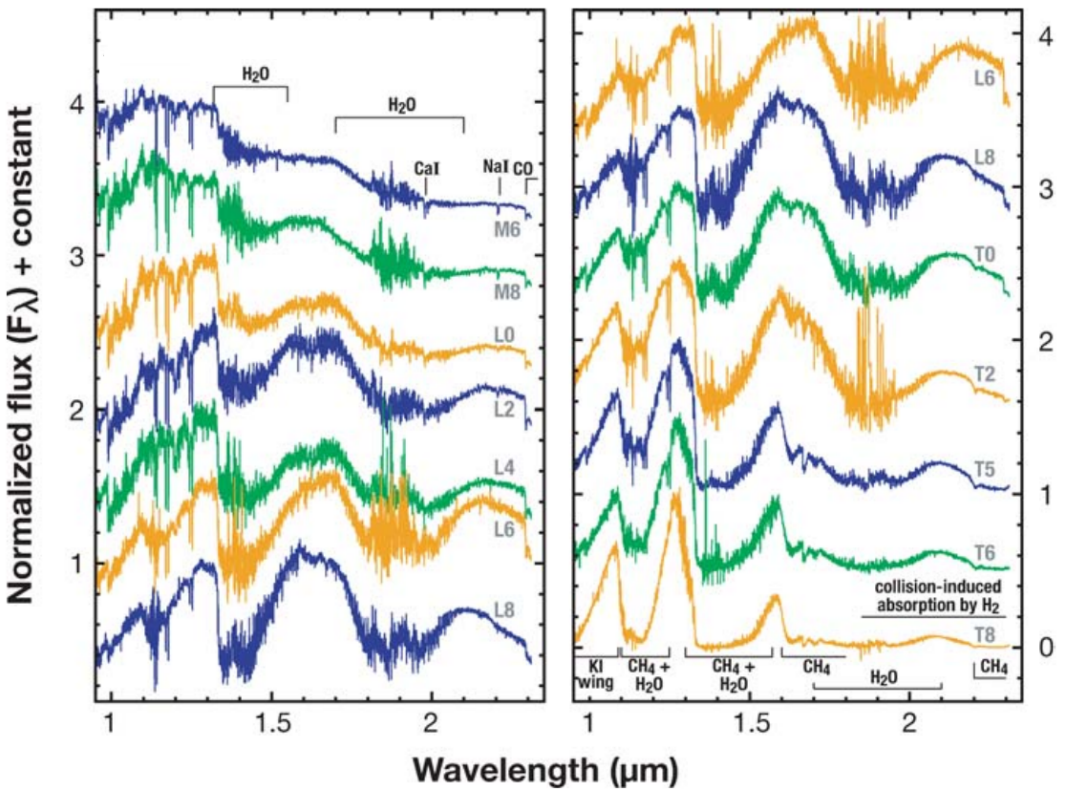

FIGURE 1.3: NIR Spectra for a range of L and T dwarf standards from Kirkpatrick (2005).

T dwarfs have a $T_{\rm eff}$ range of $\sim 1450-500$K with strong absorption of H_2O and CH_4 increasing through the T dwarf series so that late T dwarfs spectra are only a series of flux peaks at 1.08, 1.27, 1.69 and 2.08 μm (Geballe et al. 2002, Burgasser et al. 2006). Clouds, such as clouds of sulphides, also affect the spectra of T dwarfs, however iron and silicate clouds, believed to be present in L dwarfs, are thought to be too low to affect the spectra of T dwarfs (Morley et al., 2012). GL 229B was confirmed as the prototype of the T spectral type (Marley et al., 1996) with a lower surface temperature of $T_{\rm eff} \lesssim 1300$K (Kirkpatrick, 2005).

The spectral features of L and T dwarfs were defined in the review by Kirkpatrick (2005) defining these spectral types and predicting the existence of a later Y dwarf spectral type. Figures 1.2, 1.3 and 1.4 show spectra from a range of L and T dwarf standards in optical, NIR and J band spectra respectively. Absorption regions are labelled.

Y dwarfs have a $T_{\rm eff}$ range of $\lesssim 500$K. The coolest Y dwarf identified at the time of writing is WISE J085510.83-071442.5 with $T_{\rm eff} \sim 250$K (Luhman, 2014). A very small number of Y dwarfs have been identified. Even fewer have constrained parallaxes. A small sample of spectra can be identified. They appear as extreme T dwarfs, with absorption from H_2O, CH_4 and NH_4

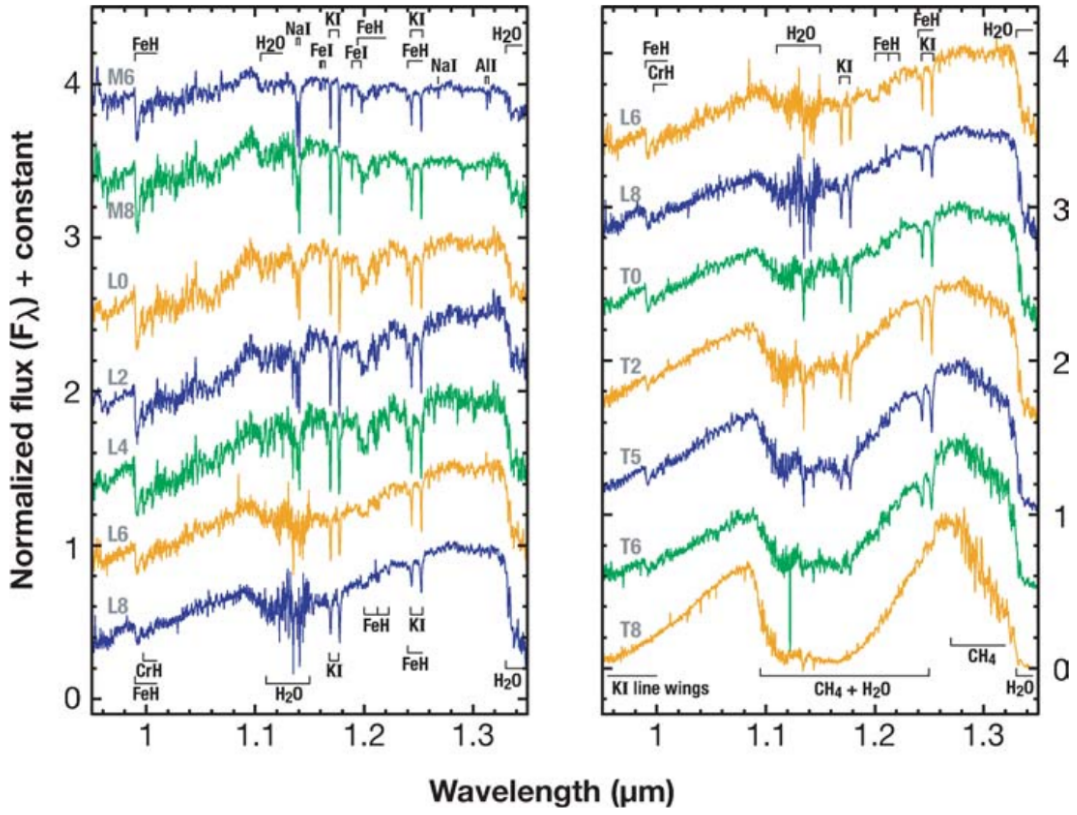

FIGURE 1.4: J Band Spectra for a range of L and T dwarf standards from Kirkpatrick (2005).

leaving only peaks at 1.08, 1.27 and 1.69 μm (Burrows et al., 2003). Figure 1.5 shows the first Y Dwarf discoveries from the Wide-field Infrared Survey Explorer (WISE) (Cushing et al., 2011).

For Y dwarfs, the peak 2.08 μm present from early L dwarfs and later is suppressed as a key indicator that the object is a Y dwarf. Water clouds are also present in the coldest Brown Dwarfs (Morley et al. 2014, Luhman and Esplin 2016).

Temperature definitions of different spectral types are driven by temperatures of the objects classified by their spectral types. Figure 1.6 shows the effective surface temperature ranges of UCDs from Kirkpatrick (2005).

The process of observing a spectra for a candidate object is required to confirm spectral type. However, Skrzypek et al. (2015) developed a phototyping system with a similar accuracy range of ± 1 spectral subtype based on only the observed photometry colours of the Brown Dwarfs. This system requires as many bands as possible from the r band through to K. This enables candidate objects to be identified by photometry from optical and NIR catalogues and to assign the candidate a predicted spectral type with a high degree of accuracy.

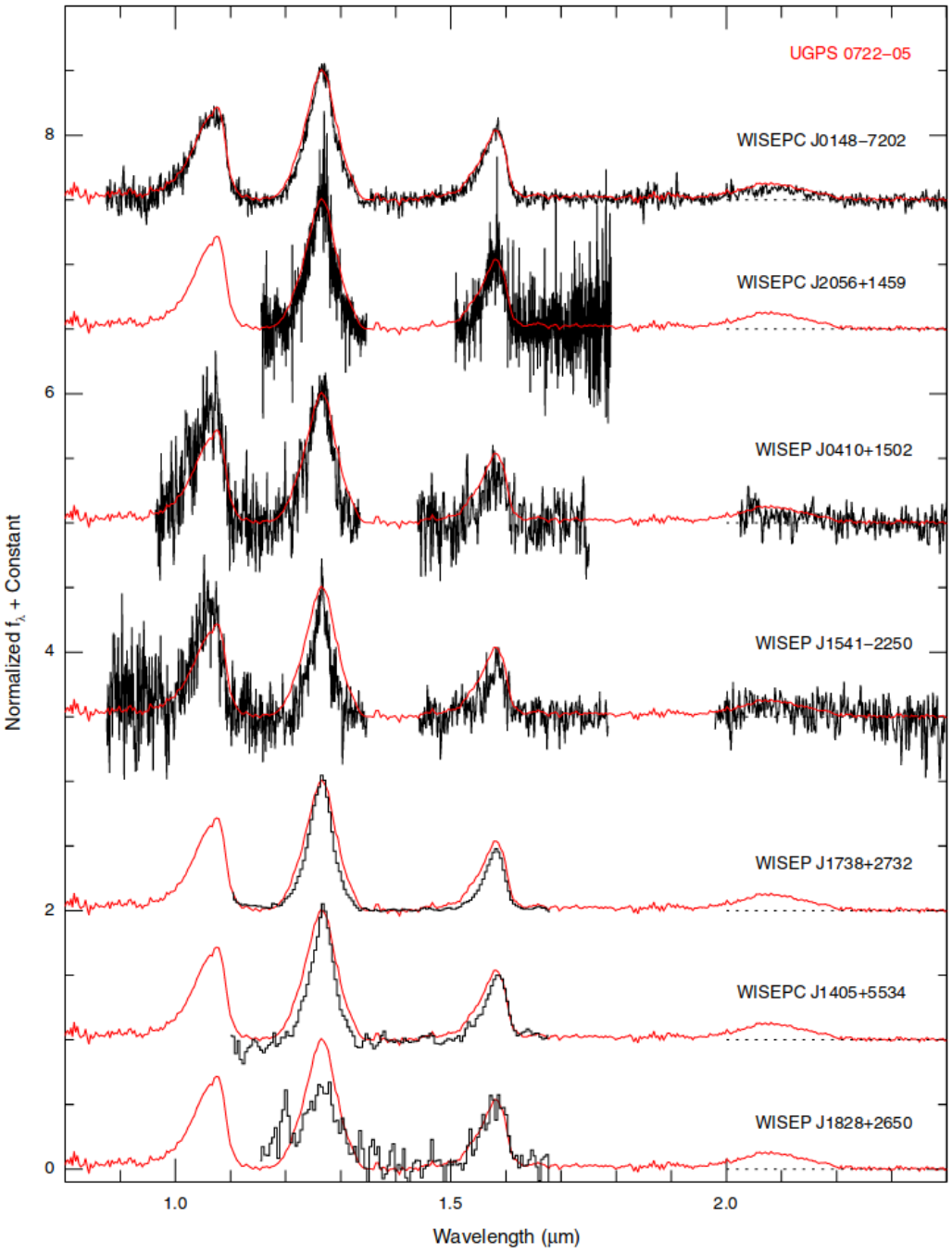

FIGURE 1.5: NIR Spectra from first Y dwarf discoveries showing suppression of peak at 2.08 μm from Cushing et al. (2011).

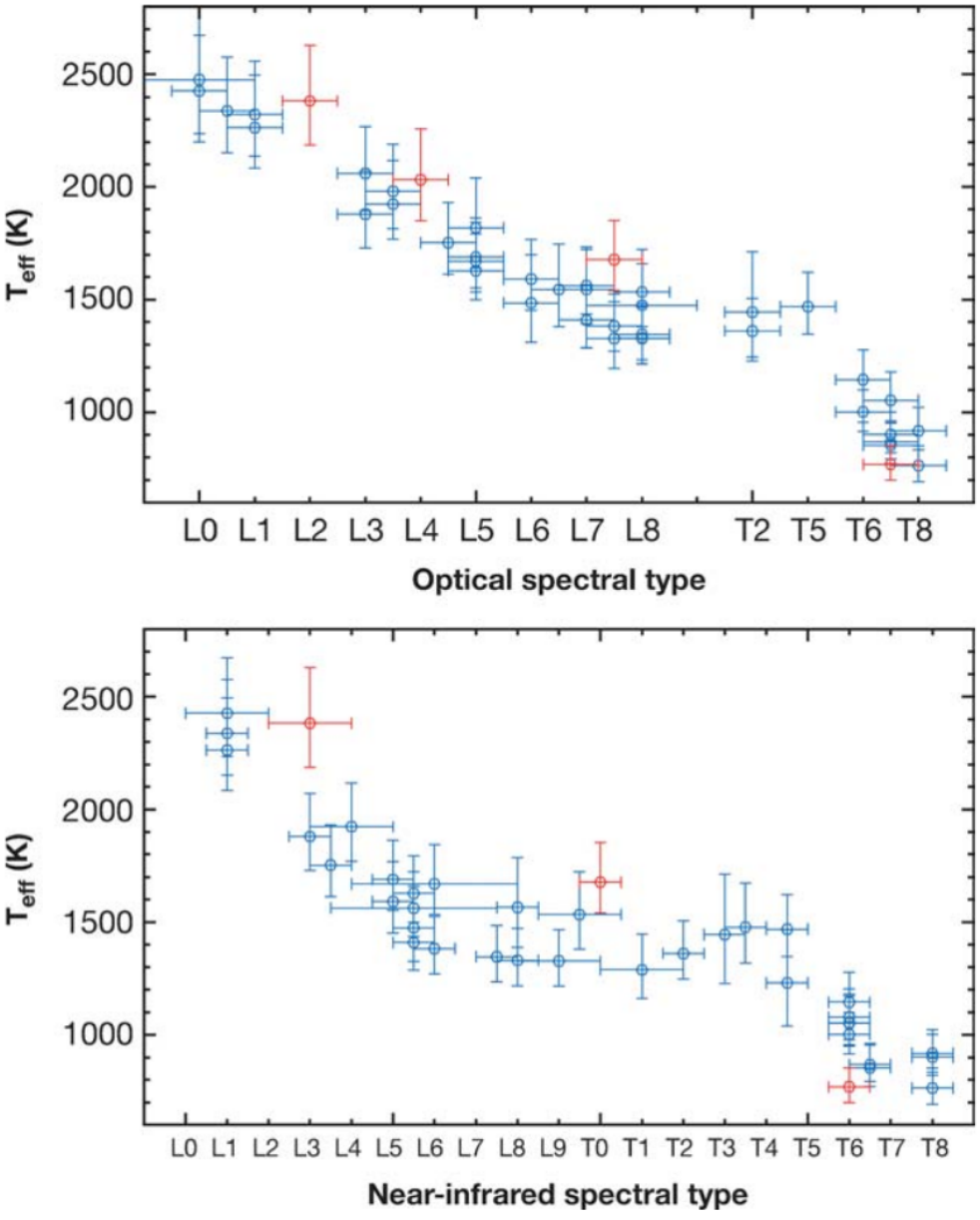

FIGURE 1.6: Spectral Type to Effective Surface Temperature for a range of UCDs. Taken from Kirkpatrick (2005).

The Two Micron All-Sky Survey (2MASS) was the source of the first large sample of L and late T dwarfs, leading to the definition of these spectral types (Kirkpatrick et al. 1999, 2000) while the Sloan Digital Sky Survey (SDSS) was the source of the first L and T transition objects (Leggett et al., 2000b). NIR surveys such as the UKIRT Infrared Deep Sky Survey (UKIDSS) extended the T dwarf regime to the end in the search of the coolest dwarfs (Pinfield et al. 2008, Lucas et al. 2010, Burningham et al. 2013). The concept of Y dwarfs as a spectral type was discussed by Kirkpatrick et al. (1999) and confirmed by the discovery of seven UCDs in observations from the Wide-field Infrared Survey Explorer (WISE) (Cushing et al., 2011).

Found in multiple optical and NIR surveys, the task of collating and curating the list of detections has been taken on by a small group. Jonathan Gagné of the Department of Terrestrial Magnetism, Carnegie Institution of Washington, maintains a list of all UCD discoveries [1] while Trent Dupuy of The University of Texas curates a list (hereafter referred to as the Dupuy sample) of all UCD discoveries with parallaxes based on Dupuy and Liu (2012) (for field objects and binaries); Dupuy and Kraus (2013) (for late-T and Y dwarfs); and Liu et al. (2016) (for young objects and companions)[2].

With the recent discovery of Y Dwarf examples, Michael Cushing of the University of Toledo maintains an online compendium of the twenty-four (at the time of writing) known Y dwarfs [3].

1.2.2 Colours and Magnitudes of UCDs

As the coolest spectral types that contain both stars and UCDs, M and L dwarfs are the reddest. M and L dwarfs have very high J-K colour and form a sequence in the J-K to M_J colour magnitude diagram (CMD). For late M through L dwarfs, objects get fainter and redder as shown in Figure 1.7 as dusty clouds reduce luminosity.

For early T dwarfs, the effect is reversed and there is a sudden reduction in J-K as the K band is suppressed by CH_4 and H_2O absorption. This change is very rapid over small changes in temperature. From mid T dwarfs and later, this stabilises and J-K colour is relatively constant, while temperatures for later T in to Y dwarfs continue to be lower, resulting in reduced luminosity.

The full tract of J-K to Absolute J magnitude is shown in Figure 1.7 showing the J-K to M_J CMD for UCDs with parallaxes from the Dupuy sample.

[1] `https://jgagneastro.wordpress.com/list-of-ultracool-dwarfs/`
[2] `http://www.as.utexas.edu/~tdupuy/plx/Database_of_Ultracool_Parallaxes.html`
[3] `https://sites.google.com/view/ydwarfcompendium`

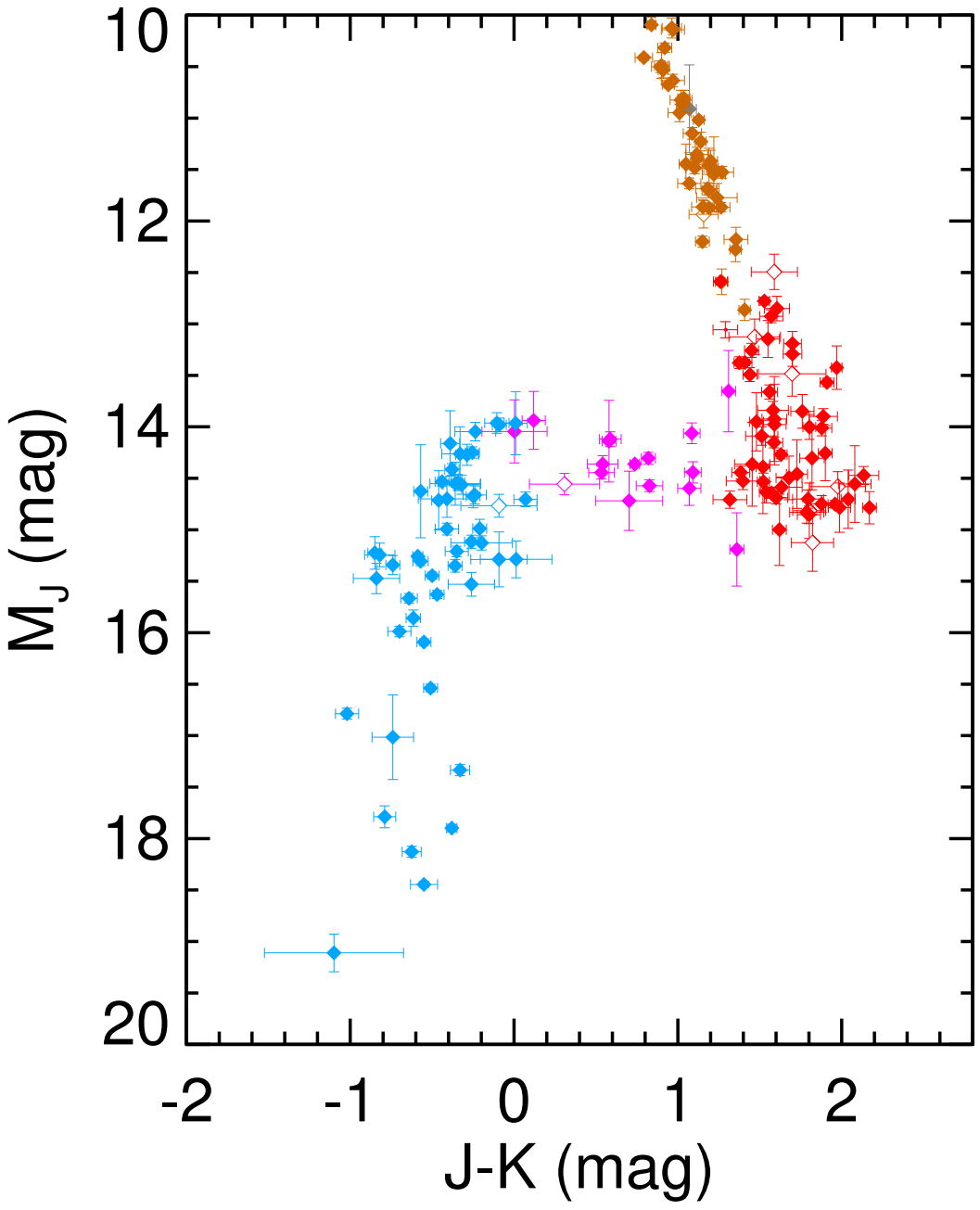

FIGURE 1.7: J-K to Absolute J for all objects within the Trent Dupuy sample, maintained online and drawn from multiple sources. Orange markers are late M to early L dwarfs. Red markers are early L dwarfs to L9. Purple markers are early T dwarfs (< T5). Blue markers are mid T dwarfs through to early Y dwarfs.

1.3 Ultracool Dwarfs: Evolution

As a consequence of the core of a Brown Dwarf being supported by electron degeneracy pressure rather than radiative pressure, Brown Dwarfs have relatively similar radii regardless of spectral type of $\sim 0.90 \pm 0.15 R_{\rm Jup}$ for L to T dwarfs (Burgasser, 2001). Burgasser (2001) calculates this value using Monte Carlo simulations of the evolutionary models of Burrows et al. (1997). Despite the similar radii, young UCDs are still larger than older UCDs of the same type as they are still contracting. Increased radii resulting in lower surface gravity. The radii for young UCDs is simulated to be 25% to 75% larger than the radii of dwarfs of 1–3 Gyr age with equivalent temperatures (Faherty et al., 2012).

Brown Dwarfs do not have a hydrogen fusing cores to add energy in to their systems. The age and surface temperature of a Brown Dwarf is degenerate as the Brown Dwarf cools over time. An object of any specific spectral type can be either a younger, lower mass object that has formed at that spectral type, or an older object that has cooled from a higher temperature and now occupies the same spectral type. Figure 1.8 shows the work by Kirkpatrick et al. (1999) using stellar evolutionary model codes by Burrows et al. (1997) and Baraffe et al. (1998) demonstrating the degeneracy between temperature and age for UCDs and shows how cooling UCDs will move to later spectral types. For example, the $0.01 M_{\odot}$ model in both the Burrows et al. (1997) and Baraffe et al. (1998) models drops to later spectral types on very short timescales.

As a result of the continually reducing radii and that younger objects will be lower mass objects than older, higher mass UCDs that have cooled to the same spectral type, the surface gravity (g) of an object is linked to age. As UCDs continue to contract over time, so the surface gravity increases with time. Identifying young UCDs is a key scientific goal and the function of this work and so this goal could be considered analogous with identifying low surface gravity UCDs.

1.4 Photometric and Spectral Indicators of Young Ultracool Dwarfs

1.4.1 Spectral Features of Young UCDs

Some of the first detections of young UCDs were found in young clusters and comoving groups such as 2MASS J01033563-5515561, identified in the $\sim$ 25Myr (Kraus et al., 2014) Tucana-Horologium (Tuc-Hor) moving group (Delorme et al., 2013) and HIP65423B and HIP65517B,

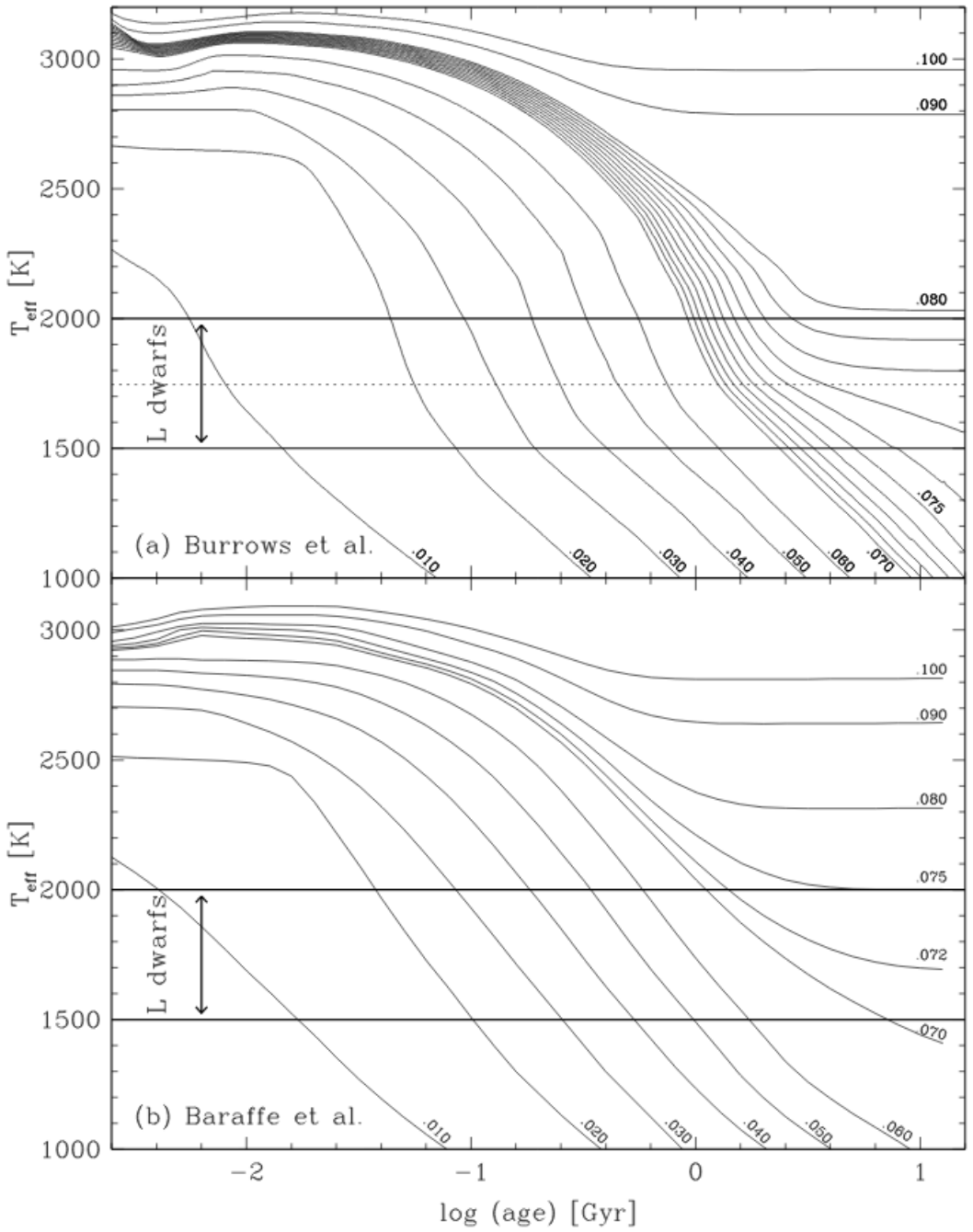

FIGURE 1.8: Kirkpatrick et al. (1999) Age to Temperature degeneracy based on model code by Burrows et al. (1997) and Baraffe et al. (1998). Each line is a model with a mass ($M_{\odot}$) shown. The dashed line in the top panel shows the limit where objects evolve on to a stable configuration and so are not Brown Dwarfs.

found in the $\sim$ 5Myr (Preibisch et al., 2002) Upper Scorpius (USco) region (Janson et al., 2012). UCDs in the field have also been found to have low gravity features indicating youth, with $\sim 7.6\% \pm 1.6\%$ of field UCDs showing signs of low gravity (Kirkpatrick et al., 2008).

Assuming hydrostatic equilibrium, the lower surface gravity of young UCDs will affect the photospheric pressure. The lower photospheric pressure affects chemical paths of molecules and atoms (Lodders, 1999). This has observable consequences on spectral features (Allers and Liu 2013, Martin et al. 2017).

Cruz et al. (2009) study a sample of L0-5 field objects to describe a system to categorise UCD spectra into very low surface gravity objects (VL-G, γ, $\sim$ 10Myrs) and intermediate surface gravity objects (INT-G, β, $\sim$ 100Myrs). This categorisation system has been adopted by other authors with γ & β appended to spectral type designations to categorise UCDs with indications of VL-G and INT-G.

For late M and L dwarfs, the *H*-band continuum shape for both INT-G and VL-G objects has a very triangular shape, with the peak at $\sim 1.69\mu$m (Lucas et al., 2001). In late M and L field dwarfs, there is H_2O absorption up to 1.55μm and above 1.7μm but the slope in-between in shallower (Lucas et al., 2001) as seen in late-M and L dwarfs presented by Leggett et al. (2001). The shape of the spectra for the youngest objects have the clearest and 'peakiest' triangular shape in the spectra between $\sim$ 1.45 and $\sim 1.78\mu$m. This shape is attributed to increased absorption from FeH and increased H_2 collision induced absorption (Allers and Liu 2013) due to higher pressures for higher surface gravity objects. Alternatively, the absorption features in the *J* band region have been interpreted as dusty atmospheres with thick clouds of small particles (Liu et al., 2016). However, these dusty atmosphere models often return radii that are implausibly small (Marley et al. 2012; Liu et al. 2013).

Numerous molecular absorptions are shown to be gravity dependent. Allers and Liu (2013) propose a system of gravity dependent spectral indices to categorise VL-G and INT-G spectra using FeH, K_I, NA_I, VO and the H continuum (see tables 4 and 7 within Allers and Liu 2013). The bandwidths of these indices are carefully selected to ensure they are sensitive to gravity dependent features at moderate and low resolution spectra (to $R \sim 75$, Allers and Liu 2013). Different indices are more or less sensitive for different spectral types. The FeH index is sensitive to gravity features for M6–L7 spectral types while the VO index is described by the authors as "an excellent gravity indicator for L0–L4 dwarfs". When using the Allers and Liu spectral

indices method to categorise UCD spectra by gravity features, objects are scored based on these absorption indices with specific scores corresponding to VL-G, INT-G or field classifications.

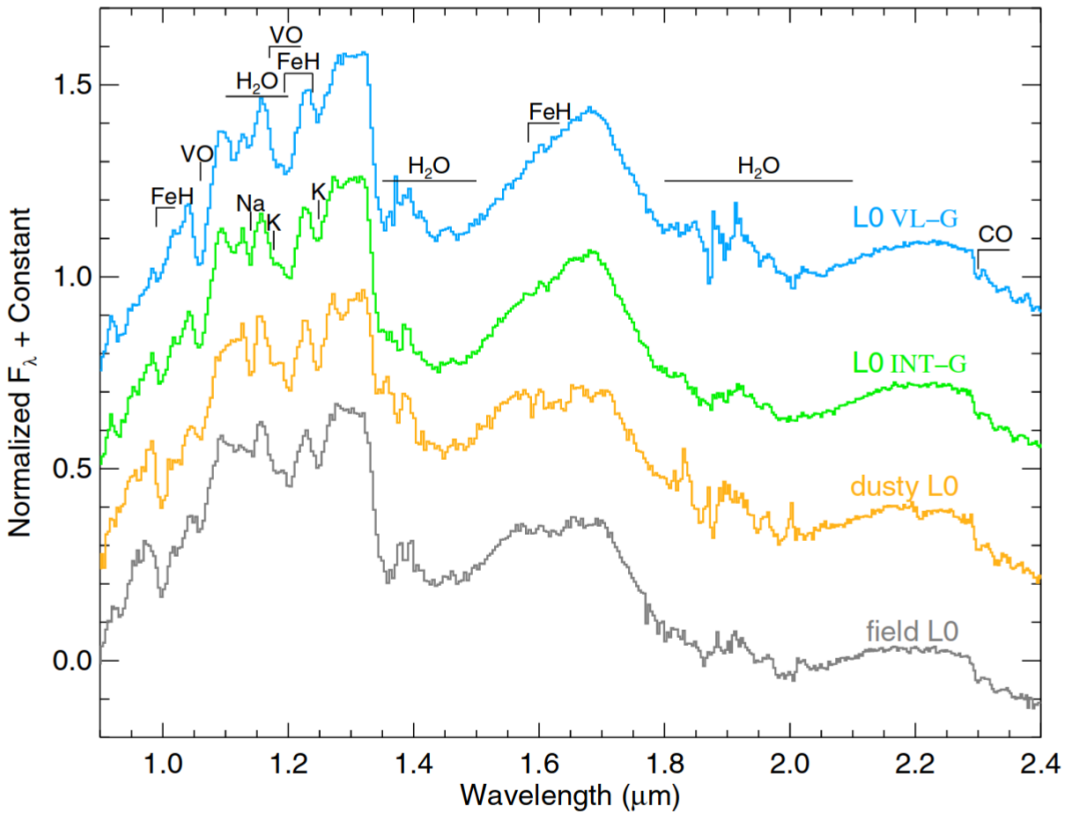

FIGURE 1.9: Four comparison L0 spectra showing a range of gravity dependent features from Allers and Liu (2013). Spectral flux is normalised and a constant added to separate the spectra. Objects are classified by their optical spectra. The blue object is VL-G, L0γ (2M 014146, Cruz et al. 2009) and the green object is classified INT-G, L0β (2M 1552+29, Cruz et al. 2009) . The dusty L0 object is in orange (2M 1331+34, Kirkpatrick et al. 2010). The grey object is the L0 standard (2M 0345+25, Burgasser and McElwain 2006).

Figure 1.9 is taken from Allers and Liu (2013) showing four example spectra of different L0 UCDs with different gravity classifications. The blue objects is VL-G, green is INT-G. A dusty object (orange) and a field object (grey) are shown for comparisons. FeH, Na_I and K_I all show lower absorption at lower gravities while VO absorption is stronger. The H continuum shows the clearest and most triangular peak for VL-G spectra. Allers and Liu (2013) contains numerous example spectra not reproduced here, including comparisons for VL-G, INT-G and Field M8, L0 and L3 UCDs.

The system designed by Allers and Liu (2013) does not categorise late L objects in to the L-T transition. There is no systematic categorisation system for the spectra of VL-G and INT-G T dwarfs due to the lack of T dwarfs with independent age constraints.

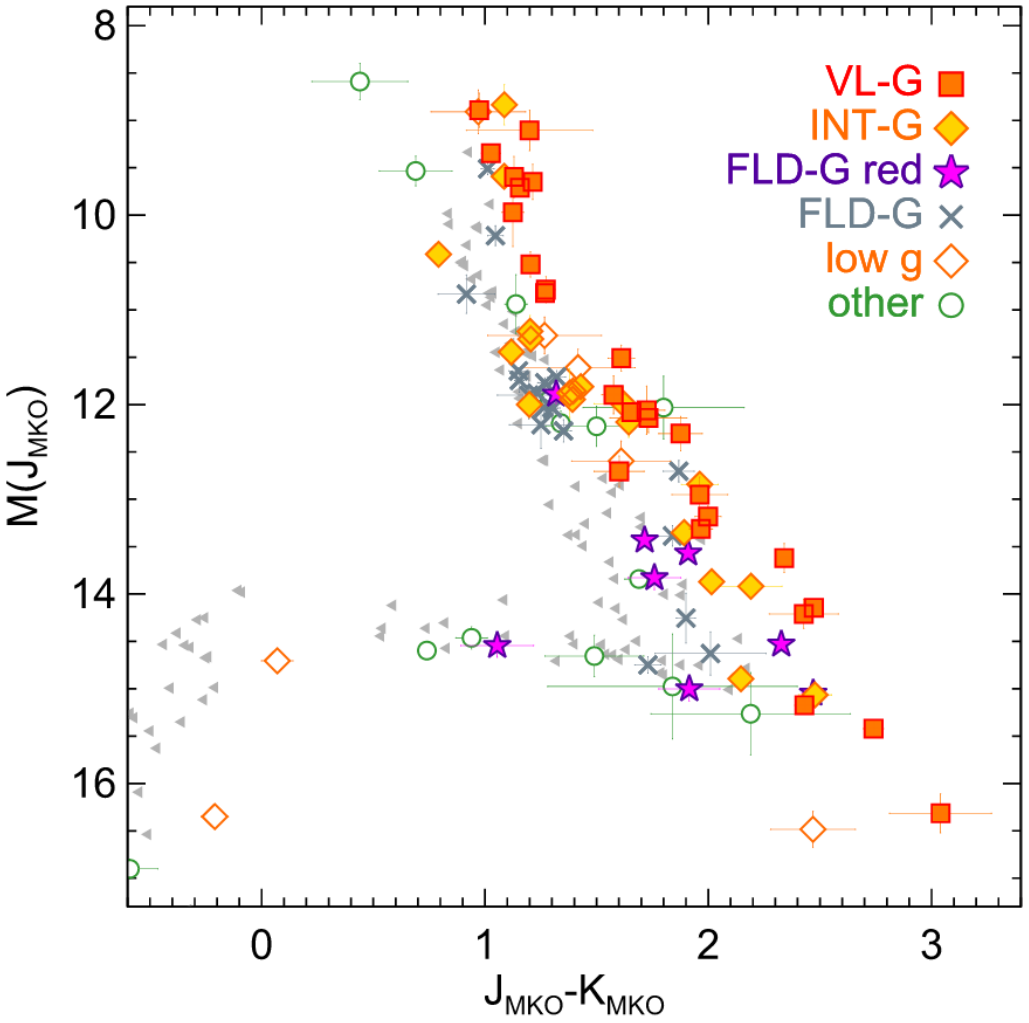

FIGURE 1.10: Absolute J magnitude to J-K for field, INT-G and VL-G UCDs, showing the offset in J-K for VL-G objects compared to field objects, reproduced from Liu et al. (2016). Orange squares are objects spectroscopically confirmed through NIR spectra as being Very Low surface Gravity (VL-G) while yellow diamonds are spectroscopically confirmed through NIR spectra as Intermediate surface gravity (INT-G) and green crosses have been spectroscopically confirmed as not having VL-G or INT-G features and so are considered Field surface Gravity (FLD-G) objects. Grey triangles are objects without spectra to confirm or deny INT-G or VL-G status. Blue triangles filled in purple are objects confirmed spectroscopically to not be VL-G or INT-G but regardless are red in J-K for their spectral type. Unfilled orange diamonds are objects considered to have low surface gravity based on other observation such as optical spectra. Green circles are other unusual objects such as spectroscopic binaries, see Liu et al. (2016) for more information on these.

1.4.2 Colours and Magnitudes of Young UCDs

Young UCDs ($\leq$ 100 Myrs) of M and L spectral type dominate the redder end of the J-K to M_J Colour Magnitude Diagram (CMD) and form an offset sequence in the CMD from the field UCDs (Faherty et al., 2016). This is shown in Figure 1.10, taken from Liu et al. (2016). For M and L objects, this offset trend in J-K is clear with VL-G objects being redder in J-K and/or brighter in M_J.

Considering the absorption features of VL-G and INT-G objects (Section 1.4.1), the reddening in J-K can be explained by a relatively similar K band continuum shape of VL-G, INT-G and field objects while absorption in the J band suppresses the flux and increases the J-K colour for lower surface gravity objects.

The increased radii described in Section 1.3 is the equivalent to an overluminosity of 0.5–1.2 mag for 10 Myr old objects with a mass range of 10 - 75 M_{jup} (Faherty et al., 2012). This overluminosity is in all bands and causes, amongst other effects, lower surface gravity objects to be appear brighter in M_J on the J-K versus M_J CMD. However low surface gravity objects have been observed with contradictory underluminosity (Faherty et al., 2012).

Overluminosity combined with a UCD being redder in J-K colour would provide an explanation for the direction in the offset in the J-K to M_J CMD (Figure 1.10). This offset provides an opportunity to select young M and L dwarfs based on photometry and absolute magnitude.

1.4.3 Metallicity and Metallicity Effects on UCD Photometry

Another physical property that can affect the photometry of UCDs is metallicity. The metallicity of a star or UCD is most often expressed as either [M/H] (the abundance of all metals, elements excluding Hydrogen and Helium, as a ratio to the abundance of Hydrogen) or [Fe/H] (the abundance of Iron only as a ratio to the abundance of Hydrogen). Both metallicity values are a log scale normalised to the solar metallicity, so that the Sun is [M/H] = [Fe/H] = 0. This is done by estimations of the abundances as a fraction of the total so that the combined abundance of X (Hydrogen), Y (Helium) and Z (all other elements), adds up to 1 as per Equation 1.1.

$$X + Y + Z = 1.00 \tag{1.1}$$

The calculation for [Fe/H] is shown in Equation 1.2, where N is the number of molecules of that element. In practice, the relative abundance of Iron to Hydrogen is the most practical for astronomy. The relative absorption line depths can be compared to calculate values for [Fe/H].

$$[\mathrm{Fe/H}] = \log_{10}\left(\frac{N_{\mathrm{Fe}}}{N_{\mathrm{H}}}\right) - \log_{10}\left(\frac{N_{\mathrm{Fe}}}{N_{\mathrm{H}}}\right)_{*} \tag{1.2}$$

The relation of [M/H] to [Fe/H] is shown in Equation 1.3. Practical observations have given the constraints $0.9 < A < 1.0$. For the practical identification of UCD candidates the similarity between [M/H] and [Fe/H] means they can be treated as being equal ($A = 1$).

$$[\mathrm{M/H}] = A \times [\mathrm{Fe/H}] \tag{1.3}$$

The effect of metallicity upon the colours and spectral features of UCDs is entangled with other effects due to low surface gravity and age. L dwarfs that are metal poor can appear bluer in J-K and J-H colours (Kirkpatrick et al., 2010). This causes a shift in the J-K to M_J CMD in the opposite direction to the shift in the CMD caused by very low surface gravity (Section 1.4.2).

Figure 1.11 shows the Dupuy sample of UCDs with parallaxes with confirmed subdwarfs and suspected metal poor objects. Subdwarfs are a classification of stellar objects and UCDs that are very old and are metal poor, as they lack the metal enrichment presented in later populations of stars. This figure demonstrates that low metallicity has the effect of moving a UCD to bluer J-K colours. Low gravity features associated with age have the effect of pushing an object to be redder in J-K. Disentangling a UCD's colours is often reliant upon an understanding of the object's metallicity and surface gravity as an indicator of age.

1.4.4 L-T Transition UCD Photometry

Figure 1.10 shows young L-T transition objects at the bottom of the M/L linear sequence as shown in Figure 1.7. The turnoff at the bottom of this linear sequence in the CMD marks the transition between L and T dwarfs. Low surface gravity L-T transition dwarfs occupy a region of the CMD at the bottom of the M/L sequence that is devoid of field objects. Surface gravity is the second most important property determining the photometry of L-T transition objects, second only to spectral type (Burrows et al., 2006).

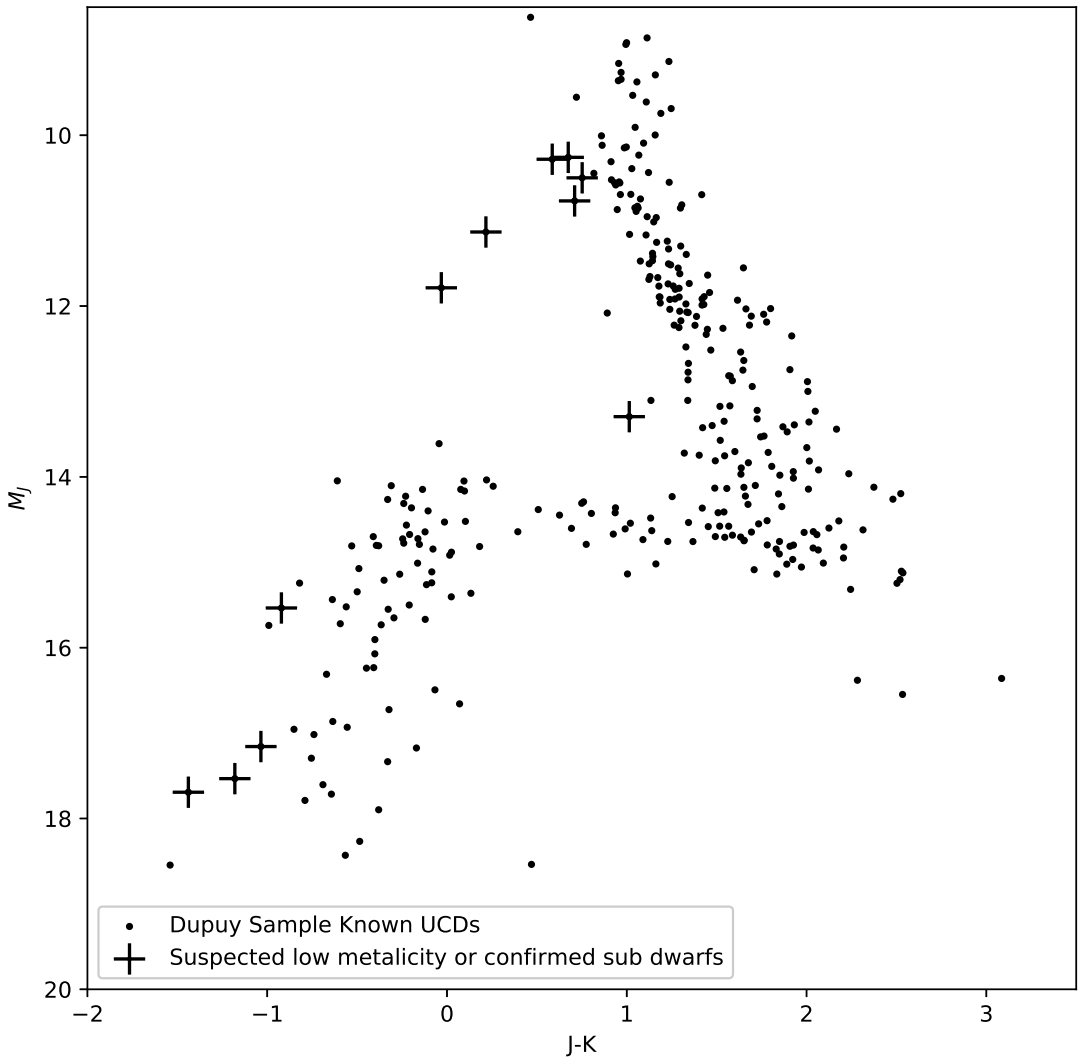

FIGURE 1.11: Sample UCDs with parallaxes shown with suspected metal poor and spectroscopically confirmed subdwarfs. Points are Dupuy sample UCDs with parallaxes. Plus symbols are Dupuy sample objects with associations to subdwarf primaries or metal poor primaries.

1.4.5 Narrow Band Photometry

An example NIR instrument available for follow up photometric observations of candidate UCD objects is the FourSTAR NIR camera on the Magellan Baade 6.5m telescope at Las Campanas Observatory, Chile 1.12. FourSTAR is able to acquire photometric observations of candidates to much lower magnitudes than NIR catalogues ($J \lesssim 25$).

As well as J, H and K filters, FourSTAR also has several narrow band filters. Most importantly for the identification of young objects is the $J3$ band and the $H_{\rm short}$ (Hs) and $H_{\rm long}$ (Hl) bands

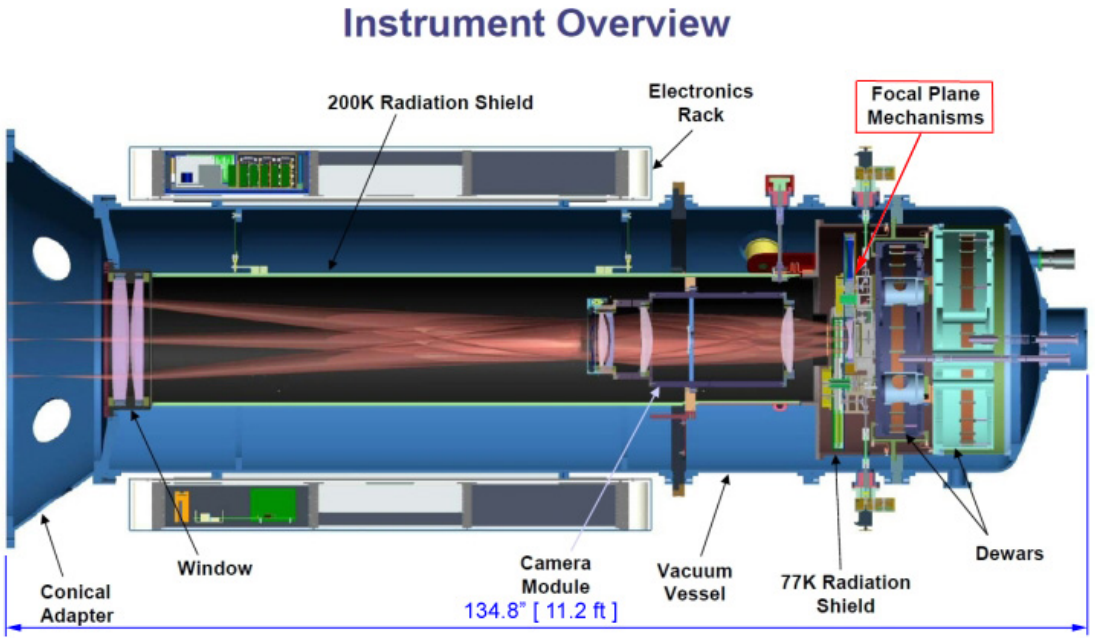

FIGURE 1.12: Design of the FourSTAR NIR camera on the Magellan Baade 6.5m telescope at Las Campanas Observatory, Chile. ©Trustees of the Carnegie Institution of Washington

which divide the *H* band equally (see Figure 1.13). These narrow bands allow for the observation of UCDs in a number of narrow band colours.

The SpeX Prism Library Analysis Toolkit (SPLAT[4], Burgasser 2014) is based on the SpeX database of low resolution NIR spectra of low temperature stars and Brown Dwarfs. The library contains 2000+ spectra obtained from the SpeX NIR spectrograph located on a 3m telescope at the NASA Infrared Telescope Facility (IRTF) on Mauna Kea, Hawaii (Rayner et al., 2003), Figure 1.16. SpeX covers $\sim 0.65 - 2.55\mu$m. The code package SPLAT can be used to examine template SpeX spectra and by simulating a range of filter sets, predict magnitudes for the narrow band filters available on FourSTAR. A range of different simulated narrow band colours are shown in Figure 1.14 to demonstrate the difference between VL-G and field objects in the narrow band colours available with FourSTAR.

J-J3 against Hs-Hl shows the clearest differentiation between field objects and VL-G objects. This is because J-J3 is relatively constant across spectral types, while Hs-Hl is elevated for VL-G against field objects, as shown in figure 1.15. No observations were made as part of this program to confirm these simulated colours match actual FourSTAR observations. The limitations are discussed in Section 3.3.5.

[4] `http://pono.ucsd.edu/~adam/browndwarfs/splat/`

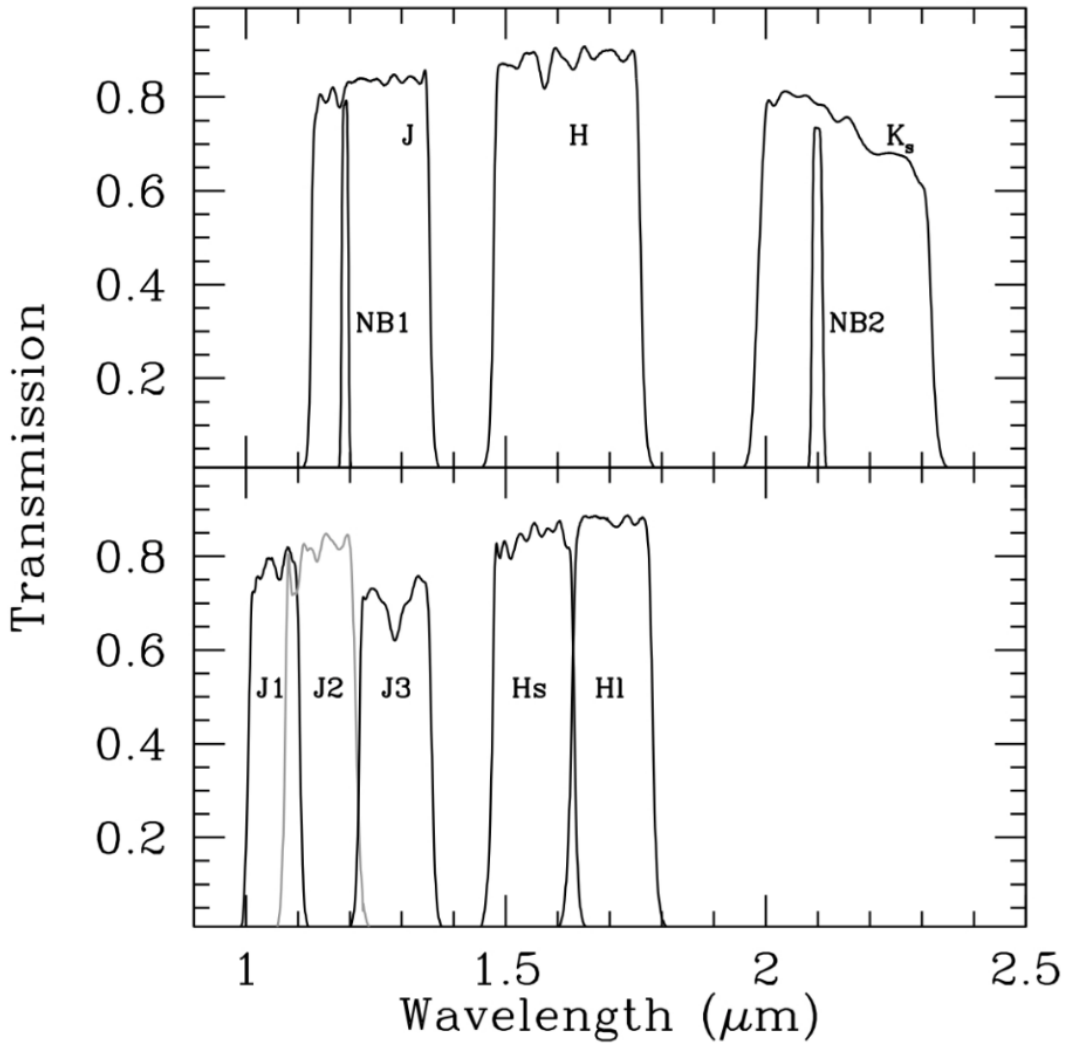

FIGURE 1.13: Filter transmission profiles for the FourSTAR NIR camera on the Magellan Baade 6.5m telescope at Las Campanas Observatory, Chile. ©Trustees of the Carnegie Institution of Washington

Hs-Hl narrow bands each represent half of the H band (Figure 1.13). As detailed in section 1.4.1, the H band region of the infrared spectra of an object is an indicator of that object being very young, with VL-G objects having a more triangular-shaped profile, peaking at $\sim 1.63\mu$m.

Simulated colours from template spectra show that Hs-Hl colour can be used to differentiate between VL-G and field objects. FeH (Iron Hydride) has an absorption region at $\sim 1.60 - 1.75\mu$m correlated with the Hl band. The difference in the simulated template colours shows that VL-G UCDs have a higher Hs-Hl colour, meaning the Hs band is suppressed by FeH absorption in VL-G Objects.

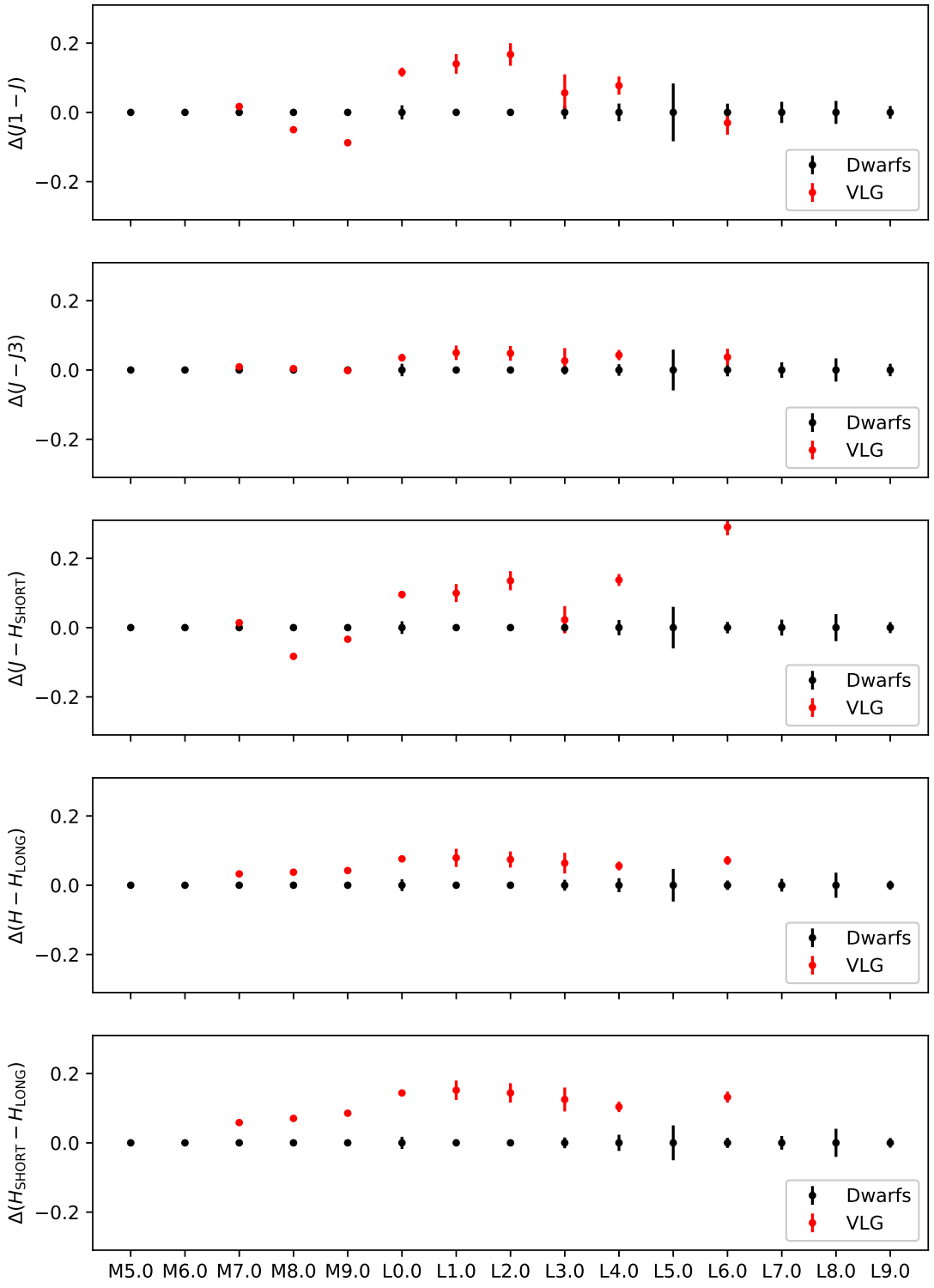

FIGURE 1.14: Simulated FourSTAR narrow band colours, simulated with the SPLAT package. Magnitudes show the difference between the simulated value for a field object of spectral types M5 - L9 and equivalent spectral type VL-G objects.

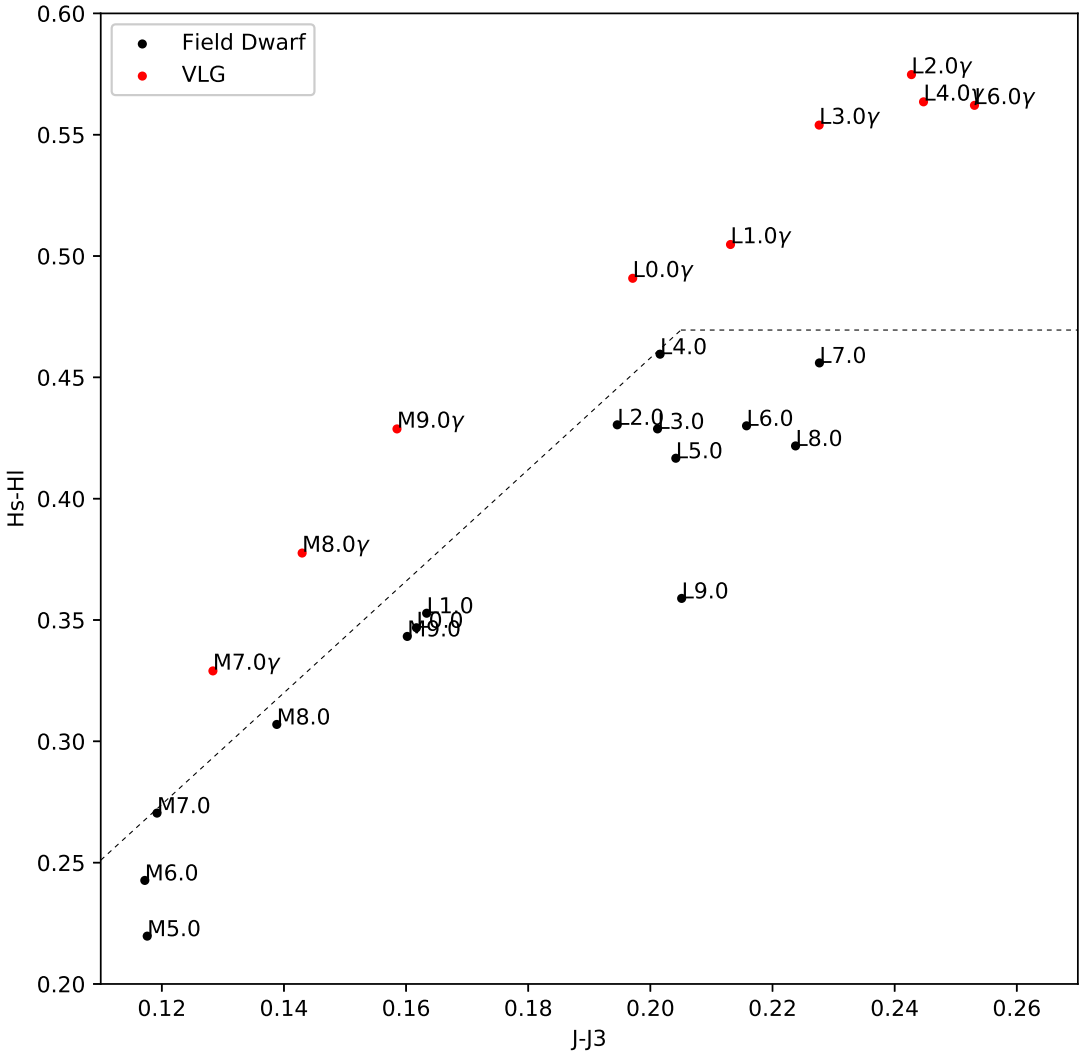

FIGURE 1.15: Simulated J-J3 against Hs-Hl 2 colour diagram with selection region based on template spectra for field and very low gravity objects. Dashed region indicates a 2 colour selection region for candidate young objects.

1.5 Ultracool Dwarfs as Companions

UCDs are thought to form through the same star formation mechanisms as stellar objects, through fragmentation of turbulent molecular clouds (Bate et al., 2002). Similar to other dwarf stars, UCDs are found in a variety of different multiple system arrangements. These can include close binaries to stars and other stellar objects such as the Brown Dwarf companion to White Dwarf 0137-349 (Burleigh et al., 2006). The Brown Dwarf here has a close orbit with a semi-major axis of only $0.65R_{\odot}$ (Maxted et al., 2006). For UCD binaries to stellar objects, statistical analysis of exoplanet discoveries shows there is a lack of UCDs as close companions to FGK stars with orbits of $<$ 5AU, the so called 'Brown Dwarf Desert' (Marcy and Butler, 2000)

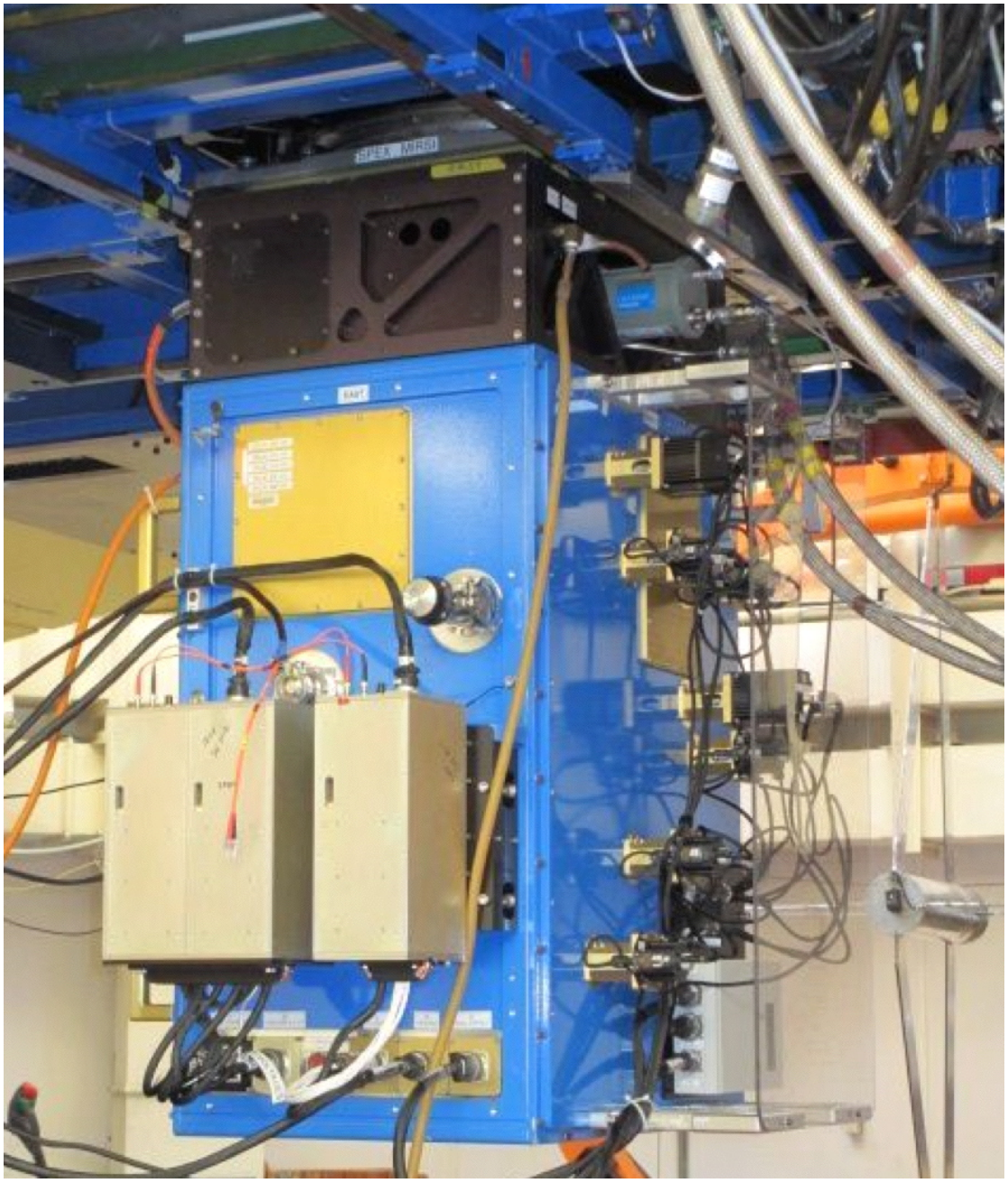

FIGURE 1.16: SpeX NIR Spectrograph mounted on the 3m telescope at the NASA Infrared Telescope Facility (IRTF) on Mauna Kea, Hawaii ©NASA Infrared Telescope Facility

UCDs can be found in binary pairs consisting of two UCDs. These object pairs have been observed to have a very similar mass ratio close to unity (Burgasser et al., 2007), closer to unity than for the observed fraction for stellar binaries of 0.25 - 0.50 (Duquennoy and Mayor, 1991). UCD binaries are rare as the low mass of the components means that the system is weakly bound. UCD binaries are likely to be young as older pairs of objects are increasingly likely to be disrupted and broken apart as they age.

UCDs are also observed as wide companions to FGK stars, such as Gomes et al. (2013) detection of an L2 UCD at $\sim$ 1400 AU from the K8 dwarf primary and the detection of L5 UCD at $\sim 10^5$ AU from the G499AB system. G499AB is a close binary consisting of a K5 star and a M4 dwarf (Reid et al., 2004). The G499 triple system demonstrates how UCDs can be found at wide separation to multiple systems. Other detections of wide UCDs have demonstrated the frequency of these wide binaries to be 0.33% of stellar objects having an L dwarf companion at a separation of between 30 - 10,000 AU (Gomes et al., 2013).

Wide UCD companionship can be confirmed through having common proper motion (CPM) with another object (Marocco et al., 2017). Object pairs with common proper motion relationships are statistically unlikely to be chance line of sight associations (Marocco et al., 2017). A pair with common proper motion, even at a wide separation of the order of 10^5 AU, will have a similar distance as 1 pc $\sim 2 \times 10^5$ AU. When a candidate pair has been shown to have a likely CPM relationship, a common distance is a reasonable assumption. Assuming a common distance allows the absolute magnitude of the object to be calculated. Once the absolute magnitude of a candidate UCD has been estimated based on the primary object's distance, the status of the candidate as a UCD can be dismissed due to the candidate being too bright, indicating an object that is not a UCD or indicating a chance alignment. If the absolute magnitude value is still within the UCD range then the object keeps its status as a candidate UCD at that common distance.

The simulated sample work of Marocco et al. (2017) provides other detection analysis. Within the sample of objects, any UCD candidate within 30pc and with on sky separation of less than 6 arcseconds between the primary and UCD candidate can be confirmed with a false-alarm-probability < 0.0001 from common distance alone (Figure 1.17, Marocco et al. 2017). This is because close objects are unlikely to have other line of sight contaminating objects between the primary and the candidate companion and because for close objects the volume where a line of sight object could mimic a UCD shrinks with distance. However, this simulated sample

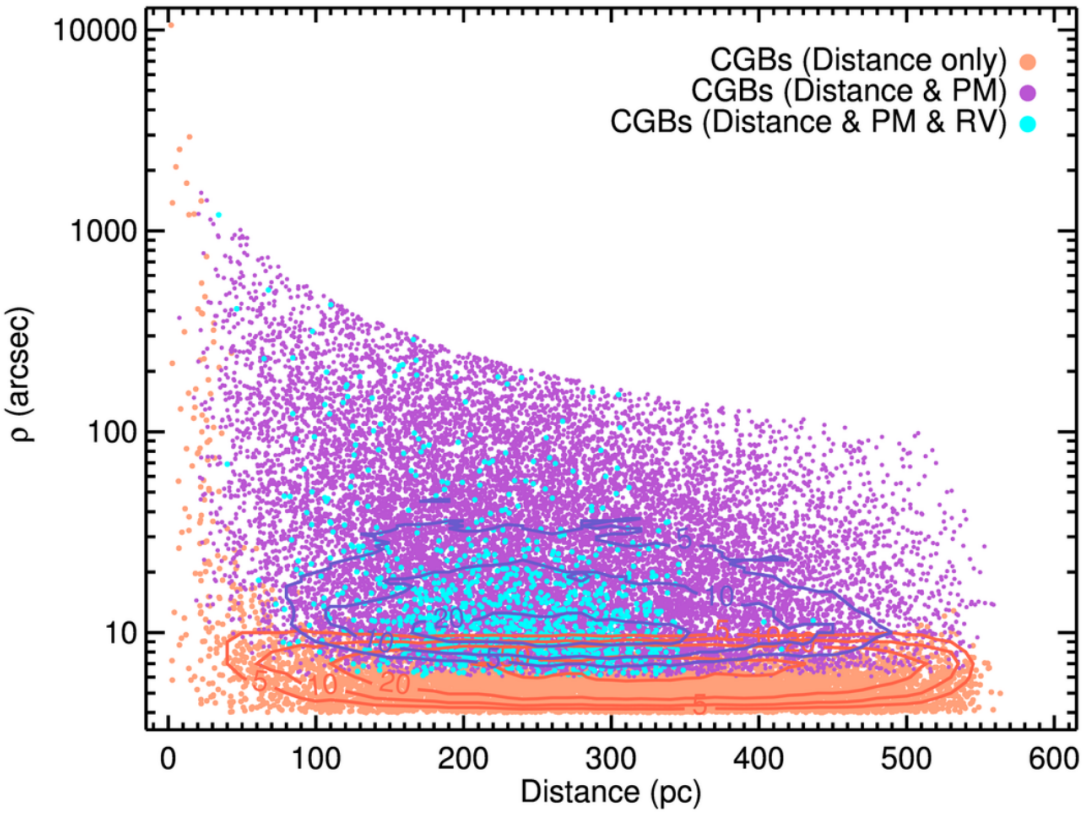

FIGURE 1.17: Simulated UCD sample from Marocco et al. 2017 showing separation and distance. Colour coded for the different confirmation methods required to confirm companionship and be below false-alarm-probability < 0.0001.

considered objects within the 550 pc simulated field of objects. Background objects reddened through dust extinction can still mimic a UCD in this space.

In order to complete a common distance estimate, a candidate must be given a spectral type by either observing a spectra or using a phototyping system as developed by Skrzypek et al. (2015). By determining the spectral type of the candidate, the absolute magnitude can be compared to the apparent magnitude to give spectral type distance estimate.

1.5.1 Candidate UCD Objects from Optical and NIR Surveys

UCD candidates can, depending upon their spectral type and parallax, be found through selection from optical and near infrared surveys. Example optical catalogues include the Sloan Digital Sky Survey (SDSS, DR9, York et al. 2000) and the Panoramic Survey Telescope and Rapid Response System (PanSTARRS, PS1, Magnier et al. 2016). Example near infrared catalogues include the UKIRT Infrared Deep Sky Survey (UKIDSS LAS, DR9, Lawrence et al.

2007) and the VISTA Hemisphere Survey (VHS, DR3, Emerson et al. 2004). Large number of UCDs have also been found through The Two Micron All-Sky Survey (2MASS, Skrutskie et al. 2006) and The Wide-Field Infrared Survey Explorer (WISE, Wright et al. 2010).

Numerous candidate objects have been found previously using such catalogues, with their status as substellar objects confirmed with subsequent spectral observations (e.g. Burningham et al., 2010, 2011, Schmidt et al., 2010, Day-Jones et al., 2013, Zhang et al., 2017).

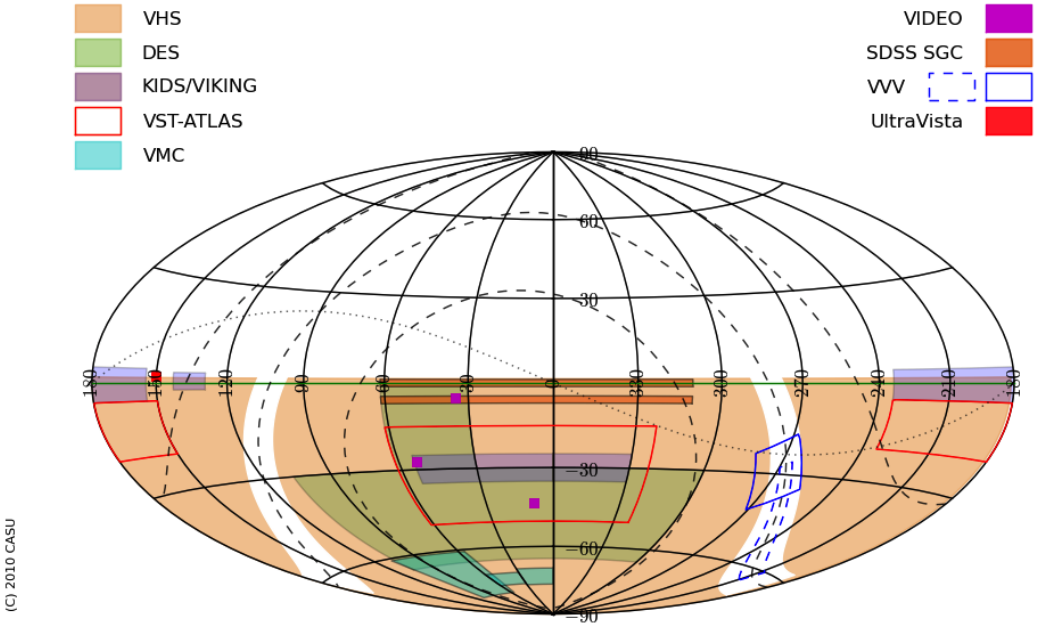

FIGURE 1.18: Footprint of the VISTA Hemisphere Survey including other VISTA surveys ©CASU.

The SDSS uses g, r, i and z broadband filters while PanSTARRS uses g, r, i, z and Y. PanSTARRS band values are calibrated to be comparable to SDSS values. The Y filter bridges the gap between the optical and the NIR J, H and K filters. As a result, the Y filter is present in both the optical PanSTARRS catalogue and the NIR VHS and UKIDSS lists. Filter systems exist in different magnitude systems and so can need conversions. PanSTARRS Y is given in the AB magnitude system where as UKIDSS and VHS give their values in the Vega system. The values can be converted to a shared system using conversions such as Blanton and Roweis (2007). UKIDSS gives K band in NIR while VHS gives a slightly different broadband of K_s. These have slightly different centre points. These also can be converted in to a shared system (Leggett et al., 2006).

Young UCDs known so far have been predominantly found in the southern hemisphere, due to the chance location of young associations (Cruz et al., 2009). As such, the VHS survey is likely to have a number of candidate young UCDs due to its range below 0° declination as shown in Figure 1.18 .

1.5.2 Primary Star Candidates from GAIA

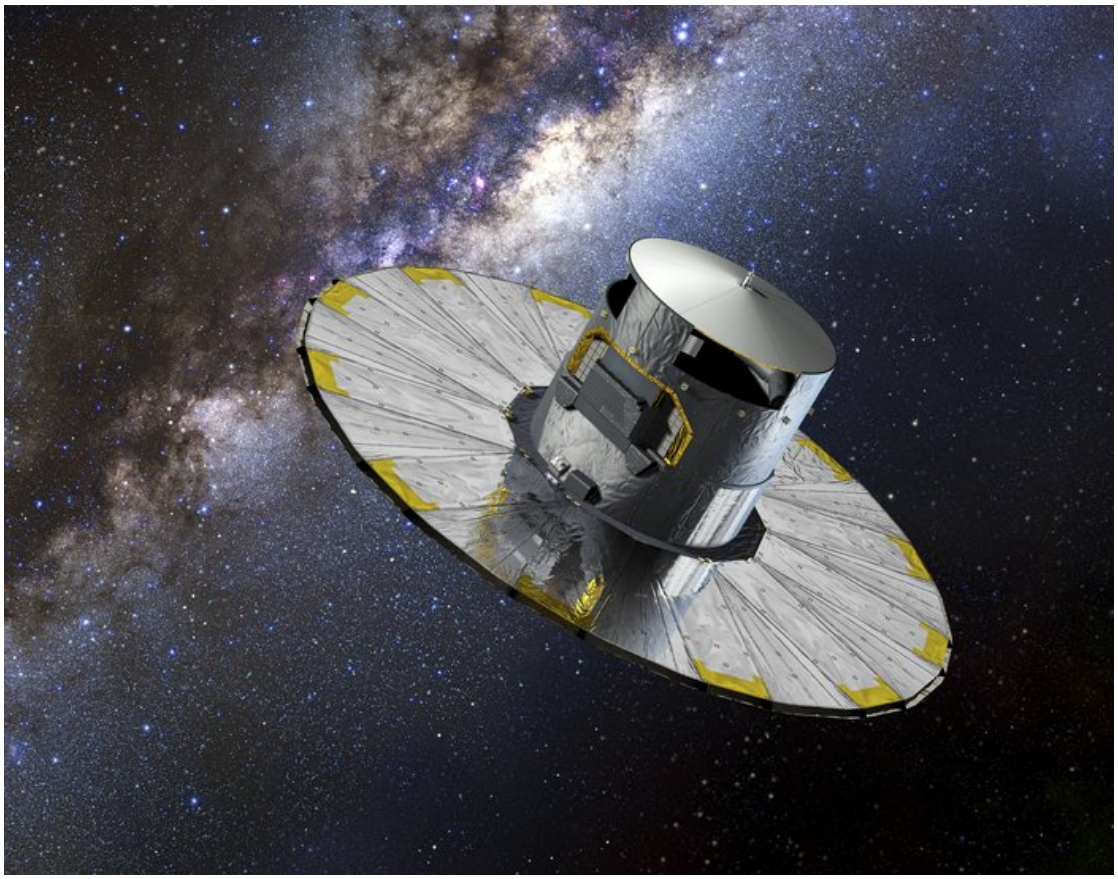

FIGURE 1.19: Artist Impression of *Gaia* satellite. ©ESA/ATG medialab.

Gaia is an orbital observatory launched in December 2013 (Figure 1.19, Gaia Collaboration et al. 2016b). The instrument will record the positions of $\sim 10^9$ stars, representing $\sim 1\%$ of the Milky Way, at multiple epochs. These multiple epochs are used to calculate the precise position of the objects via the parallax method. The measured positions of each object compared to the background field at different points during the Earth's orbit of the Sun enables the distance of the object to be calculated, as detailed in Figure 1.20. *Gaia* will take radial velocity (RV) measurements for a subsample of tese objects, enabling three dimensional positions to be given for over $\sim 10^6$ stars (Bailer-Jones et al., 2013).

The multiple epoch observations of *Gaia* and the parallax measurement allow the proper motion of the stars to be calculated by considering the change in the objects position over time greater than the parallax movement over 12 months.

Gaia is equipped with a high resolution narrow band spectrograph covering 845-872 nm to calculate RV and a low resolution spectrograph covering 330-1050 nm. This spectrograph data, combined with the B and r band photometers, will ensure objects from the *Gaia* database will have a well defined spectral type and photometric magnitude information.

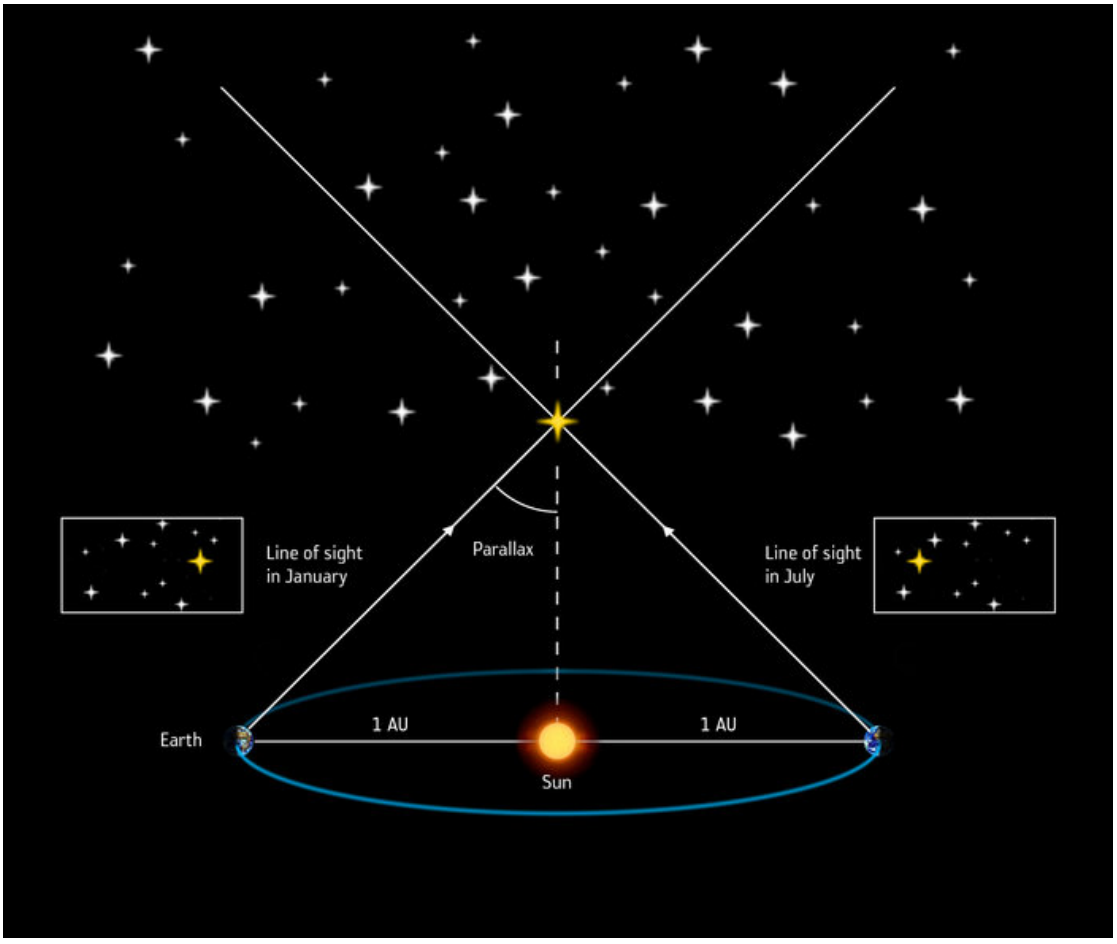

FIGURE 1.20: Diagram indicating the stellar parallax method of distance. ©ESA/ATG medialab.

Gaia presents an opportunity to identify primary stars for systems containing candidate Brown Dwarfs with very well constrained parallaxes. *Gaia* Data Release 1 (DR1) consisted of two parts. The position and G magnitude of each *Gaia* target was released for the full catalogue in DR1 (Gaia Collaboration et al., 2016a). The second part is the full catalogue positions combined with the *Tycho-2* and *Hipparcos* catalogues to produce the *Tycho-Gaia* Astrometric Solution

(TGAS) catalogue of $\sim 2.0 \times 10^6$ objects with astrometric measurements (sky position, parallax and proper motion, Lindegren et al., 2016).

1.6 Benchmark Brown Dwarfs and Ultracool Dwarf Systems

Physical properties (mass, radius, composition) and atmospheric properties (effective surface temperature, T_{eff}, surface gravity, Log(g) and metallicity, [M/H]) cannot be reliably observed directly from UCDs. As discussed in Section 1.3, surface gravity changes with age as UCDs contract further over time, as does T_{eff} with UCDs cooling with time. This degeneracy is complicated by the effect of metallicity on observed UCD photometry. UCDs with independent constraints on these properties are required as a fiducial calibrator. Such systems are often referred to as "Benchmark" systems (Pinfield et al., 2006).

"Benchmark" systems are any system where the characteristics of the UCD can be independently constrained. This can be through membership of clusters or comoving groups or being part of a multiple system such as eclipsing binaries and wider multiple systems. This work focuses on the search for "Benchmark" systems consisting of a primary with constrained characteristics that can be applied to a companion UCD at a wide separation. Hereafter, references to "Benchmark" systems in this work refer to wide binaries of this type.

UCDs close to their primary stars absorb and re-emit energy from their primary star (Marley and Robinson, 2015). A bright primary with $M_V \sim 0.3$ is ~ 12 times as luminous as the Sun. A wide binary with a low separation of ~ 500 AU will mean the companion is ~ 25 times as far away from the primary star as Uranus is from the Sun. UCD radii are of the same order of magnitude as that of giant planets as both are set by the electron degeneracy (Burgasser, 2001). All of this means that even if a bright primary is irradiating a wide separation companion and the candidate was young with a radius of $\sim 10\ R_J$, then the candidate would still only absorb about the same amount of radiation as Uranus does from the Sun, and absorption by Uranus can be ignored when considering the emission spectrum (Pearl et al., 1990). Therefore the effect of irradiation from the primary is ignored when considering the colours and magnitudes of the UCDs in this work.

It is predicted that there will be up to $\sim 24,000$ benchmark systems within the full dataset (Marocco et al., 2017). The authors simulate a population of UCDs of M, L, T and Y spectral types at a density of 0.0024^{-3}. Simulated objects are given a mass within the range $0.001 <$

$M/M_{\odot} < 0.12$ and an age following the Chabrier (2005) IMF. Each UCD object is given simulated observable properties based on BT-Settl models (Baraffe et al. 2003, 2015). The simulated population includes UCDs that are unresolved binaries at a rate of 30% (Marocco et al., 2015). This population is then linked to random field stars with a random separation up to 50,000 AU, normalised to the rate of 0.33% for L dwarfs between 30 - 10,000 AU from Gomes et al. (2013).

The field of simulated primary stars is taken from GUMS (Robin et al., 2012), a simulated field of *Gaia* stars, including main-sequence stars, giants, subgiants, white dwarfs and chemically peculiar stars and other rare objects. GUMS simulates stars of various ages, based on a constant formation rate for objects between 0 and 10 Gyr and three bursts of formation at 10 Gyr for the Bulge, 11 Gyr for thick desk and 14 Gr for the spheroid (Marocco et al., 2017).

Considering this sample of field stars and simulating the detection criteria of *Gaia* and the detection depths in various bands of optical and NIR surveys, the predicted number of benchmarks available within the full *Gaia* release is calculated to be $\sim 24,000$.

This large sample allows searches to focus on finding benchmark systems with outlier characteristics, such as having young age and extreme low surface gravity. Figure 1.21 shows the Mass Age relationship from within the sample simulated by Marocco et al. (2017) showing the population young UCD benchmarks that are likely to be found within the full *Gaia* release. Marocco et al. (2017) predict ~ 2100 metal rich/metal poor UCDs outlier benchmarks within the full *Gaia* release. Marocco et al. (2017) first search for outlier UCD population following the simulations found that 94% of their candidates were confirmed as UCDs with 60% confirmed to be benchmark companions based on common proper motion and common distance.

UCD evolution as shown in Figure 1.8 indicates that young objects are likely to be spectral types of M and L. T and Y dwarfs are most likely older objects that have cooled to these temperature ranges. The simulated sample from Marocco et al. (2017) as shown in Figure 1.21 shows that that only a small fraction of the potential young objects to identify will be T dwarfs, with M and L dwarfs dominating. As such, this work will concentrate on the detection of M and L dwarfs as this work itself uses only a small fraction of the overall *Gaia* sample. Searching specifically for young T dwarfs will not be possible until *Gaia* DR2.

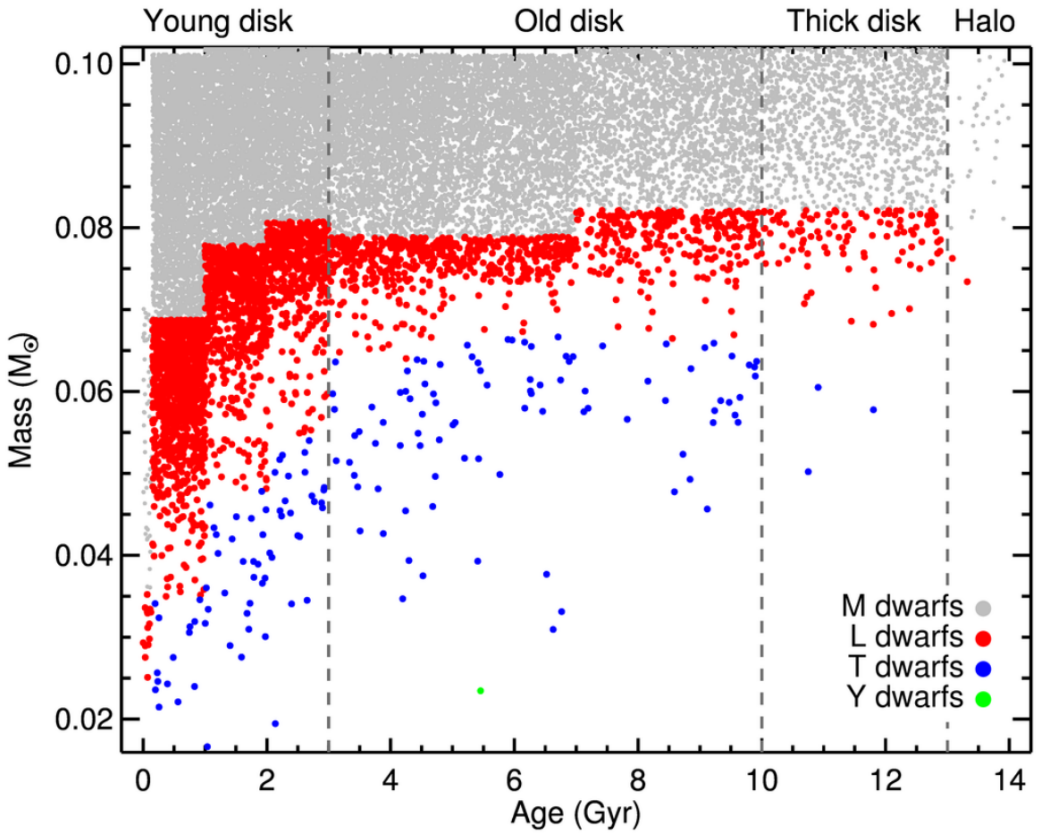

FIGURE 1.21: Simulated *Gaia* UCD Benchmark sample from Marocco et al. 2017 showing age versu mass relationship for simulated benchmarks. Grey points are simulated M dwarfs, red points are L dwarfs. Blue points are T dwarfs and green points are Y dwarfs.

1.6.1 Primary Age

A benchmark system would have shared age with both the primary and the companion having formed at the same time. Indications of youth can be determined from information available about potential primaries. Many of the objects with the *TGAS* sample are well studied and have entries in the SIMBAD astronomical database (Wenger et al., 2000). SIMBAD is a searchable database of objects containing numerous measured characteristics for $\sim 10^6$ objects(Wenger et al., 2000). The database provides a searchable flag system which can be searched for characteristics of youth. These range from objects considered members of comoving groups with known ages to proto-stars to various types of variable star types known to be young.

Various types of variable stars are young objects. As the star evolves, prior to reaching the point of relative equilibrium represented by main sequence position, disruptive processes can cause young stars to vary in distinctive fashion, such as T Tau stars. Primary stars that have been flagged as certain types of variables can be considered to be young and so any companion

would share this age constraint. Other published research has been incorporated in to SIMBAD with a number of objects simply flagged as Protostars or Young Stellar Objects.

Some primaries have confirmed membership of comoving groups with well defined ages. These groups reflect only a small subsection of the total TGAS primaries, but a large number of currently known young UCD benchmarks have been found associated with young groups (Cruz et al. 2003, Scholz et al. 2005, Liu et al. 2016). Primary candidates with confirmed membership of young comoving groups and associations will share the age constraints with the whole group.

Without moving group membership or other independent method of determining an age, main sequence stars cannot be aged directly from observation. The age of the Sun is constrained based on geological records indicating the age of the planets within the solar system. Sun like stars can be aged based on Asteroseismology, where pulsating variation of the star can be used to model the interior structure and compared to models to indicate core contraction and stellar age. However, this method requires detailed modelling and light curves from long period observation missions such as from CoRoT (Baglin et al., 2002) or Kepler (Koch et al., 2010). Using this information, Chaplin et al. (2014) estimated ages for ~ 500 main sequence and subgiant stars and were able to estimate ages with errors less than 1 Gyr for $\sim 36\%$ of their sample. In addition, detailed models on a case by case basis can enable ages to be calculated to even greater accuracy (e.g. Lebreton and Goupil 2014). However, this small sample, both in terms of sky area and total number, mean it is unlikely detailed age estimates from Asteroseismology will be available for any of our primary candidates.

While ages cannot be determined from observation, a maximum age can be estimated from the star's bolometric timescale. This is based on an estimation of the star's spectral type to give a bolometric correction and the object's luminosity. Assuming the star is a main sequence object, this enables a maximum main sequence lifespan to be estimated. These values are maximum ages and do not represent an estimate of the current age of the star.

Structural models of main sequence stars' evolutionary tracks produce isochrones that indicate that young stars will be brighter than field age stars of their temperature, such as isochrones from the online PARSEC isochrone generator[5] (Marigo et al., 2017). This over-luminosity potentially enables young primaries to be preferentially selected. As metal content can also cause over-luminosity (seen again in the isochrones from Marigo et al. 2017), known object metallicity can

[5] `http://stev.oapd.inaf.it/cgi-bin/cmd`

be incorporated to ensure that objects selected are not being selected for being over-luminous due to metal content. However, this is likely to also have a large amount of contamination from older stars beginning to evolve off the main sequence. As such, indications of youth due to over-luminosity should be used only in conjunction with other indicators.

1.6.2 Primary Metallicity

A large fraction of the TGAS primaries have well constrained metallicity measurements. Metallicity surveys from spectra include the Radial Velocity Experiment (RAVE, DR5, Kordopatis et al. 2013) and the Large Sky Area Multi-Object Fibre Spectroscopic Telescope survey (LAMOST, DR3, Yuan et al. 2015). Metallicity of the primary can also be estimated from photometry, with Ammons et al. (2006) providing metallicity estimates for as many as $\sim 88\%$ of the *TGAS* sample. However, this work uses metallicity estimates, also from photometry, as a training set. This introduces an inherent error due to the inaccuracy in the metallicity values used to train the process.

One goal of the *Gaia* collaboration is to use the ground based spectrograph observations to produce high resolution spectra for 100,000 stars to a magnitude of 19 (Gilmore et al., 2012).

In addition to identifying if candidate objects are metal rich, reducing the possibility that redder colours indicate age, these catalogues also enable objects that are metal rich or metal poor without signs of youth to be identified as a comparison to objects with known young age. While metal-rich or metal-poor systems are not the main focus of this work, benchmarks with known outlier metallicity properties are needed to properly disentangle the effect of age and metallicity. Outlier metallicity systems are among the target benchmark groups identified by Marocco et al. (2017).

1.7 Aims and Document Structure

This report documents the work carried out to select young candidate benchmark UCDs. The aim is to identify a list of candidate objects that have a high degree of probability of being a young UCDs and being wide companions to a primary object found in the *Gaia* catalogue.

Candidate UCDs are searched for within a search radius of a potential primary from the *TGAS* catalogue. UCD candidates are selected based on optical and NIR photometry based on colour

and absolute magnitude. Candidates with indications of youth are high priority. Pairs of wide companions and primaries are ruled out based on proper motion differences, leaving objects that are either promising CPM pairs or objects where the proper motion of the companion is not well enough defined to confirm or rule out a CPM relationship. An additional sample of benchmarks with primaries with outlier metallicities will also be prepared.

A program of observation was developed, based on the selected result that were available and the available observation time. This program included both NIR photometry and NIR spectroscopy. Several observing proposals were submitted with three being accepted. Results were gained from two nights of NIR narrow band photometry observations. These results were analysed to evaluate the effectiveness of the selection process developed.

Chapter 2 describes the selection procedure to identify candidate objects. Chapter 3 describes and discusses the selection results and the sample of candidate UCDs identified and describes the results of the observing program. Chapter 4 draws conclusions from these results and sets out a program of future work.

Chapter 2

Candidate Selection Process

2.1 TGAS Sample Selection

The *Tycho-Gaia* Astrometric Solution (TGAS) catalogue contains $\sim 2.0 \times 10^6$ objects with astrometric measurements (sky position, parallax and proper motion, Lindegren et al. 2016). The TGAS sample defines the list of candidate primaries and so sets the areas of sky to search for candidate companion UCDs.

The small number of erroneous results with negative parallax measurements are removed from the full TGAS list of objects. TGAS objects within 10 parsecs are removed as it is believed most UCDs within this distance will have been found and well studied (Deacon et al., 2014). In addition, targets are selected based on a maximum separation between target and candidate companions of 10^5 AU (Section 2.2). This varies the sky search radius with inverse proportion to the distance of the primary. Objects at low distance (high parallax) have very large search areas, increasing the amount of contamination in the candidate sample from background objects.

Using the sensitivity of these surveys, a maximum parallax of the primary objects to consider is calculated by considering the absolute magnitude of UCDs. The absolute magnitudes of an M7 UCD in J and i is shown in Table 2.1.

TABLE 2.1: M7 spectral type template absolute magnitudes.

	M7	Citation
M_i	12.50	Dahn et al. (2002)
M_J	10.31	Dupuy and Liu (2012)

TABLE 2.2: Survey sensitivity limits in multiple bands

Survey	i	J
SDSS	21.3	
Pan-STARRS	22.7	
UKIDSS		19.5
VHS		20.2

TABLE 2.3: Parsec maximums based on survey sensitivity

Survey	i	J
SDSS	575pc	
Pan-STARRS	1096pc	
UKIDSS		676pc
VHS		950pc

The distance maximums can then be calculated in equation 2.1, where D is distance and x is any band.

$$\mathrm{Log}_{10}\,\mathrm{D} = \frac{x - \mathrm{M}_x}{5} + 1 \tag{2.1}$$

The distance limits in the different bands for each catalogue for a candidate of spectral type M7 is shown in Table 2.3. TGAS primary candidates were limited to a maximum distance of 500pc. This is to ensure that candidate UCD companions would not be too faint to be detected in the surveys used. This reduced the TGAS sample to 907,962 objects.

For primaries of greater distance, the percentage error on the parallax value increases with greater distance, as the magnitude of the parallax value decreases while the errors remain of similar magnitude. By removing all objects more than 500pc distance the quality of the TGAS subsample significantly improved, as shown in Figure 2.1.

The remaining primary TGAS primary candidate sample was reduced further by only selecting objects with a percentage parallax error of $\leq 30\%$. Previous analysis of other parallax missions such as Hipparcos show that errors of 17.5% can lead to a bias in distance of up to 30% (e.g. Lutz and Kelker 1973, Oudmaijer et al. 1998), so primaries with large parallax errors are not considered. This removes the higher error candidates from the long tail as shown in Figure 2.1. The final sample of candidate TGAS primaries contains 880,121 objects.

2.2 Cone Search Sky Surveys

Companion candidates were searched for in the databases of the SDSS DR9, UKIDSS DR10, VHS DR3 and PanSTARRS, PS1. Cone searches were completed in the SDSS, UKIDSS, VHS

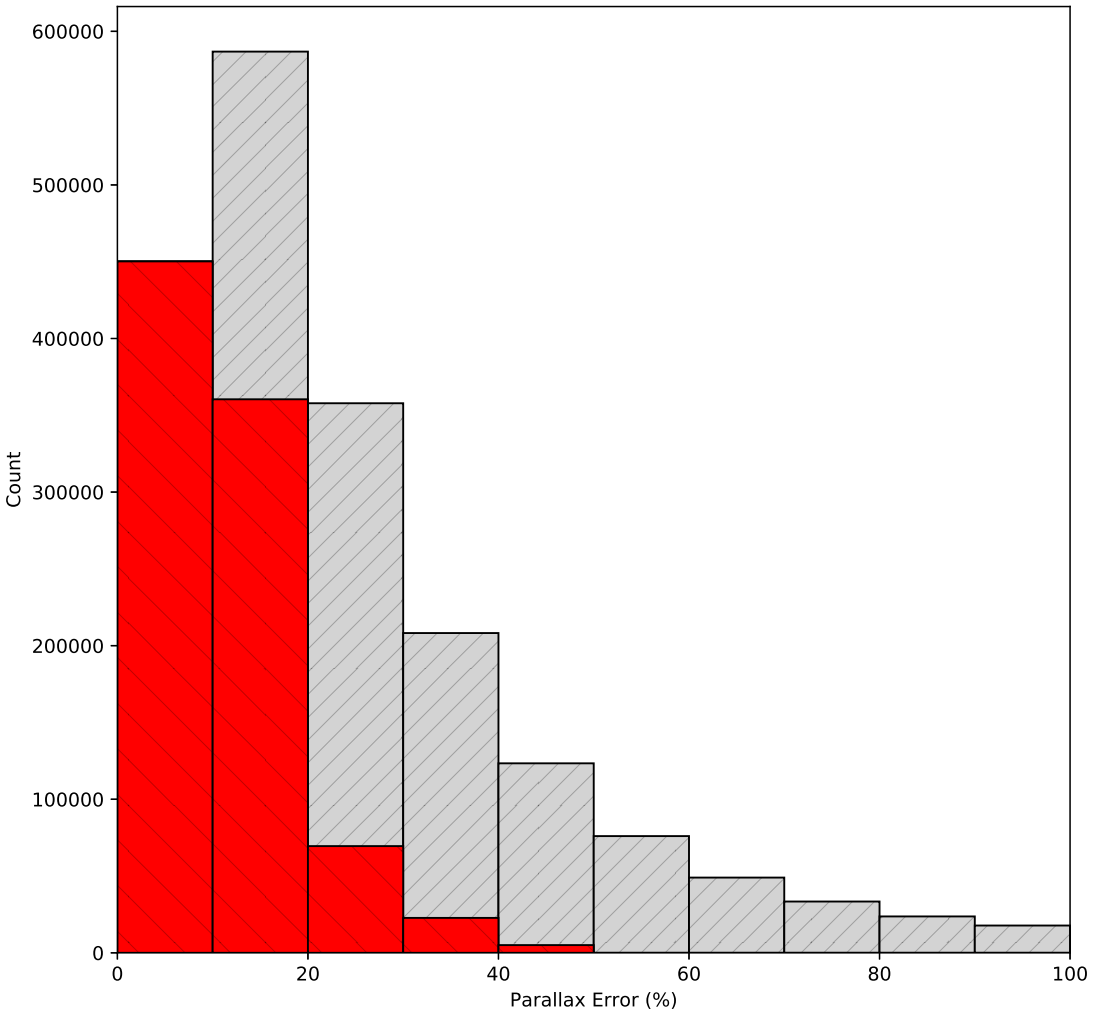

FIGURE 2.1: Histogram of Frequency Distribution of Parallax Error as a %. Light grey sample shows all TGAS objects. Red sample shows TGAS objects within 500pc.

and PS1 catalogues with a variable search radius around each candidate TGAS primary object to the equivalent projected separation of 10^5 AU from each TGAS object.

Candidates were removed from the SDSS, PanSTARRS, UKIDSS and VHS candidate samples based on various quality measures. SDSS summarises all quality checks, such as the target being close to saturated or a bad pixel in the aperture of the target, and lists candidates without any issues as 'CLEAN = yes' within the SDSS database (York et al., 2000). Candidates without 'CLEAN = YES' are removed from consideration.

UKIDSS, PanSTARRS and VHS all employ various checks in to a number system. Each different type of error or fault that could result in a candidate having unreliable values is given an integer value. These numbers are summing in to a quality check value. The IR catalogues give

TABLE 2.4: Quality Cuts for each catalogue search

SDSS
Clean: YES
PanSTARRS
qualityFlag < 64
UKIDSS
ypperrbits < 256
j_1pperrbits < 256
hpperrbits < 256
kpperrbits < 256
priorsec $= 0$
VHS
yppErrBits < 256
jppErrBits < 256
hppErrBits < 256
ksppErrBits < 256
priOrSec $= 0$

TABLE 2.5: Quantity of Candidates within 10,000 AU sky projected separation of a TGAS sample objects and passing quality checks.

Surveys	No.
SDSS	3,541,215
Pan-STARRS	51,238,015
UKIDSS	1,745,124
VHS	8,213,132

this value as a separate value for each band. Candidates outside a certain quality threshold in any of the required bands are removed from consideration. The values used to exclude candidates are described in Table 2.4.

The number of candidates found in different surveys is shown in Table 2.5 with a total of 64,737,486 candidates found within 10^5 AU of one of the sample TGAS primary objects and with candidate catalogue values passing the quality checks. As to be expected due to the area of coverage of the sky, sensitivity and that this catalogue bridges optical and NIR with the Y band observations, PanSTARRS returned the largest number of candidates by an order of magnitude.

2.3 Colour Conversions for Cross-Comparison between Catalogues

2.3.1 Verifying Photometric Consistency Between Surveys

Candidate selection relies significantly on the efficacy of later magnitude and colour cuts detailed in later sections. These magnitude and colour cuts rely on the accuracy and consistency of the photometric measurements within the selected surveys. We made a comparison between

magnitude measurements from the different catalogues. The intention is to identify any photometric offset that may be required in order to bring all magnitude values in to a uniform system. This will enable the combined sample between all surveys to be selected from using consistent colour and magnitude selections regardless of the source of magnitude values.

Figure 2.2 shows the results of these comparisons, with cross matched candidates with accurate magnitude values ($\sigma < 0.05$) plotted and an offset plotted in red. i, J and H magnitudes were found to have no significant offsets. z magnitudes had a small offset required, with a constant of -0.10 magnitudes to be applied to PanSTARRS z values to move these to the reference frame of the SDSS values. It is chosen to bring PanSTARRS magnitudes in to the SDSS frame. This is due to the Dupuy sample of UCDs with parallaxes, used in later sections to guide 2 colour cuts of the selection sample, listing SDSS magnitudes for each target candidate.

2.3.2 Ks to K band conversion

In order to properly select candidates based on the $J-K$ colour as well as calculate other colours involving K, the K_s-band values (from VHS observations) were converted to K based on Table 4 from Leggett et al. (2006) which gives the conversion relationship as described in Equation 2.2. Conversions, such as Leggett et al. (2006), are derived from main sequence stars and as such will not be as accurate for unusual candidates such as UCDs, meaning the introduced errors will likely be slightly larger than shown here. Our wide selection criteria will account for this.

$$K - K_s = -0.025 \times (J - K_s) - 0.003 \tag{2.2}$$

Error in $K - K_s$ is shown in Equation 2.3.

$$\sigma(K - K_s) = 0.012 \times (J - K_s) + 0.008 \tag{2.3}$$

2.3.3 Combining Y Band Values for Different Catalogues

Some candidates have both a Y value from PanSTARRS and a Y value from either UKIDSS or VHS. The Y-magnitude in PanSTARRS is given as part of the AB system where as UKIDSS and VHS values in the Vega system. To correct for this, the Y correction of $+0.634$ from Blanton and Roweis (2007) is applied to the Y-magnitude of PanSTARRS. No one catalogue

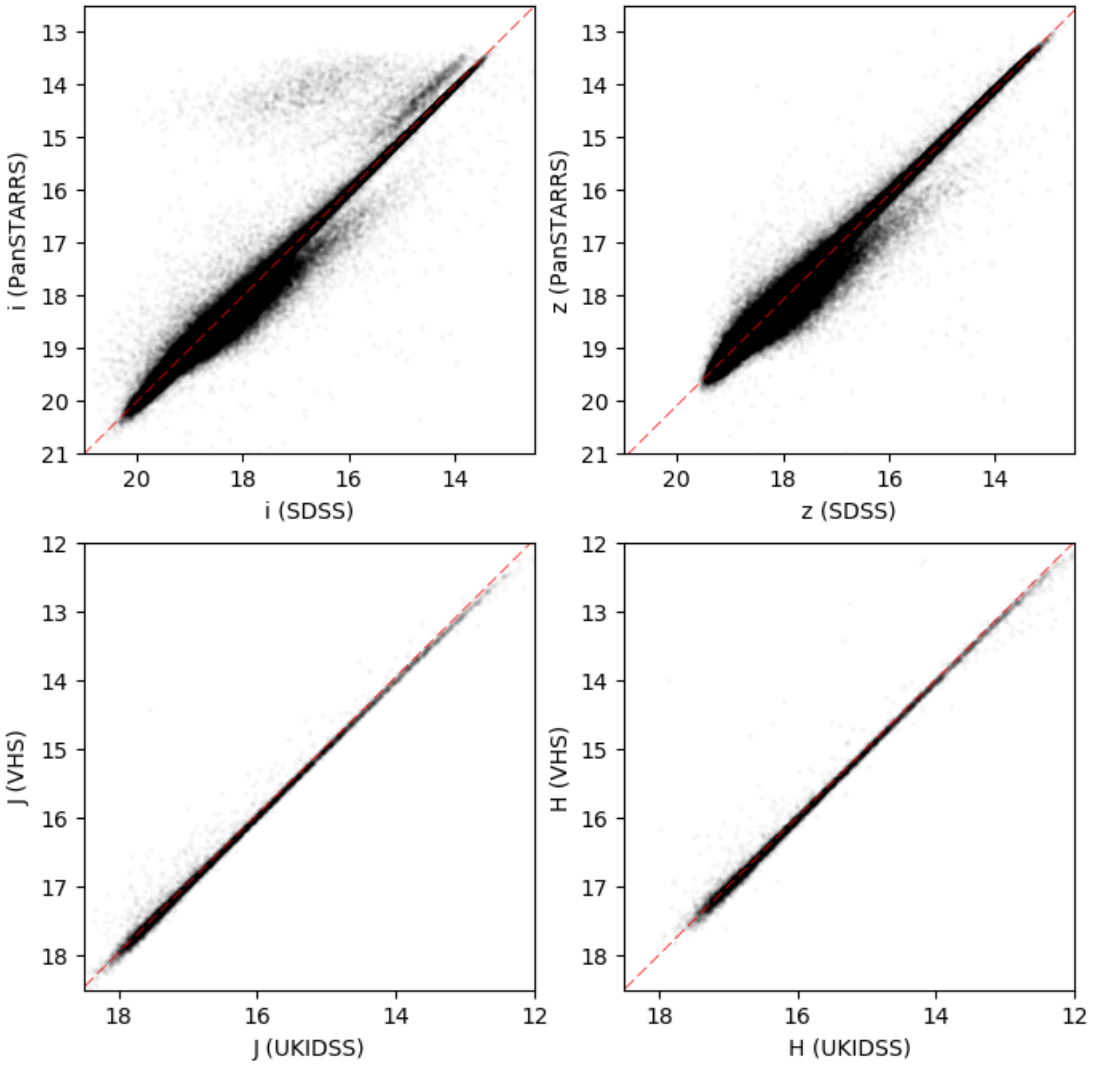

FIGURE 2.2: Cross matched candidates in optical (SDSS to PanSTARSS) and NIR (UKIDSS and VHS). i, z, J and H magnitude comparisons are shown. The red line shows the offsets between the two samples in any band. No significant offset is found in i, J and H. An offset of -0.10 magnitudes is required to move PanSTARRS z to being equivalent of SDSS values.

has systematically higher errors on Y values than the other. Where a candidate has a Y-band value from either PanSTARRS or the infrared catalogue detections then either the infrared Y-magnitude or the corrected PanSTARRS Y-magnitude is used depending upon which has the lowest associated error.

Figure 2.3 shows candidates in both VHS (as an example) and PanSTARRS and the relative Y magnitudes from each. The $+0.634$ conversion between Y in Vega and Y in the AB system from Blanton and Roweis (2007) is shown as the dashed line and fits well. The data sets diverge at very faint candidates where the magnitude limit of the instrument is reached.

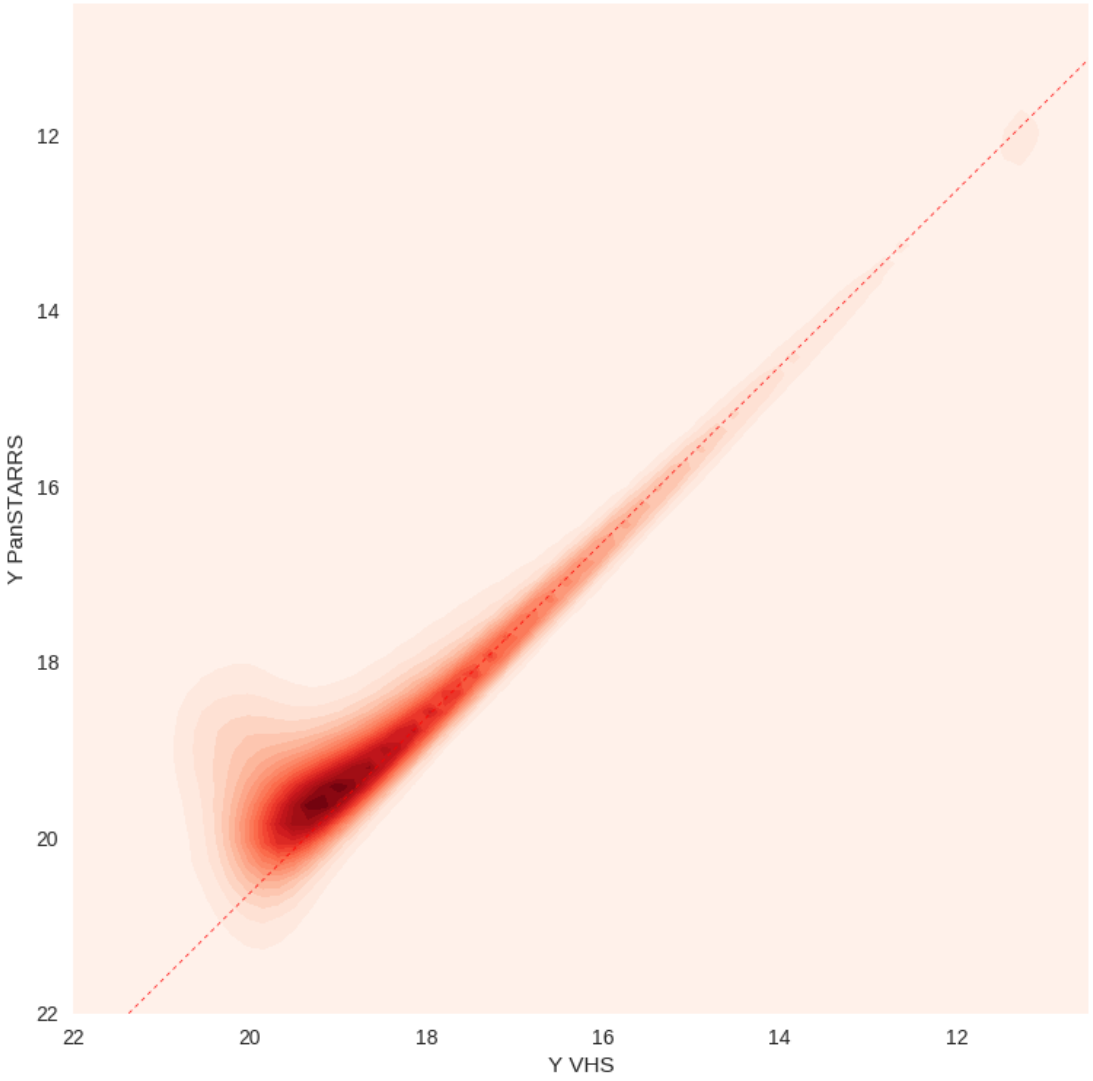

FIGURE 2.3: Cross matched candidates in both PanSTARRS and VHS shown as 2 dimensional density histogram. Y magnitude of each compared. Dashed line shows the +0.634 AB to Vega correction from Blanton and Roweis (2007).

2.4 Two Catalogue Detections

Candidates that are detected in two or more catalogues, at least one in the infrared and a second in visual bands, are selected separately to candidates without an optical observation.

2.4.1 Cross Matching Optical and NIR Surveys

Different surveys with variable epoch differences would require different radii when cross matching them to find common candidates, in order to account for the maximum expected movement

TABLE 2.6: Quantity of cross matched candidates found in two or more surveys.

Surveys	No.
SDSS & UKIDSS	323,983
SDSS & VHS	191,747
PanSTARRS & UKIDSS	795,480
PanSTARRS & VHS	2,465,214
Total	3,776,424

TABLE 2.7: Bands available for each catalogue used.

Surveys							
SDSS	r	i	z				
Pan-STARRS	r	i	z	Y			
UKIDSS				Y	J	H	K
VHS				Y	J	H	K_s

of the candidates on the sky. $\sim 95\%$ of the primaries in the TGAS sample have proper motion in Right Ascensionn ($\mu_\alpha \cos\delta$) and proper motion in Declination (μ_δ) < 50mas/yr. At the maximum epoch difference of 15 years between the NIR catalogues of VHS and UKIDSS and the optical catalogues SDSS and PanSTARRS, the maximum expected sky movement would be 0.75 arcseconds in either RA or DEC. The error in the catalogues in the RA and DEC values is also considered. For SDSS, $\sim 97\%$ of candidates have an error in RA and DEC < 0.25 arcseconds whereas for PanSTARRS this increases to $\sim 99\%$.

A matching radius of 5 arcseconds was used. While a smaller radius could be selected, 5 arcseconds ensured no fast moving pairs or poorly located candidate was excluded. This means care needs to be taken in the visual inspection stage to spot and remove mismatched pairs.

The number of candidates that were cross matched and found to be within 2 of the 4 surveys is shown in Table 2.6 and there were a total of 3,776,424 matched within 2 catalogues.

2.4.2 Colour Cuts - Two Catalogue Results

The different magnitude values fetched for each catalogue are shown in Table 2.7. Candidate UCDs are selected based on colours as well as absolute magnitudes. Absolute magnitude estimates are only correct if the candidate is at the same distance as the primary used for selection. This will be a correct assumption for candidates that are genuine wide companions but will not be the case for line of sight associations.

Colours were only calculated where the error on the apparent magnitude in that band is below 0.3, instead magnitudes with errors above this are treated as non-detections and no colours are calculated that require those magnitudes.

Many of the cuts are influenced by Table 1 of Skrzypek et al. (2015). By plotting different 2 colour plots of the Dupuy sample of UCDs with parallaxes (section 2.6), the cuts inspired by the template colours of Skrzypek et al. (2015) have then been adjusted to bluer colours to allow for outliers to be included. When applying optical and NIR colours, we limit our selection to be based on colours from the Dupuy sample only, as the optical photometry for these UCDs is given in SDSS (AB) magnitudes, consistent with our UCD candidates, whereas the NIR magnitudes are in the Vega system, meaning that any colour crossing from optical to NIR will be across magnitude systems. Y magnitudes have been converted into the same magnitude system (Vega) as other NIR magnitudes (Section 2.3.3) and so $Y-J$ colour cuts from Table 1 of Skrzypek et al. (2015) can be used.

The following selection criteria were applied to the sample of candidates:

- REMOVE $J > 19$ and J non-detections
  Candidates fainter than $J = 19$ will not be included due to the difficulty in following up UCD candidates fainter than $J = 19$. The expense and time required to observe a spectra to the required signal to noise ratio means a focus should be made on candidates $J < 19$ as a large sample of these will be available.

- Candidates with an error in $J > 0.3$ will not be retained as it is required to have higher accuracy for later $J-K$ and $J-H$ cuts.

- REMOVE $M_Y \geq 8$, $M_J \geq 8$, $M_H \geq 8$ and $M_K \geq 8$
  Bright candidates that are not UCDs are removed.

- KEEP $i-z > 0.85$ or not detected in i or z
  Remove candidates bluer in $i-z$ than a UCD but allow candidates without an i or z magnitude to continue through selection. Based on the Spectral Type Template Colours for an object of spectral type M6 from Table 1 of Skrzypek et al. (2015) but adjusted to conservatively allow for the colour spread seen in the Dupuy sample.

- KEEP $i-J > 1.05$ or not detected in i
  Remove candidates bluer in $i-J$ than a UCD but allow candidates without an i magnitude to continue through selection. Based on the lowest SDSS - NIR sample colour in the Dupuy sample of UCDs.

- KEEP $z-J > 2.10$ or not detected in z
  Remove candidates bluer in $z-J$ than a UCD but allow candidates without a z magnitude

to continue through selection. Based on the lowest SDSS - NIR sample colour in the Dupuy sample of UCDs.

- KEEP $Y-J>0.3$ or not detected in Y
  Remove candidates bluer in $Y-J$ than a UCD but allow candidates without a Y magnitude to continue through selection. Based on the Spectral Type Template Colours for an object of spectral type M6 from Table 1 of Skrzypek et al. (2015) but adjusted to conservatively allow for the colour spread seen in the Dupuy sample.

- KEEP $J-H>0.15$ or not detected in H
  Remove candidates bluer in $J-H$ than a UCD but allow candidates without an H magnitude to continue through selection. Based on the Spectral Type Template Colours for an object of spectral type M6 from Table 1 of Skrzypek et al. (2015) but adjusted to conservatively allow for the colour spread seen in the Dupuy sample.

- KEEP $H-K>0.2$ or not detected in H or K
  Remove candidates bluer in $H-K$ than a UCD but allow candidates without an H or K magnitude to continue through selection. Based on the Spectral Type Template Colours for an object of spectral type M6 from Table 1 of Skrzypek et al. (2015) but adjusted to conservatively allow for the colour spread seen in the Dupuy sample.

- KEEP $J-K>0.4$ or not detected in K
  Remove candidates bluer in $J-K$ than a UCD but allow candidates without a K magnitude to continue through selection. Based on the M_J vs $J-K$ CMD as discussed in Section 2.6.

2.4.3 Colour-Magnitude cuts following known UCD sample

Based on the database of UCD objects within the Dupuy sample and following the method as set out in Marocco et al. (2017), the following cuts were made based on the M_Z to $i-z$ CMD (Figure 2.4) and the M_J to $J-K$ CMD (Figure 2.5).

The cut gradients are:

- KEEP where $11.5<M_z<[3.5714\times(i-z)+13.03574]$ or $i-z>0.91$ or no i or z detection. (Figure 2.4).

- REMOVE where $M_z<15$ AND $M_z<[3.5714\times(i-z)+6.5]$ AND $(i-z)>2.1$ Figure 2.4.

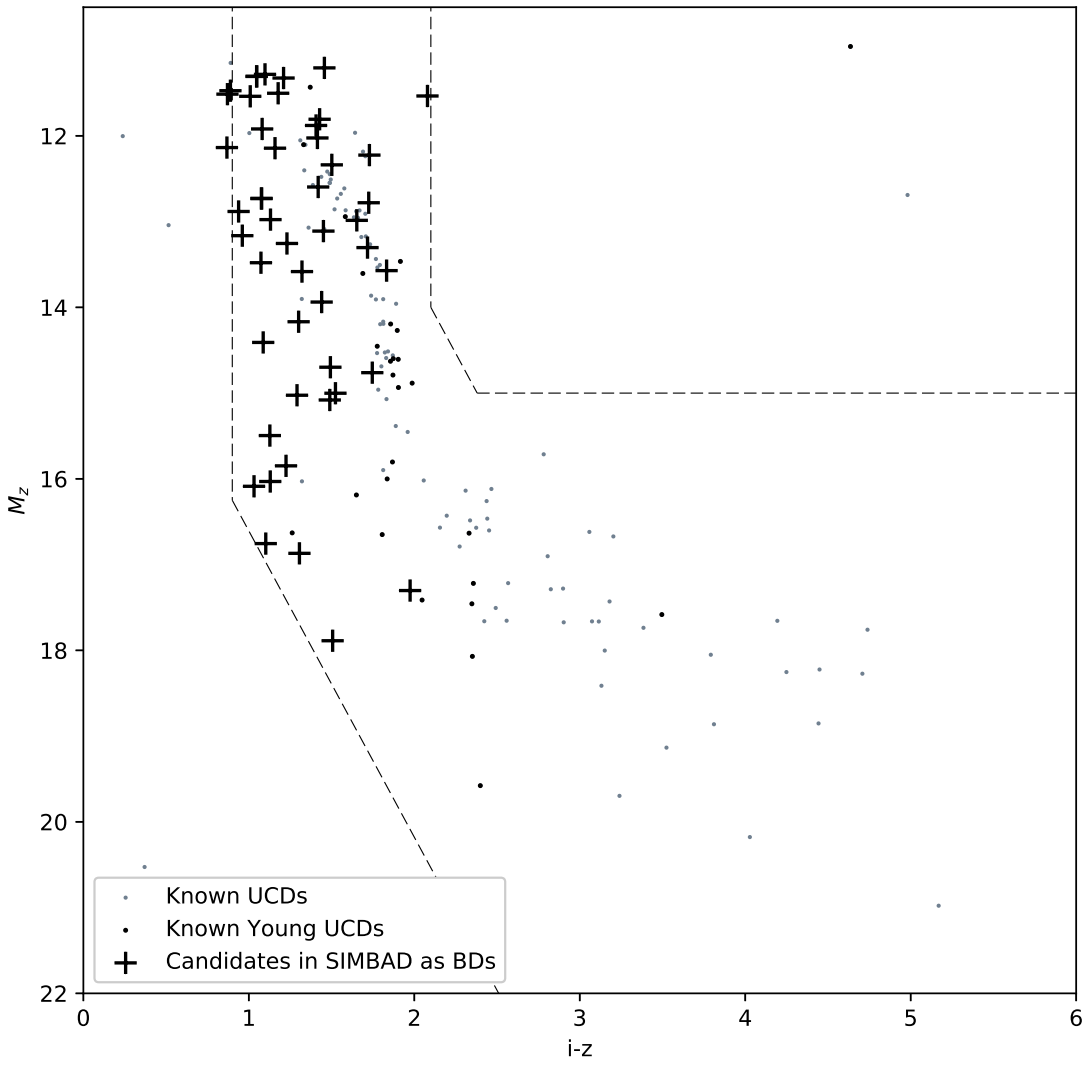

FIGURE 2.4: Known UCD i - z against absolute z magnitude. UCDs from the Dupuy sample as grey points, with objects known to be young or low surface gravity as black points. Candidate UCDs from this work previously identified by other authors as a Brown Dwarf or Brown Dwarf candidate and given the BD flag in the SIMBAD database are marked as black plus symbols. Selection region used as dashed lines. Right hand selection line based on Marocco et al. (2017). Left side cut based on angle from cut used in Marocco et al. (2017) but moved bluer as the black points indicate that VL-G objects are often bluer than field dwarfs in i-z.

- KEEP where $M_J < 4.115 \times (J-K) + 8$ OR $M_J \geq 13.6$ (Figure 2.5).

The cuts described in Section 2.4.3 were tested against UCDs in the Dupuy sample with $J < 19$ and with an L or M spectral type. Whilst each level removed a small number of outliers from the original 219 objects, the cuts did not result in any significant trimming of the Dupuy sample and 174 objects remained after these cuts (a rate of $\sim 80\%$ of the total number of UCDs with the required magnitude values), including fifty-six objects previously identified in the literature to be young or low g.

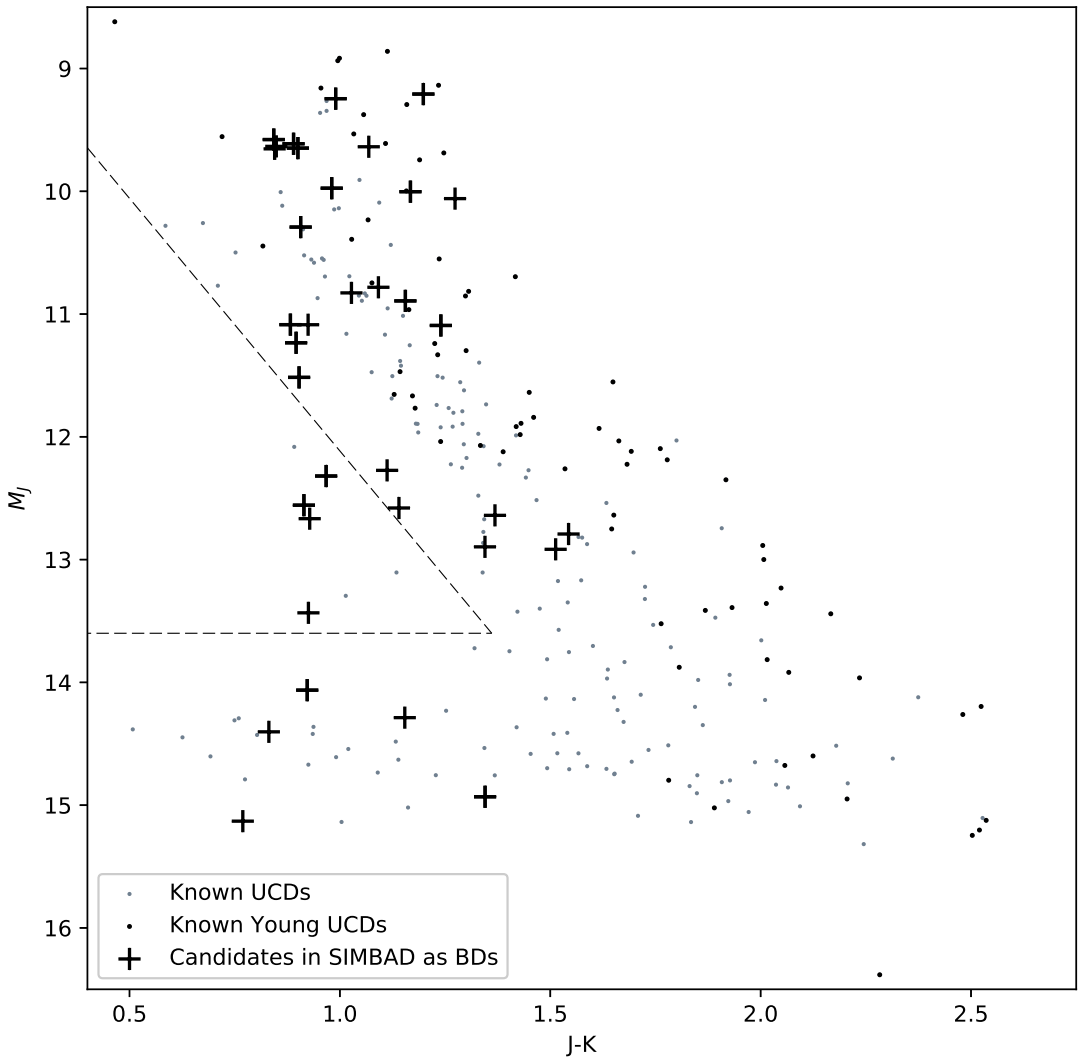

FIGURE 2.5: Known UCD J - K Against Absolute J Magnitude. UCDs from the Dupuy sample as grey points, with objects known to be young or low surface gravity as black points. CCandidate UCDs from this work previously identified by other authors as a Brown Dwarf or Brown Dwarf candidate and given the BD flag in the SIMBAD database are marked as black plus symbols. Selection region used as dashed lines. Selection line was chosen to retain all Dupuy sample while removing chance alignments which would have spurious J-K to M_J relationship.

Previous work has also limited selection based on the M_J to $z-J$ CMD (Marocco et al., 2017). However, when overlaying the candidates found in the preliminary group of all candidates and marking candidates identified in the SIMBAD Astronomical database as being Brown Dwarfs (Figure 2.6) we see that Brown Dwarfs have a wide range in this colour magnitude diagram. As such, the selection from Marocco et al. (2017) is not applied to our candidate selection.

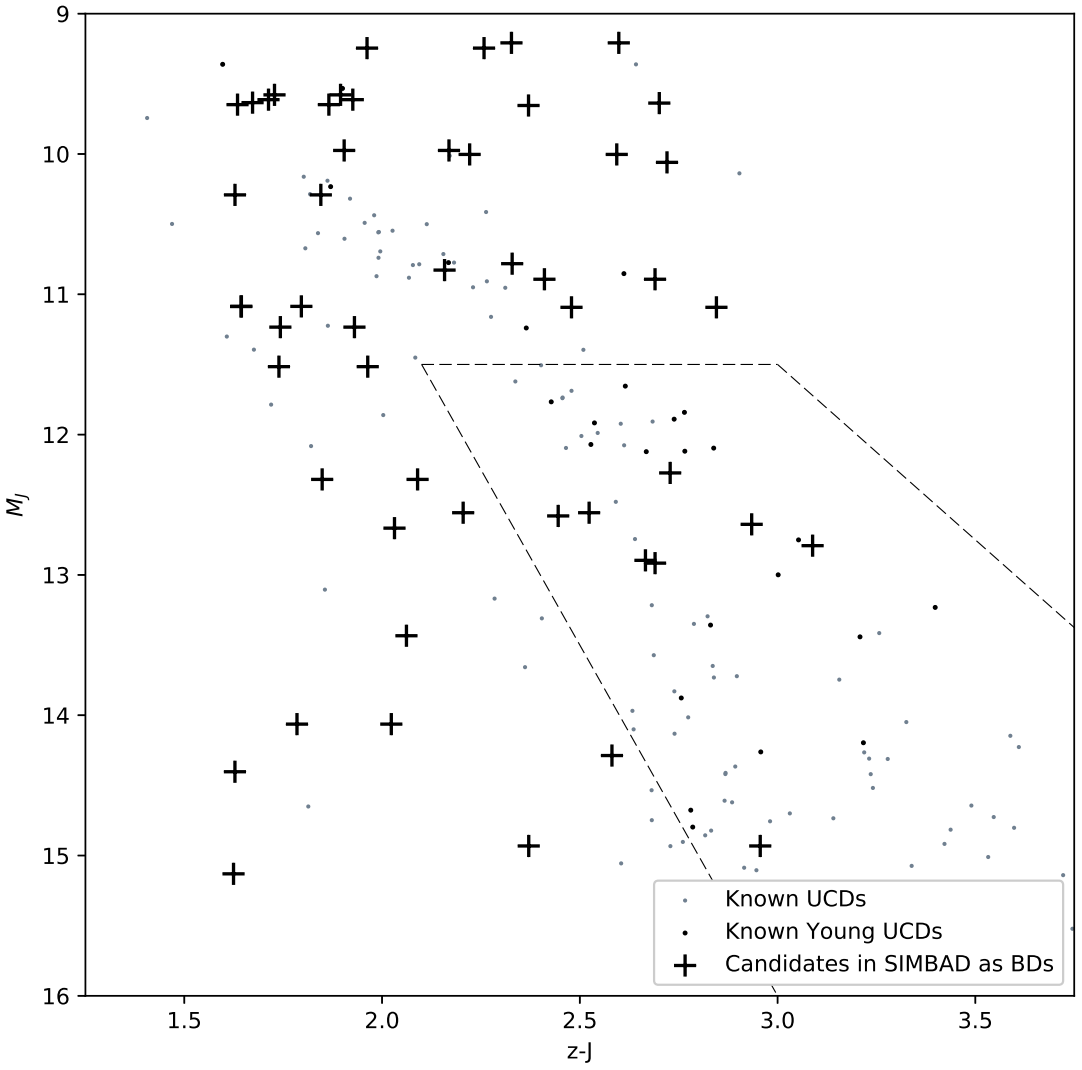

FIGURE 2.6: Known UCD z - J Against Absolute J Magnitude. UCDs from the Dupuy sample as grey points, with objects known to be young or low surface gravity as black points. Candidate UCDs from this work previously identified by other authors as a Brown Dwarf or Brown Dwarf candidate and given the BD flag in the SIMBAD database are marked as black plus symbols. Selection region used in Marocco et al. 2017 as dashed lines, however this selection was not used in our sample.

2.5 Single Catalogue Detections

Candidates that are detected in the *J* but not in *i* and *z* are of particular interest as being faint red candidates. As such, a method has been developed to select candidates detected in the NIR in either UKIDSS or VHS but not observed in optical, in either SDSS or PanSTARRS, whilst still being within the survey regions.

2.5.1 Cross Matching to Find Optical Non-Detections

Key to this process is ensuring that the candidates found are in the overlap region, meaning that the missing observation in the optical photometry is because the spectral type of the candidate is such that it is bright enough to be seen in infrared and not in the optical and not because the candidate lies in a region inspected by the infrared catalogue but not surveyed by the optical.

To ensure sure this is the case, candidates found in the infrared surveys, UKIDSS and VHS (as described in Section 2.2) are cross matched against candidates from the optical survey results of Section 2.2, SDSS and PanSTARRS, out to a radius of 200 arcseconds. For this work, the quality cut requiring SDSS = 'Clean' was not used, as any results in the search area shows that the candidate is within the search region of SDSS. Candidate pairings where no companion match was found in the optical within an angular separation of 200 arcseconds were removed as not being candidates within the overlap region of the two surveys.

For each resultant list, the frequency distribution of separation was analysed. For the UKIDSS-PanSTARRS pairing and the VHS-PanSTARRS pairing, pairs of candidates matched to less than 0.8 arcseconds were considered as matches to an optical observation of the infrared candidate. For the SDSS-UKIDSS and SDSS-VHS pairings this limit was set at 1 arcsecond. As such, these candidate pairings were excluded as candidates with optical observations which will have been selected for in the method described in Section 2.4.

2.5.2 Colour Cuts - Single Catalogue

As the only magnitudes available in VHS and UKIDSS are the NIR $YJHK$ magnitudes, the colour cuts of Section 2.4.2 are not all applicable. Instead, cuts were made in $J-H$, $H-K$ and $J-K$. Detections in J and K are required. For VHS candidates, K_s values were converted into K magnitude values as described in Section 2.4.1.

- REMOVE $J > 19$ and J non-detections
  Candidates fainter than $J = 19$ removed.
- REMOVE $\sigma J > 0.3$
  Candidates with an error in $J > 0.3$ will not be retained as it is required to have higher accuracy for later $J-K$ and $J-H$ cuts.

- REMOVE $M_Y \geq 8$, $M_J \geq 8$, $M_H \geq 8$ and $M_K \geq 8$
  Bright candidates that are not UCDs are removed.

- KEEP $Y - J > 0.3$ or not detected in Y
  Remove candidates bluer in $Y - J$ than a UCD but allow candidates without a Y magnitude to continue through selection. Based on the Spectral Type Template Colours for a candidate of spectral type M6 from Table 1 of Skrzypek et al. (2015), but adjusted to conservatively allow for the colour spread seen in the Dupuy sample.

- KEEP $J - H > 0.15$ or not detected in H
  Remove candidates bluer in $J - H$ than a UCD but allow candidates without an H magnitude to continue through selection. Based on the Spectral Type Template Colours for a candidate of spectral type M6 from Table 1 of Skrzypek et al. (2015) but adjusted to conservatively allow for the colour spread seen in the Dupuy sample.

- KEEP $H - K > 0.2$ or not detected in H or K
  Remove candidates bluer in HK than a UCD but allow candidates without an H or K magnitude to continue through selection. Based on the Spectral Type Template Colours for a candidate of spectral type M6 from Table 1 of Skrzypek et al. (2015) but adjusted to conservatively allow for the colour spread seen in the Dupuy sample.

- KEEP $J - K > 0.4$ or not detected in K
  Remove candidates bluer in $J - K$ than a UCD but allow candidates without a K magnitude to continue through selection. Based on the M_J vs $J - K$ CMD as discussed in Section 2.6.

2.5.3 Colour-Magnitude cuts following known UCD sample

As with the method described in Section 2.4.3, further cuts are made guided by the database of UCDs from the Dupuy sample. Only the cut in M_J and $J - K$ as used in Marocco et al. (2017) can be made due to lack of i and z magnitudes.

- KEEP where $M_J < 4.115 \times (J - K) + 8$ OR $M_J \geq 13.6$

It should be noted that the SDSS catalogue has the z-magnitude as its reddest band, while PanSTARRS also has the Y-magnitude. This means the results will be very different depending upon which optical survey is used. PanSTARRS has a much higher magnitude limit, meaning

it can detect optical candidates that are much fainter. It also covers a far greater area, meaning it will produce a far higher quality result, with candidates that are fainter, but still detectable by PanSTARRS in the optical to be rejected.

Candidates that are also only detected by PanSTARRS in Y and not in the optical will also be rejected from this method but these candidates will have been selected in the method described in Section 2.4.

2.5.4 Optical Non-Detection Limit

Any candidate non-detection has a theoretical minimum z-J colour for the candidate to be a UCD (spectral type $>$ M7). If the z-J colour for any candidate were any lower (the candidate were any brighter in z) than the candidate would have been detected in the optical survey.

Based on a z-J limit of 1.2 for an M7 candidate (Skrzypek et al., 2015) and the z limits of the catalogue, the minimum z-J for any candidate in the PanSTARRS observed region is 21.1 - J and SDSS observed region is 19.5 - J. This is a minimum z-J for each candidate as later spectral types will have higher z-J values and be fainter in z, denoted as "z-J Limit".

Figure 2.7 shows the known UCDs from the Dupuy list with z-J plotted against M_J. This shows the selection region in which to select objects with no optical detection based on the minimum z-J colour expected for an object. The region is delineated by the dashed line in Figure 2.7 and given by the relationship described in equation 2.4.

$$M_J < 5.23 \times (\mathrm{z} - \mathrm{J}) + 3.850 \tag{2.4}$$

2.5.5 Elliptical Cut

Unlike candidates with both optical and NIR detection (Section 2.4), optical non -detections will be prone to more contamination from faint galaxies, that will appear red in NIR due to dust emissions. A visual inspection of the sample of optical non-detection candidates indicates that $\sim$ 30% of the initially selected infrared sources are galaxies. To reduce the contamination, we considered database measurements of the source's ellipticity in an attempt to reject partly resolved galaxies.

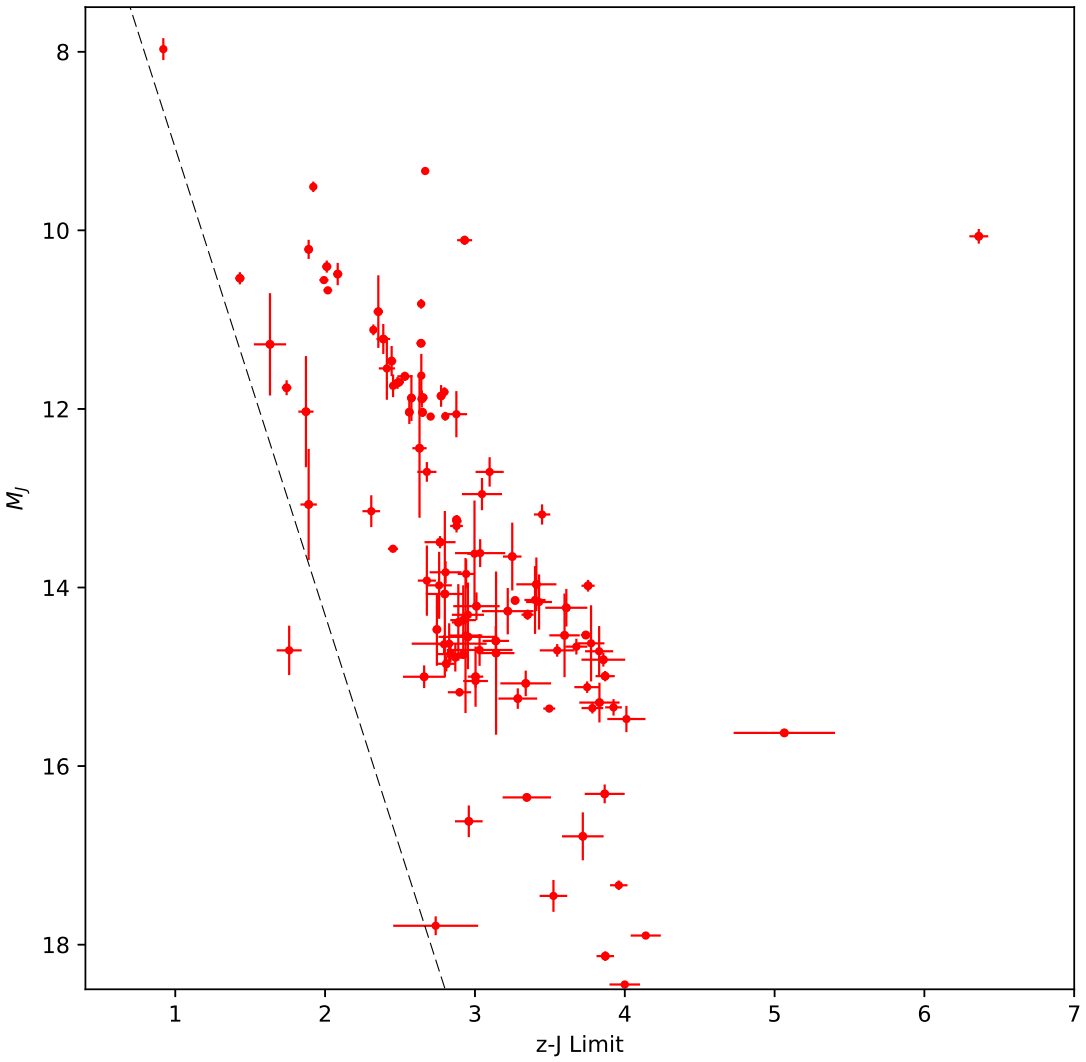

FIGURE 2.7: Known UCDs from the Dupuy sample used to set a z-J limit based on each candidate's M_J at the presumed distance.

Both VHS and UKIDSS give a measure of how elliptical a candidate appears and the angle of the ellipse to the galactic plane. These measures are provided in the catalogue as a separate value associated with any bands where the candidate is present. In order to remove galaxies, we require that in at least three of the four bands the ellipticity was less than 0.4. Candidates where the orientation angle of the ellipse was similar in the different bands (to within 15°) were removed as this was considered an indication of a partially resolved elliptical source.

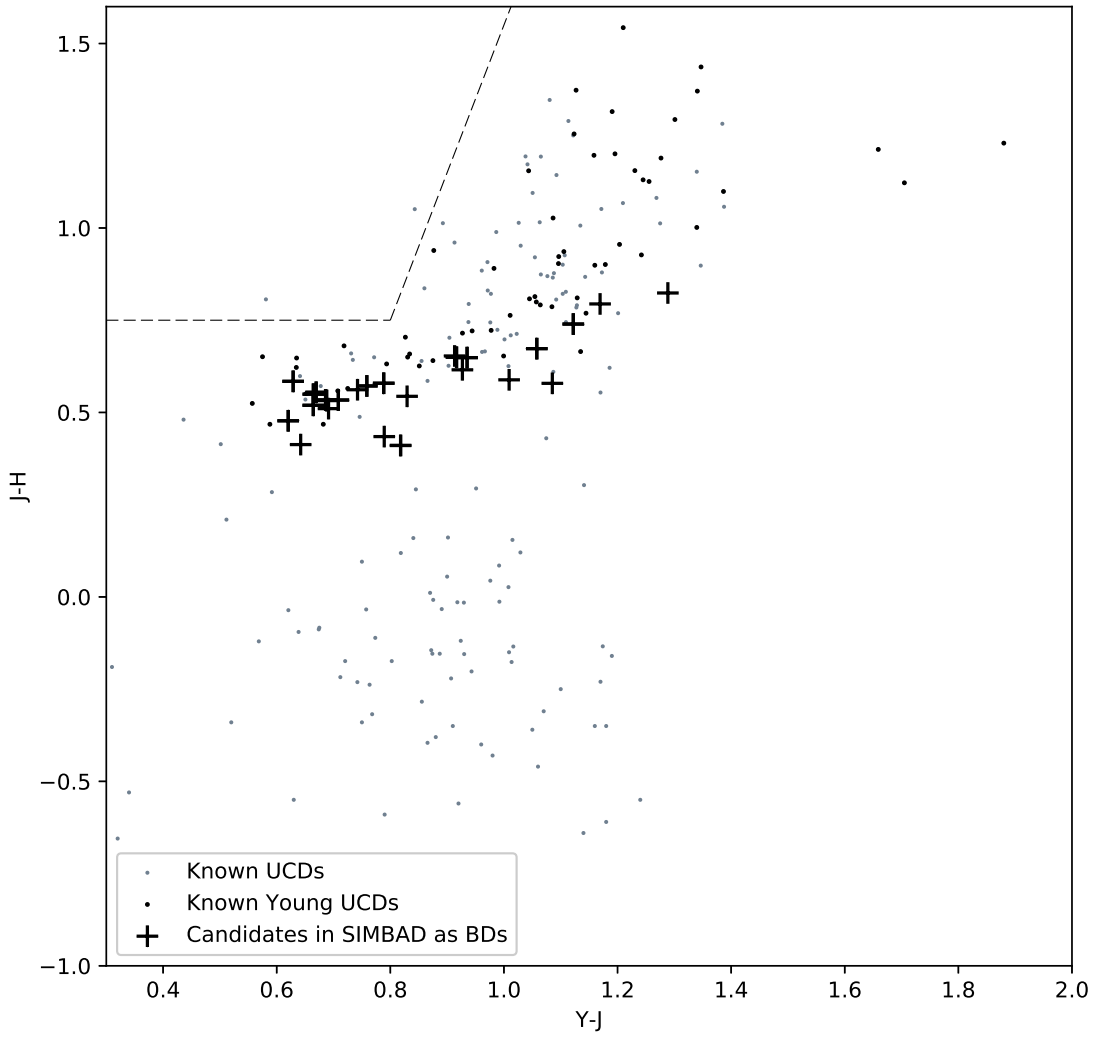

FIGURE 2.8: UCD J-H Against Y-J. UCDs from the Dupuy sample as grey points, with Dupuy sample UCDs known to be young or low surface gravity as black points. Candidate UCDs from this work previously identified by other authors as a Brown Dwarf or Brown Dwarf candidate and given the BD flag in the SIMBAD database are marked as black plus symbols. The selection region is delineated with a dashed lines, set based on the positions of Dupuy sample objects to remove objects with high J magnitude without corresponding high H magnitude.

2.6 Colour - Colour Cuts Following known UCD sample

Further cuts were made based on the 2 colour plots in Figures, 2.11, 2.8 and 2.9 for the colour-colour diagrams $Y-J$ against $z-Y$, $J-H$ against $Y-J$ and $H-K$ against $J-H$. These 2 colour cuts were made to ensure the selected candidates are field UCDs and young UCDs by overlaying the colour observations of UCDs from the Dupuy sample and candidate UCDs with a SIMBAD classification as a Brown Dwarf. We are interested in candidates with unusually red J-K indicating youth (Section 2.12), but only want to select candidates if their $Y-J$, $J-H$ or $H-K$ is indicative of field or young UCDs.

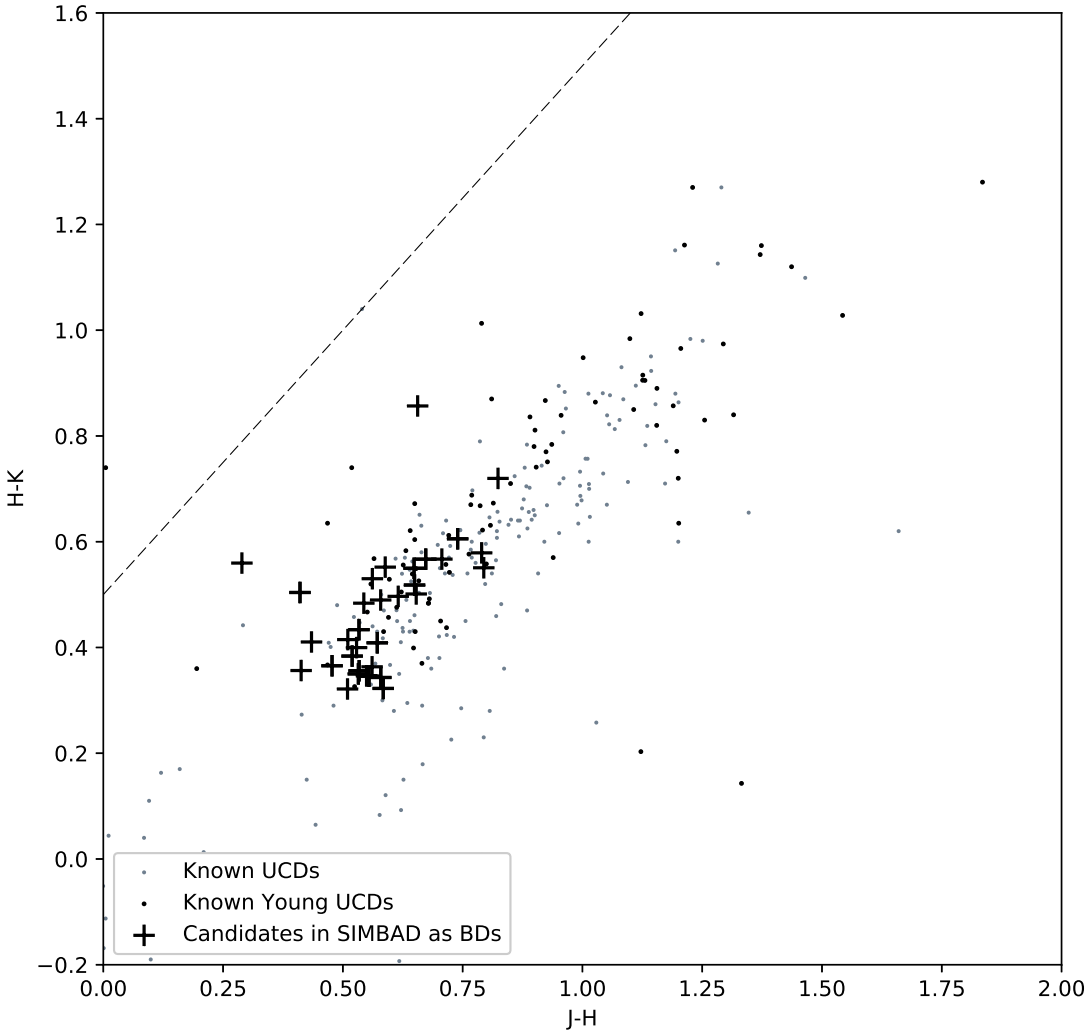

FIGURE 2.9: UCD H-K Against J-H. UCDs from the Dupuy sample in grey, with Dupuy sample UCDs known to be young or low surface gravity in black. Candidate UCDs from this work previously identified by other authors as a Brown Dwarf or Brown Dwarf candidate and given the BD flag in the SIMBAD database are marked as black plus symbols. The selection region is delineated with a dashed lines, set based on the positions of Dupuy sample objects to remove objects with high J magnitude without corresponding high H magnitude, in support of the cut shown in Figure 2.8.

The selection criteria are as follows:

- KEEP where $z-Y < Y-J$ OR $z-Y > 1.25$
- KEEP where $J-H < 0.75$ OR $J-H < (4 \times Y-J)-0.24$
- KEEP where $H-K < J-H+0.5$:

Figure 2.10 shows the 2 colour diagram for $z-Y$ against $i-z$. No restraints were set based on these colours as UCDs have a wide range within this 2 colour space.

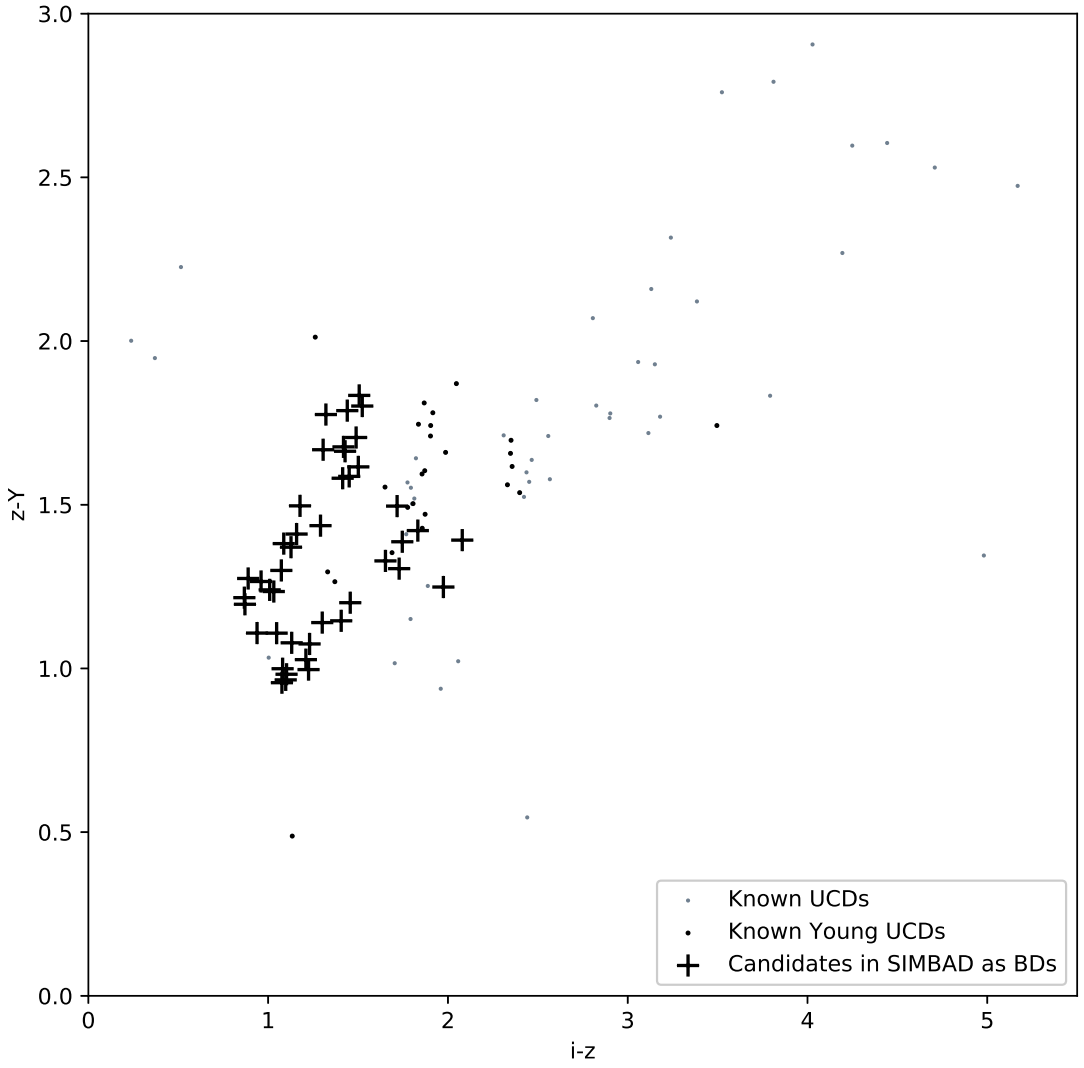

FIGURE 2.10: UCD z-Y Against i-z. UCDs from the Dupuy sample in grey, with Dupuy sample UCDs known to be young or low surface gravity in black. Candidate UCDs from this work previously identified by other authors as a Brown Dwarf or Brown Dwarf candidate and given the BD flag in the SIMBAD database are marked as black plus symbols. No selection region set.

2.7 Proper Motion Calculations

Proper motions can be calculated for candidate UCDs by considering multiple epoch observations across multiple catalogues based on the observed positions in the J2000 epoch system. Considering the change in position between two or more epochs allows a proper motion to be calculated in both right ascension (α) and declination (δ). To aid this, additional catalogues such as the SuperCOSMOS Science Archive (SSA, Hambly et al. 2004) can be used to provide additional epochs for proper motion calculations with an extremely long baseline between recent catalogue observations and SSA catalogue values. Due to the epoch differences between

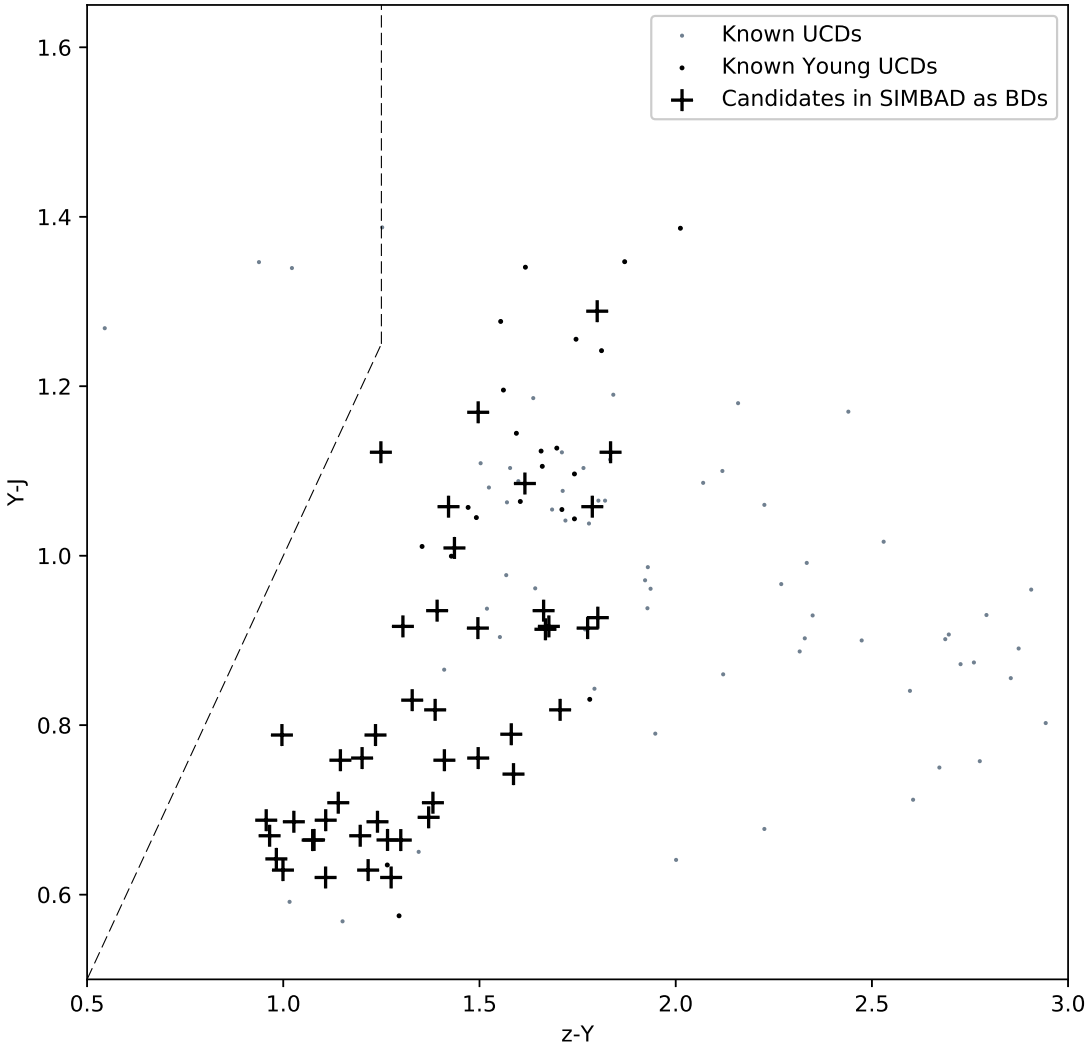

FIGURE 2.11: UCD J-H Against Y-J. UCDs from the Dupuy sample in grey, with Dupuy sample UCDs known to be young or low surface gravity in black. Candidate UCDs from this work previously identified by other authors as a Brown Dwarf or Brown Dwarf candidate and given the BD flag in the SIMBAD database are marked as black plus symbols. The selection region is delineated with a dashed lines, set based on the positions of Dupuy sample objects to remove objects to blue to be a UCD based on the Dupuy sample.

the UKIDSS and VHS observations and the SSA observations, care had to be taken to ensure mismatches were avoided, as detailed in Section 2.7.4. Some of the candidates from UKIDSS also have calculated proper motion values in the columns for proper motion right ascension ($\mu_\alpha \cos\delta$) and proper motion declination (μ_δ) calculated from multi-epoch UKIDSS observations. Other candidates were found to have proper motion values from multi-epoch analysis of UKIDSS observations by Smith et al. (2014).

The majority of candidates did not have proper motions available from these sources, where as all candidates found through the method described in Section 2.4 had observations from at least

two different epochs. A small number of candidates had three epochs. Sections 2.7.2 and 2.7.3 describe the calculation of proper motions made from multi-epoch observations.

2.7.1 Right Ascension and Declination Error

To calculate proper motions for candidates and an associated error, an epoch is required to be associated with each Right Ascension (α) value and Declination (δ) value. Also required is an associated σ_α and σ_δ. SDSS catalogue entries are based on a single epoch. For PanSTARRS, multiple observations are compiled to give an epoch mean and RA and DEC mean with associated position errors. UKIDSS entries are each for a single epoch, however $\sim 50\%$ of the UKIDSS candidates have an erroneous value for σ_α and σ_δ.

In order to provide a reasonable estimate of UKIDSS positional uncertainties for all sources, we relied upon the objects within the initial UKIDSS candidate sample where positional uncertainties were known and made plots of positional uncertainty against magnitude for each band. Figure 2.12 shows candidate's σ_α against J magnitude. A binned average of σ_α and σ_δ were taken across the full range of Y, J, H and K measurements. These binned averages were then interpolated across to create a relationship which could be used to estimate σ_α and σ_δ in circumstances where the value in the catalogue was erroneous but a magnitude of either Y, J, H or K is known. In order to ensure high accuracy within the sample used to define this relationship, only UKIDSS candidates with $\sigma < 0.1$ are used. It is noted that this relationship is identical for σ_α and σ_δ in each band but each band had a different relationship. The resultant interpolated relationship is shown on Figure 2.12 as the black line.

Figure 2.12 shows four distinct lines levels of positional uncertainty based on the four different bands observed with UKIDSS. The plot reflects how the UKIDSS LAS table will contain the best constrained positional uncertainty for any candidate from any of the four possible vales. Where no σ_α and σ_δ value is given in the UKIDSS LAS table, a σ_α and σ_δ is estimated based on the interpolated averages, applying the relationships determined from $YJHK$ consecutively. The majority of UKIDSS candidates are given an estimated σ_α and σ_δ, as the majority of candidates have a magnitude within the relationship range in at least one band.

For VHS, the x and y pixel error for each observation was available by matching the candidate against the detections table to find a suitable observation with known epoch, α and δ. The highest of either x error or y error was selected and a pixel scale of 0.339 milli-arcseconds per

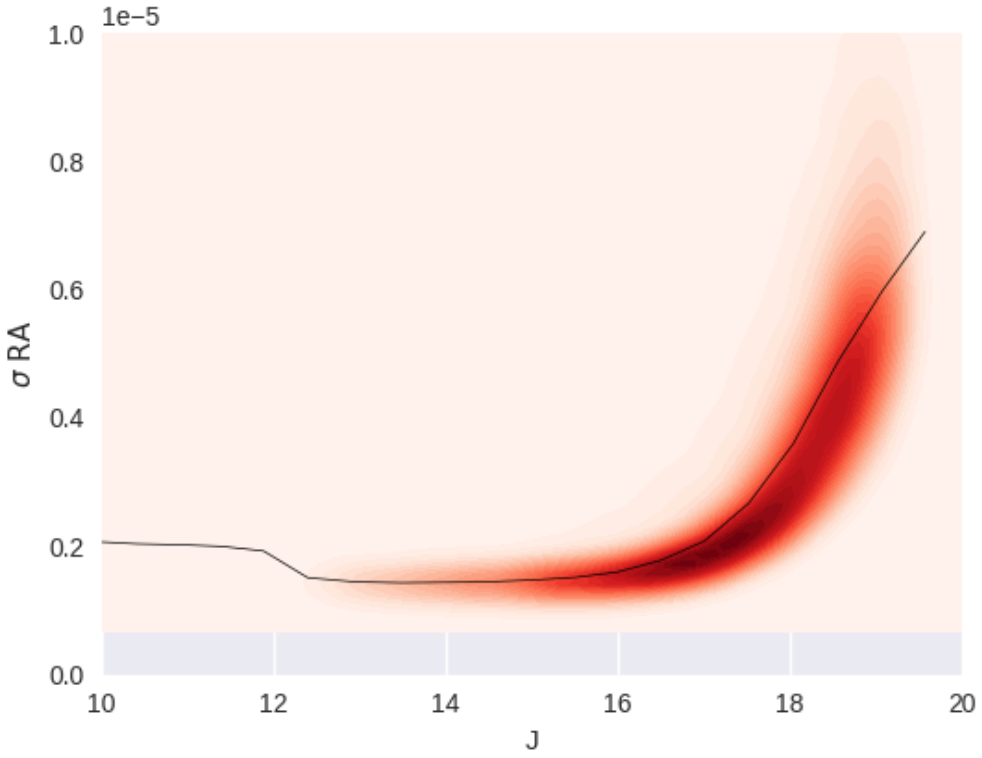

FIGURE 2.12: Error in RA again J magnitude for each UKIDSS candidate with $\sigma J < 0.1$ plotted as a 2d density histogram. Black line shows the interpolated line between the binned averages that was subsequently used to estimate σ_α and σ_δ for candidates with erroneous RA error values.

pixel was used to work out the error for both α and δ. This was faster than manually checking the orientation for each observation and provided a more conservative error in each case.

2.7.2 Proper Motion Calculations from Two Observations

Proper motions (PM, μ) are calculated based on an observation in either SDSS or PanSTARRS and an observation from within either UKIDSS or VHS. Proper motion is calculated as a change in α and δ ($\Delta\alpha$, $\Delta\delta$) divided by the difference in epochs of the two candidates (ΔEpoch) and shown in mas/yr as Proper Motion Right Ascension ($\mu_\alpha \cos\delta$) and Proper Motion Declination (μ_δ). Candidates with no optical observation but an SSA match use this pair of observations to calculate a two point proper motion.

Change in right ascension is the change as measured across the celestial equator. To calculate the on-sky change, this difference needs to be multiplied by the cosine of the declination. The notation of Proper Motion Right Ascension as $\mu_\alpha \cos\delta$ shows this.

2.7.3 Proper Motion Calculations from Three Observations

Candidates found in two catalogues are then checked against a third catalogue, with each optical-NIR candidate cross match checked against both of the optical and NIR catalogues not used in the original match. This results in a small number of candidates having three separate observations. In addition, each 2 catalogue cross match candidate with an additional epoch from a match in the SSA is added to the three epoch candidate list.

Proper motion for these candidates is then calculated from these three observations. This is done by considering the motion in α and δ separately. A straight line best fit matched to the candidate position on the y-axis against the time of observation on the x-axis using the Interpolate function as part of the Python package, SciPy. The gradient of this fit function is therefore the rate of change of position over time, the proper motion (μ). The Interpolate function also gives an error on this gradient, σ_μ, taken from the covariance matrix of the function output.

2.7.4 Matching to SuperCOSMOS Archive

SuperCOSMOS Science Archive contains photometric parameters from scans of the SuperCOSMOS photographic plates (Hambly et al., 2001). Due to the age of some of the observations and the high proper motion of some of the SSA detections, extreme care was taken when cross matching candidates with the archive. For each candidate, all potential matches within 0.2 arcminutes were selected from SSA. This radius was calculated to allow for the most extreme moving candidates to be correctly matched. For example, a candidate with Proper Motion of 200 mas / yr will move 10 arcseconds over the most extreme 50 year epoch difference between SSA and VHS.

Any SSA match with a B magnitude was removed as being too bright and too blue to be a UCD.

For each SSA match, the proper motion of the candidate from the SuperCOSMOS archive was used to calculate an updated estimated position at the Epoch of the observation of the UCD

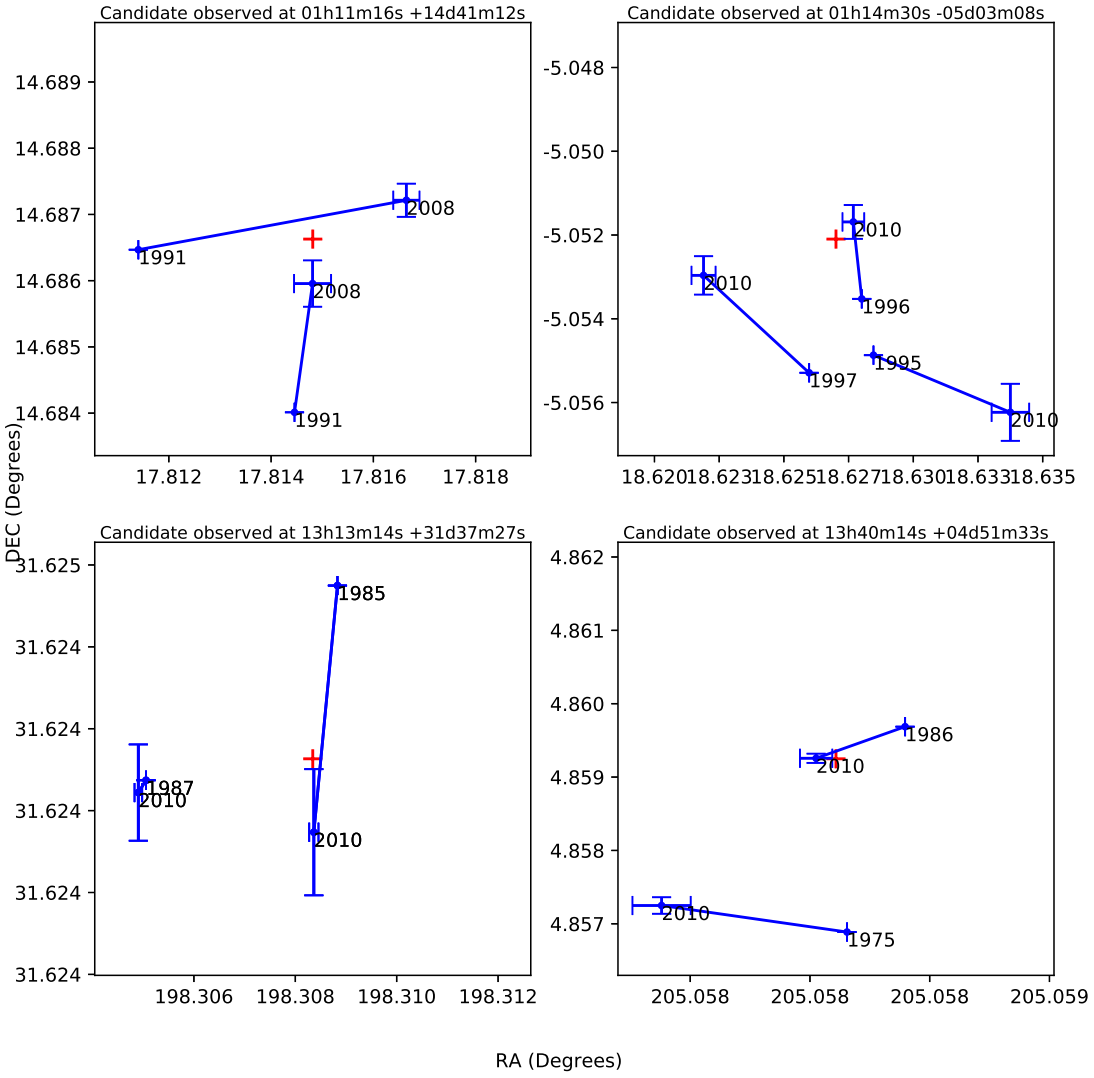

FIGURE 2.13: Matching 4 example candidate UCD candidates (Red, centred) matched to updated positions of SuperCOSMOS archive matches (Blue, with expanded error bars on the updated positions and estimated motion shown). Epoch dates shown in text. Proper motion corrected positions are adjusted to the epoch of the NIR observation of the candidate UCD.

candidate. The error in the proper motion within SSA resulted in the error bars of this estimated position usually being an order of magnitude larger than the error on the original SSA position. Only matches where the UCD candidate was within twice the error bars of the proper-motion-corrected position of the potential SSA entry were matched. If there was more than one candidate SSA, the UCD candidate was matched to the SSA entry with the closest updated position.

This work showed that a simple 'nearest' selection for SSA would have often selected a candidate which, when taking in to account proper motion would not be located near to the candidate

UCD candidate at the Epoch of the observation. Figure 2.13 shows four selections with multiple SSA matches for each NIR detection, with updated SC positions in the NIR detection epoch shown, based on the SSA proper motion value, with expanded error bars based on the proper motion error. These examples show how the updated position enabled the closest updated position match to be selected.

Most importantly, matching was completed blind to the proper motion of the potential primary to the candidate companion. If matching was completed based upon the best proper motion match then it would most likely be that this method would preferentially selected the SSA entry for the primary, or instead we may have matched a different companion to the primary that was also within the 0.2 arcminute search radius.

The matches from SSA give proper motions but also provide an additional epoch and position for two and three observation proper motion calculations.

2.8 Proper Motion Difference

Equation 2.5 gives a means to conservatively quantify the number of standard deviations between the proper motion value of the primary star and the associated candidate companion, with subscript 1 referring to the primary and subscript 2 referring to the candidate companion.

$$\sigma_{\Delta\mu} = \frac{\sqrt{|\mu_{\alpha 1}\cos\delta_1 - \mu_{\alpha 2}\cos\delta_2|^2 + |\mu_{\delta 1} - \mu_{\delta 2}|^2}}{\max(\sigma\mu_{\alpha 1}\cos\delta_1, \sigma\mu_{\alpha 2}\cos\delta_2, \sigma\mu_{\delta 1}, \sigma\mu_{\delta 2})} \tag{2.5}$$

We use $\sigma_{\Delta\mu}$ as a means to remove candidates that cannot be related but keep all candidates that may be binary pairs. For a candidate and primary to qualify as a potential wide seperation binary pair, we require that the difference between the primary proper motion and the companion proper motion must be significant ($\sigma_{\Delta\mu} < 3$, ruling out associations where we can be 99.7% confident that they are not a common proper motion pair, Marocco et al. 2017). The resulting passed candidates are shown in Figures 2.14 and 2.15. We see a 'trend of ignorance' where candidates are below the $\sigma_{\Delta\mu} < 3$ but this is only because the proper motion of the candidate is poorly constrained. This trend is along the line of $(\mu_{\text{companion}} \,/\, \sigma\mu_{\text{companion}}) = \sigma_{\Delta\mu}$. This is consistent with the $\sigma_{\Delta\mu}$ being a measure of difference between primary and companion μ in terms of number of σ error difference. Objects with poorly constrained μ are likely to have a $\sigma_{\Delta\mu}$ of similar value.

All candidate pairs below this $\sigma_{\Delta\mu} < 3$ could be CPM pairs, however the majority of them are only below this limit due to the poorly measured value of μ for the companion. Instead, candidates where the proper motion of the companion is well defined ($\mu_{\text{companion}}$ / $\sigma\mu_{\text{companion}} > \sigma_{\Delta\mu} + 1$) and the difference between the companion and primary proper motions is not significant $\sigma_{\Delta\mu} < 2$ are considered promising CPM pairs.

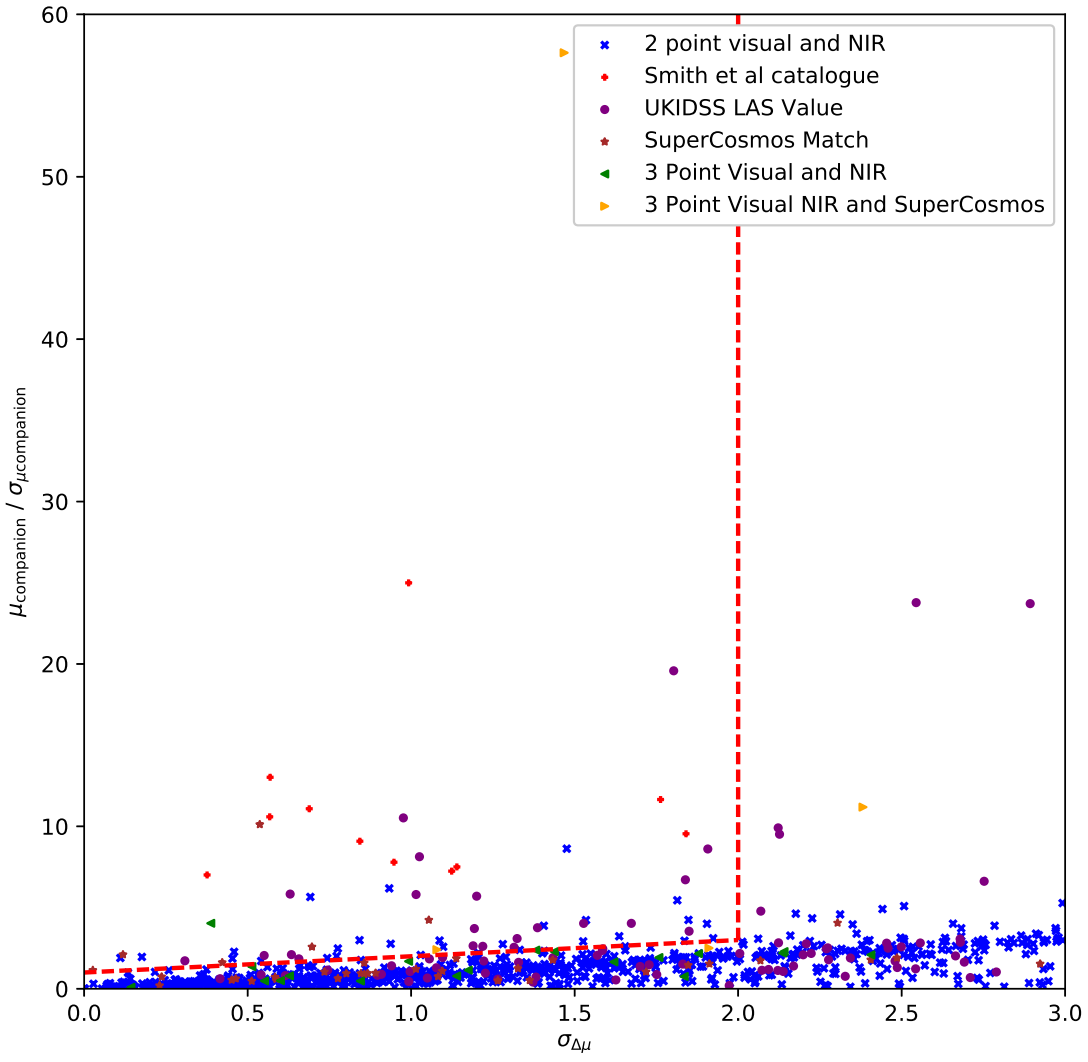

FIGURE 2.14: Quality of the proper motion measurement of the candidate against the significance of proper motion difference between the candidate and the primary. Red dashed region shows the selection region for candidates considered to be promising CPM pairs.

Multiple candidates have PM values available from multiple sources, such as candidates with an observation in both the optical and the NIR, but also a value from the UKIDSS LAS table. In order to ensure that candidates that are promising CPM pairs despite the possibility of mismatches between catalogues, any candidate pairing where any PM value from any source matches the promising CPM criteria defined in Section 2.8 is selected as a potential pairing. For candidates

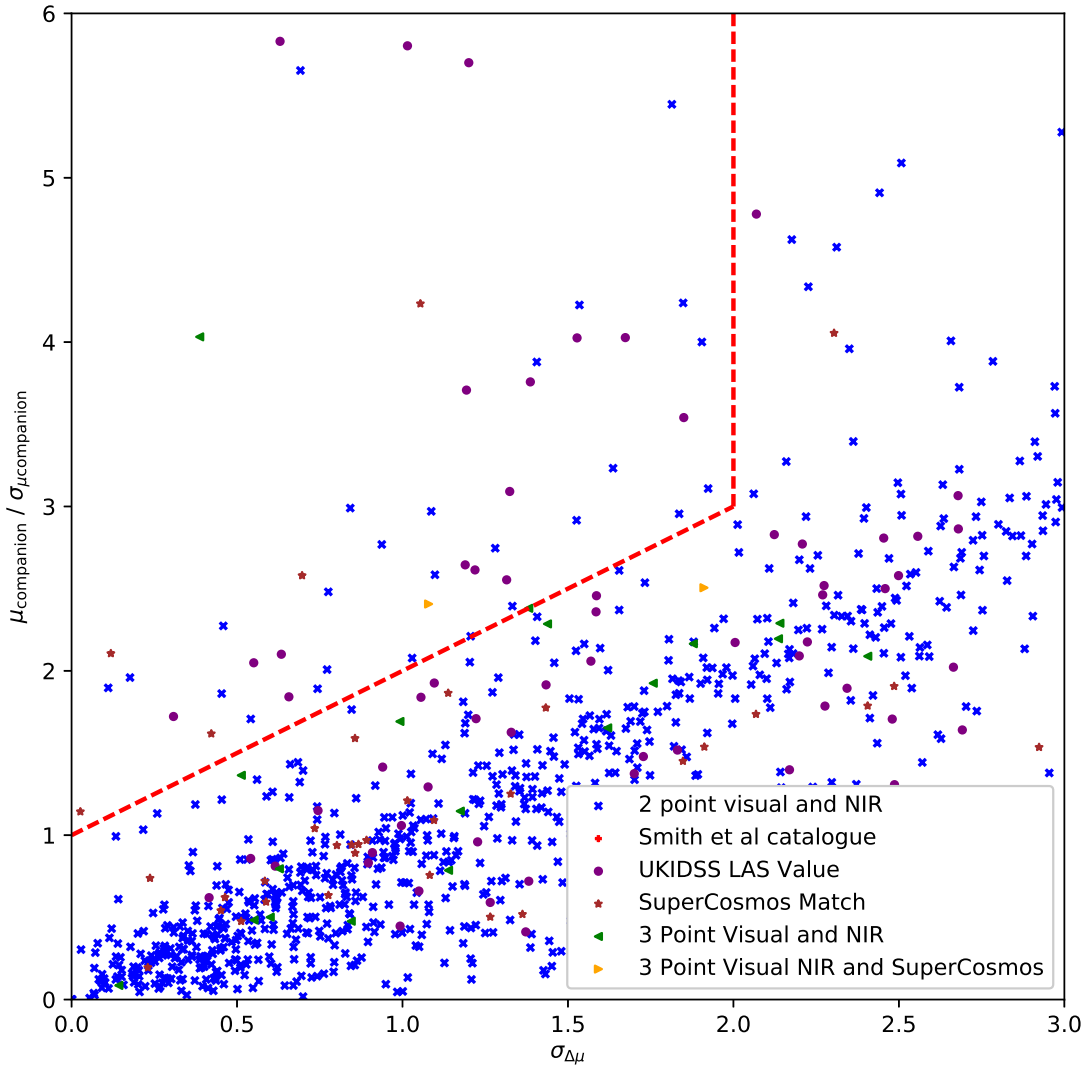

FIGURE 2.15: Close-up of Figures 2.14 showing error in PM of candidate against sigma PM difference. Red dashed region shows the selection region for candidates considered to be promising CPM pairs.

with multiple values where none qualify the pairing as a promising CPM pair, then the significant difference between the primary and the candidate companion is calculated using the proper motion value for the companion from the best defined proper motion (the highest μ / $\sigma\mu$ value) where $\sigma\mu$ is which ever is greater, $\sigma\mu_\alpha \cos\delta$ or $\sigma\mu_\delta$.

For candidates observed in two catalogues, 66,650 candidate pairings were selected following the 2 colour cuts described in Section 2.6. Of this total, 2,828 candidates had no value of proper motion that could be assigned from other sources or calculated from two epochs. 1,256 of the 66,650 are considered promising CPM pairs by the definition in Section 2.8. 19,926 pairings were not considered promising CPM pairs but still have a significantly low difference between

the proper motion of the primary and the candidate companion based on the proper motion from the best defined companion proper motion, below the cut of $\sigma_{\Delta\mu} < 3$ as set in Section 2.8.

For candidates observed taken from the NIR catalogues alone, 686 candidate pairings were selected following the 2 colour cuts described in Section 2.6. 474 candidates had no value of proper motion that could be assigned from other sources, a far higher proportion of the total compared to the candidates with observations within both an optical and a NIR catalogue. Two candidates are considered promising CPM pairs by the definition in Section 2.8. Ninety-one pairings were not considered promising CPM pairs but still have a significantly small difference between the proper motion of the primary and the candidate companion based on the proper motion from the best defined companion proper motion, below the cut of $\sigma_{\Delta\mu} < 3$ as set in Section 2.8.

In total, 24,577 candidate pairs were either selected as promising CPM pairs, or selected due to having no PM value or due to a low significant PM difference due to poorly defined companion proper motion. Of all candidate pairs with a well defined PM, only 4.5% are considered promising CPM pairs. In total there are 1,258 promising CPM benchmark systems found.

2.9 Common Distance Selection

Target UCD candidates not confirmed as having a promising CPM relationship with the potential primary based on Section 2.8 and without a candidate common proper motion that rules it out as a companion, can still be identified as a potential wide separation binary with the primary based on common distance. Candidate pairs < 30pc or with a sky separation between the pair of < 6 arcseconds are likely to be companions to within a false-alarm-probability < 0.0001 (Marocco et al., 2017) if the objects are confirmed to be at a a similar distance as the primary, as best shown by Figure 1.17.

The candidate distance is presumed to be the same as the value for the TGAS primary when considering CMD selection. The candidate distance must be confirmed separately by observing the spectra to assign the candidate a spectral type and calculate the absolute magnitude of the candidate. The distance of the companion can then be estimated using the spectroscopically estimated absolute magnitude of the candidate and the measured apparent magnitude.

The false-alarm-probability of < 0.0001 from Marocco et al. (2017) is based on the simulated sample within 550pc. However distant background candidates can still contaminate the selection sample. The various CMDs used for selection of candidates from Sections 2.4.3 and 2.5.3 allow some candidates to be removed based on CMD positions that are not likely UCDs, or a background contamination candidate. In order to reduce the possibility of background candidates, reddened through dust extinction, contaminating the sample, candidates with dust heavy background regions are also removed (Section 2.10 below).

2.10 Dust Extinction Removal

As this work is aiming to identify young UCDs that could be particularly red in J-K, the photometric selection method is particularly susceptible to contamination by background dust obscured objects. The magnitude limited low distance at which UCD candidates can be observed means that it is unlikely that genuine UCDs will be affected by significant reddening. Candidate companions not confirmed as promising CPM pairs may be background objects reddened due to dust extinction. Primary candidates within the galactic plane will be particularly susceptible to this.

The galactic plane is an area of the night sky with particularly high dust extinction. While searching for UCDs within the galactic plane can be difficult, it can provide rewards due to this being a relatively unexplored region (e.g Lucas et al., 2010) but is a difficult search towards the galactic plane due to mismatches and contamination (as shown by the method employed by Folkes et al., 2012).

Each candidate position is checked against the map of Galactic Dust Reddening and Extinction based upon Schlafly and Finkbeiner (2011) and hosted by the NASA/IPAC Infrared Science Archive[1]. Candidates that are considered promising CPM pairs as defined in Section 2.8 can be considered likely to be within 500pc due to their relationship to a primary in our TGAS subsample. As such, their photometry is presumably not influenced by the dust extinction within their region of sky and we retain all such candidates.

Candidates that are not considered promising CPM matches to their candidate primary may be background candidates. As such, if they are located on the sky in a region with high dust extinction, there is strong reason to believe that they are not related to the primary and are

[1] `http://http://irsa.ipac.caltech.edu/applications/DUST/`

instead dust obscured background candidates. Any candidates not defined as being a promising pair and in an area of sky with an extinction ($e(B-V)) > 0.4$ were removed.

2.11 Visual Inspection

Candidates were then visually inspected in optical and NIR images from the SDSS, Pan-STARRS, VHS and UKIDSS surveys. WISE images were also checked to look for contamination from features such as nebula and galaxies. Extended candidates were removed as well as candidates obscured by proximity in the sky to the primary. Obvious mismatches were also removed.

Visual inspection also demonstrated that associated pairs with angular separation < 3 arcseconds were always found to be a mismatch, where the NIR catalogue entry of the primary had in fact been retrieved from the catalogue entry for UCD candidate. Any pairs with a separation of < 3 arcseconds were removed.

2.12 Identifying Potential Young Pairs

Multiple selection criteria were investigated to identify potential young candidates.

2.12.1 UCD Candidates with Unusually Red $J-K$

Bowler et al. (2017) suggest a relationship shown in M_J vs $J-K$ where their Brown Dwarf population, known to be $<\sim 120$ Myrs old due to membership of the AB Dor moving group, are redder in $J-K$ than field dwarfs of the same M_J. This matches the findings of Liu et al. (2016) who give the relationship of absolute brightness (M_J) to $J-K$ for young candidates to be $M_J = 4.115 \times (J-K) + 4.938$. The candidates within Bowler et al. (2017) identified as members of the AB Dor group have a scatter around this relationship of ± 0.23 in $J-K$, despite these candidates theoretically having very similar ages. The reasons for this scatter are multiple but one possible explanation is viewing angle. By using the small number of UCDs where viewing angle can be estimated, Vos et al. (2017) show that the scatter in $J-K$ due to viewing angle can be up to ± 0.7. This study uses estimates of candidates' radii and measurements of rotational velocity to estimate viewing inclination. The authors were only able to do this for

TABLE 2.8: M and L Samples with apparent moving group or association membership and identified as 'young' or 'VL-G' from the Trent Dupuy catalogue and where values for M_J and $J-K$ available.

Group	Qty	Age	Age Citation
Ab Doradus (Ab Dor)	7	$\sim 110-130$ Myr	Barenfeld et al. (2013)
Argus	3	$\sim 30-50$ Myr	Makarov and Urban (2000)
TW Hydrae association (TWA)	7	$\sim 5-15$ Myr	Weinberger et al. (2013)
Tucana–Horologium (Tuc-Hor)	4	$\sim 20-30$ Myr	Kraus et al. (2014)
Upper Scorpius (USco)	1	~ 5 Myr	Preibisch et al. (2002)
β Pictoris (bPic)	8	$\sim 15-28$ Myr	Malo et al. (2014)

~ 20 candidates, meaning this result is not robust, but it begins to guide how wide our selection in $J-K$ needs to be.

The objects used in Bowler et al. (2017) are from the AB Dor moving group with approximate age of $<\sim 120$ Myrs. The catalogue managed by Trent Dupuy (as described in section 2.4.3) includes M and L dwarfs from other moving groups that are also identified as young, as given in Table 2.8. It is worth noting that the metallicity of the AB Dor group is $[\mathrm{Fe/H}] = 0.02 \pm 0.02$ (Barenfeld et al., 2013) so the outlying nature of the $J-K$ colour cannot be attributed to high metallicity.

Due to the absence of typical field UCDs fainter and redder than the bottom of the L dwarf sequence ($M_J \gtrsim 15$, $J-K \gtrsim 2.2$), and the identification of several very young UCDs in this region (see Best et al. 2015), we identify possible young candidates in this region by selecting any candidate with $J-K > 2.2$ as a young candidate.

In addition to the trend in the M_J versus $J-K$ CMD identified by Liu et al. (2016), an additional trend is identified in the sample of known young UCDs in the $J-H$ versus M_J CMD. This straight line fit trend is given by $M_J = 5.556 \times (J-H) + 6.907$.

These objects are shown in Figure 2.16 and 2.17. Also shown as black markers are UCDs with signs of low or intermediate surface gravity observed in their spectra but without any co-moving group association. All references are available on the website associated with the Dupuy sample[2]. The objects with membership of young groups show as clear offset in $J-K$ and $J-H$ compared to field objects without VL-G or INT-G spectra and supports the trend identified in Liu et al. (2016).

In order to identify potential young UCD candidates, candidates were selected from within a region defined by the Liu et al. (2016) sequence with offsets appropriate to allow for the scatter

[2] `http://www.as.utexas.edu/~tdupuy/plx/Database_of_Ultracool_Parallaxes.html`

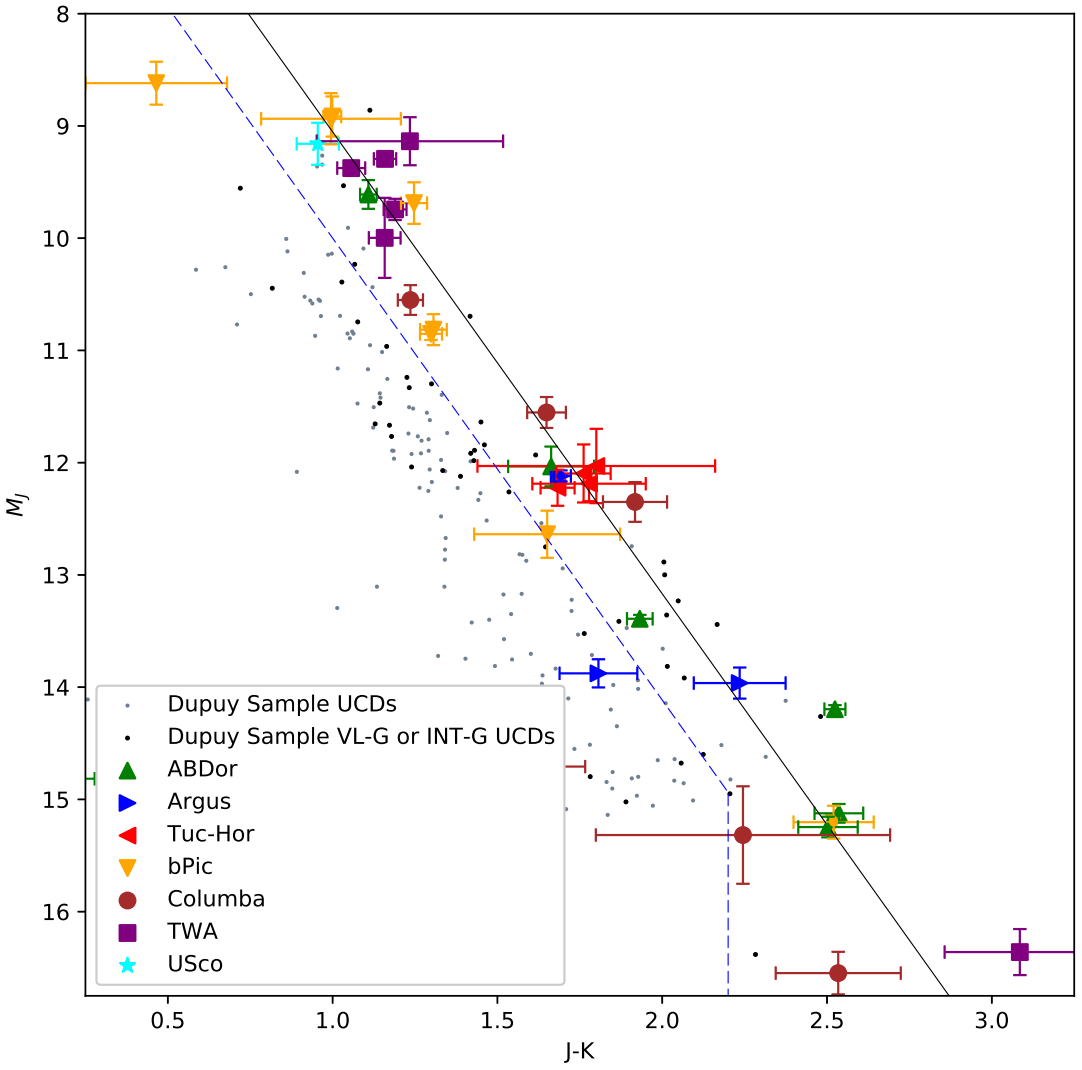

FIGURE 2.16: Absolute J magnitude to J-K for UCDs from the catalogue maintained by Trent Dupuy with objects with known membership of co-moving groups highlighted. Black line shows the fit by Liu et al. (2016). Blue dashed delineation indicates the selection region for objects to be considered potentially young, set by the Liu et al. (2016) trend, with a scatter of -0.23 down to $J-K > 2.2$ for selection of the L-T transition region.

around this relationship. Each sequence was offset by $+0.946$ in M_J (consistent with the ± 0.23 offset in J-K seen by Liu et al.). Candidates were selected if their M_J values lay above these offset sequences in the M_J versus $J-K$ and M_J versus $J-H$ CMDs. If a candidate has a qualifying detection in either H or K but a non-detection in the other, then it is selected as potentially young.

The scatter suggested by Vos et al. (2017) based on viewing angle was not used as this would have resulted in a selection range that would have an unacceptable contamination rate from candidates not believed to be young when applied to the candidates shown in Figure 2.16. It is

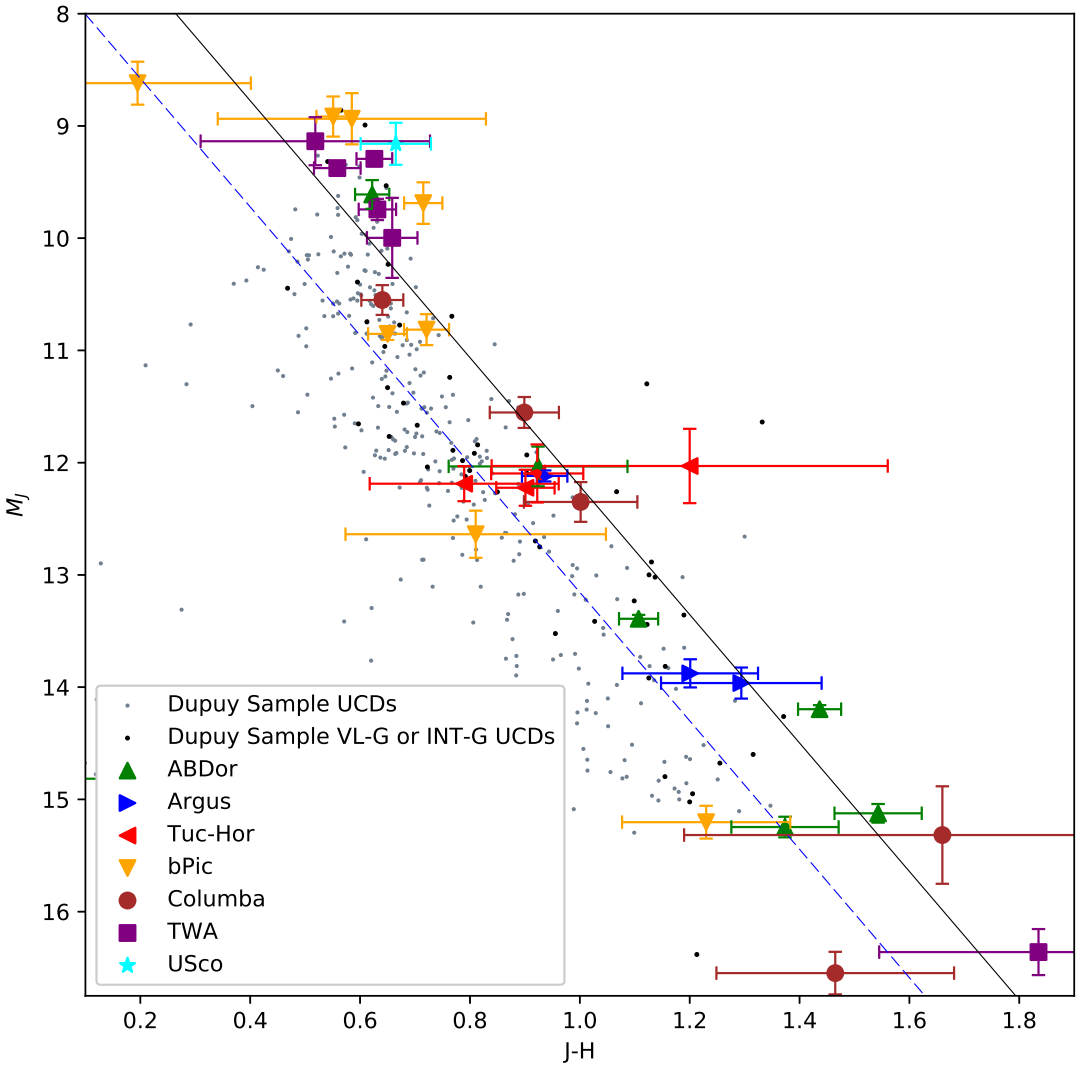

FIGURE 2.17: Absolute J magnitude to J-H for UCDs from the catalogue maintained by Trent Dupuy with objects with known membership of co-moving groups highlighted. Black line shows straight line fit to objects.

worth considering viewing angle as a possible reason for scatter in $J-K$ but colour variation due to viewing angle alone is not yet well understood when considering the small number of objects investigated by Vos et al. (2017).

2.12.2 Selection Due to Identified Primary Type within SIMBAD

The SIMBAD database has flags where it is indicated in the literature that certain criteria for a candidate are fulfilled. To select young primary candidates, any primary with specific flags detailed in Table 2.9 indicating the candidate may be young are selected.

TABLE 2.9: Young Stellar SIMBAD Flags

Flag	Description	Young Citation
Y*O / YSO	Young Stellar Object	
Y*?	Young Stellar Candidate	
pr*	Pre-mainsequence star	
Be*/Be?	Be Star	Percy (2011)
Ae*/Ae?	Herbig Ae star	Percy (2011)
TT*	T Tau-type Star	Green and Jones (2004)

Certain types of variable star types may also be young, especially stars with variability due to high rotation speed. Other types of variable stars, such as Gamma Doradus variables, are young objects with varying luminosity due to surface pulsation (Percy, 2011). However other variables can be old. So only candidates whose associated primaries are identified in SIMBAD as being young or candidate young variables were selected (Table 2.10 lists these young variable types selected by).

TABLE 2.10: Young Variable Stellar SIMBAD Flags

Flag	Description
bC*	Variable Star of Beta Cephei type
gD*	Variable Star of γDor type
Ro*	Rotationally variable Star
Ir*	Variable Star of irregular type
Or*	Variable Star of Orion Type
RI*	Variable Star with rapid variations
Er*	Eruptive variable Star
FU*	Variable Star of FU Ori type
RC* / RC?	Variable Star of R CrB type

2.12.3 Primary Candidate Main Sequence Timescale Based on Photometry

The main sequence timescale for each primary was estimated using the bolometric magnitude of the star based on the $T_{\rm eff}$ or spectral type depending on what information was available. Table 2.11 shows the different sources of $T_{\rm eff}$ and spectral type for the potential primaries from the TGAS sample (see Section 2.1).

The primary TGAS candidates may have multiple different spectral types or estimates of $T_{\rm eff}$ from different sources, allowing multiple values of the Bolometric Correction (BC) to be estimated for some TGAS candidates. LAMOST and RAVE calculate $T_{\rm eff}$ from observed spectra. LAMOST also estimates a spectral type from this information. SIMBAD is an astronomical database with values of spectral types for multiple candidates compiled from multiple literature sources. Ammons et al. (2006) use photometry to estimate both metallicity and $T_{\rm eff}$ values for

TABLE 2.11: Source for $T_{\rm eff}$ and Spectral Type information

$T_{\rm eff}$		
Survey	Count	Percentage of Total Primary Candidates
RAVE	82,660	9%
LAMOST	82,463	9%
Ammons et al. (2006)	796,180	88%
Total with $T_{\rm eff}$	808,531	89%
Spectral Type		
Survey	Count	Percentage of Total Primary Candidates
LAMOST	82,463	9%
SIMBAD	209,815	23%
Total with Spectral Type	286,110	32%
Total with either $T_{\rm eff}$ or Spectral Type	836,806	95%

TABLE 2.12: $T_{\rm eff}$ to BC Coefficients of Polynomial Fit from Reed (1998) for use with Equation 2.6.

c_0	c_1	c_2	c_3	c_4
−0.438	−3.901	−8.13	+13.42	−8.499

FGK stars and have applied this method to create an estimate for almost 800,000 *Tycho2* objects. Source counts for these values are shown in Table 2.11.

The BC has been estimated for all dwarf stars spectral types (Pecaut and Mamajek 2013, maintained online[3]), so for primary stars where the spectral type has been determined, the main sequence timescales can be estimated. Alternatively, the BC can be estimated from the $T_{\rm eff}$ of the star from the relationship shown in Equation 2.6 using the polynomial coefficients listed in Table 2.12 (Reed, 1998). This applies only for dwarf stars on the main sequence. Thus the BC is only calculated for objects on the M_V versus B-V CMD (Figure 2.18) below the black cutoff line between main sequence and subgiant branch.

$$\mathrm{BC} = \sum_{i=0} c_i [\mathrm{Log}(T) - 4]^i \tag{2.6}$$

With a value of BC estimated, the bolometric magnitude can be calculated from the V magnitude (Equation 2.7).

$$M_{\rm bol} = M_v - \mathrm{BC} \tag{2.7}$$

[3] `http://www.pas.rochester.edu/~emamajek/EEM_dwarf_UBVIJHK_colors_Teff.txt`

The Luminosity can be calculated from the luminosity-M_{bol} (Pogson) relationship (Equation 2.8).

$$-2.5\ \mathrm{Log}_{10}\left(\frac{L}{L_{\odot}}\right) = M_{\mathrm{bol}} - M_{\mathrm{bol}\odot} \tag{2.8}$$

The mass can be estimated using the Luminosity-Mass Relationship (Equation 2.9).

$$L = L_{\odot}\left(\frac{M}{M_{\odot}}\right)^{3.5} \tag{2.9}$$

Finally, the main sequence timescale can be estimated from the mass of the star from the main sequence timescale estimation, shown in Equation 2.10.

$$\tau \approx 10^{10}\left(\frac{M_{\odot}}{M}\right)^{2.5} \tag{2.10}$$

The final rearranged form of the combined equations is shown in Equation 2.11 showing that a value for τ can be estimated from an absolute V magnitude and a BC estimated from spectral type or T_{eff}.

$$\mathrm{Log}_{10}\tau \approx \frac{10\times(M_V - \mathrm{BC} - M_{\mathrm{bol}\odot})}{35} + 10 \tag{2.11}$$

Due to multiple sources for the T_{eff} and spectral type for each candidate primary, multiple values of the main sequence timescale can be estimated. For our selection, any candidates with any timescale values below 1Gyr were selected as a potentially young primary.

It should be noted that the spectral types of candidates are often several subtypes different between LAMOST and SIMBAD. There is up to a $\sim$ 500 K variation in values of T_{eff} depending upon the source of the value. Reconciling these differences is not part of our candidate selection process.

2.12.4 Primary Overbright in M_V from Main Sequence compared to Primary Metallicity

Metallicity affects main sequence stars photometry by causing a candidate to appear brighter in M_V. However, young candidates are also brighter as they evolve on to the main sequence. This

is shown in Figure 2.18 where a series of Isochrones from Marigo et al. (2017) are plotted.

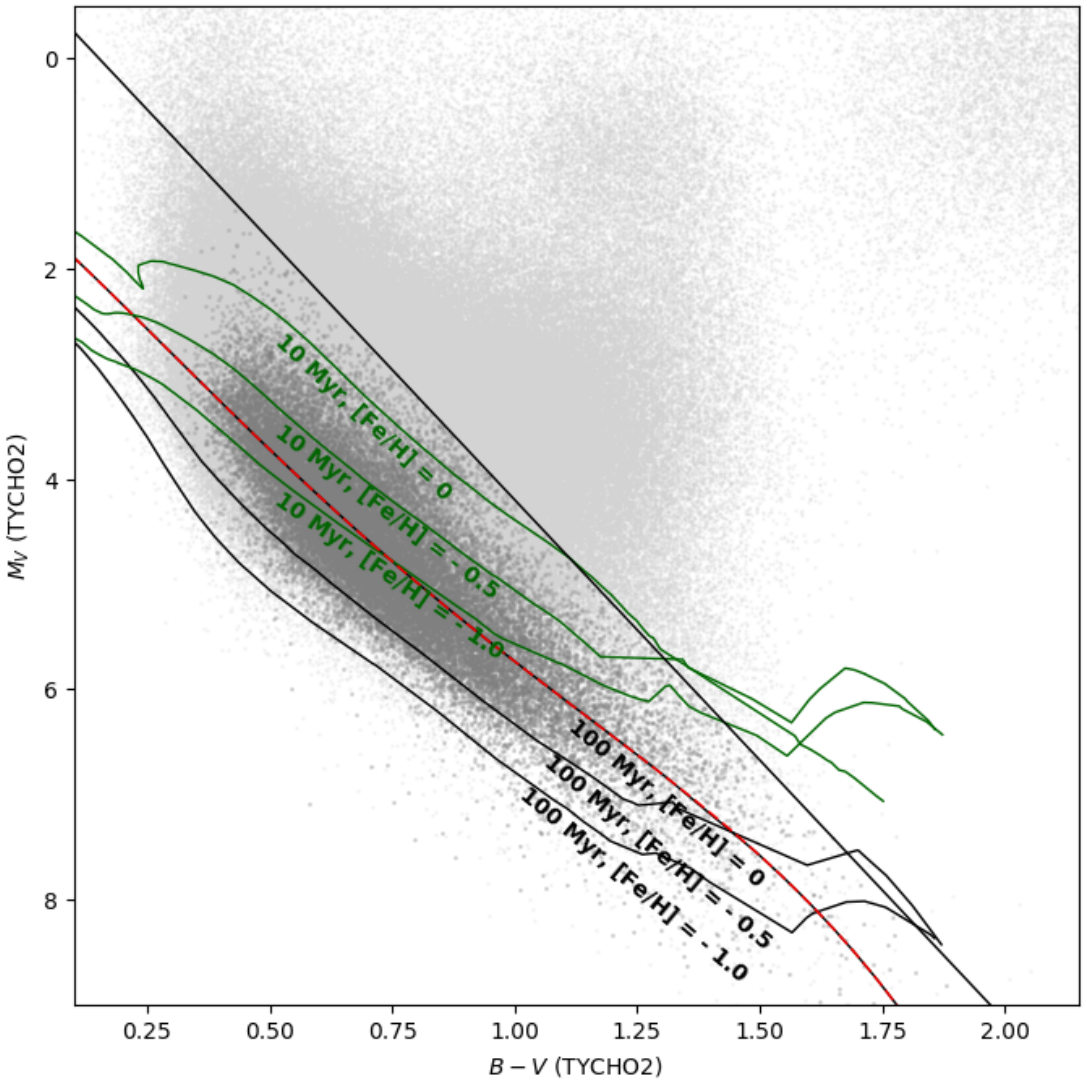

FIGURE 2.18: Tycho B-V against M_V CMD for candidate primary TGAS stars. Light grey points show all objects, while dark grey points are objects with well defined distance and BV magnitude. The straight solid line shows the cut imposed to remove subgiants when carrying out the main sequence fitting. The red dashed line is my 5th order polynomial fit to the TGAS main sequence. A set of modified (see text) isochrones ([M/H] = 0, -0.5, -1.0) are over-plotted in black (100 Myr) and green (10 Myr ages).

Figure 2.18 shows all objects within both TGAS and Ammons et al. (2006). Objects shown in dark grey are objects where $\sigma V < 0.2$ and $\sigma B-V < 0.2$ as well as the flagging system of Ammons et al. (2006) has indicated the object is a dwarf. This flag system has some contamination so a final cut of $M_V > 4.95 \times (B-V) - 0.75$ is applied to remove remaining subgiants. The cut objects are shown in light grey.

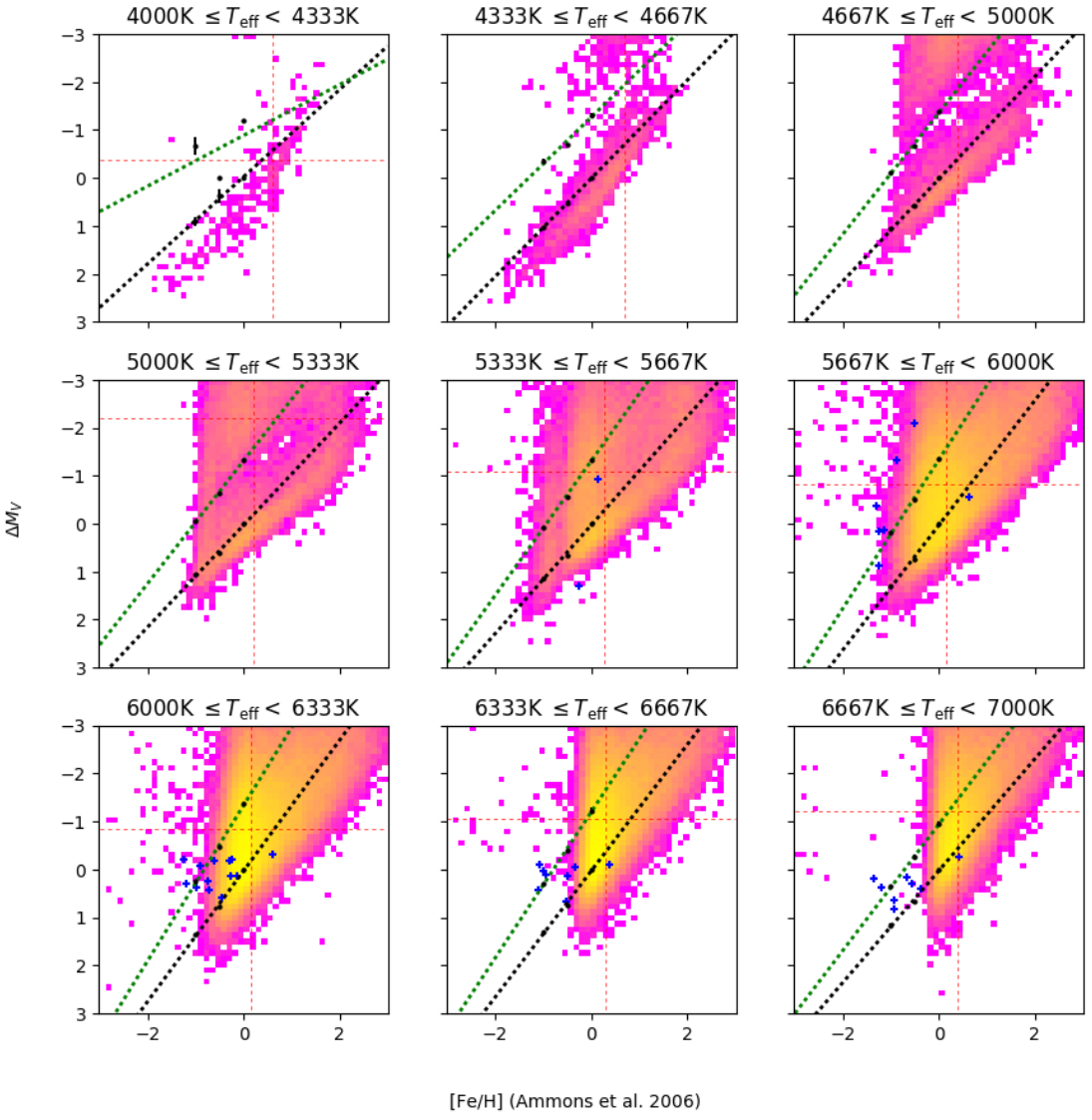

FIGURE 2.19: Dwarf stars from Ammons et al. (2006) with ΔM_V plotted against [Fe/H]. Blue crosses are objects selected as being young based on the object type flags detailed in Table 2.9. Red dashed lines show the median of the ΔM_V for that bin and the median metallicity. Colour scale shows the log of the quantity of stellar objects in each bin.

To characterise the effects of age and metallicity in this CMD, a polynomial function is fitted to the TGAS dwarf sequence, which was done using a 5th order polynomial and a least-square fitting method. The result is shown as a red dashed line in Figure 2.18. This is then inter-compared to a range of model isochrones (from the online PARSEC Isochrone generator[4] (Marigo et al., 2017)). It was noted that the 100 Myr isochrones were a close match to their 1-3 Gyr counterparts over most of the colour range of the TGAS stars (except for the hotter OBA stars, which are evolving off the main sequence in the older isochrones). The 100 Myr [Fe/H]=0 isochrone

[4] `http://stev.oapd.inaf.it/cgi-bin/cmd`

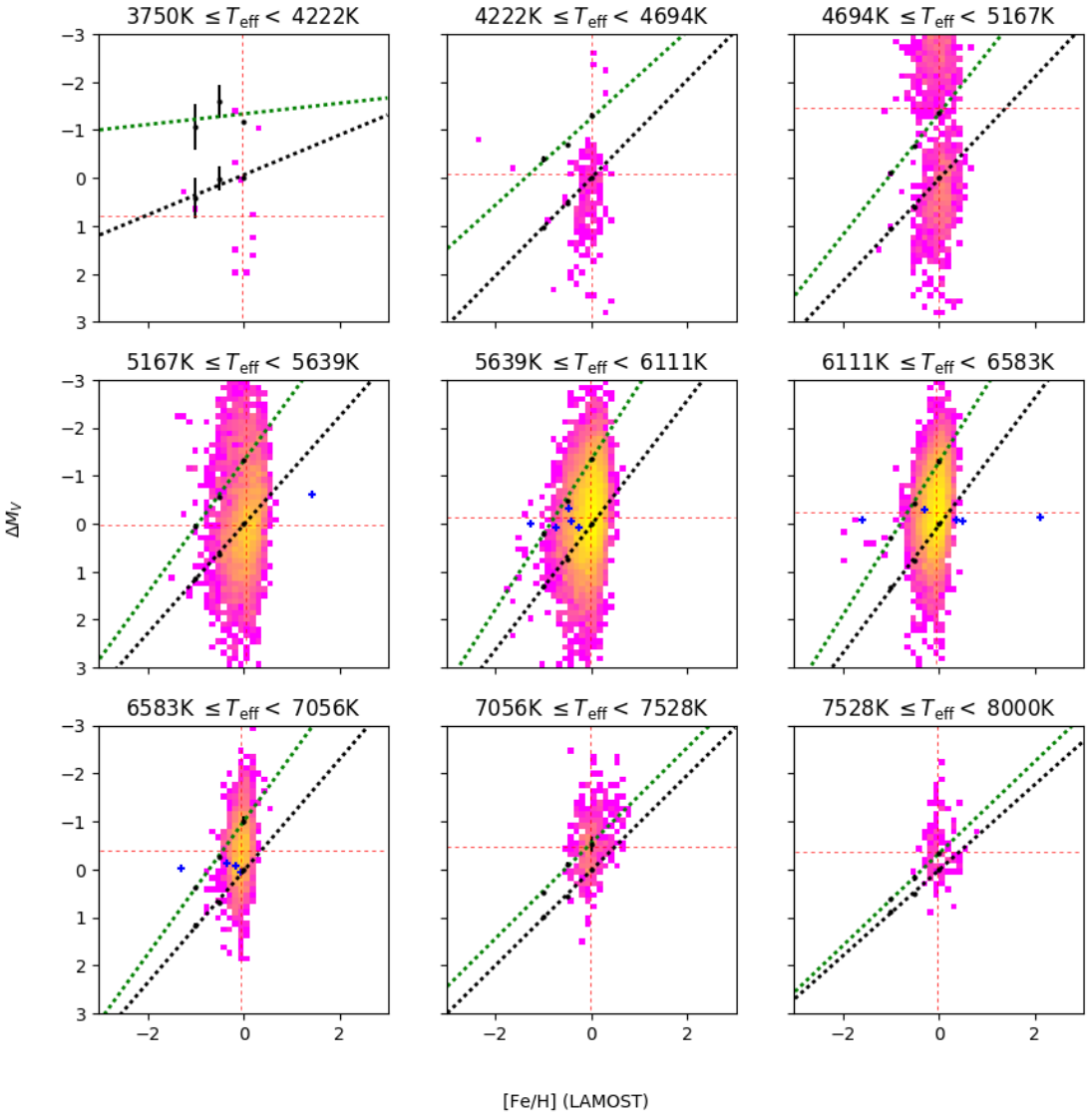

FIGURE 2.20: Dwarf stars from LAMOST with ΔM_V plotted against [Fe/H]. Blue crosses are objects selected as being young based on the object type flags detailed in Table 2.9. Red dashed lines show the median of the ΔM_V for that bin and the median metallicity . Colour scale shows the log of the quantity of stellar objects in each bin.

is therefore taken as a representative of average stars in the main sequence, despite some differences between this isochrone and the observed TGAS sequence. To acquire relative consistency between model and observation, an offset function f(B-V) is applied that forced the 100 Myr [Fe/H]=0 isochrone to be identical to the polynomial fit. The same "correction" is also applied to all the other model isochrones. A set of these "modified isochrones" ([M/H] = 0, -0.5, -1.0 where Y=0.2485+1.78Z and Z=0.0152, for 100 Myr and 10 Myr ages) is overplotted in Figure 2.18. As a result of the modification the 100 Myr [Fe/H]=0 isochrone is identical to the

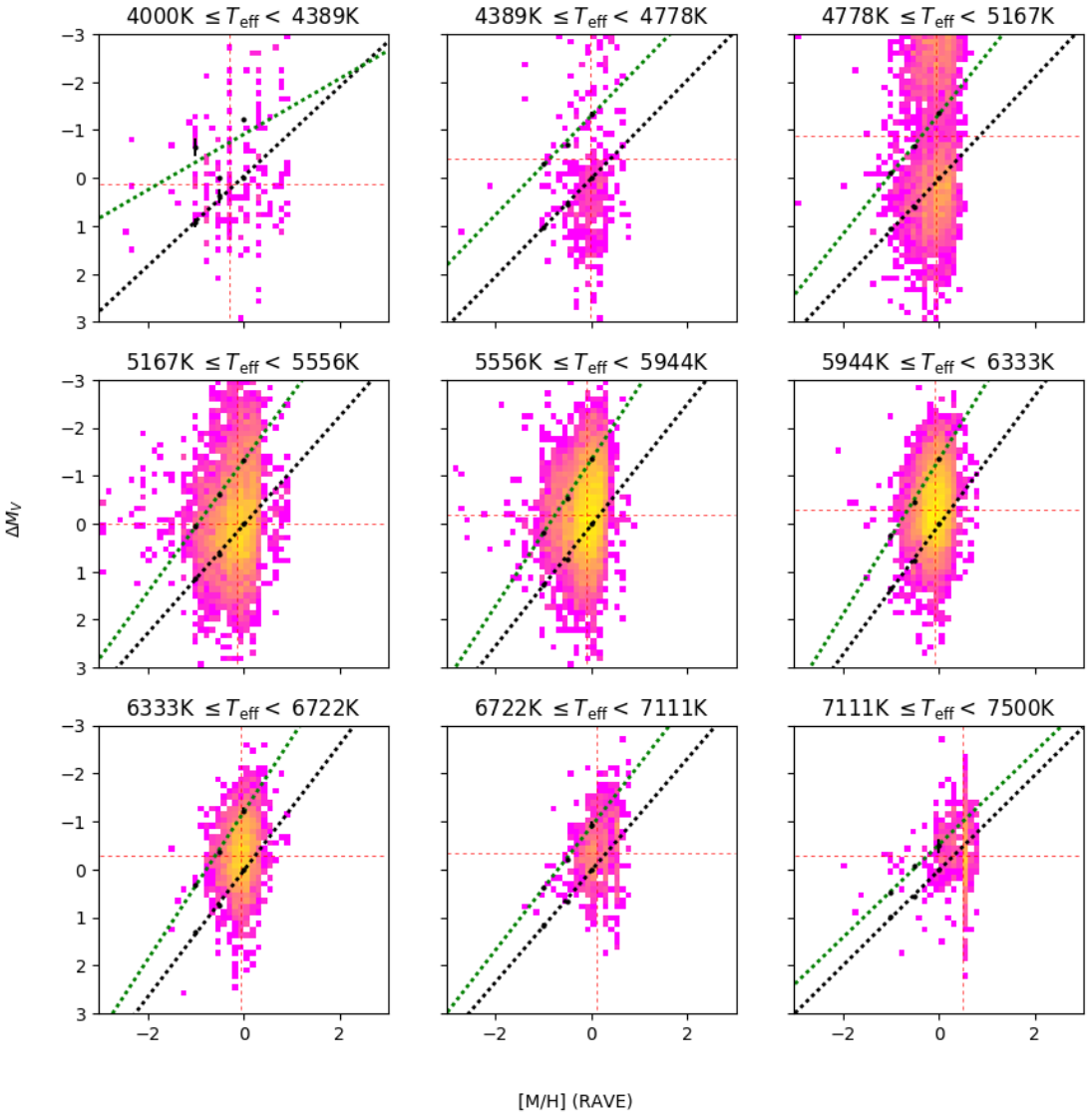

FIGURE 2.21: Dwarf stars from RAVE with ΔM_V plotted against [Fe/H]. Blue crosses are objects selected as being young based on the object type flags detailed in Table 2.9. Red dashed lines show the median of the ΔM_V for that bin and the median metallicity . Colour scale shows the log of the quantity of stellar objects in each bin.

polynomial sequence fit, with the other isochrones demonstrating the relative effects of non-solar metallicity and youth.

It can be seen from Figure 2.18 that both metal richer stars and younger stars are relatively brighter in M_V. As such, metallicity must be considered when using CMD location to preferentially select younger stars. For example, primaries that are over-bright in M_V but also slightly metal poor are more likely to be young. However it is noted that by considering over-brightness and metallicity alone, this method ignores post-main sequence evolution and unresolved binarity which also lead to over-brightness. Post-main sequence evolution will be less of an issue for

later (more common) primaries, but will be more important for earlier stars. Unresolved binarity can be addressed at some level using spectroscopic constraints, but these are only available for a small fraction of stars. While this method should have some efficacy, it will also retain some degeneracies due to these factors.

To apply the over-brightness analysis, each potential primary is given a predicted "mid-sequence M_V" (from its measured B-V value) generated from the polynomial sequence fit to the middle of the TGAS sample main sequence. A value is then given to each primary for the object's over-brightness (ΔM_V with respect to the sequence fit) by subtracting the predicted M_V from the measured M_V.

In order to disentangle the effect of metallicity upon the brighter M_V, ΔM_V is plotted against the value of [Fe/H] from Ammons et al. (2006) in Figure 2.19. In this plot, objects are shown in nine separate temperature bins according to the effective temperature of the primary estimated from photometry by Ammons et al. (2006). For each bin, the median metallicity and the median brightness in M_V compared to the fit function (ΔM_V) is shown. The black dashed line is a straight line of best fit to the 100Myr isochrone data and the green dashed line is a straight line of best fit to the 10Myr isochrone data. Blue crosses are objects selected as being young based on the object type flags detailed in Table 2.9. The green line is, as expected, over-bright compared to the black line in these plots, and although there is some scatter evident amongst the blue crosses, there is a clear preference for over-brightness in a number of these plots.

This exercise is repeated for candidates with temperatures estimated from spectra, not photometry from the LAMOST (Figure 2.20) and RAVE (Figure 2.21) catalogues.

2.13 Selecting Priority Targets

Candidates are assigned an initial priority for observing based upon the properties of the candidate and potential primary star, as described in the previous subsections. The ordering of these priorities has been done in such a way as to favour indications of youth that are less likely to spurious, or less likely to result from degeneracies and observation uncertainties. At some level this contains ambiguities, but the only robust way to refine these priorities would be to account for followup confirmation, which is only available for a small fraction of the candidate sample.

A Priority - Candidate is red in J-K and J-H (as per Section 2.12.1), primary average/lowish FeH but overbright (for it's B-V and metallicity, as per Section 2.12.4). Suggestive of extreme youth in both components.

B Priority - Candidate is red in J-K (as per Section 2.12.1), and primary may be young based on bolometric main sequence lifetime (Section 2.12.3).

C Priority - Primary is unambiguously very young due to SIMBAD flag (as per Section 2.12.2), but candidate looks normal.

D Priority - Candidate is red in J-K (as per Section 2.12.1), primary looks normal but is low or average metallicity based on RAVE or LAMOST metallicity being $\lesssim 0$. Possible double UCD or chance alignment. The chance of an unresolved double UCD makes this potentially more interesting.

E Priority - Candidate is red in J-K (as per Section 2.12.1) In each case the primary has no signs of youth.

F Priority - Primary may be young based on bolometric main sequence lifetime (Section 2.12.3).

G Priority - Primary is average/low metallicity, but is overbright for its B-V and metallicity as per Section 2.12.4. The candidate UCD looks normal. A possible unresolved multiple primary.

H Priority - Primary is over-bright for its B-V and metallicity as per Section 2.12.4. Primary could be an unresolved binary.

Chapter 3

Results and Discussion

3.1 Spectral Type Diagnosis of Selected Sample

J-K colours were assessed from a prioritisation perspective in Chapter 2. This section takes a more expansive approach to assessing the nature of candidate UCD companions based on all available photometry (NIR/optical apparent and absolute magnitudes). Dupuy and Liu (2012) plot many relationships, including the relationship between Spectral Type and Absolute J Magnitude. The plot of M_J versus Spectral Type from Dupuy and Liu (2012) is shown in Figure 3.1. Dupuy and Liu (2012) fit a polynomial of the form described in Equation 3.1 using the coefficients from Table 3.1.

$$y = \sum_{i=0} c_i x^i \tag{3.1}$$

The spectral type to M_J relationship shown in Equation 3.1 is used in this work to calculate absolute magnitude boundaries to enable spectral type to be estimated based on absolute magnitude alone. These boundaries are given in Table 3.2. Using these boundaries, each candidate is given a spectral type estimate from absolute M_J designated SpT(M_J).

TABLE 3.1: SpT to M_J Coefficients of Polynomial Fit from Dupuy and Liu (2012) for use with Equation 3.1.

c_0	c_1	c_2	c_3	c_4	c_5	c_6
-2.83129×10^{1}	1.63986×10^{1}	-2.74405	2.32771×10^{-1}	-1.03332×10^{-2}	2.27641×10^{-4}	-1.94920×10^{-6}

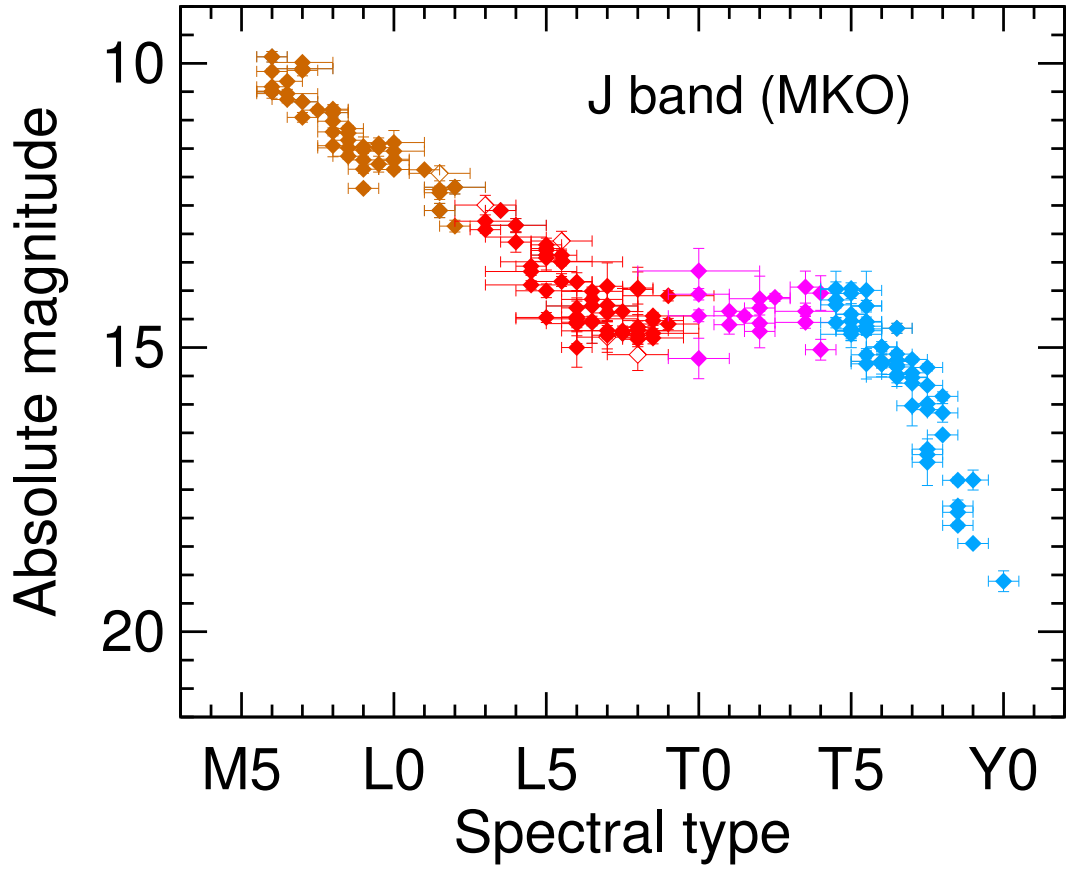

FIGURE 3.1: Spectral Type against Absolute J Magnitude from Dupuy and Liu (2012). Can be fitted from Mid M dwarfs to Late L dwarfs with the polynomial described in Equation 3.1 using the coefficients from Table 3.1.

Skrzypek et al. (2015) use the same method to calculate a phototyping system of template colours for UCDs. Template colours for each spectral type is given in Table 3.3. By matching candidate colours to these template colours, three further spectral type estimates were determined; SpT(opt) from optical photometry, SpT(NIR) from near-infrared photometry, and SpT(izJ) from combined optical and infrared photometry.

Optical Spectral Type, Spt(Opt), is based on the i-z colour. Near Infrared spectral type, Spt(NIR), is primarily based on the J-K colour but for candidates without a K detection, J-H is chosen. The Optical to Infrared spectral type, SpT(izJ), is based preferentially on the candidate's z-J colour. For candidates without a z detection but with an i detection, the i-J colour is used.

As can be seen in Table 3.3, the reversal of the colour trend in Y-J and J-H at the L+T transition means that spectral type estimations for L9 and above cannot be relied upon. The spectral typing

TABLE 3.2: M_J Boundaries for SpT estimation.

SpT	M_J Boundaries
M5	$7.291 < M_J \leq 9.235$
M6	$9.235 < M_J \leq 10.315$
M7	$10.315 < M_J \leq 10.883$
M8	$10.883 < M_J \leq 11.192$
M9	$11.192 < M_J \leq 11.411$
L0	$11.411 < M_J \leq 11.641$
L1	$11.641 < M_J \leq 11.934$
L2	$11.934 < M_J \leq 12.300$
L3	$12.300 < M_J \leq 12.724$
L4	$12.724 < M_J \leq 13.174$
L5	$13.174 < M_J \leq 13.612$
L6	$13.612 < M_J \leq 13.998$
L7	$13.998 < M_J \leq 14.300$
L8	$14.300 < M_J \leq 14.497$
L9	$14.497 < M_J \leq 14.584$

TABLE 3.3: Adjusted from Table 1 from Skrzypek et al. (2015). Template colours of M5–L9 dwarfs. Some colours not relevant to this work omitted. Additional colours of i-J, z-J & J-K added based on summing the colours available.

SpT	i-z	z-Y	Y-J	J-H	H-K	i-J	z-J	J-K
M5	0.91	0.47	0.55	0.45	0.32	1.93	1.02	0.77
M6	1.45	0.60	0.67	0.53	0.39	2.72	1.27	0.92
M7	1.77	0.70	0.78	0.56	0.44	3.25	1.48	1.00
M8	1.93	0.77	0.87	0.58	0.47	3.57	1.64	1.05
M9	1.99	0.82	0.96	0.60	0.51	3.77	1.78	1.11
L0	2.01	0.86	1.04	0.63	0.54	3.91	1.90	1.17
L1	2.02	0.88	1.11	0.67	0.58	4.01	1.99	1.25
L2	2.04	0.90	1.18	0.73	0.63	4.12	2.08	1.36
L3	2.10	0.92	1.23	0.79	0.67	4.25	2.15	1.46
L4	2.20	0.94	1.27	0.86	0.71	4.41	2.21	1.57
L5	2.33	0.97	1.31	0.91	0.74	4.61	2.28	1.65
L6	2.51	1.00	1.33	0.96	0.75	4.84	2.33	1.71
L7	2.71	1.04	1.35	0.97	0.75	5.10	2.39	1.72
L8	2.93	1.09	1.21	0.96	0.71	5.23	2.30	1.67
L9	3.15	1.16	1.20	0.90	0.65	5.51	2.36	1.55

system only functions for candidates on the main M/L linear sequence. As such, spectral typing system is only applied to candidates with $M_J < 4.115 \times (J-K) + 8$.

Figure 3.3 shows various spectral type estimations for the Dupuy sample of UCDs with parallaxes. Some young UCDs display characteristic photometric differences with older more typical UCDs, and these are manifest in plots showing the spectral type estimations of the sample. Figure 3.3 shows SpT(izJ) - SpT(M_J) against SpT(NIR) - SpT(M_J). Here, the estimation of spectral type based on the J-K colour, SpT(NIR), is greater than the spectral type estimation from M_J for VL-G candidates, the equivalent of the candidate being shifted redder on the J-K to M_J CMD.

Based on the young and normal UCDs from the Dupuy sample (in Figure 3.3) a selection region

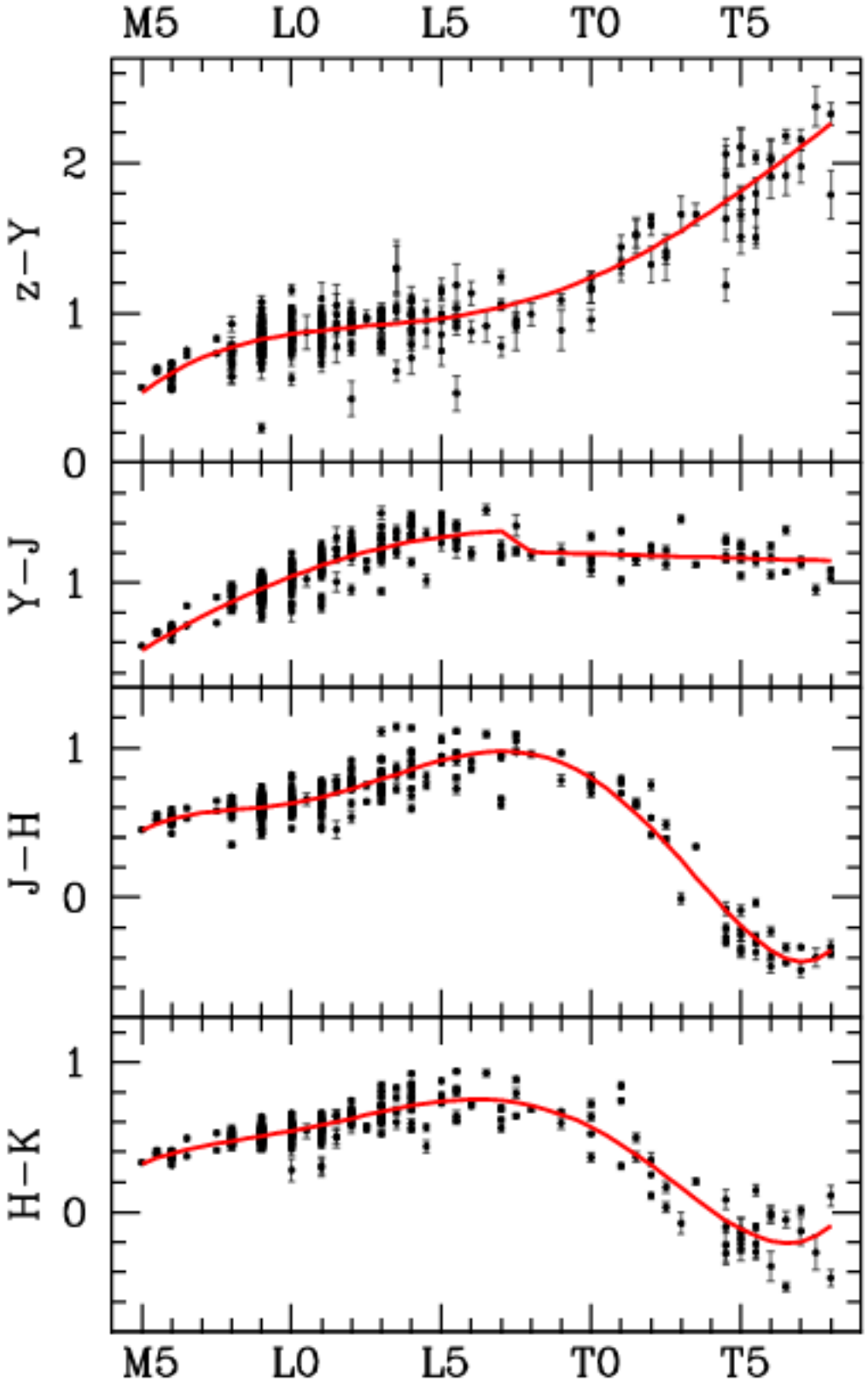

FIGURE 3.2: Spectral Type against a range of colours from Skrzypek et al. (2015). Skrzypek et al. generated polynomial fits to this data (shown as red lines) that provide a means to determine "template colours" for spectral types ranging from M5-T8 (which have been used in Table 3.1).

has been identified that can preferentially select youthful UCDs (the grey region in the Figure 3.3). If a candidate is within this selection region it is flagged as a "Potential Young UCD" based on all available apparent and absolute magnitudes.

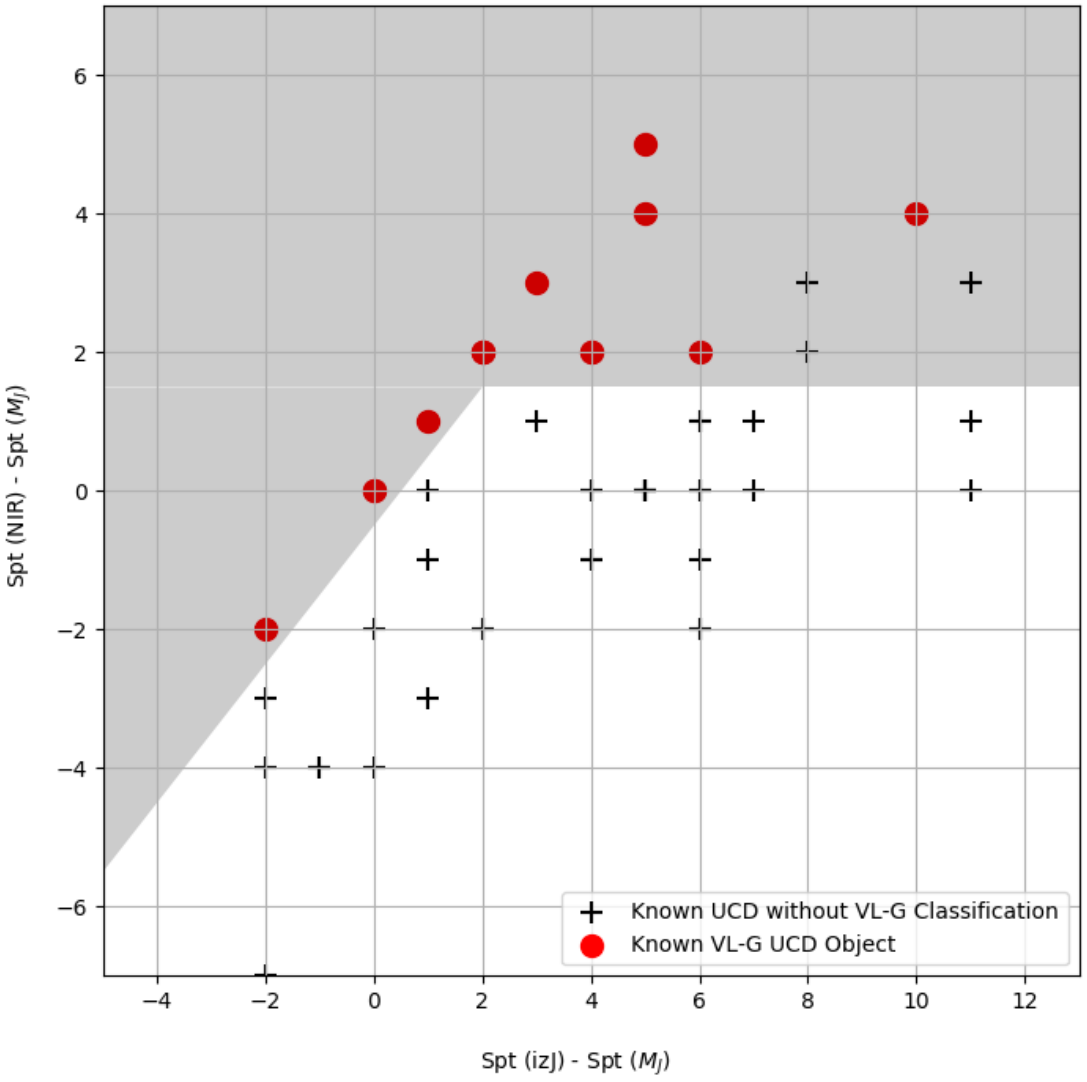

FIGURE 3.3: Spectral Type diagnosis plot, showing spectral type estimate SpT(izJ) - SpT(M_J) against SpT(NIR) - SpT(M_J). Dupuy sample of UCDs with Parallax are shown as black crosses, with Dupuy list objects with a VL-G classification which indicates youth and within the selected red J-K colour region as red circles

In Figure 3.3 the "normal" UCDs occupy a "dog-leg" shaped region of the plot, encompassing the (0,0) point but also extending from bottom left of the plot up towards the top right. We expect these "normal" variations to encompass effects such as UCD metallicity (e.g. metal rich/poor UCDs are known to show redder/bluer J-K colour), and also unresolved L+T binarity (where unresolved T dwarf companions enhance the combined J-band flux significantly, but not the optical and K-band fluxes). By comparison to the normal UCDs, "young region" clearly

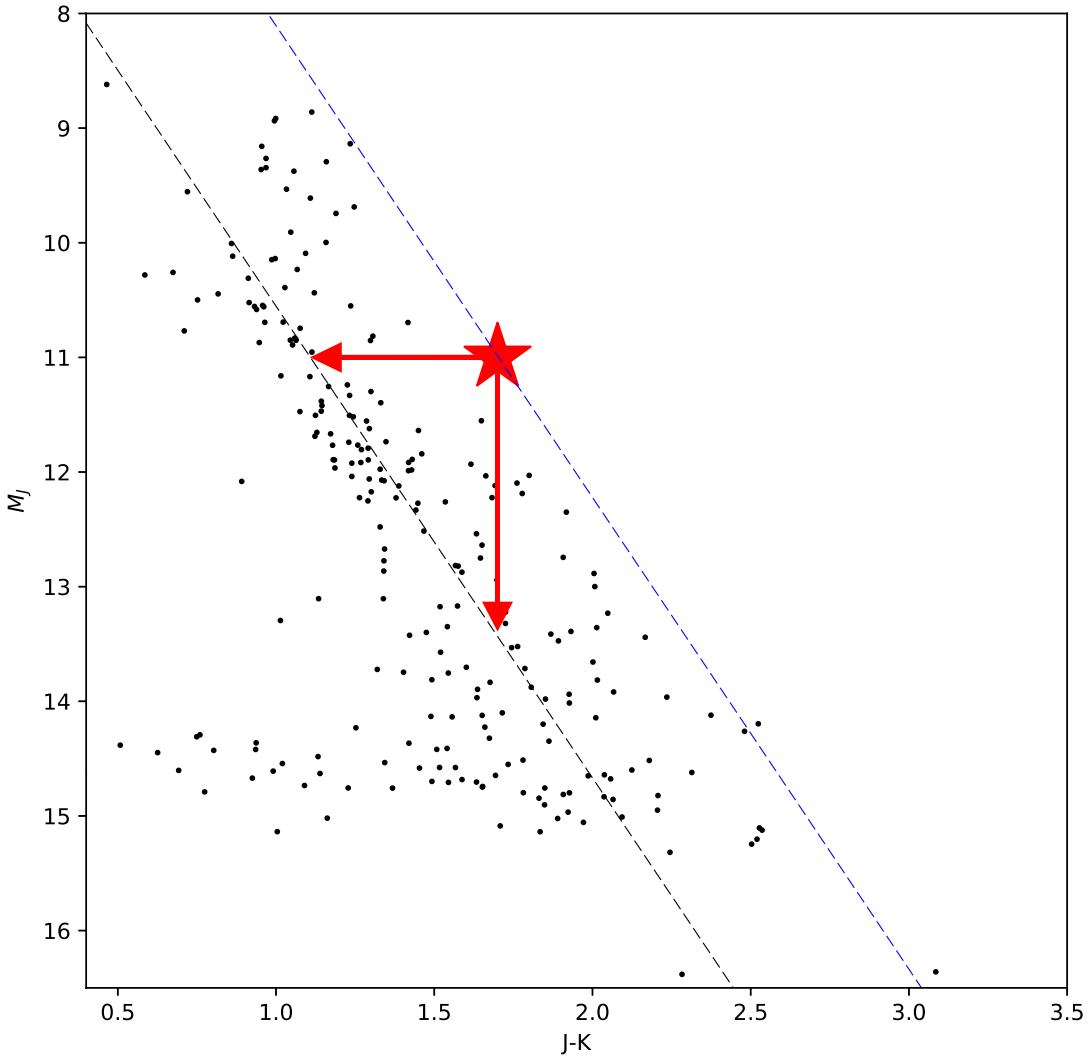

FIGURE 3.4: J-K to M_J Colour Magnitude Diagram with Dupuy sample objects. Red star represents a theoretical UCD. Red arrows track the position on to the linear M/L trend.

provides a good means to identify the kind of young objects highlighted in the Dupuy sample (and plotted in red in the figure) since these all occupy the grey area, in which one only finds relatively few contaminating "normal" UCDs (which tend to lie towards the top right of the plot). The young UCDs are systematically shifted towards the top left of the plot, resulting from two factors. The SpT(NIR) estimate will be larger for objects which have enhanced J-K colour, and the SpT(M_J) estimate may be decreased due to young UCDs being over-bright. These two effects are shown schematically in Figure 3.4, in which an "imagined" young L dwarf is shown on the "red J-K sequence", with arrows extending towards the M_J and J-K axis. The points where the arrows pass through the "normal UCD sequence" are significantly separated, thus establishing that SpT(NIR)-SpT(M_J) will have a positive offset.

A candidate that is in fact an unresolved L+T binary would have enhanced J flux but unaffected K and optical fluxes. As a result, the spectral types would change with SpT(J-K) $<$ SpT(izJ), as the SpT(J-K) diagnosis would decrease with increased J flux while increasing the SpT(izJ) estimate. Candidates that fulfill the criteria of SpT(J-K) $<$ SpT(izJ) without another spectral type diagnosis are given the spectral type diagnosis prediction of "Potential Unresolved L+T binary".

A candidate on the red Liu et al. (2016) J-K sequence that is actually a foreground L dwarf (closer than the primary) would have SpT(Opt) = SpT(izJ) = SpT(J-K) $>$ SpT(M_J). On Figure 3.4 this would have the effect of the "imagined" young dwarf having the correct spectral type estimate based on colours (SpT(Opt) = SpT(izJ) = SpT(J-K)) but be underestimated on SpT(M_J) as the object is infact a fainter foreground object. Candidates that fulfill this criteria without another spectral type diagnosis are given the spectral type diagnosis prediction of "Potential Foreground L Dwarf".

Figure 3.5 shows the spectral diagnosis system applied to the sample of candidates identified as promising CPM pairs with the candidates defined as likely young based on the spectral type diagnosis system shown in red.

3.2 Summary of Candidate Samples

This work has found 1,623 candidate benchmark pairings where the proper motion of the primary and candidate UCD is within 3σ as defined by Section 2.8 or where no proper motion of the candidate companion could be obtained. In addition, each of these pairings has some indications of youth as defined by Section 2.13.

Fifty of the 1,623 candidate benchmarks are considered promising CPM pairs as defined in Section 2.8, shown in Appendix A Tables A.2 and A.3. A further 348 pairings of the 1,623 have signs of youth and have fast moving primary candidates ($\mu > 50$mas/yr) and so could have their CPM status assessed by additional observations of the companion to constrain proper motion.

Thirty-eight of the 1,623 candidates have angular separation of <6 arcseconds or $<$30 pc distance and so are considered candidates based on common distance selection (Section 2.9), shown in Table A.4. These candidates require spectral type distance estimates to confirm companionship using only common distance.

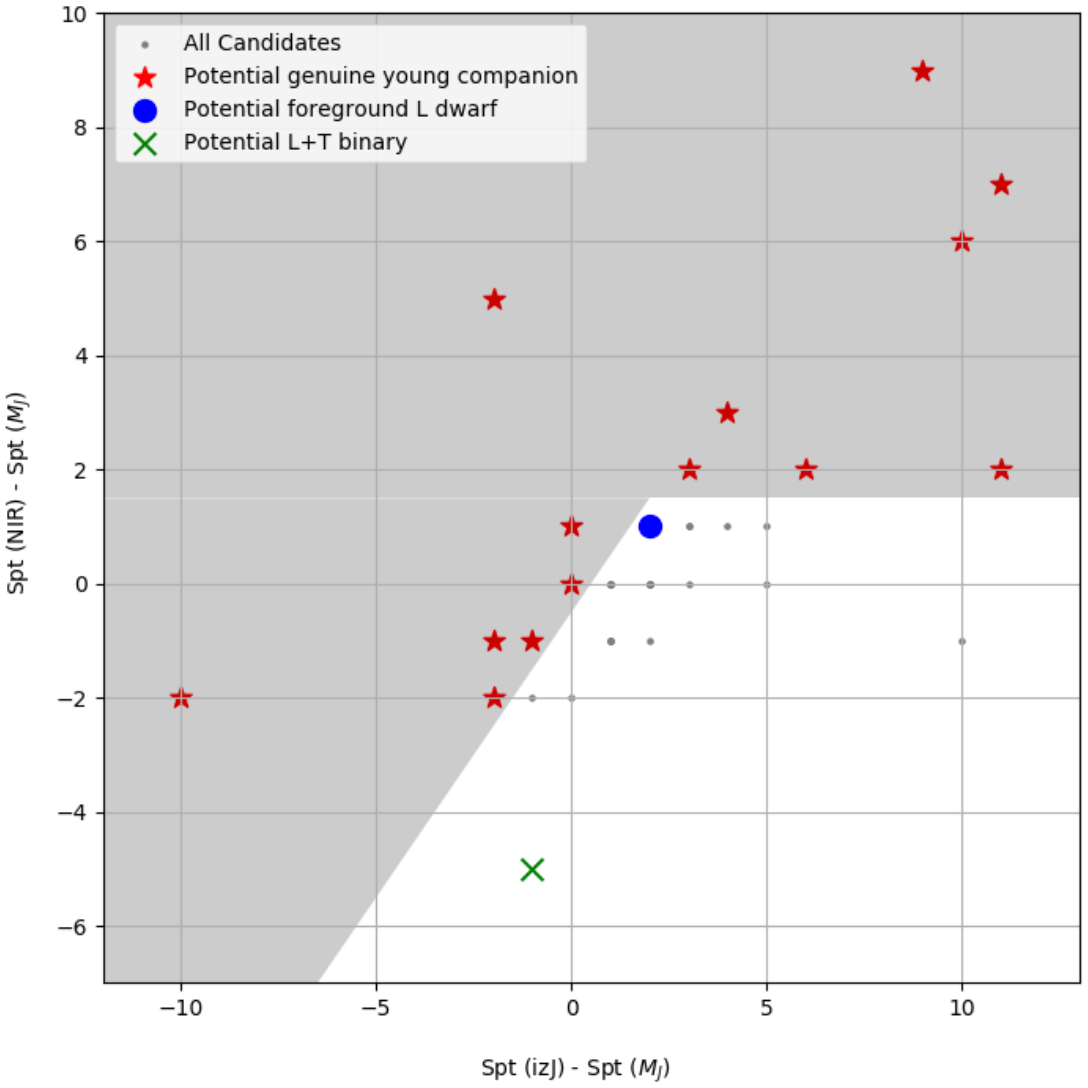

FIGURE 3.5: Spectral Type diagnosis plot, showing spectral type estimate SpT(izJ) - SpT(M_J) against SpT(NIR) - SpT(M_J). All likely CPM candidates shown as grey dots with candidates considered likely young companions shown as red stars. The green cross is a potential unresolved L+T binary. The blue circle is a potential foreground L dwarf.

Many additional candidates have low primary proper motion, meaning that the companion proper motions can not be constrained with further observation, but twenty-four of the 1,623 candidates selected have strong indicators of youth in both the candidate primary and companion (Priority A or B by the method described in Section 2.13) and the companion has spectral type diagnosis as a likely young object (by the method described in Section 3.1). These candidates are shown in Table A.5.

Table A.6 contains 10 additional candidates that are likely CPM pairs to primaries with outlier metallicity ([Fe/H] or [M/H] > 0.2 or < -0.3) not in the sample of potentially young candidates.

This is included to support the program of work by the Marocco et al. (2017) team identifying benchmark systems with outlier characteristics.

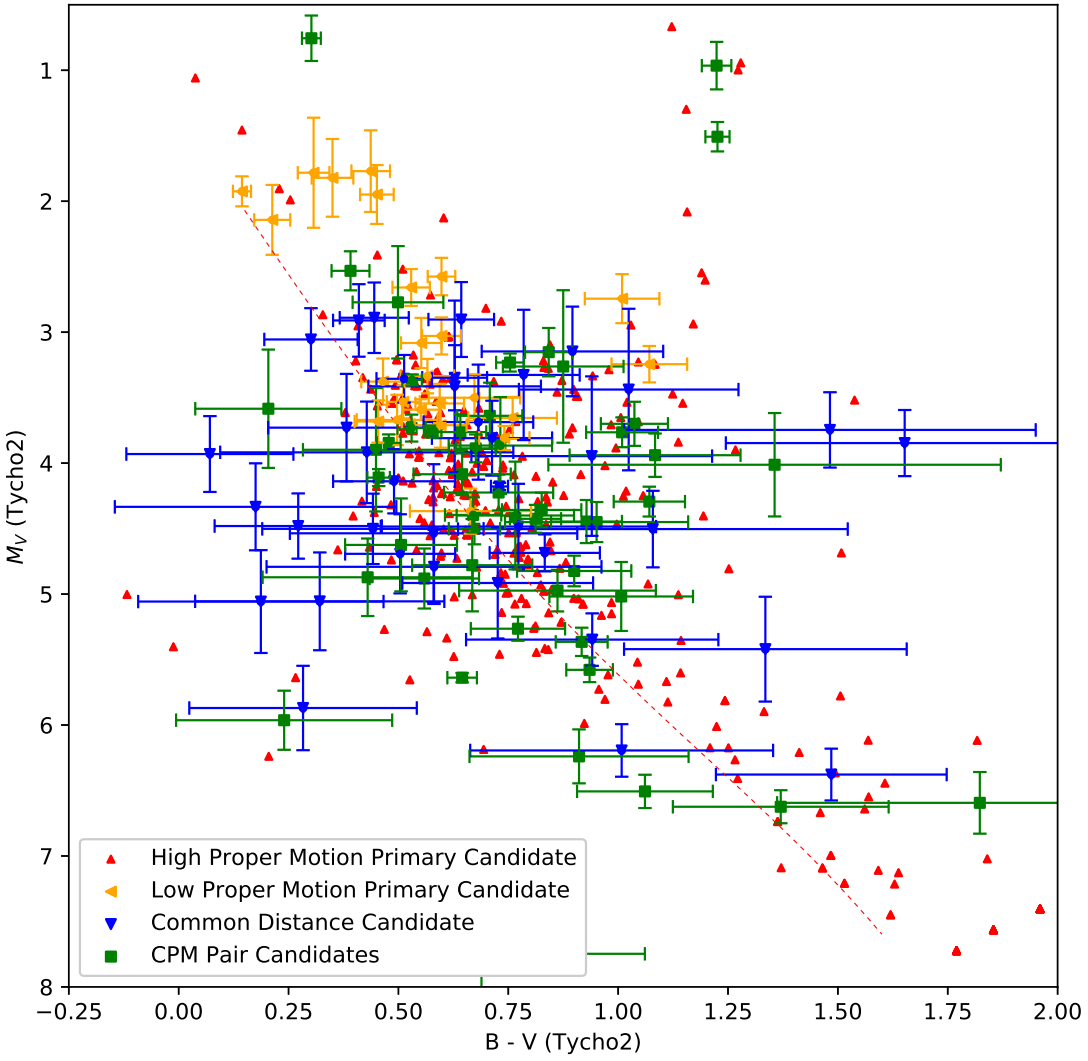

FIGURE 3.6: Plot of Primary candidates with known B and V magnitudes showing absolute V magnitude against $B-V$. Red and orange triangles are candidate pairs below 3σ Proper Motion Difference check but without well defined companion proper motion. Red markers are candidates with high primary proper motion needing additional photometric observation to constrain candidate proper motion. Orange markers are candidates with low primary proper motion but are high priority for obtaining spectra due to indicators of youth in both the candidate UCD and primary. Blue triangles are common distance candidates within 6 arcsecond separation between primary and candidate. Green squares are matches considered good common proper motion pairings.

Figures 3.6 to 3.13 show a variety of parameter combinations, with different symbols identifying different candidate subsets or comparison samples from the literature. Dupuy UCDs are shown as grey and black symbols (for normal and young objects respectively) in Figures 3.6 to 3.12. Candidate associations with promising CPM are plotted as green squares. Candidates without

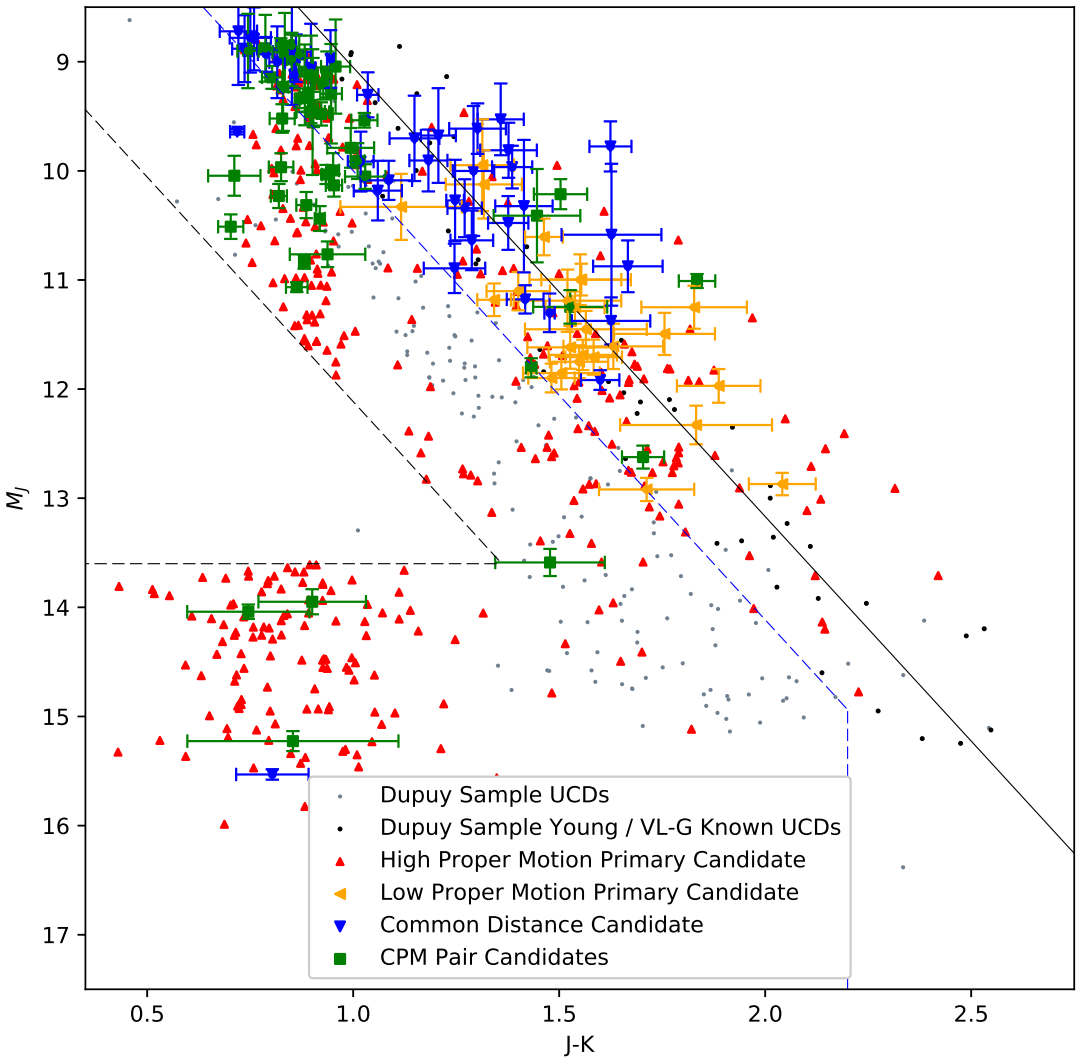

FIGURE 3.7: Plot of candidate companions, ofabsolute J magnitude based on primary parallax against $J-K$ (converted $J-Ks$). Black line shows Liu et al. (2016) proposed young substellar $J-K$ to M_J relationship. Colours and symbols as defined in Figure 3.6 except grey markers which are known UCD from the Dupuy sample and black markers which are candidates from the Dupuy sample confirmed as young or VL-G.

a promising CPM but with high/low proper motion primaries are shown as red/orange triangles respectively. Candidates whose distance and separation would make them statistically robust if the UCD companions was confirmed spectroscopically, are shown as blue triangles.

Figure 3.6 shows the $B-V$ colour for all primaries where it is known. The middle of the main sequence as calculated for Section 2.12.4 is shown as the dashed line. The main sequence is clearly visible, as well as a population of overluminous primaries. These may be a combination of young primaries moving on to the main sequence or massive primaries that have already evolved off the main sequence.

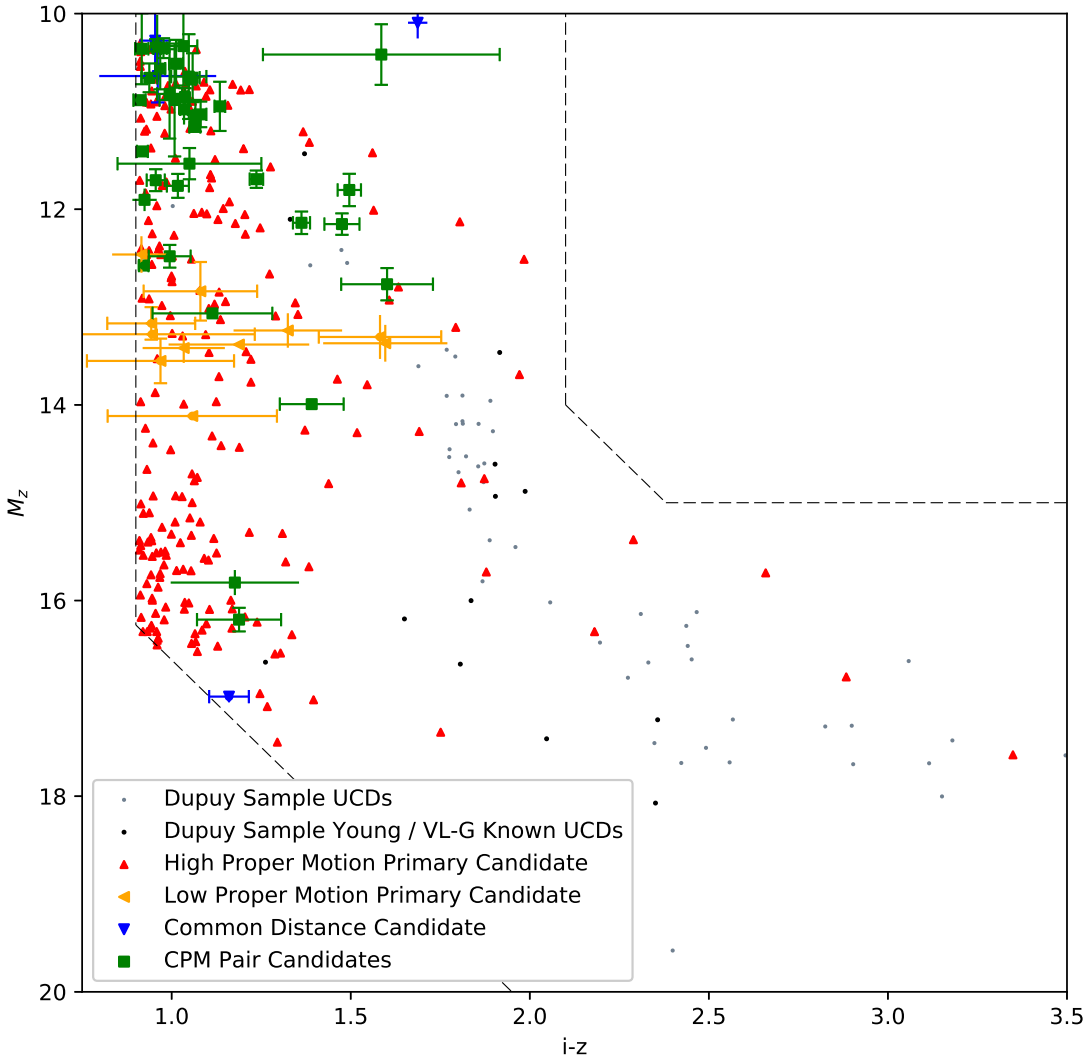

FIGURE 3.8: Plot of candidate companions, of absolute z magnitude based on primary parallax against i-z. Colours and symbols as defined in Figure 3.7.

Figure 3.7 shows the M_J from assumed candidate distance against J-K colour - magnitude diagram of the sample. The selection criteria detailed in Section 2.4.3 are shown as dashed black lines. The selection region constrained within the blue dashed line to select young M and L dwarfs will exclude young T dwarfs. This is discussed in the future work section. The blue dashed region indicates the linear M/L sequence where the spectral typing system described in Section 3.1 is applied to candidates.

Figures 3.9, 3.10, 3.11 and 3.12 replicate the Colour-Colour plots based on the sample of known UCDs from Section 2.6 and show how the final selected sample compares to the known UCD population. The $H-K$ against $J-H$ plot shows one of the trends to be aware of. We see candidates with a high $H-K$, without a high $J-H$. As candidates are being selected for

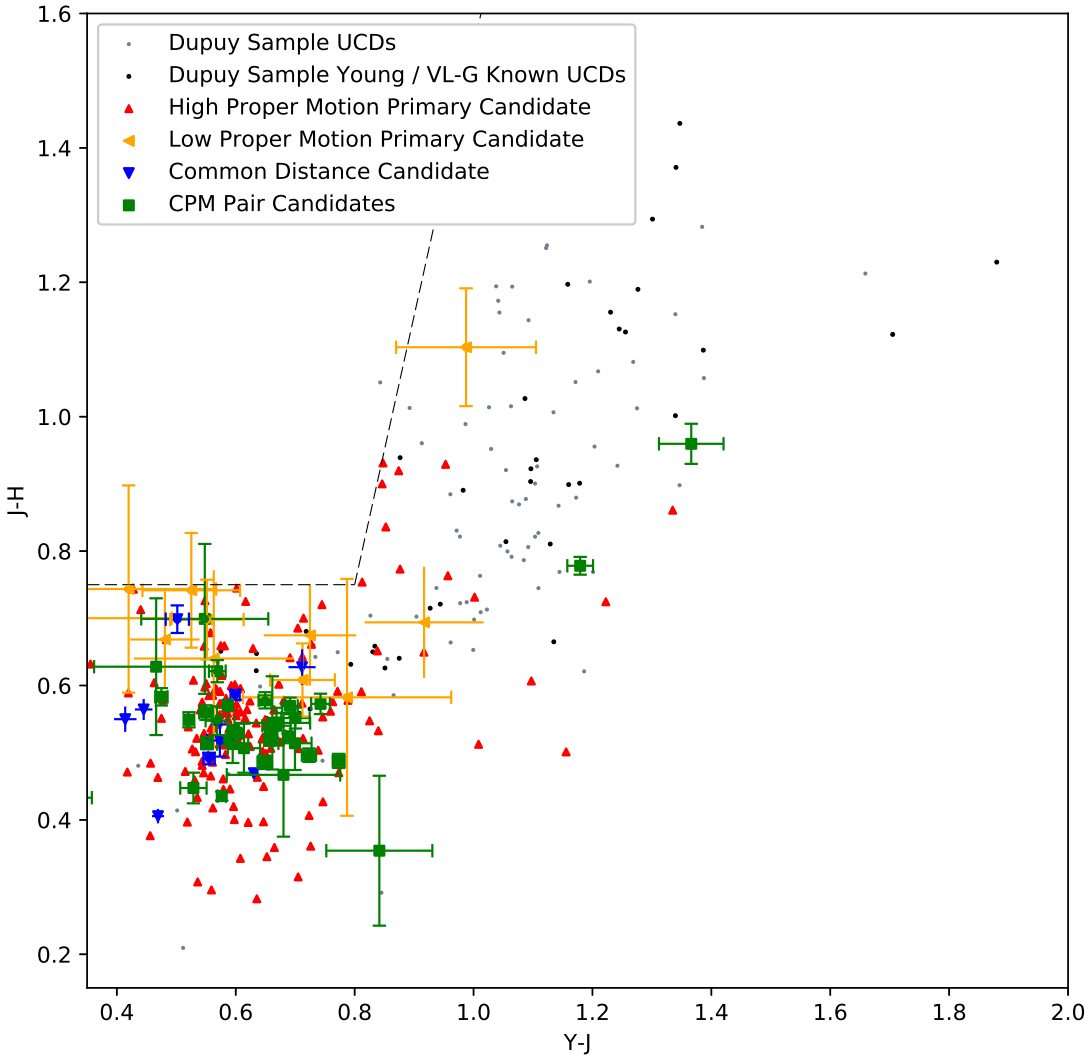

FIGURE 3.9: Plot of candidate companions, of J-H against Y-J. Colours and symbols as defined in Figure 3.7.

a high J-K colour, this could be due to enhanced J-H and/or enhanced H-K. However the H-K versus J-H colour-colour plot (Figure 3.10) shows that as the J-H colour of young UCDs increases, we generally expect the H-K colour to increase as well. This therefore suggests that the numerous candidates lying to the upper left of the Dupuy sequence may contain significant levels of (non-UCD) contamination.

Figures 3.11 and 3.12 shows a large scatter in the $i-z$, $z-Y$ and $Y-J$ colours as shown in the sample of known UCD candidates. Figure 3.9 show that candidates are consistent with the Dupey sample in this colour space.

Figure 3.13 reproduces Figure 9 from Marocco et al. (2017) and shows on sky separation (arc-seconds) to distance (pc) for each candidate based on the TGAS object distance. Two candidates

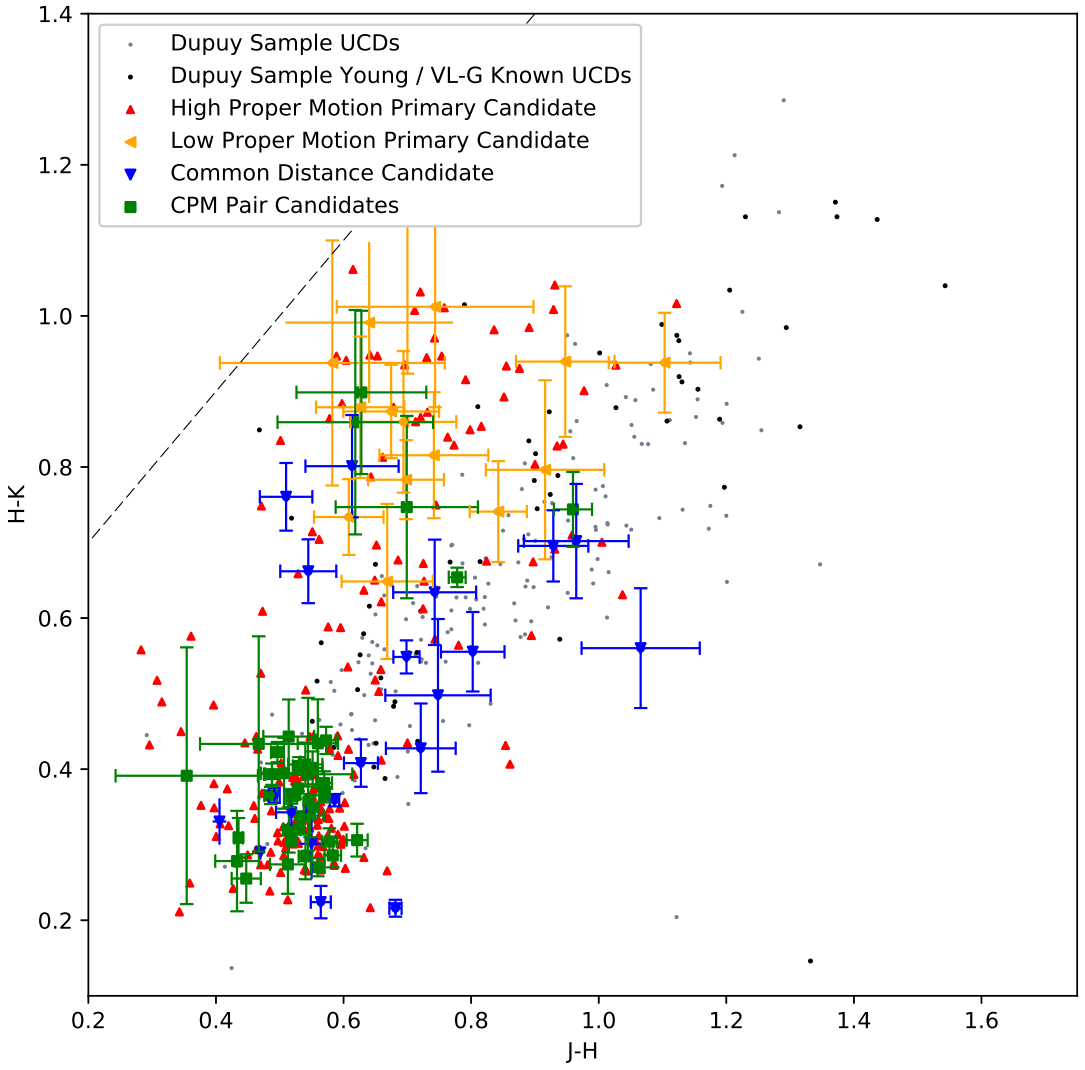

FIGURE 3.10: Plot of candidate companions, of H-K against J-H. Colours and symbols as defined in Figure 3.7.

have potential primaries closer than 30 parsecs. Thirty-six other pairs have an angular separation below 6 arcseconds. Both factors mean that these candidates only require confirmation of common distance via a spectral type distance estimate in order to statistically rule out a false positive to a probability below 0.0001 (Marocco et al., 2017).

3.3 Narrow Band Photometry

Radostin Kurtev of the Universidad de Valparaíso was granted CNTAC proposal CN2017B-36 for two observing nights on 6.5m the Magellan telescope at Las Campanas Observatory using the FIRE NIR spectrograph in PRISM mode to observe targets from this work.

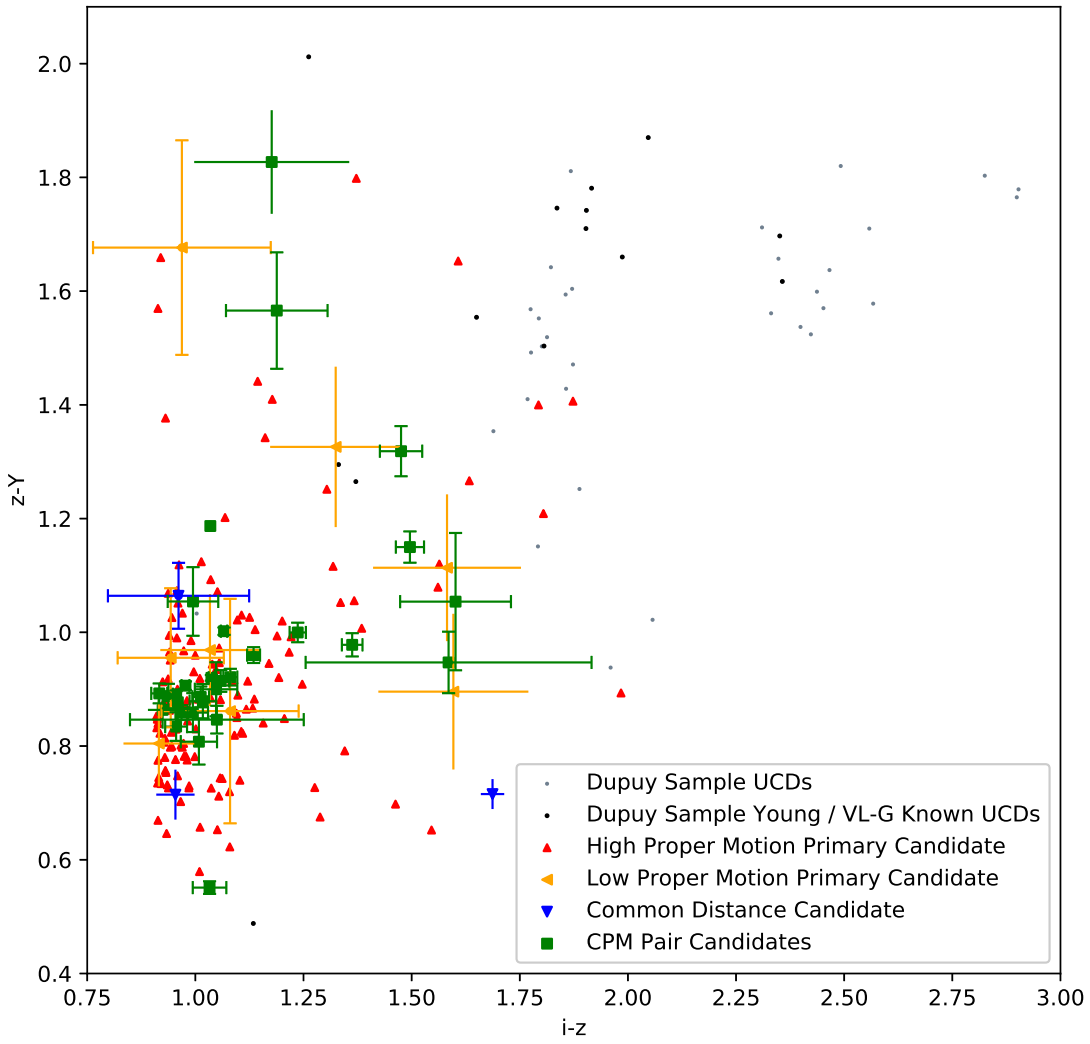

FIGURE 3.11: Plot of candidate companions, of z-Y against i-z. Colours and symbols as defined in Figure 3.7.

FIRE produces spectra with resolutions $R_J = 500$, $R_H = 450$ and $R_K = 300$[1], which are considered low resolution spectra for the purpose of UCD spectral typing (Allers and Liu, 2013). These spectra would be able to allow surface gravity sensitive features in the UCD candidate spectra to be identified.

The FIRE instrument was under repair for all of September, October and part of November 2017, including the dates assigned. As a result, the observing time was switched to photometric observations with the FourSTAR NIR camera. A program was designed to use the narrow band filters available with FourSTAR. Using the SPLAT package (Burgasser, 2014), simulated Hs-Hl and J-J3 colours for field-age and young UCDs were compared and a colour difference was

[1] `http://www.lco.cl/telescopes-information/magellan/instruments/`

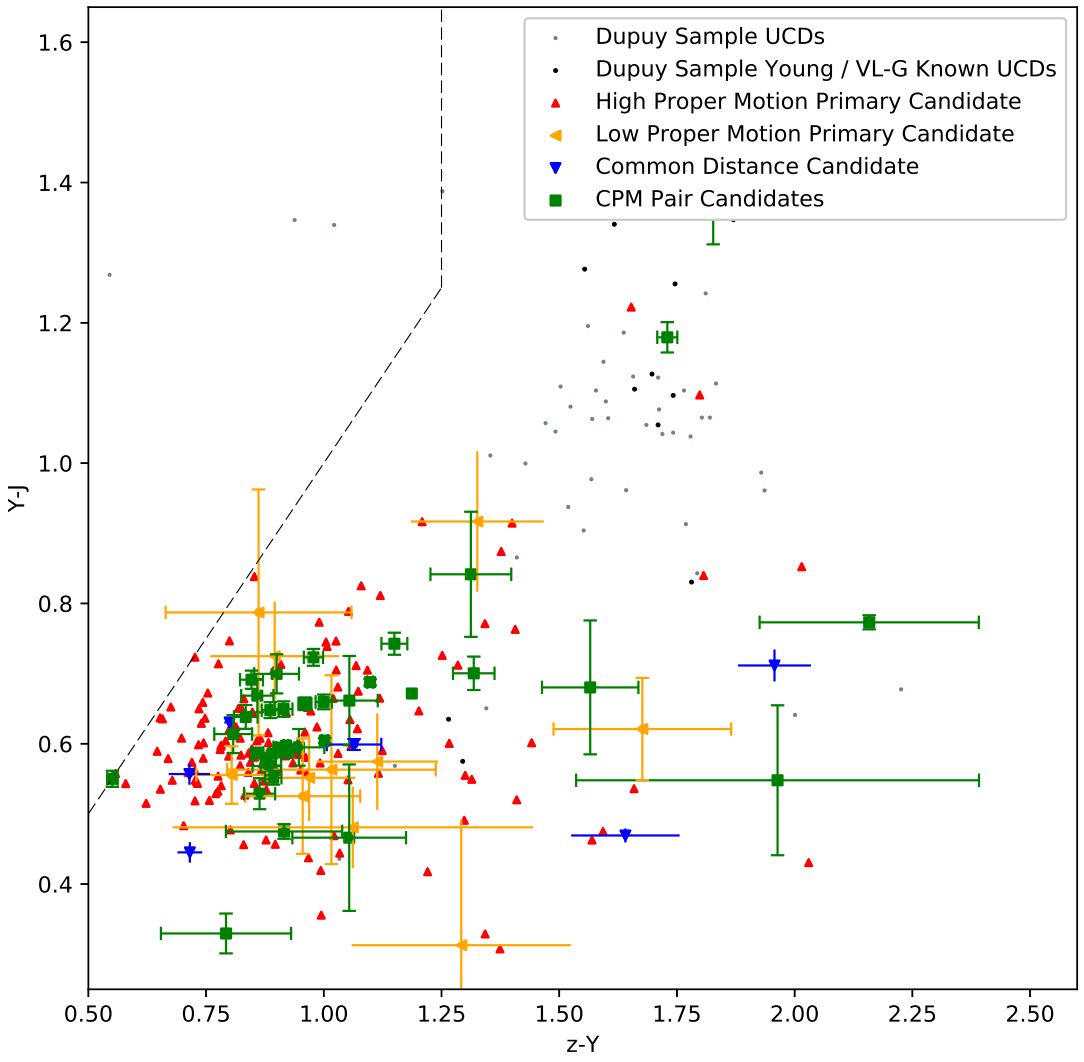

FIGURE 3.12: Plot of candidate companions, of Y-J against z-Y. Colours and symbols as defined in Figure 3.7.

identified in the Hs-Hl to J-J3 colour diagram. Section 1.4.5 details the simulated narrow band colours Hs-Hl verses J-J3 for field compared to VL-G UCDs from template spectra.

3.3.1 Instrumental Setup and Exposure Times

The difference between a VL-G object and a field object is $\lesssim 0.1$ magnitude in Hs-Hl as shown in the simulated 2-colour diagram in Figure 1.14. Exposure times were chosen to give the required accuracy. For example, candidate J2028-1346 at J $\sim$ 18.8 required exposure times of J $= 600s$, J3 $= 300s$, Hs $= 600s$, Hl $= 600s$. This means the total exposure time of some candidates was greater than 30 minutes.

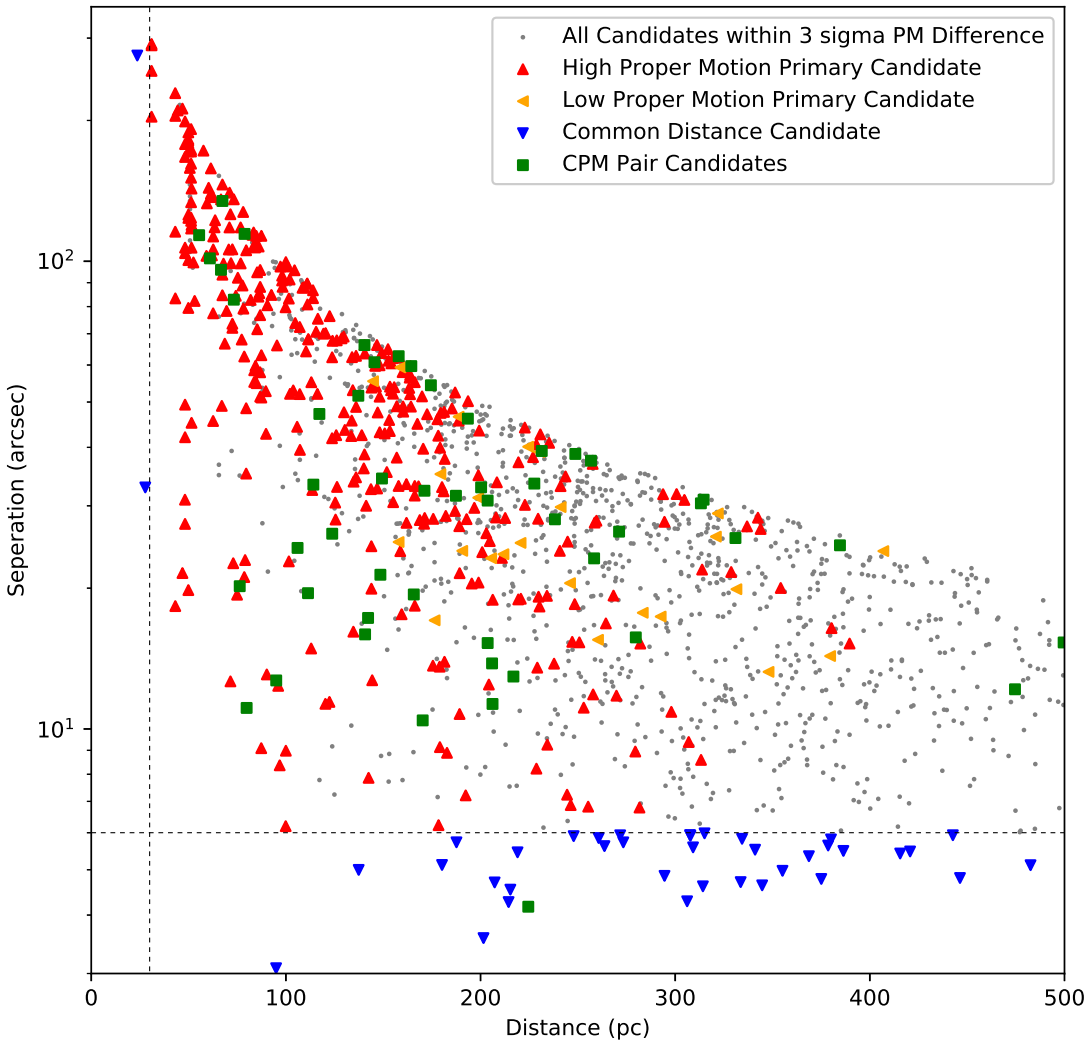

FIGURE 3.13: Angular separation (arcseconds) to distance (pc) of the whole sample of candidates. Full sample of all candidates within 3σ in grey. The remaining colours and symbols follow the convention as defined in Figure 3.7. Dashed regions indicate the range of candidate that only require common distance confirmation to confirm a primary-UCD relationship.

3.3.2 Observed Targets and Data Obtained

Observations were carried out on the 17th and 18th of November 2017. Fourteen targets identified from this work were observed in narrow band photometry. Two candidates were not observed in two of the required bands due to time restraints. One could not be resolved from the primary and one was over exposed due to proximity in the sky to a bright star and so could not be processed. Ten candidates remaining had narrow band colours calculated. Figure 3.15 shows 1 arcminute by 1 arcminute thumbnails of J band images from FourSTAR.

Most of the candidates passed the 3σ CPM check by having poorly defined PMs as discussed in

TABLE 3.4: Observed Candidates Spectral Type Estimates

Candidate Name	SpT(M_J)	SpT(Opt)	SpT(izJ)	SpT(NIR)
VHS J2226-0433	M4	M5	M5.5	M5
UKIDSS J0009+0037	M5	M5	M7	M7
VHS J2028-1346	L9	M4	-	M7
UKIDSS J2204+0234	L9	-	L0	M9
UKIDSS J2204+0235	L7	M4	M4	M7
VHS J22101-0124	L7	M4	M5	M5
UKIDSS J2236+0010	M7	M4	M4	M6
VHS J2141-0246	L2	M6	L1	L5
UKIDSS J2218-0108	M5	M6	M6	M7
VHS J2309-0227	L8	M6	M5	M6

TABLE 3.5: Observed Primary Metallicity Information

Candidate Name	Primary Candidate	Primary Metallicity	Metallicity Source
VHS J2226-0433	TYC 5229-858-1	[Fe/H] = -0.10	LAMOST
UKIDSS J0009+0037	TYC 1-1187-1	[M/H] = 0.42	RAVE
VHS J2028-1346	TYC 5766-592-1	-	-
UKIDSS J2204+0234	TYC 561-236-1	-	-
UKIDSS J2204+0235	TYC 561-236-1	-	-
VHS J2210-0124	TYC 5225-575-1	-	-
UKIDSS J2236+0010	TYC 567-536-1	-	-
VHS J2141-0246	TYC 5213-545-1	[M/H] = 0.04	RAVE
UKIDSS J2218-0108	TYC 5225-719-1	[Fe/H] = 0.92	Ammons et al. (2006)
VHS J2309-0227	TYC 5242-324-1	[M/H] = -0.10	RAVE

TABLE 3.6: Observed Primary Information and Priority Selection

Candidate Name	Primary Candidate	Primary Type	Source	Priority
VHS J2226-0433	TYC 5229-858-1	F5V	LAMOST	A
UKIDSS J0009+0037	TYC 1-1187-1	K4Ve, RotV*, pr*	SIMBAD	B
VHS J2028-1346	TYC 5766-592-1	G6V, pr*	SIMBAD	C
UKIDSS J22048+0234	TYC 561-236-1	K5V, pr*	SIMBAD	C
UKIDSS J22041+0235	TYC 561-236-1	K5V, pr*	SIMBAD	C
VHS J2210-0124	TYC 5225-575-1	K3V, pr*	SIMBAD	C
UKIDSS J2236+0010	TYC 567-536-1	K0IV, pr*	SIMBAD	C
VHS J2141-0246	TYC 5213-545-1	-	-	D
UKIDSS J2218-0108	TYC 5225-719-1	-	-	E
VHS J2309-0227	TYC 5242-324-1	K4Ve, RotV*, pr*	SIMBAD	C

TABLE 3.7: Observed Candidates with CPM Relationships

Candidate Name	Primary Candidate	$\mu_{\text{companion}}$ / $\sigma\mu_{\text{companion}}$	μ source	$\sigma\Delta\mu$
VHS J2141-0246	TYC 5213-545-1	5.7	2 Point Calculation	0.72
UKIDSS J2218-0108	TYC 5225-719-1	19.6	UKIDSS LAS	1.8

section 2.8 and instead were observed speculatively as potential companions to their respective candidate TGAS primary. These candidates are discussed below.

J0009+0037 - Selected as very red in J-K (~ 1.01) in the M_J to $J-K$ CMD. The candidate primary (TYC 1-1187-1) is rotational variable (Kiraga, 2012) and potentially young (Elliott et al., 2015). The proper motion of the candidate UCD is well defined with μ / $\sigma_\mu \sim 24$. However the proper motion difference between the candidate primary and companion is

only just within the selection limit at $\sim 2.9\sigma$. It is very likely the companion is not related to the potential primary.

J2028-1346 - Selected as the candidate primary (TYC 5766-592-1) is a proto-star candidate (Torres et al., 2006). The candidate companion has no well defined PM.

J2204+0234 & J2204+0235 - Both candidates selected as potential companions to TYC 561-236-1, a candidate proto-star (Torres et al., 2006). Neither candidate has well constrained PMs so both were selected based only proximity in the sky to the primary and absolute photometry based on presumed distance.

J2210-0124 - Selected as the primary (TYC 5225-575-1) is a candidate protostar (Torres et al., 2006). The candidate companion has no well defined PM.

J2226-0433 - Selected due to redness in J-K (~ 0.91) and position on the M_J to $J-K$ CMD. Spectral type predictions were ranging from M4 based on M_J to M5 based on izJ. The candidate primary is metal poor ([Fe/H] = -0.103 - LAMOST) and overbright in B-V, however further investigation indicates the primary likely has an unresolved NIR companion (Richichi et al., 2012). This would affect both the brightness and the metallicity values.

J2236+0010 - Selected for the same reasons as J2210-0124, with the potential primary TYC 567-536-1 being noted as a protostar candidate within SIMBAD (though it is notable that followup checks reveal no reference for this SIMBAD categorization).

J2309-0227 - Selected as the candidate primary (TYC 5242-324-1) is a rotational variable star (Kiraga, 2012) and potentially very young. The primary is metal poor ([M/H] = -0.096 - RAVE) and overbright in B-V, but as a rotationally variable star, these parameters may be unreliable.

Only two of the observed candidates have a well defined CPM relationship with the candidate TGAS primary. The details of these candidates are listed here:

J2141-0246 - Was selected due to its position on the $J-K$ against M_J and for being very red ($J-K \sim 1.7$). The spectral type estimates put this candidate as an L2 based on M_J, and L5 based on NIR, and L1 based on combination of izj. It is a promising CPM pair candidate with its primary with a well defined proper motion based on two epoch observations with

μ / $\sigma\mu \sim 5.7$ and a significant difference between the proper motions of the companion and primary of only $\sim 0.72\sigma$.

J2218-0108 - A likely CPM pair with the primary TYC 5225-719-1. Selected only for being very red in $J-K$ (~ 1.01) and position on the $J-K$ against M_J, the spectral type estimates were M5 based on M_J, M6.5 based on izJ and M7 based on NIR. As such, the candidate was selected speculatively, based on the principle that a young candidate may have the spectral estimate from M_J over estimated. Spectral type estimates put this candidate as borderline between the hydrogen fusing and non-hydrogen fusing transition.

3.3.3 Narrow Band Imaging Data Reduction

Target objects were centred in the second chip of the FourSTAR camera. For each exposure, multiple short exposures are taken and presented as FITS files. Only exposures from the second chip were used. The command language for running IRAF tasks from within the Python scripting language, PyRAF, was used to deduct dark exposures from each file. For each filter, a flattered and normalised sky flat field is created from the mean of all exposures and then applied to each FITS files by dividing each exposure by this flat field. The resultant images are aligned using the PyRAF command "IMALIGN" before being combined.

Sources are extracted from each stacked image using the PyRAF "DAOFIND". This function gives each source an instrumental magnitude and error in each band. The position of each source is calculated by identifying 5 - 10 field of view objects in VHS or UKIDSS catalogue data and identifying the catalogue positions. This enables the position of each field of view object to be calculated. This allows sources in different bands to be cross matched and for instrumental colours to be calculated.

3.3.4 The Narrow Band 2-Colour Diagram

Figure 3.14 shows the J-J3 against Hs-Hl 2 colour diagram extracted from the instrumental magnitudes observed with the FourSTAR bands. Grey candidates are stars in the field of view. No standard starss were observed within the observing program, meaning that only instrumental colours could be used rather than colours adjusted based on standards. The instrumental colour was tuned by taking the mean average colour of the field candidates with highly accurate colour value ($\sigma < 0.02$ magnitudes) and using this to calibrate and shift all colours, including those of

the target, until the average value is 0. The dashed section shows the predicted region for VL-G candidates based on the template spectra as detailed in Section 1.4.5. The failure to include standards and the impact on the results is discussed in Section 3.3.5.

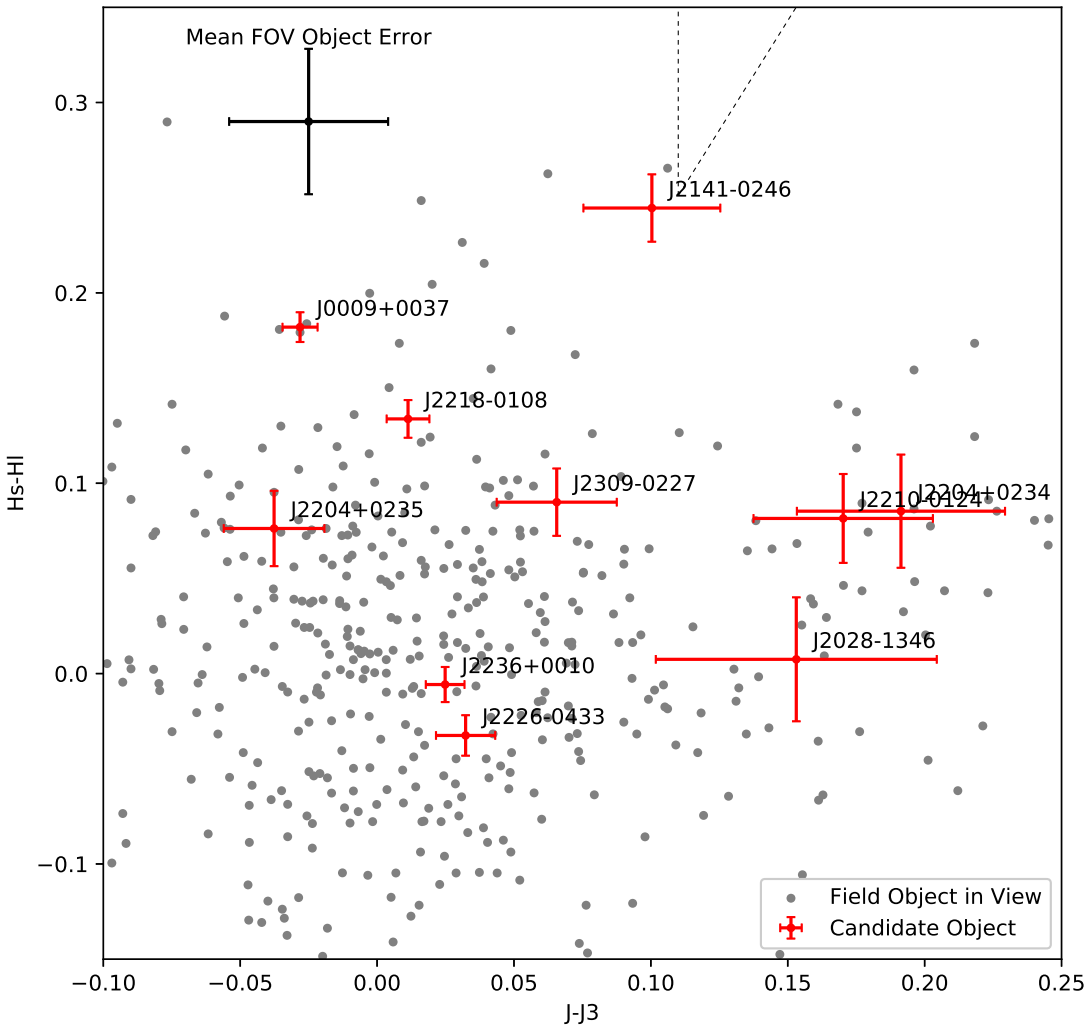

FIGURE 3.14: Hs-Hl against J-J3 colour diagram for observed young UCD candidates. Targets shown in red with colour errors. Grey markers are background candidates used to calibrate colour values. The mean of the Field of View errors is shown as a single example. Selection region shown in dashed lines separates the region for very young candidates based on template spectra as detailed in Figure 1.15.

The narrow band colour diagram in Figure 3.14 has a large amount of scatter around the expected 0 value for field candidates. Three candidates, J2210-0124, J2210-0124 and J2204+0234, have large errors on the colour values. The quality of the processed observation for these candidates meant a large number of the candidates in the field had large errors, meaning only a small number of field candidates could be used to calibrate the colour. The smaller the number of calibration candidates, the less accurate the calibration factor.

Two candidates, J2236+0010 and J2226+0433 have small errors and are close to Hs-Hl = 0 and J-J3 = 0 and so can be dismissed as being uninteresting candidates and are likely background field candidates. Two other candidates, J2204+0235 and J2309-0227, have larger errors, reflecting the error values in the observations and in the calibration value. While they are higher in Hs-Hl as predicted as an indicator of youth, this may still be within scatter around Hs-Hl = 0 and J-J3 = 0. These candidates will be revisited if further PM calculations confirm a CPM relationship with their young primaries.

Three candidates, including the two observed with likely CPM relationships to their primaries, remain for discussion, J2218-0108, J0009+0037 and J2141-0246. All of these lie outside of the selection region predicted by the simulated narrow band photometry from template spectra. J2141-0246 may lie within the region according to these instrumental colours, however the bottom end of the region would be the selection region for young M7, while spectral type estimations predict this candidate to be in the range L1 - L5 which would be to the top right of the selection region.

J2218-0108 is predicted to be in the range of M5 - M7 which would be to the bottom left of the selection region. It may be that the calibration of these instrumental colours cannot be compared to the simulated colours without further calibration. If these spectral type estimations are accurate and could be used to calibrate the selection region, then all three candidates, J2218-0108, J0009+0037 and J2141-0246, would be likely young UCDs.

3.3.5 Potential Improvements for and Discussion of Narrow Band Followup

Of the ten observed candidates, eight candidates were included where the candidates do not have a well defined proper motion. Six of these eight candidates were selected based solely on categorisation of the primary as a young candidate by other literature sources (found through a SIMBAD search) while the final two were selected due to the properties of their primaries, despite the pairings not being considered promising CPM matches.

Selection based on photometry used position on the CMD using absolute magnitude and so relied upon common-distances for the UCD and the TGAS primary. This means that all candidates, regardless of whether or not the primary is noted in the literature as likely being young, are selected based on the presumed distance and so are vulnerable to mismatching. As shown in Section 2.8, only 4.5% of the candidates that had a well defined companion PM were retained

as CPM. This means that when the companion proper motion is well defined, only 4.5% of candidates are then found to be possible CPM pairs with the primary. Extrapolating this to the set of candidates observed without a well defined UCD proper motion, the majority of these candidates would not likely be related to the candidate primary and cannot be assumed to be at the same distance. This means the candidate's CMD positions used for selection cannot be relied upon. With the observations completed for these targets, an additional proper motion value can be calculated using the observations from this set combined with catalogue images.

When considering the priority of targets where the proper motion of the companion is not known, a higher threshold must be applied than if the target has a likely CPM relationship to the candidate primary. As a parent-sibling relationship is not confirmed, targets should only be selected in this work if signs of youth exist in observations of both the candidate companion and primary. This will provide further evidence that the candidates are related. This was not done for the selection in this work.

The simulated narrow band colours show that the difference in Hs-Hl between VL-G UCDs and field UCDs is ~ 0.1 magnitudes. The instrumental 2 colour diagram cannot show this differentiation without further calibration using a standard star. This could be achieved by finding previous observations of standard stars in order to change the instrumental colours in to colours that could be compared to the simulated colours used in Figure 1.15.

A narrow band observing program would need observation of reference known VL-G UCDs and field UCDs in order to confirm the narrow band colour relationship predicted in Figure 1.15. This would have a significant impact on the time requirements for any such observing program.

The total observing time to obtain narrow band colours Hs-Hl and J-J3 for a candidate with $J \sim 18.5$ would be approximately thirty minutes, meaning that NIR spectroscopy from the FIRE instrument would have approximately the same required observation time. While FourSTAR can observe to fainter magnitudes than FIRE, the observing times needed to achieve the required signal to noise ratio to enable differentiation between field and VL-G candidates on the colour-colour diagram renders this approach impractical.

The only benefit of FourSTAR over FIRE is that multiple candidates could be observed in the 10 arcminute square field of view in any one observation. As such, an observing program over the course of a few nights could cover up to a fraction of a square degree. In theory, a very tight and distant co-moving group could be surveyed in this way and multiple VL-G dwarfs

identified. The group would need to be tighter and further away than any currently known co-moving group. While *Gaia* has the potential to identify many new co-moving groups (Oh et al., 2017), the distance the group would need to be at in order to be contained within a fraction of a degree would place it beyond the limit where a reasonable number of UCDs may be observed due to their low absolute magnitude.

The NIR spectrograph FIRE would provide a better test of a candidate UCD's age than narrow band photometry. The only circumstance where narrow band observation might be considered is when FIRE is unavailable. Only candidates with likely CPM relationships should be observed.

Due to the low rate of promising CPM relationships found when the proper motion of the candidate UCD is well defined, a better use of the observing time would have been to better constrain candidate PMs and either confirm or deny primary/companion CPM relationships.

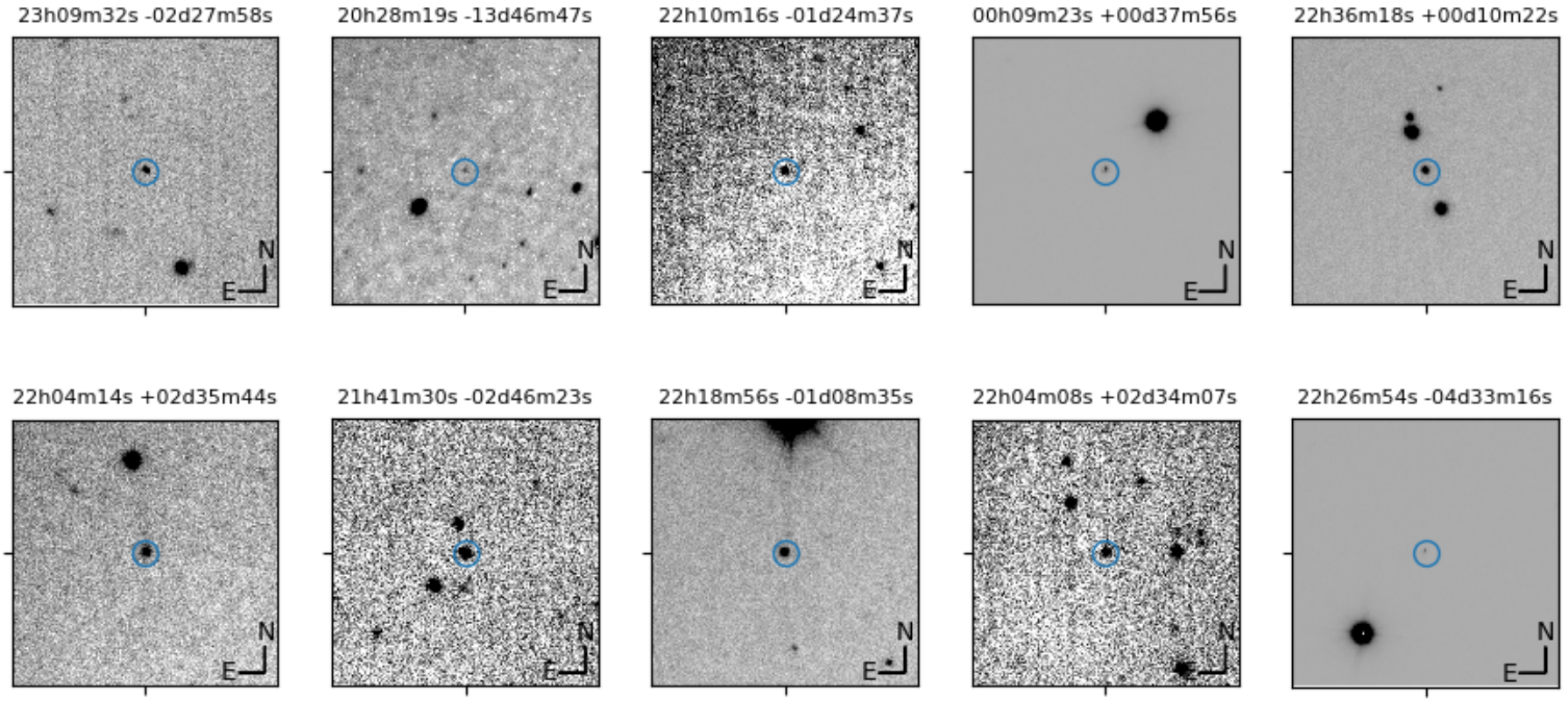

FIGURE 3.15: J band FourSTAR observation for each target. Target is centred and highlighted inside the circle. Each frame is 1 arcminute by 1 arcminute.

Chapter 4

Conclusion and Future Work

4.1 Conclusion

The selection method described in Chapter 2 is similar to other successful methods for selecting UCD candidates, with colour and magnitude requirements set by samples of known UCDs. Several studies have shown that UCDs can be effectively selected using photometry from NIR surveys (Cruz et al. 2007, Pinfield et al. 2008, Burningham et al. 2010, Schmidt et al. 2010, Kirkpatrick et al. 2010, Lucas et al. 2010, Day-Jones et al. 2013, Burningham et al. 2013, Zhang et al. 2017). The full sample of candidate benchmarks within this work numbers 1,623 candidates. The selection is likely to have identified multiple young UCDs amongst the sample of candidates. The Dupuy sample has 96 UCDs with parallaxes with indications of youth of low surface gravity. The samples within this work have the potential to substantially increase the quantity of known young UCDs with parallaxes. It is not possible within this work to determine the rate of false positives due to the low number of candidates observed and the lack of NIR spectra obtained. Further observations are required to estimate the false positive rate.

Two UCD candidates observed with promising CPM relationships to TGAS primaries have Hs-Hl and J-J3 colours consistent with being a VL-G UCD based on simulated narrow band colours. Target J2141-0246 is a candidate UCD with extremely red J-K and a promising CPM relationship to a TGAS primary. The narrow band observations support the conclusion that this object is a VL-G UCD. This target requires followup observation with a NIR spectrograph.

TGAS represents a marked increase on the number of candidate primaries with accurate distances available for benchmark work compared to previous parallax surveys. *Gaia* DR2 (scheduled 25th April 2018) will increase the number of primary candidates. With fifty promising CPM candidate young UCD benchmark systems identified from TGAS in this work, it is likely the same method applied to *Gaia* DR2 data will identify many times more candidates for study. This satisfies the main objective of this work.

4.2 Future Work

4.2.1 NIR Spectroscopic Observation of Candidate UCD Benchmarks

A number of young UCD candidates have been identified through this work. The highest priority targets of this work, including candidates with promising CPM relationships between very red candidate UCDs and very young primary candidates, should be singled out for NIR spectroscopic observations as potential young UCD benchmark systems. Appendix A shows a list of the highest priority targets.

It has been shown that a broad range of photometry and astrometry, combined with available spectroscopy and database information has been successfully used not only to identify a large sample of banchmarks, but also to establish a wide range of prioritisation levels that facilitate the identification of the most compelling systems, the fast-track followup of rapidly confirmable candidates and the larger "high volume samples" in which extremely young benchmarks should be forthcoming via optimised followup and statistical assessment of false alarm rate.

An ESO P101 proposal for the use of Xshooter submitted by supervisor Federico Marocco has been granted with priority C and scheduled as a filler program. Target list of candidates and finder charts have been provided. If any targets are observed, these spectra will be analysed to confirm spectral type, allowing distance estimates to be made, confirming if the candidates are at the same distance as the primary. This gives further evidence that the candidates are companions. The spectra will be analysed to look for signs of youth in the gravity dependent absorption indices.

4.2.2 Photometric Observations of potential Fast Moving CPM Pairs

348 candidates were selected where the proper motion of the companion is not well defined. With additional high signal to noise imaging, combined with observations at earlier epochs, long baseline proper motions can be calculated for fast moving pairs. In this way, CPM criteria can confirm or refute the association of the pair.

While earlier selections indicate only 4.5% of possible pairs are confirmed as promising CPM pairs, this low rate can be increased by only considering candidate pairs where both the primary and the companion have indications of youth, thus providing additional evidence that the candidates may be related prior to any observation. Only potential companions to fast moving primaries should be considered to ensure that any proper motion of the candidate UCD can provide meaningful constraints on the association of the pair.

Slow moving objects are more common and more prone to false positives. Figure 4.1 shows the simulated population from Marocco et al. (2017) and the required observation confirmations needed to confirm companionship between primary and companion to a false alarm probability of < 0.0001. The figure shows the boundary at $\mu \sim 20$mas yr^{-1} where objects below this proper motion value will also require radial velocity (RV) confirmation between the primary and candidate companion to demonstrate a relationship. Even with RV confirmation, the size difference of the samples above and below $\mu \sim 20$mas yr^{-1} shown in Figure 4.1 shows that the precision requirements and the magnitude required for RV measurements limit the number of candidates to be found in this sample. With such a large sample available at higher proper motion it is clear this should be the priority over slow moving candidates.

While this motion limit will vary depending on the number of observed epochs of the target, the time between the earliest epoch and the date of observation and magnitude limit of the instrument being used, a cutoff of $\mu > 50$mas yr^1 for primary proper motion results in 348 candidate UCDs to observe and measure proper motion which is sufficient at present.

An ESO P101 proposal for the use of SofI instrument submitted by supervisor Federico Marocco has been granted. Observing dates granted are the 18$^{\text{th}}$, 19$^{\text{th}}$ and 20$^{\text{th}}$ of July 2018. While the time has been granted based on the potential companions to fast moving TGAS objects, the timing of these granted observation dates after *Gaia* DR2 means higher priority targets may be identified as potential companions to fast moving primaries from the *Gaia* DR2 release. The target list used will be adjusted to ensure the maximum benefit from this observing run.

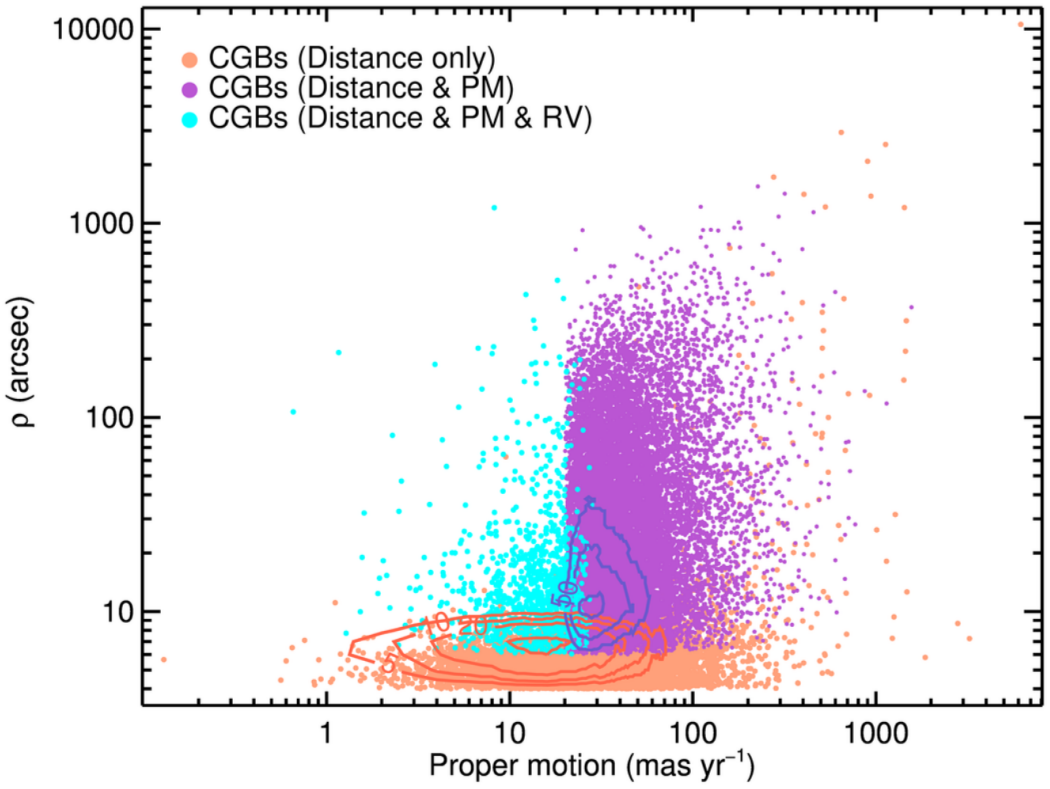

FIGURE 4.1: Simulated sampled of UCDs from Marocco et al. (2017) and the required observation confirmations needed to confirm companionship between primary and companion to a false alarm probability of < 0.0001.

4.3 Further Future Work

In addition to the future work detailed in Sections 4.2.1 and 4.2.2 which revolve around granted observation proposals for 2018, further additional work is available. The second data release for *Gaia* is scheduled for release on 25$^{\text{th}}$ of April 2018 and have astrometric measurements for $> 10^9$ objects (Gaia Collaboration et al., 2016b). This will provide a huge increase in the sample of potential primaries and allow for the identification of highest priority UCD candidates matched to *Gaia* DR2 primaries. This will influence the selection for our observation run on SofI in July 2018.

Gaia will reveal a large number of extra stars, but the detection of UCD candidates will still be limited due to the photometry limit of the optical and NIR catalogues used in this work. As a result, the maximum distance used in this work will still apply. Primaries from TGAS favour brighter stars within the 500pc distance limit due to the combination of the older *Tycho-2* and

Hipparcos catalogues. *Gaia* DR2 will increase the number of fainter primaries to match UCD candidates.

Additional all sky surveys will be released, including the Australian SkyMapper Southern Sky Survey (Wolf et al., 2018) which has surveyed the whole southern hemisphere to magnitude 18 in bands *griz*. It is currently only available to Australian astronomers but its release to the wider community will enable visual cross-matches to the southern hemisphere NIR VHS candidates.

There are further proper motion sources available for candidates that can be incorporated in to this selection process, such as the VISTA Variables in the Via Lactea survey (VVV, Smith et al. 2018), a NIR proper motion and parallax catalogue and the upcoming CatWISE catalogue to combine multi-epoch NIR observations from WISE to obtain parallaxes and proper motions, the need for which is laid out by Kirkpatrick et al. (2014). These catalogues will enable further candidates to be identified as potential CPM companions to *Gaia* primaries.

Appendix A

High Priority Targets for NIR Spectroscopy

This section contains full details of target lists identified in this work for further NIR spectroscopic observations.

Table A.2 is the list of promising CPM candidates. This table shows the colours and magnitudes of the companion candidates, spectral typing information and observing priority.

Table A.3 contains the same candidate list as Table A.2. The table contains the best defined proper motion value used as well as primary properties.

Table A.4 contains UCD candidates companions that can be confirmed on common distance alone. The candidates are all within 6 arcseconds of their primary or the primary is at < 30 pc.

Table A.5 contains UCD candidate companions to low proper motion primaries ($\mu < 50$mas yr^{-1}) with a priority of 'A' or 'B' from Section 2.13.

Table A.6 contains additional candidates that are likely CPM pairs to primaries with metal outlier characteristics ([Fe/H] or [M/H] > 0.2 or < -0.3) not in the sample of potentially young candidates.

The key for reading the Proper Motion source from Table A.3 and Table A.6 is given in Table A.1.

TABLE A.1: Proper Motion Source Key

Source	Description	Citation or Section
2P	2 point proper motion calculation	Section 2.7.2
3P	3 point proper motion calculation	Section 2.7.3
SC	Proper motion value from SuperCOMOS science archive	Section 2.7.4
3PSC	3 point proper motion calculation using SSA epoch	Sections 2.7.4 and 2.7.3
Smith	Multi-epoch proper motion calculation	Smith et al. 2014
UKIDSS	Proper motion value from UKIDSS LAS table	

TABLE A.2: Young Candidate Companions with a Promising CPM Relationship - Candidate Companion Information

Name	RA (J2000)	Dec. (J2000)	M_J	$J-K$	SpT(M_J)	SpT(Opt)	SpT(izJ)	SpT(NIR)	SpT Diagnosis	Priority
VHS J1626-0522	16h 26m 41.09s	-05d 22m 38.95s	9.46 ± 0.11	0.90 ± 0.03	M6	M9	M7	M6	-	A
VHS J2118-0224	21h 18m 15.28s	-02d 24m 44.45s	8.90 ± 0.34	0.74 ± 0.03	M5	M9	M7	M5	-	D
UKIDSS J1621+2225	16h 21m 19.52s	+22d 25m 20.00s	10.41 ± 0.43	1.45 ± 0.11	M7		L7	L3	Potential genuine young companion	D
VHS J2141-0246	21h 41m 29.83s	-02d 46m 23.05s	12.62 ± 0.11	1.70 ± 0.05	L3	L2	L7	L6	Potential genuine young companion	D
VHS J1759-1411	17h 59m 35.85s	-14d 11m 17.38s	9.54 ± 0.07	1.03 ± 0.03	M6		M9	M8	Potential genuine young companion	D
UKIDSS J0902+0210	09h 02m 01.16s	+02d 10m 22.23s	9.33 ± 0.25	0.88 ± 0.01	M6	L2	M8	M6	-	D
VHS J0909+0054	09h 09m 30.25s	+00d 54m 56.43s	8.92 ± 0.36	0.83 ± 0.03	M5	M9	M7	M5	-	D
UKIDSS J0916+0132	09h 16m 45.85s	+01d 32m 12.65s	9.23 ± 0.40	0.83 ± 0.01	M5	L0	M5	M5	Potential genuine young companion	D
UKIDSS J2308+0050	23h 08m 10.67s	+00d 50m 00.39s	9.04 ± 0.43	0.96 ± 0.04	M5	L1	M8	M6	-	D
UKIDSS J1158-0127	11h 58m 45.35s	-01d 27m 30.55s	9.44 ± 0.16	0.90 ± 0.00	M6	L1	M8	M6	-	D
UKIDSS J0852+2832	08h 52m 06.44s	+28d 32m 55.66s	9.29 ± 0.17	0.89 ± 0.00	M6		M9	M6	-	D
UKIDSS J0852+2637	08h 52m 27.07s	+26d 37m 57.91s	9.10 ± 0.34	0.90 ± 0.01	M5			M6	Potential genuine young companion but no Optic...	D
VHS J1828+0007	18h 28m 23.42s	+00d 07m 40.55s	11.01 ± 0.06	1.83 ± 0.04	M8	L5	L7	L7	Potential genuine young companion	E
UKIDSS J1453+0742	14h 53m 52.76s	+07d 42m 41.65s	8.88 ± 0.31	0.79 ± 0.04	M5	L8	M7	M5	-	E
UKIDSS J1303+1027	13h 03m 00.76s	+10d 27m 34.62s	9.34 ± 0.09	0.87 ± 0.00	M6	L0	M7	M6	-	E
UKIDSS J0925+0416	09h 25m 21.87s	+04d 16m 30.41s	8.93 ± 0.17	0.87 ± 0.01	M5		M7	M6	Potential foreground L dwarf	E
VHS J2157+0036	21h 57m 04.92s	+00d 36m 34.09s	9.79 ± 0.18	0.99 ± 0.06	M6		M6	M7	Potential genuine young companion	E
VHS J1831-0125	18h 31m 38.47s	-01d 25m 34.52s	10.21 ± 0.14	1.50 ± 0.06	M6	L1	L7	L3	Potential genuine young companion	E
VHS J0513+0051	05h 13m 35.06s	+00d 51m 08.63s	9.14 ± 0.10	0.80 ± 0.02	M5	L1	M7	M5	-	E
UKIDSS J1352+3353	13h 52m 36.93s	+33d 53m 59.10s	9.12 ± 0.16	0.90 ± 0.01	M5	L0	L0	M6	-	E
VHS J1641-0642	16h 41m 51.59s	-06d 42m 09.83s	9.48 ± 0.11	0.92 ± 0.03	M6	L1	M8	M6	-	E
UKIDSS J1122+0323	11h 22m 21.31s	+03d 23m 24.71s	9.12 ± 0.21	0.94 ± 0.01	M5	M9	M7	M6	-	E
UKIDSS J1607+2929	16h 07m 25.28s	+29d 29m 50.45s	11.25 ± 0.15	1.53 ± 0.09	M9	L8	M7	L4	Potential genuine young companion	E
UKIDSS J0850+2733	08h 50m 48.58s	+27d 33m 16.88s	9.09 ± 0.25	0.88 ± 0.01	M5	L1	M8	M6	-	E
UKIDSS J0858+0421	08h 58m 39.45s	+04d 21m 17.71s	9.46 ± 0.58	0.90 ± 0.04	M6	L0	M7	M6	-	E
UKIDSS J0818+0717	08h 18m 02.93s	+07d 17m 06.67s	8.85 ± 0.10	0.85 ± 0.00	M5	L0	M7	M6	-	E
UKIDSS J1052+1008	10h 52m 36.99s	+10d 08m 54.37s	9.20 ± 0.15	0.93 ± 0.02	M5	M9	M7	M6	-	E
UKIDSS J0855-0200	08h 55m 42.15s	-02d 00m 30.19s	8.85 ± 0.06	0.82 ± 0.00	M5	M9	M7	M5	-	E
VHS J1831+0026	18h 31m 12.62s	+00d 26m 09.03s	10.05 ± 0.11	1.03 ± 0.05	M6		L7	M8	Potential genuine young companion	E
UKIDSS J0019+1532	00h 19m 21.99s	+15d 32m 08.16s	9.29 ± 0.46	0.95 ± 0.03	M6	L0	M7	M6	-	E
UKIDSS J2218-0108	22h 18m 55.61s	-01d 08m 34.82s	9.91 ± 0.16	1.01 ± 0.02	M6	L8	L0	M7	-	E
UKIDSS J1357-0117	13h 57m 58.38s	-01d 17m 00.27s	8.98 ± 0.24	0.85 ± 0.01	M5	L0	M7	M6	-	E
VHS J2142+0105	21h 42m 02.13s	+01d 05m 33.13s	9.97 ± 0.13	0.82 ± 0.03	M6	M9	M7	M5	-	G
VHS J2138-0812	21h 38m 34.00s	-08d 12m 15.76s	9.52 ± 0.13	0.83 ± 0.03	M6	L1	M7	M5	-	G
VHS J2222-0201	22h 22m 53.98s	-02d 01m 24.82s	13.95 ± 0.11	0.90 ± 0.13					-	G
VHS J1603-0439	16h 03m 12.12s	-04d 39m 59.38s	10.05 ± 0.18	0.71 ± 0.06	M6		M5	M5	Potential genuine young companion	G
VHS J1427-1823	14h 27m 17.97s	-18d 23m 46.97s	15.23 ± 0.09	0.85 ± 0.26					-	G
VHS J1528-0518	15h 28m 28.10s	-05d 18m 05.09s	10.76 ± 0.12	0.94 ± 0.09	M7	L0	M9	M6	-	G
UKIDSS J0940+3110	09h 40m 56.15s	+31d 10m 30.34s	10.44 ± 0.11	0.92 ± 0.01	M7	L5	M8	M6	-	G
VHS J1653-0106	16h 53m 34.36s	-01d 06m 01.49s	11.07 ± 0.04	0.86 ± 0.03	M8	M9	M7	M6	-	G
UKIDSS J1315+1126	13h 15m 21.18s	+11d 26m 18.85s	11.81 ± 0.09	1.43 ± 0.01	L1		L7	L3	Potential genuine young companion	G
UKIDSS J1205+1119	12h 05m 01.40s	+11d 19m 56.87s	10.83 ± 0.06	0.88 ± 0.01	M7		L7	M6	-	G
UKIDSS J1538+0921	15h 38m 23.45s	+09d 21m 04.65s	10.03 ± 0.09	0.93 ± 0.01	M6	L3	M8	M6	-	G
UKIDSS J1551+2638	15h 51m 14.24s	+26d 38m 34.67s	10.13 ± 0.10	0.95 ± 0.02	M6	L8	L1	M6	-	G
UKIDSS J0800+2149	08h 00m 54.55s	+21d 49m 53.71s	10.31 ± 0.12	0.89 ± 0.02	M6	L0	M7	M6	-	G
UKIDSS J1511+1037	15h 11m 29.61s	+10d 37m 47.28s	10.23 ± 0.11	0.82 ± 0.02	M6	M9	M7	M5	-	G
VHS J1521-0650	15h 21m 36.62s	-06d 50m 50.80s	14.04 ± 0.07	0.75 ± 0.15					-	H
UKIDSS J1444+0847	14h 44m 24.86s	+08d 47m 45.15s	10.51 ± 0.11	0.70 ± 0.03	M7	M9	M7	M5	-	H
VHS J2310+0040	23h 10m 08.47s	+00d 40m 26.62s	13.59 ± 0.12	1.48 ± 0.13	L5		M5	L3	Potential genuine young companion	H
UKIDSS J0936+0006	09h 36m 24.68s	+00d 06m 19.47s	10.00 ± 0.16	0.95 ± 0.01	M6	L1	M7	M6	-	H

TABLE A.3: Young Candidate Companions with a Promising CPM Relationship - Primary and CPM Information

Name	Primary Candidate	Parallax mas	Primary $\mu_\alpha \cos\delta$ mas yr^{-1}	Primary μ_δ mas yr^{-1}	Companion $\mu_\alpha \cos\delta$ mas yr^{-1}	Companion μ_δ mas yr^{-1}	CPM Source	$\sigma\Delta\mu$	$\mu \setminus \sigma\mu$	Primary Metallicity	Metallicity Source
VHS J1626-0522	TYC 5043-770-1	5.17 ± 0.25	$+16 \pm 0.9$	-27 ± 0.6	$+14 \pm 15.0$	-25 ± 15.1	2P	0.2	2.0	[M/H] = -0.27	RAVE
VHS J2118-0224	TYC 5198-471-1	6.33 ± 0.99	-6 ± 3.1	-65 ± 2.3	-17 ± 8.1	-69 ± 8.3	2P	1.5	8.6	[M/H] = -0.43	RAVE
UKIDSS J1621+2225	TYC 1517-365-1	2.00 ± 0.39	-4 ± 1.8	$+13 \pm 1.9$	$+3 \pm 8.4$	$+21 \pm 8.4$	UKIDSS	1.3	2.6	[Fe/H] = -0.14	LAMOST
VHS J2141-0246	TYC 5213-545-1	12.69 ± 0.60	-74 ± 2.2	-109 ± 1.1	-88 ± 26.6	-122 ± 24.5	2P	0.7	5.7	[M/H] = +0.04	RAVE
VHS J1759-1411	TYC 5686-158-1	7.11 ± 0.22	-19 ± 1.0	-57 ± 0.9	-22 ± 18.7	-55 ± 31.7	2P	0.1	1.9	[Fe/H] = -0.25	Ammons et al. (2006)
UKIDSS J0902+0210	TYC 226-889-1	6.03 ± 0.70	-2 ± 2.6	-13 ± 1.3	-1 ± 2.7	-15 ± 2.7	UKIDSS	1.0	5.8	[Fe/H] = -0.02	LAMOST
VHS J0909+0054	TYC 4879-1093-1	3.87 ± 0.65	$+16 \pm 2.4$	-11 ± 1.2	$+32 \pm 13.1$	-15 ± 13.0	2P	1.3	2.7	[Fe/H] = -0.12	LAMOST
UKIDSS J0916+0132	TYC 227-1587-1	4.85 ± 0.90	-25 ± 2.9	$+2 \pm 2.1$	-19 ± 7.7	-3 ± 7.2	2P	1.1	2.6	[Fe/H] = +0.05	LAMOST
UKIDSS J2308+0050	TYC 576-1131-1	2.60 ± 0.52	$+23 \pm 1.9$	$+1 \pm 0.7$	$+33 \pm 9.2$	-3 ± 9.2	UKIDSS	1.2	3.7	[Fe/H] = +0.07	LAMOST
UKIDSS J1158-0127	TYC 4932-376-1	13.11 ± 0.97	$+56 \pm 3.2$	-63 ± 1.3	$+57 \pm 8.2$	-59 ± 7.3	Smith; SC	0.5	10.1	[Fe/H] = -0.02	LAMOST
UKIDSS J0852+2832	TYC 1949-292-1	8.98 ± 0.70	$+22 \pm 2.4$	$+14 \pm 1.4$	$+22 \pm 5.5$	$+21 \pm 5.5$	2P; UKIDSS	1.2	5.7	[Fe/H] = -0.11	LAMOST
UKIDSS J0852+2637	TYC 1946-516-1	4.45 ± 0.70	-8 ± 2.3	-19 ± 1.3	-4 ± 5.5	-13 ± 5.5	UKIDSS	1.2	2.6	[Fe/H] = -0.21	LAMOST
VHS J1828+0007	TYC 5099-310-1	8.08 ± 0.23	-17 ± 1.8	-37 ± 1.5	-37 ± 18.3	-46 ± 20.3	2P	1.1	3.0	[Fe/H] = +0.02	Ammons et al. (2006)
UKIDSS J1453+0742	TYC 918-1274-1	2.11 ± 0.30	$+27 \pm 5.7$	-27 ± 3.5	$+28 \pm 5.5$	-32 ± 5.6	Smith	0.9	7.8	[Fe/H] = +0.32	LAMOST
UKIDSS J1303+1027	TYC 886-1284-1	16.41 ± 0.68	-141 ± 1.1	-71 ± 0.8	-147 ± 5.5	-74 ± 6.6	Smith	1.0	25.0		
UKIDSS J0925+0416	TYC 231-63-1	4.02 ± 0.32	-13 ± 0.4	-4 ± 0.5	-38 ± 9.4	$+0 \pm 9.7$	UKIDSS	1.4	3.8		
VHS J2157+0036	TYC 545-321-1	3.19 ± 0.27	$+55 \pm 0.9$	-10 ± 0.6	$+108 \pm 29.2$	-30 ± 34.9	2P	1.6	3.2		
VHS J1831-0125	TYC 5112-137-1	3.90 ± 0.24	$+26 \pm 2.0$	-23 ± 1.9	$+56 \pm 24.7$	-46 ± 25.2	2P	1.5	2.9		
VHS J0513+0051	TYC 4751-467-1	6.87 ± 0.33	$+9 \pm 0.8$	-11 ± 0.7	$+13 \pm 6.3$	-5 ± 6.2	3PSC	1.1	2.4		
UKIDSS J1352+3353	TYC 2547-289-1	7.03 ± 0.50	-24 ± 0.8	-27 ± 0.9	-30 ± 8.6	-20 ± 8.4	SC	1.1	4.2		
VHS J1641-0642	TYC 5061-973-1	6.70 ± 0.33	-24 ± 0.6	$+5 \pm 1.0$	-28 ± 13.5	-10 ± 13.6	2P	1.2	2.2		
UKIDSS J1122+0323	TYC 267-688-1	5.73 ± 0.56	-64 ± 1.8	-15 ± 0.8	-59 ± 6.3	-3 ± 6.3	2P	1.5	4.2	[Fe/H] = +0.11	LAMOST
UKIDSS J1607+2929	TYC 2041-447-1	3.57 ± 0.23	-7 ± 0.7	-16 ± 0.8	-6 ± 12.0	-19 ± 12.0	UKIDSS	0.3	1.7	[Fe/H] = +0.18	Ammons et al. (2006)
UKIDSS J0850+2733	TYC 1949-1035-1	4.39 ± 0.50	$+8 \pm 1.4$	-29 ± 0.9	$+10 \pm 0.6$	-30 ± 0.5	3PSC; UKIDSS; SC	1.5	57.6	[Fe/H] = +0.13	LAMOST
UKIDSS J0858+0421	TYC 221-92-1	3.02 ± 0.80	-13 ± 2.9	-4 ± 1.6	-10 ± 5.5	-5 ± 5.5	UKIDSS	0.6	2.1	[Fe/H] = +1.22	Ammons et al. (2006)
UKIDSS J0818+0717	TYC 208-345-1	8.76 ± 0.41	-34 ± 0.7	-32 ± 0.5	-37 ± 4.4	-31 ± 4.3	Smith	0.7	11.1	[Fe/H] = +0.24	LAMOST
UKIDSS J1052+1008	TYC 849-1318-1	3.69 ± 0.25	-40 ± 0.2	$+0 \pm 0.1$	-76 ± 16.5	$+15 \pm 17.2$	UKIDSS	0.6	2.0		
UKIDSS J0855-0200	TYC 4869-1326-1	9.43 ± 0.27	-38 ± 0.7	-11 ± 0.7	-38 ± 4.1	-19 ± 4.5	Smith	1.8	9.5	[Fe/H] = +0.22	Ammons et al. (2006)
VHS J1831+0026	TYC 5112-232-1	4.91 ± 0.25	-35 ± 0.6	-18 ± 0.6	-54 ± 32.0	-34 ± 32.0	2P	0.8	2.0		
UKIDSS J0019+1532	TYC 1179-1318-1	3.18 ± 0.67	$+37 \pm 3.0$	$+20 \pm 1.0$	$+36 \pm 4.2$	$+24 \pm 4.2$	UKIDSS	1.0	10.5		
UKIDSS J2218-0108	TYC 5225-719-1	5.84 ± 0.44	$+43 \pm 1.7$	-55 ± 0.7	$+43 \pm 3.4$	-49 ± 3.4	UKIDSS	1.8	19.6	[Fe/H] = +0.92	Ammons et al. (2006)
UKIDSS J1357-0117	TYC 4968-339-1	4.32 ± 0.49	-63 ± 5.3	$+1 \pm 1.5$	-68 ± 9.2	$+11 \pm 8.7$	Smith	1.1	7.5		
VHS J2142+0105	TYC 543-4-1	7.12 ± 0.42	$+52 \pm 1.5$	$+15 \pm 0.8$	$+34 \pm 10.3$	$+22 \pm 9.7$	2P	1.9	4.0	[M/H] = -0.47	RAVE
VHS J2138-0812	TYC 5787-985-1	6.08 ± 0.37	$+16 \pm 1.3$	-11 ± 0.7	$+32 \pm 13.5$	-2 ± 13.4	2P	1.3	2.4	[M/H] = +0.06	RAVE
VHS J2222-0201	TYC 5226-219-1	13.65 ± 0.65	$+3 \pm 1.2$	-58 ± 1.5	$+24 \pm 39.3$	-62 ± 38.8	2P	0.5	1.7	[M/H] = -0.09	RAVE
VHS J1603-0439	TYC 5040-269-1	4.61 ± 0.39	$+6 \pm 1.1$	-41 ± 0.8	-11 ± 27.2	-102 ± 34.8	2P	1.8	3.0	[M/H] = -0.49	RAVE
VHS J1427-1823	TYC 6156-21-1	18.04 ± 0.25	-72 ± 0.1	-313 ± 0.1	-258 ± 111.9	-427 ± 117.9	2P	1.8	4.2	[M/H] = -1.25	RAVE
VHS J1528-0518	TYC 5011-753-1	4.20 ± 0.22	$+21 \pm 0.7$	-36 ± 0.5	$+48 \pm 39.9$	-67 ± 38.1	2P	1.0	2.1	[M/H] = -0.14	RAVE
UKIDSS J0940+3110	TYC 2501-1218-1	7.29 ± 0.38	$+36 \pm 1.3$	$+0 \pm 0.8$	$+38 \pm 4.6$	$+8 \pm 4.6$	UKIDSS	1.9	8.6	[Fe/H] = -0.18	LAMOST
VHS J1653-0106	TYC 5051-104-1	14.84 ± 0.30	-46 ± 0.1	-22 ± 0.0	-51 ± 13.4	-4 ± 12.9	2P	1.4	3.9	[M/H] = -0.06	RAVE
UKIDSS J1315+1126	TYC 887-667-1	12.53 ± 0.50	-51 ± 1.8	-41 ± 0.8	-48 ± 9.4	-44 ± 7.5	Smith	0.4	7.0	[Fe/H] = -0.03	LAMOST
UKIDSS J1205+1119	TYC 868-1157-1	10.52 ± 0.31	$+107 \pm 0.1$	-92 ± 0.0	$+122 \pm 6.3$	-86 ± 6.3	Smith	0.6	13.0	[Fe/H] = -0.68	LAMOST
UKIDSS J1538+0921	TYC 929-156-1	6.73 ± 0.27	-69 ± 1.4	$+0 \pm 0.8$	-72 ± 6.8	$+1 \pm 6.0$	Smith	0.6	10.6	[Fe/H] = -0.14	LAMOST
UKIDSS J1551+2638	TYC 2037-326-1	4.91 ± 0.23	$+10 \pm 0.6$	-34 ± 0.7	$+7 \pm 4.1$	-32 ± 4.1	UKIDSS	1.0	8.1	[Fe/H] = +0.07	LAMOST
UKIDSS J0800+2149	TYC 1388-126-1	4.99 ± 0.27	-3 ± 0.9	-11 ± 0.6	-2 ± 6.7	-23 ± 6.7	UKIDSS	1.8	3.5	[Fe/H] = +0.08	LAMOST
UKIDSS J1511+1037	TYC 923-1143-1	5.34 ± 0.27	$+56 \pm 1.4$	-112 ± 0.9	$+58 \pm 110.5$	-111 ± 109.3	SC	0.0	1.1	[Fe/H] = -0.63	LAMOST
VHS J1521-0650	TYC 5014-770-1	15.00 ± 0.28	-168 ± 0.1	-28 ± 0.0	-103 ± 39.5	-68 ± 39.8	2P	1.9	3.1	[M/H] = +0.12	RAVE
UKIDSS J1444+0847	TYC 911-222-1	4.86 ± 0.25	-30 ± 2.4	$+7 \pm 1.0$	-28 ± 13.6	$+6 \pm 13.9$	SC	0.1	2.1	[Fe/H] = +0.14	LAMOST
VHS J2310+0040	TYC 577-386-1	8.53 ± 0.40	$+121 \pm 1.4$	-88 ± 0.6	$+77 \pm 60.2$	-83 ± 60.2	2P	0.7	1.9	[M/H] = +0.25	RAVE
UKIDSS J0936+0006	TYC 4894-1594-1	5.87 ± 0.43	$+21 \pm 1.6$	-40 ± 0.8	$+15 \pm 5.5$	-38 ± 5.7	Smith	1.1	7.2	[M/H] = +0.38	RAVE

TABLE A.4: Common Distance Candidates

Name	RA (J2000)	Dec. (J2000)	Primary Candidate	Separation (arcsec)	Distance (pc)	e(B-V)	M_J	$J-K$	SpT(M_J)	SpT(Opt)	SpT(izJ)	SpT(NIR)	SpT Diagnosis
UKIDSS J1301+2348	13h 01m 25.77s	+23d 48m 34.58s	TYC 1993-2205-1	3.08	94.97 ± 7.73	0.018	11.30 ± 0.18	1.48 ± 0.01	M9			L3	Potential genuine young companion but no Optic...
VHS J1130-0510	11h 30m 58.42s	-05d 10m 19.41s	TYC 4936-96-1	5.45	219.01 ± 30.88	0.048	8.88 ± 0.31	0.74 ± 0.03	M5		L2	M5	-
UKIDSS J0107+0203	01h 07m 37.05s	+02d 03m 20.94s	TYC 19-649-1	5.92	271.74 ± 30.53	0.021	10.48 ± 0.25	1.38 ± 0.05	M7			L2	Potential genuine young companion but no Optic...
UKIDSS J1103+0201	11h 03m 50.39s	+02d 01m 12.37s	TYC 262-89-1	4.70	333.64 ± 91.38	0.036	10.00 ± 0.60	1.29 ± 0.05	M6			L1	Potential genuine young companion but no Optic...
VHS J0804-0424	08h 04m 36.66s	-04d 24m 40.61s	TYC 4854-2344-1	5.34	368.70 ± 83.44	0.033	8.72 ± 0.49	0.72 ± 0.05	M5			M5	-
UKIDSS J0908+0025	09h 08m 41.97s	+00d 25m 44.81s	TYC 226-758-1	4.26	214.42 ± 28.45	0.032	8.79 ± 0.29	0.76 ± 0.01	M5		M7	M5	-
UKIDSS J2323+0255	23h 23m 37.85s	+02d 55m 57.68s	TYC 581-756-1	5.72	273.34 ± 34.45	0.047	9.92 ± 0.27	1.02 ± 0.03	M6			M7	Potential genuine young companion but no Optic...
UKIDSS J1146+1148	11h 46m 47.58s	+11d 48m 06.93s	TYC 867-737-1	5.90	247.84 ± 37.51	0.025	9.01 ± 0.33	0.82 ± 0.02	M5	M9	M6	M5	-
UKIDSS J1305+3557	13h 05m 27.30s	+35d 57m 11.74s	TYC 2534-1430-1	4.80	446.32 ± 65.21	0.013	8.78 ± 0.32	0.75 ± 0.05	M5			M5	-
UKIDSS J1341+1410	13h 41m 49.50s	+14d 10m 03.58s	TYC 899-267-1	5.81	380.04 ± 40.01	0.020	10.88 ± 0.24	1.67 ± 0.08	M7			L5	Potential genuine young companion but no Optic...
UKIDSS J1201+1208	12h 01m 16.10s	+12d 08m 09.41s	TYC 868-456-1	4.63	344.68 ± 68.67	0.025	9.68 ± 0.43	1.21 ± 0.04	M6			L0	Potential genuine young companion but no Optic...
UKIDSS J1521+0808	15h 21m 15.67s	+08d 08m 04.05s	TYC 927-659-1	5.93	307.63 ± 22.52	0.027	8.93 ± 0.16	0.79 ± 0.02	M5	L8	M6	M5	-
UKIDSS J0821+2419	08h 21m 53.52s	+24d 19m 07.87s	TYC 1928-822-1	5.62	263.65 ± 27.20	0.026	10.89 ± 0.23	1.25 ± 0.07	M8			L1	Potential genuine young companion but no Optic...
UKIDSS J2318+0704	23h 18m 14.38s	+07d 04m 30.69s	TYC 583-554-1	5.42	415.57 ± 123.14	0.097	10.59 ± 0.65	1.63 ± 0.12	M7			L5	Potential genuine young companion but no Optic...
UKIDSS J1511-0108	15h 11m 34.46s	-01d 08m 48.04s	TYC 5001-358-1	4.61	314.24 ± 27.86	0.064	9.97 ± 0.20	1.39 ± 0.05	M6			L2	Potential genuine young companion but no Optic...
UKIDSS J0128+0537	01h 28m 08.55s	+05d 37m 03.79s	TYC 27-1086-1	5.84	260.68 ± 32.61	0.022	10.64 ± 0.27	1.29 ± 0.05	M7			L1	Potential genuine young companion but no Optic...
UKIDSS J1217+0223	12h 17m 59.22s	+02d 23m 44.71s	TYC 281-42-1	5.91	307.83 ± 39.99	0.017	9.91 ± 0.28	1.18 ± 0.05	M6			L0	Potential genuine young companion but no Optic...
UKIDSS J1307+2356	13h 07m 03.00s	+23d 56m 57.41s	TYC 1994-1632-1	4.85	294.52 ± 27.36	0.013	11.38 ± 0.22	1.63 ± 0.10	M9			L5	Potential genuine young companion but no Optic...
UKIDSS J1352+2411	13h 52m 56.37s	+24d 11m 41.23s	TYC 1999-309-1	5.11	482.56 ± 72.58	0.012	9.53 ± 0.33	1.36 ± 0.06	M6			L2	Potential genuine young companion but no Optic...
UKIDSS J2342+1100	23h 42m 24.00s	+11d 00m 45.01s	TYC 1173-1046-1	5.47	420.69 ± 75.39	0.045	9.70 ± 0.39	1.15 ± 0.06	M6			L0	Potential genuine young companion but no Optic...
UKIDSS J0213-0110	02h 13m 11.77s	-01d 10m 18.81s	TYC 4690-470-1	5.00	137.40 ± 5.19	0.021	11.92 ± 0.09	1.60 ± 0.05	L1			L4	Potential genuine young companion but no Optic...
UKIDSS J1518+3044	15h 18m 40.51s	+30d 44m 33.75s	TYC 2563-1121-1	4.97	355.13 ± 28.83	0.016	10.09 ± 0.18	1.09 ± 0.06	M6			M9	Potential genuine young companion but no Optic...
VHS J1219-1455	12h 19m 40.96s	-14d 55m 04.06s	TYC 5532-794-1	5.82	334.35 ± 74.79	0.044	8.91 ± 0.49	0.85 ± 0.05	M5		M5	M6	Potential genuine young companion
UKIDSS J1329+2851	13h 29m 58.70s	+28d 51m 31.99s	TYC 2003-196-1	4.53	215.31 ± 12.45	0.009	11.18 ± 0.13	1.42 ± 0.04	M8			L3	Potential genuine young companion but no Optic...
VHS J1656-1821	16h 56m 34.12s	-18d 21m 36.92s	TYC 6223-1652-1	4.78	375.06 ± 39.67	0.331	9.61 ± 0.23	1.30 ± 0.07	M6			L1	Potential genuine young companion but no Optic...
UKIDSS J0202+0424	02h 02m 42.23s	+04d 24m 51.10s	TYC 40-717-1	5.58	309.18 ± 29.30	0.055	9.30 ± 0.21	1.04 ± 0.03	M6		L7	M8	Potential genuine young companion
UKIDSS J2133-0106	21h 33m 11.88s	-01d 06m 40.19s	TYC 5208-453-1	3.57	201.52 ± 37.50	0.045	9.06 ± 0.40	0.90 ± 0.01	M5			M6	Potential genuine young companion but no Optic...
UKIDSS J2312+1127	23h 12m 29.06s	+11d 27m 47.81s	TYC 1164-226-1	5.63	378.58 ± 105.44	0.052	10.32 ± 0.61	1.41 ± 0.07	M7			L3	Potential genuine young companion but no Optic...
UKIDSS J0140+0359	01h 40m 44.29s	+03d 59m 00.90s	TYC 32-575-1	5.52	341.04 ± 34.10	0.027	8.97 ± 0.22	0.86 ± 0.03	M5		L3	M6	-
UKIDSS J2344+1138	23h 44m 02.53s	+11d 38m 17.88s	TYC 1173-1626-1	5.12	180.21 ± 21.91	0.054	8.98 ± 0.26	0.94 ± 0.01	M5	M9	M8	M6	-
UKIDSS J1316+1444	13h 16m 53.09s	+14d 44m 18.44s	TYC 897-1003-1	5.72	187.62 ± 10.21	0.019	9.12 ± 0.12	0.86 ± 0.01	M5			M6	Potential genuine young companion but no Optic...
UKIDSS J0032+0513	00h 32m 54.83s	+05d 13m 38.33s	TYC 16-815-1	4.70	207.25 ± 35.53	0.017	10.27 ± 0.37	1.25 ± 0.02	M6			L1	Potential genuine young companion but no Optic...
UKIDSS J2356+0427	23h 56m 49.32s	+04d 27m 14.19s	TYC 590-1017-1	4.28	306.13 ± 38.22	0.037	10.18 ± 0.27	1.06 ± 0.06	M6			M8	Potential genuine young companion but no Optic...
UKIDSS J1443+0929	14h 43m 20.48s	+09d 29m 26.60s	TYC 911-141-1	5.98	315.08 ± 38.28	0.027	10.34 ± 0.27	1.27 ± 0.04	M7			L1	Potential genuine young companion but no Optic...
UKIDSS J1349+2959	13h 49m 38.36s	+29d 59m 34.37s	TYC 2005-140-1	5.93	442.65 ± 50.60	0.014	9.81 ± 0.25	1.38 ± 0.07	M6			L2	Potential genuine young companion but no Optic...
UKIDSS J0234+0225	02h 34m 31.94s	+02d 25m 05.02s	TYC 46-151-1	5.49	386.41 ± 40.18	0.024	9.78 ± 0.23	1.62 ± 0.05	M6			L5	Potential genuine young companion but no Optic...
VHS J2018+0043	20h 18m 36.37s	+00d 43m 25.35s	TYC 5162-1149-1	275.31	23.65 ± 0.40	0.091	15.53 ± 0.05	0.80 ± 0.09					-
VHS J1607-1404	16h 07m 03.60s	-14d 04m 48.55s	TYC 5624-1433-1	32.84	27.76 ± 0.32	0.190	9.64 ± 0.02	0.72 ± 0.02	M6			M5	-

TABLE A.5: Low Proper Motion Primary Candidates

Name	RA (J2000)	Dec. (J2000)	Primary Candidate	Primary $\mu_\alpha \cos\delta$ mas yr^{-1}	Primary μ_δ mas yr^{-1}	M_J	$J-K$	SpT(M_J)	SpT(Opt)	SpT(izJ)	SpT(NIR)	Primary Metallicity
VHS J1423-1911	14h 23m 20.78s	-19d 11m 39.16s	TYC 6147-1464-1	-4 ± 0.8	-27 ± 0.3	11.10 ± 0.18	1.40 ± 0.08	M8	M9	M6	L2	
UKIDSS J0218+0422	02h 18m 26.85s	+04d 22m 56.69s	TYC 41-1014-1	-4 ± 1.9	-10 ± 0.8	11.61 ± 0.21	1.63 ± 0.12	L0		M8	L5	
VHS J0542+0043	05h 42m 09.83s	+00d 43m 04.62s	TYC 4767-1039-1	$+1\pm1.4$	-2 ± 1.3	11.25 ± 0.20	1.83 ± 0.13	M9	M9	L1	L7	
VHS J1057-1944	10h 57m 52.08s	-19d 44m 02.91s	TYC 6079-1744-1	$+12\pm1.0$	-5 ± 0.5	11.62 ± 0.20	1.53 ± 0.10	L0	L8	M8	L4	
UKIDSS J0259+0619	02h 59m 28.48s	+06d 19m 37.81s	TYC 54-859-1	$+0\pm0.2$	-32 ± 0.2	12.87 ± 0.10	2.04 ± 0.08	L4		L9	L7	
UKIDSS J0136+1309	01h 36m 24.34s	+13d 09m 43.15s	TYC 627-892-1	-6 ± 1.5	-29 ± 0.4	11.49 ± 0.19	1.76 ± 0.12	L0		M6	L7	LAMOST [Fe/H] = -0.35
UKIDSS J0020+0557	00h 20m 51.03s	+05d 57m 28.10s	TYC 9-770-1	$+43\pm0.9$	$+8\pm0.5$	11.90 ± 0.13	1.48 ± 0.06	L1	L0	M7	L3	
VHS J2031-1329	20h 31m 51.28s	-13d 29m 16.11s	TYC 5766-205-1	-27 ± 1.4	$+0\pm0.7$	10.61 ± 0.17	1.46 ± 0.05	M7		M8	L3	
VHS J2122-0102	21h 22m 45.88s	-01d 02m 49.27s	TYC 5195-1289-1	$+17\pm1.4$	$+12\pm0.9$	11.71 ± 0.16	1.58 ± 0.07	L1		M5	L4	RAVE [M/H] = -0.38
VHS J0436+0028	04h 36m 32.60s	+00d 28m 36.84s	TYC 4734-806-1	$+9\pm0.9$	-22 ± 0.8	11.00 ± 0.15	1.55 ± 0.10	M8	L4	L4	L4	
VHS J1705-0325	17h 05m 50.69s	-03d 25m 30.36s	TYC 5068-19-1	$+0\pm0.6$	-25 ± 0.5	11.45 ± 0.17	1.56 ± 0.15	L0		M6	L4	
VHS J0217-0610	02h 17m 55.32s	-06d 10m 38.47s	TYC 4696-821-1	-9 ± 1.5	-4 ± 0.8	11.97 ± 0.15	1.89 ± 0.10	L2	L2	M7	L7	
VHS J1303-1058	13h 03m 55.16s	-10d 58m 01.37s	TYC 5539-737-1	$+6\pm0.9$	-7 ± 1.2	10.12 ± 0.31	1.32 ± 0.09	M6		M7	L2	
VHS J1728-1601	17h 28m 56.12s	-16d 01m 33.83s	TYC 6235-2653-1	-2 ± 1.0	-3 ± 0.9	10.33 ± 0.30	1.12 ± 0.15	M7		M5	M9	
VHS J0201-0606	02h 01m 57.68s	-06d 06m 26.06s	TYC 4695-704-1	$+32\pm0.7$	$+0\pm0.5$	11.85 ± 0.15	1.51 ± 0.09	L1		M6	L3	
UKIDSS J1126+1558	11h 26m 58.35s	+15d 58m 09.43s	TYC 1437-11-1	-28 ± 0.9	$+11\pm0.6$	11.75 ± 0.15	1.55 ± 0.07	L1	L8	M8	L4	
VHS J0839-1530	08h 39m 49.28s	-15d 30m 16.76s	TYC 6011-751-1	$+1\pm1.1$	-4 ± 0.7	11.00 ± 0.23	1.55 ± 0.12	M8		M6	L4	
VHS J2112-0557	21h 12m 01.60s	-05d 57m 28.60s	TYC 5205-1282-1	$+13\pm0.1$	-19 ± 0.0	12.33 ± 0.18	1.83 ± 0.18	L3		M8	L7	
UKIDSS J0910+1035	09h 10m 28.46s	+10d 35m 10.83s	TYC 815-136-1	-4 ± 1.2	-24 ± 0.8	11.18 ± 0.15	1.34 ± 0.04	M8		M6	L2	
UKIDSS J1425+0844	14h 25m 12.59s	+08d 44m 01.38s	TYC 909-885-1	-24 ± 1.6	-3 ± 0.7	11.25 ± 0.15	1.54 ± 0.07	M9	M9	L5	L4	
UKIDSS J0210+0217	02h 10m 36.66s	+02d 17m 02.28s	TYC 38-542-1	-4 ± 0.9	-3 ± 0.6	11.19 ± 0.29	1.52 ± 0.13	M8	L1	M8	L4	
UKIDSS J1535+0731	15h 35m 20.42s	+07d 31m 05.00s	TYC 929-768-1	$+10\pm1.3$	$+2\pm1.0$	11.69 ± 0.14	1.56 ± 0.08	L1	M9	M7	L4	
VHS J0159+0044	01h 59m 47.66s	+00d 44m 24.52s	TYC 4686-745-1	$+0\pm1.8$	-42 ± 0.6	12.92 ± 0.11	1.71 ± 0.12	L4	L1	M6	L6	
VHS J0750-0843	07h 50m 00.01s	-08d 43m 34.45s	TYC 5411-2014-1	-1 ± 0.8	$+5\pm0.7$	9.95 ± 0.42	1.31 ± 0.08	M6		M6	L2	

TABLE A.6: Additional Metallicity Outlier Candidates

Name	RA (J2000)	Dec. (J2000)	Primary Candidate	Parallax mas	Primary $\mu_\alpha \cos\delta$ mas yr^{-1}	Primary μ_δ mas yr^{-1}	Companion $\mu_\alpha \cos\delta$ mas yr^{-1}	Companion μ_δ mas yr^{-1}	CPM Source	$\sigma\Delta\mu$	$\mu \setminus \sigma\mu$	Primary Metallicity
UKIDSS J1323+0133	13h 23m 28.79s	+01d 33m 03.63s	TYC 300-28-1	10.98 ± 0.49	-10 ± 2.4	-54 ± 0.3	-19 ± 15.9	-36 ± 15.9	UKIDSS	1.2	2.6	LAMOST [Fe/H] = -0.68
UKIDSS J1528+2841	15h 28m 29.52s	+28d 41m 00.51s	TYC 2032-1306-1	3.76 ± 0.24	-18 ± 0.6	$+10 \pm 1.1$	-17 ± 3.3	$+9 \pm 3.3$	UKIDSS	0.6	5.8	LAMOST [Fe/H] = +0.24
UKIDSS J1229+0339	12h 29m 09.77s	+03d 39m 53.58s	TYC 285-281-1	9.82 ± 0.92	$+38 \pm 3.7$	-38 ± 1.8	$+64 \pm 17.7$	-30 ± 17.7	UKIDSS	1.5	4.0	LAMOST [Fe/H] = +0.24
UKIDSS J0012+0035	00h 12m 17.67s	+00d 35m 07.87s	TYC 2-56-1	7.02 ± 0.74	$+6 \pm 3.0$	-49 ± 1.3	$+0 \pm 6.0$	-40 ± 6.0	UKIDSS	1.8	6.7	RAVE [M/H] = -0.47
VHS J2214-0119	22h 14m 48.89s	-01d 19m 16.98s	TYC 5225-498-1	6.14 ± 0.64	$+66 \pm 2.4$	$+5 \pm 1.1$	$+55 \pm 24.6$	$+7 \pm 24.4$	2P	0.5	2.3	LAMOST [Fe/H] = +0.24
VHS J1546-1518	15h 46m 11.70s	-15d 18m 45.64s	TYC 6186-1376-1	4.78 ± 0.27	-78 ± 0.8	-89 ± 0.4	-62 ± 84.4	-121 ± 82.6	SC	0.4	1.6	RAVE [M/H] = -0.45
UKIDSS J0001+0010	00h 01m 44.49s	+00d 10m 43.16s	TYC 4663-94-1	19.73 ± 0.27	$+20 \pm 0.1$	-114 ± 0.0	-27 ± 36.2	-108 ± 36.2	UKIDSS	1.3	3.1	RAVE [M/H] = -0.33
UKIDSS J1058+0837	10h 58m 28.11s	+08d 37m 33.19s	TYC 847-850-1	6.04 ± 0.59	-97 ± 2.0	-60 ± 0.9	-88 ± 8.6	-48 ± 8.4	Smith	1.8	11.7	LAMOST [Fe/H] = +0.42
UKIDSS J1104+0041	11h 04m 20.98s	+00d 41m 58.80s	TYC 4921-362-1	4.44 ± 0.54	-53 ± 1.4	-40 ± 0.8	-81 ± 36.2	-38 ± 25.4	2P	0.8	2.5	RAVE [M/H] = +0.25
VHS J2113-0807	21h 13m 02.67s	-08d 07m 36.31s	TYC 5772-539-1	10.61 ± 0.65	$+7 \pm 2.4$	$+79 \pm 1.2$	$+11 \pm 42.7$	$+119 \pm 43.4$	2P	0.9	2.8	RAVE [M/H] = -0.31

Appendix B

Summary Of Observation Proposals

Based on the selected candidates, two distinct programs of observation are employed, outlined in Sections B.1 and B.2.

B.1 Spectroscopic Targets

Candidates considered to be a promising CPM match (as defined by Section 2.8) were considered for spectroscopic observation regardless of the priority score given to the candidate in Section 2.13 and regardless of the spectral typing diagnosis from Section 3.1. All of the candidates selected this way (listed in Tables A.2 and A.3 in Appendix A) have some indicator of youth.

Candidates with a potential primary that has low proper motion ($\mu < 50$mas yr^{-1}) cannot be confirmed as being part of a CPM pair with further imaging. These candidates were moved forward to the spectroscopic observation list. In order to maximize the chances of identifying young benchmarks, only candidates considered likely to be a potentially genuine young companion based onthe spectral type estimations from Section 3.1 and candidates with at least a 'B' priority from Section 2.13 are considered.

Finally, possible L+T unresolved binaries from Section 3.1 with low proper motion primaries were also added to the target list for spectrography.

The following spectrographic observing proposals were submitted:

- CNTAC proposal CN2017B-36 for use of the FIRE instrument submitted by collaborator Radostin Kurtev of the Universidad de Valparaíso - Granted, swapped to FourSTAR NIR camera due to FIRE being under maintanence. Carried out 17th and 18th of November 2017.

- NASA IRTF proposal for use of the SpeX instrument submitted by supervisor Federico Marocco - Not Granted.

- ESO P101 proposal for the use of Xshooter instrument submitted by supervisor Federico Marocco - Granted. Given priority C and scheduled as a filler program for 2018.

B.2 Photometry Observation Targets

Candidates with fast moving primaries ($\mu > 50$mas yr^{-1}) were submitted for further photometry in order to further constrain the proper motion of the UCD candidate.

The following observing proposals were submitted to obtain photometry at additional epochs to aid proper motion constraining:

- ESO P100 proposal for use of EFOSC2 submitted by supervisor Federico Marocco - Not Granted.

- ESO P101 proposal for use of SofI on the NTT submitted by supervisor Federico Marocco - Granted. Observing awarded for 18th, 19th and 20th of July 2018.

Bibliography

Allers, K.N. and Liu, M.C., 2013. A Near-infrared Spectroscopic Study of Young Field Ultracool Dwarfs. *ApJ*, 772:79.

Ammons, S.M., Robinson, S.E., Strader, J., et al., 2006. The N2K Consortium. IV. New Temperatures and Metallicities for More than 100,000 FGK Dwarfs. *ApJ*, 638:1004.

Baglin, A., Auvergne, M., Barge, P., et al., 2002. COROT: asteroseismology and planet finding. In B. Battrick, F. Favata, I.W. Roxburgh, and D. Galadi, editors, *Stellar Structure and Habitable Planet Finding*, volume 485 of *ESA Special Publication*, pages 17–24.

Bailer-Jones, C.A.L., Andrae, R., Arcay, B., et al., 2013. The Gaia astrophysical parameters inference system (Apsis). Pre-launch description. *A&A*, 559:A74.

Baraffe, I., Chabrier, G., Allard, F., et al., 1998. Evolutionary models for solar metallicity low-mass stars: mass-magnitude relationships and color-magnitude diagrams. *A&A*, 337:403.

Baraffe, I., Chabrier, G., Barman, T.S., et al., 2003. Evolutionary models for cool brown dwarfs and extrasolar giant planets. The case of HD 209458. *A&A*, 402:701.

Baraffe, I., Homeier, D., Allard, F., et al., 2015. New evolutionary models for pre-main sequence and main sequence low-mass stars down to the hydrogen-burning limit. *A&A*, 577:A42.

Barenfeld, S.A., Bubar, E.J., Mamajek, E.E., et al., 2013. A Kine-chemical Investigation of the AB Dor Moving Group "Stream". *ApJ*, 766:6.

Bate, M.R., Bonnell, I.A., and Bromm, V., 2002. The formation mechanism of brown dwarfs. *MNRAS*, 332:L65.

Becklin, E.E. and Zuckerman, B., 1988. A low-temperature companion to a white dwarf star. *Nature*, 336:656.

Best, W.M.J., Liu, M.C., Magnier, E.A., et al., 2015. A Search for L/T Transition Dwarfs with Pan-STARRS1 and WISE. II. L/T Transition Atmospheres and Young Discoveries. *ApJ*, 814:118.

Blanton, M.R. and Roweis, S., 2007. K-Corrections and Filter Transformations in the Ultraviolet, Optical, and Near-Infrared. *AJ*, 133:734.

Boss, A.P., Butler, R.P., Hubbard, W.B., et al., 2007. Working Group on Extrasolar Planets. *Transactions of the International Astronomical Union, Series A*, 26:183.

Bowler, B.P., Liu, M.C., Mawet, D., et al., 2017. Planets around Low-mass Stars (PALMS). VI. Discovery of a Remarkably Red Planetary-mass Companion to the AB Dor Moving Group Candidate 2MASS J22362452+4751425*. *AJ*, 153:18.

Burgasser, A.J., 2001. *The Discovery and Characterization of Methane-bearing Brown Dwarfs and the Definition of the T Spectral Class*. Ph.D. thesis, Department of Physics, California Institute of Technology.

Burgasser, A.J., 2014. The SpeX Prism Library: 1000+ low-resolution, near-infrared spectra of ultracool M, L, T and Y dwarfs. In *Astronomical Society of India Conference Series*, volume 11 of *Astronomical Society of India Conference Series*.

Burgasser, A.J., Geballe, T.R., Leggett, S.K., et al., 2006. A Unified Near-Infrared Spectral Classification Scheme for T Dwarfs. *ApJ*, 637:1067.

Burgasser, A.J. and McElwain, M.W., 2006. Resolved Spectroscopy of M Dwarf/L Dwarf Binaries. I. DENIS J220002.05-303832.9AB. *AJ*, 131:1007.

Burgasser, A.J., Reid, I.N., Siegler, N., et al., 2007. Not Alone: Tracing the Origins of Very-Low-Mass Stars and Brown Dwarfs Through Multiplicity Studies. *Protostars and Planets V*, pages 427–441.

Burleigh, M.R., Hogan, E., Dobbie, P.D., et al., 2006. A near-infrared spectroscopic detection of the brown dwarf in the post common envelope binary WD0137-349. *MNRAS*, 373:L55.

Burningham, B., Cardoso, C.V., Smith, L., et al., 2013. 76 T dwarfs from the UKIDSS LAS: benchmarks, kinematics and an updated space density. *MNRAS*, 433:457.

Burningham, B., Lucas, P.W., Leggett, S.K., et al., 2011. The discovery of the T8.5 dwarf UGPS J0521+3640. *MNRAS*, 414:L90.

Burningham, B., Pinfield, D.J., Lucas, P.W., et al., 2010. 47 new T dwarfs from the UKIDSS Large Area Survey. *MNRAS*, 406:1885.

Burrows, A., Hubbard, W.B., Lunine, J.I., et al., 1997. Extra-Solar Giant Planet and Brown Dwarf Models. In D. Soderblom, editor, *Planets Beyond the Solar System and the Next Generation of Space Missions*, volume 119 of *Astronomical Society of the Pacific Conference Series*, page 9.

Burrows, A., Sudarsky, D., and Hubeny, I., 2006. L and T Dwarf Models and the L to T Transition. *ApJ*, 640:1063.

Burrows, A., Sudarsky, D., and Lunine, J.I., 2003. Beyond the T Dwarfs: Theoretical Spectra, Colors, and Detectability of the Coolest Brown Dwarfs. *ApJ*, 596:587.

Chabrier, G., 2005. The Initial Mass Function: From Salpeter 1955 to 2005. In E. Corbelli, F. Palla, and H. Zinnecker, editors, *The Initial Mass Function 50 Years Later*, volume 327 of *Astrophysics and Space Science Library*, page 41.

Chaplin, W.J., Basu, S., Huber, D., et al., 2014. Asteroseismic Fundamental Properties of Solar-type Stars Observed by the NASA Kepler Mission. *ApJ*, 210:1.

Cruz, K.L., Kirkpatrick, J.D., and Burgasser, A.J., 2009. Young L Dwarfs Identified in the Field: A Preliminary Low-Gravity, Optical Spectral Sequence from L0 to L5. *AJ*, 137:3345.

Cruz, K.L., Reid, I.N., Kirkpatrick, J.D., et al., 2007. Meeting the Cool Neighbors. IX. The Luminosity Function of M7-L8 Ultracool Dwarfs in the Field. *AJ*, 133:439.

Cruz, K.L., Reid, I.N., Liebert, J., et al., 2003. Meeting the Cool Neighbors. V. A 2MASS-Selected Sample of Ultracool Dwarfs. *AJ*, 126:2421.

Cushing, M.C., Kirkpatrick, J.D., Gelino, C.R., et al., 2011. The Discovery of Y Dwarfs using Data from the Wide-field Infrared Survey Explorer (WISE). *ApJ*, 743:50.

Dahn, C.C., Harris, H.C., Vrba, F.J., et al., 2002. Astrometry and Photometry for Cool Dwarfs and Brown Dwarfs. *AJ*, 124:1170.

Day-Jones, A., Marocco, F., Pinfield, D., et al., 2013. The sub-stellar birth rate from UKIDSS. *MNRAS*, 430(2):1171.

Day-Jones, A.C., Marocco, F., Pinfield, D.J., et al., 2013. The sub-stellar birth rate from UKIDSS. *MNRAS*, 430:1171.

Deacon, N.R., Liu, M.C., Magnier, E.A., et al., 2014. Wide Cool and Ultracool Companions to Nearby Stars from Pan-STARRS 1. *ApJ*, 792:119.

Delorme, P., Gagné, J., Girard, J.H., et al., 2013. Direct-imaging discovery of a 12-14 Jupiter-mass object orbiting a young binary system of very low-mass stars. *A&A*, 553:L5.

Dupuy, T.J. and Kraus, A.L., 2013. Distances, Luminosities, and Temperatures of the Coldest Known Substellar Objects. *Science*, 341:1492.

Dupuy, T.J. and Liu, M.C., 2012. The Hawaii Infrared Parallax Program. I. Ultracool Binaries and the L/T Transition. *ApJ*, 201:19.

Duquennoy, A. and Mayor, M., 1991. Multiplicity among solar-type stars in the solar neighbourhood. II - Distribution of the orbital elements in an unbiased sample. *A&A*, 248:485.

Elliott, P., Huélamo, N., Bouy, H., et al., 2015. Search for associations containing young stars (SACY). VI. Is multiplicity universal? Stellar multiplicity in the range 3-1000 au from adaptive-optics observations. *A&A*, 580:A88.

Emerson, J., Sutherland, W., McPherson, A., et al., 2004. The Visible and Infrared Survey Telescope for Astronomy. *The Messenger*, 117:27.

Faherty, J.K., Burgasser, A.J., Walter, F.M., et al., 2012. The Brown Dwarf Kinematics Project (BDKP). III. Parallaxes for 70 Ultracool Dwarfs. *ApJ*, 752:56.

Faherty, J.K., Riedel, A.R., Cruz, K.L., et al., 2016. Population Properties of Brown Dwarf Analogs to Exoplanets. *ApJ*, 225:10.

Folkes, S.L., Pinfield, D.J., Jones, H.R.A., et al., 2012. Identifying ultra-cool dwarfs at low Galactic latitudes: a southern candidate catalogue. *MNRAS*, 427:3280.

Gaia Collaboration, Brown, A.G.A., Vallenari, A., et al., 2016a. Gaia Data Release 1. Summary of the astrometric, photometric, and survey properties. *A&A*, 595:A2.

Gaia Collaboration, Prusti, T., de Bruijne, J.H.J., et al., 2016b. The Gaia mission. *A&A*, 595:A1.

Geballe, T.R., Knapp, G.R., Leggett, S.K., et al., 2002. Toward Spectral Classification of L and T Dwarfs: Infrared and Optical Spectroscopy and Analysis. *ApJ*, 564:466.

Gillon, M., Triaud, A.H.M.J., Demory, B.O., et al., 2017. Seven temperate terrestrial planets around the nearby ultracool dwarf star TRAPPIST-1. *Nature*, 542:456.

Gilmore, G., Randich, S., Asplund, M., et al., 2012. The Gaia-ESO Public Spectroscopic Survey. *The Messenger*, 147:25.

Gomes, J.I., Pinfield, D.J., Marocco, F., et al., 2013. Two new ultracool benchmark systems from WISE+2MASS. *MNRAS*, 431:2745.

Green, S, F. and Jones, M, H., 2004. *An Introduction to the Sun and Stars*. Cambridge University Press.

Hambly, N., Read, M., Mann, R., et al., 2004. The SuperCOSMOS Science Archive. In F. Ochsenbein, M.G. Allen, and D. Egret, editors, *Astronomical Data Analysis Software and Systems (ADASS) XIII*, volume 314 of *Astronomical Society of the Pacific Conference Series*, page 137.

Hambly, N.C., MacGillivray, H.T., Read, M.A., et al., 2001. The SuperCOSMOS Sky Survey - I. Introduction and description. *MNRAS*, 326:1279.

Hayashi, C. and Nakano, T., 1963. Evolution of Stars of Small Masses in the Pre-Main-Sequence Stages. *Progress of Theoretical Physics*, 30:460.

Janson, M., Jayawardhana, R., Girard, J.H., et al., 2012. New Brown Dwarf Companions to Young Stars in Scorpius-Centaurus. *ApJ*, 758:L2.

Kiraga, M., 2012. ASAS Photometry of ROSAT Sources. I. Periodic Variable Stars Coincident with Bright Sources from the ROSAT All Sky Survey. *Acta Astronomica*, 62:67.

Kirkpatrick, J.D., 2005. New spectral types L and T. *Annual Review of Astronomy and Astrophysics*, 43:195.

Kirkpatrick, J.D., Cruz, K.L., Barman, T.S., et al., 2008. A Sample of Very Young Field L Dwarfs and Implications for the Brown Dwarf "Lithium Test" at Early Ages. *ApJ*, 689:1295-1326.

Kirkpatrick, J.D., Looper, D.L., Burgasser, A.J., et al., 2010. Discoveries from a Near-infrared Proper Motion Survey Using Multi-epoch Two Micron All-Sky Survey Data. *ApJ*, 190:100.

Kirkpatrick, J.D., Reid, I.N., Liebert, J., et al., 1999. Dwarfs Cooler than "M": The Definition of Spectral Type "L" Using Discoveries from the 2 Micron All-Sky Survey (2MASS). *ApJ*, 519:802.

Kirkpatrick, J.D., Reid, I.N., Liebert, J., et al., 2000. 67 Additional L Dwarfs Discovered by the Two Micron All Sky Survey. *AJ*, 120:447.

Kirkpatrick, J.D., Schneider, A., Fajardo-Acosta, S., et al., 2014. The AllWISE Motion Survey and the Quest for Cold Subdwarfs. *ApJ*, 783:122.

Koch, D.G., Borucki, W.J., Basri, G., et al., 2010. Kepler Mission Design, Realized Photometric Performance, and Early Science. *ApJ*, 713:L79.

Kordopatis, G., Gilmore, G., Steinmetz, M., et al., 2013. The Radial Velocity Experiment (RAVE): Fourth Data Release. *AJ*, 146(5):134.

Kraus, A.L., Shkolnik, E.L., Allers, K.N., et al., 2014. A Stellar Census of the Tucana-Horologium Moving Group. *AJ*, 147:146.

Kumar, S.S., 1962. Study of Degeneracy in Very Light Stars. *AJ*, 67:579.

Lawrence, A., Warren, S., Almaini, O., et al., 2007. The UKIRT infrared deep sky survey (UKIDSS). *MNRAS*, 379(4):1599.

Lebreton, Y. and Goupil, M.J., 2014. Asteroseismology for "à la carte" stellar age-dating and weighing. Age and mass of the CoRoT exoplanet host HD 52265. *A&A*, 569:A21.

Leggett, S.K., Allard, F., Dahn, C., et al., 2000a. Spectral Energy Distributions for Disk and Halo M Dwarfs. *ApJ*, 535:965.

Leggett, S.K., Allard, F., Geballe, T.R., et al., 2001. Infrared Spectra and Spectral Energy Distributions of Late M and L Dwarfs. *ApJ*, 548:908.

Leggett, S.K., Allard, F., and Hauschildt, P.H., 1998. Infrared Colors at the Stellar/Substellar Boundary. *ApJ*, 509:836.

Leggett, S.K., Currie, M.J., Varricatt, W.P., et al., 2006. JHK observations of faint standard stars in the Mauna Kea Observatories near-infrared photometric system. *MNRAS*, 373:781.

Leggett, S.K., Geballe, T.R., Fan, X., et al., 2000b. The Missing Link: Early Methane ("T") Dwarfs in the Sloan Digital Sky Survey. *ApJ*, 536:L35.

Lindegren, L., Lammers, U., Bastian, U., et al., 2016. Gaia Data Release 1. Astrometry: One Billion Positions, Two Million Proper Motions and Parallaxes. *A&A*, 595:A4.

Liu, M.C., Dupuy, T.J., and Allers, K.N., 2016. The Hawaii Infrared Parallax Program. II. Young Ultracool Field Dwarfs. *ApJ*, 833:96.

Liu, M.C., Magnier, E.A., Deacon, N.R., et al., 2013. The Extremely Red, Young L Dwarf PSO J318.5338-22.8603: A Free-floating Planetary-mass Analog to Directly Imaged Young Gas-giant Planets. *ApJ*, 777:L20.

Lodders, K., 1999. Alkali Element Chemistry in Cool Dwarf Atmospheres. *ApJ*, 519:793.

Lucas, P.W., Roche, P.F., Allard, F., et al., 2001. Infrared spectroscopy of substellar objects in Orion. *MNRAS*, 326:695.

Lucas, P.W., Tinney, C.G., Burningham, B., et al., 2010. The discovery of a very cool, very nearby brown dwarf in the Galactic plane. *MNRAS*, 408:L56.

Luhman, K.L., 2014. Discovery of a ˜250 K Brown Dwarf at 2 pc from the Sun. *ApJ*, 786:L18.

Luhman, K.L. and Esplin, T.L., 2016. The Spectral Energy Distribution of the Coldest Known Brown Dwarf. *AJ*, 152:78.

Lutz, T.E. and Kelker, D.H., 1973. On the Use of Trigonometric Parallaxes for the Calibration of Luminosity Systems: Theory. *The Publications of the Astronomical Society of the Pacific*, 85:573.

Magnier, E.A., Schlafly, E.F., Finkbeiner, D.P., et al., 2016. Pan-STARRS Photometric and Astrometric Calibration. *ArXiv e-prints*.

Makarov, V.V. and Urban, S., 2000. A moving group of young stars in Carina-Vela. *MNRAS*, 317:289.

Malo, L., Doyon, R., Feiden, G.A., et al., 2014. BANYAN. IV. Fundamental Parameters of Low-mass Star Candidates in Nearby Young Stellar Kinematic Groups - Isochronal Age Determination using Magnetic Evolutionary Models. *ApJ*, 792:37.

Marcy, G.W. and Butler, R.P., 2000. Planets Orbiting Other Suns. *The Publications of the Astronomical Society of the Pacific*, 112:137.

Marigo, P., Girardi, L., Bressan, A., et al., 2017. A New Generation of PARSEC-COLIBRI Stellar Isochrones Including the TP-AGB Phase. *ApJ*, 835:77.

Marley, M.S. and Robinson, T.D., 2015. On the Cool Side: Modeling the Atmospheres of Brown Dwarfs and Giant Planets. *Annual Review of Astronomy and Astrophysics*, 53:279.

Marley, M.S., Saumon, D., Cushing, M., et al., 2012. Masses, Radii, and Cloud Properties of the HR 8799 Planets. *ApJ*, 754:135.

Marley, M.S., Saumon, D., Guillot, T., et al., 1996. Atmospheric, Evolutionary, and Spectral Models of the Brown Dwarf Gliese 229 B. *Science*, 272:1919.

Marocco, F., Jones, H.R.A., Day-Jones, A.C., et al., 2015. A large spectroscopic sample of L and T dwarfs from UKIDSS LAS: peculiar objects, binaries, and space density. *MNRAS*, 449:3651.

Marocco, F., Pinfield, D.J., Cook, N.J., et al., 2017. Ultracool dwarf benchmarks with Gaia primaries. *MNRAS*, 470:4885.

Martin, E.C., Mace, G.N., McLean, I.S., et al., 2017. Surface Gravities for 228 M, L, and T Dwarfs in the NIRSPEC Brown Dwarf Spectroscopic Survey. *ApJ*, 838:73.

Maxted, P.F.L., Napiwotzki, R., Dobbie, P.D., et al., 2006. Survival of a brown dwarf after engulfment by a red giant star. *Nature*, 442:543.

Morley, C.V., Fortney, J.J., Marley, M.S., et al., 2012. Neglected Clouds in T and Y Dwarf Atmospheres. *ApJ*, 756:172.

Morley, C.V., Marley, M.S., Fortney, J.J., et al., 2014. Water Clouds in Y Dwarfs and Exoplanets. *ApJ*, 787:78.

Nakajima, T., Oppenheimer, B.R., Kulkarni, S.R., et al., 1995. Discovery of a cool brown dwarf. *Nature*, 378:463.

Oh, S., Price-Whelan, A.M., Hogg, D.W., et al., 2017. Comoving Stars in Gaia DR1: An Abundance of Very Wide Separation Comoving Pairs. *AJ*, 153:257.

Oudmaijer, R.D., Groenewegen, M.A.T., and Schrijver, H., 1998. The Lutz-Kelker bias in trigonometric parallaxes. *MNRAS*, 294:L41.

Pearl, J.C., Conrath, B.J., Hanel, R.A., et al., 1990. The albedo, effective temperature, and energy balance of Uranus, as determined from Voyager IRIS data. *Icarus*, 84:12.

Pecaut, M.J. and Mamajek, E.E., 2013. Intrinsic Colors, Temperatures, and Bolometric Corrections of Pre-main-sequence Stars. *ApJ*, 208:9.

Percy, J.R., 2011. *Understanding Variable Stars*. Cambridge University Press.

Pinfield, D.J., Burningham, B., Tamura, M., et al., 2008. Fifteen new T dwarfs discovered in the UKIDSS Large Area Survey. *MNRAS*, 390:304.

Pinfield, D.J., Jones, H.R.A., Lucas, P.W., et al., 2006. Finding benchmark brown dwarfs to probe the substellar initial mass function as a function of time. *MNRAS*, 368:1281.

Preibisch, T., Brown, A.G.A., Bridges, T., et al., 2002. Exploring the Full Stellar Population of the Upper Scorpius OB Association. *AJ*, 124:404.

Rayner, J.T., Toomey, D.W., Onaka, P.M., et al., 2003. SpeX: A Medium-Resolution 0.8-5.5 Micron Spectrograph and Imager for the NASA Infrared Telescope Facility. *The Publications of the Astronomical Society of the Pacific*, 115:362.

Rebolo, R., Zapatero Osorio, M.R., and Martín, E.L., 1995. Discovery of a brown dwarf in the Pleiades star cluster. *Nature*, 377:129.

Reed, B.C., 1998. The Composite Observational-Theoretical HR Diagram. *Journal of the Royal Astronomical Society of Canada*, 92:36.

Reid, I.N., Cruz, K.L., Allen, P., et al., 2004. Meeting the Cool Neighbors. VIII. A Preliminary 20 Parsec Census from the NLTT Catalogue. *AJ*, 128:463.

Richichi, A., Fors, O., Cusano, F., et al., 2012. A Catalog of Near-IR Sources Found to be Unresolved with Milliarcsecond Resolution. *ApJ*, 203:33.

Robin, A.C., Luri, X., Reylé, C., et al., 2012. Gaia Universe model snapshot. A statistical analysis of the expected contents of the Gaia catalogue. *A&A*, 543:A100.

Schlafly, E.F. and Finkbeiner, D.P., 2011. Measuring Reddening with Sloan Digital Sky Survey Stellar Spectra and Recalibrating SFD. *ApJ*, 737:103.

Schmidt, S.J., West, A.A., Hawley, S.L., et al., 2010. Colors and kinematics of L dwarfs from the Sloan Digital Sky Survey. *AJ*, 139(5):1808.

Schmidt, S.J., West, A.A., Hawley, S.L., et al., 2010. Colors and Kinematics of L Dwarfs from the Sloan Digital Sky Survey. *AJ*, 139:1808.

Scholz, R.D., McCaughrean, M.J., Zinnecker, H., et al., 2005. SSSPM J1102-3431: A probable new young brown dwarf member of the TW Hydrae Association. *A&A*, 430:L49.

Skrutskie, M.F., Cutri, R.M., Stiening, R., et al., 2006. The Two Micron All Sky Survey (2MASS). *AJ*, 131:1163.

Skrzypek, N., Warren, S.J., Faherty, J.K., et al., 2015. Photometric brown-dwarf classification. I. A method to identify and accurately classify large samples of brown dwarfs without spectroscopy. *A&A*, 574:A78.

Smith, L., Lucas, P.W., Burningham, B., et al., 2014. A 1500 deg^2 near infrared proper motion catalogue from the UKIDSS Large Area Survey. *MNRAS*, 437:3603.

Smith, L.C., Lucas, P.W., Kurtev, R., et al., 2018. VIRAC: the VVV Infrared Astrometric Catalogue. *MNRAS*, 474:1826.

Spiegel, D.S., Burrows, A., and Milsom, J.A., 2011. The Deuterium-burning Mass Limit for Brown Dwarfs and Giant Planets. *ApJ*, 727:57.

Steele, I.A. and Jones, H.R.A., 2001. Ultracool Dwarf Stars: Surveys, Properties, and Spectral Classification. *The Publications of the Astronomical Society of the Pacific*, 113:403.

Tarter, J.C., 1986. An historical perspective - Brown is not a color. In M.C. Kafatos, R.S. Harrington, and S.P. Maran, editors, *Astrophysics of Brown Dwarfs*, pages 121–138.

Torres, C.A.O., Quast, G.R., da Silva, L., et al., 2006. Search for associations containing young stars (SACY). I. Sample and searching method. *A&A*, 460:695.

Vos, J.M., Allers, K.N., and Biller, B.A., 2017. The Viewing Geometry of Brown Dwarfs Influences Their Observed Colours and Variability Properties. *ArXiv e-prints*.

Weinberger, A.J., Anglada-Escudé, G., and Boss, A.P., 2013. Distance and Kinematics of the TW Hydrae Association from Parallaxes. *ApJ*, 762:118.

Wenger, M., Ochsenbein, F., Egret, D., et al., 2000. The SIMBAD astronomical database. The CDS reference database for astronomical objects. *Astronomy and Astrophysics Supplemen*, 143:9.

Wolf, C., Onken, C.A., Luvaul, L.C., et al., 2018. SkyMapper Southern Survey: First Data Release (DR1). *ArXiv e-prints*.

Wright, E.L., Eisenhardt, P.R.M., Mainzer, A.K., et al., 2010. The Wide-field Infrared Survey Explorer (WISE): Mission Description and Initial On-orbit Performance. *AJ*, 140:1868-1881.

York, D.G., Adelman, J., Anderson Jr, J.E., et al., 2000. The Sloan Digital Sky Survey: Technical Summary. *AJ*, 120(3):1579.

Yuan, H.B., Liu, X.W., Huo, Z.Y., et al., 2015. LAMOST Spectroscopic Survey of the Galactic Anticentre (LSS-GAC): target selection and the first release of value-added catalogues. *MNRAS*, 448(1):855.

Zhang, Z.H., Pinfield, D.J., Gálvez-Ortiz, M.C., et al., 2017. Primeval very low-mass stars and brown dwarfs - I. Six new L subdwarfs, classification and atmospheric properties. *MNRAS*, 464:3040.